UNIVERSITA' DEGLI STUDI DI MILANO
Facoltà di Scienza Matematiche, Fisiche e Naturali
Corso di Laurea in Fisica

QUENCH PROTECTION ANALYSIS FOR THE SUPERCONDUCTING QUADRUPOLES Q2a/Q2b FOR THE INNER TRIPLET OF LHC

Supervisor: Prof. **Lucio ROSSI**

External Supervisor: **Dr. Michael J. LAMM**

LAUREA Thesis by:
Luisa Chiesa
Matr. N. 533433

Academic Year 1999-2000; lll Session

CONTENTS

Introduction

The LHC (Large Hadron Collider) is the new collision synchrotron located at CERN and projected to reach a luminosity of 10^{34} $cm^{-2}s^{-1}$ and collision energy of 14TeV, values much greater than ever reached up to now.
In order to obtain this aim several scientific and technologic problems have to be solved during the past years and in particular a fundamental solution applied to the entire machine is the choice of superconducting magnets, which need a cryogenic system, instead of standard magnets.
To obtain this luminosity the magnetic structure for the focusing of the beams in proximity of intersection zones has to be very strong and precise.
In particular inner triplet quadrupoles of the focusing system have to produce a quadrupolar field very intense (gradient field of 215 T/m on length of 5.5m each quadrupole) in a big aperture of 70 mm in order to contain both incident beams.

In this thesis we studied the main characteristics of the focusing elements (superconducting quadrupoles), which will be used in the LHC Inner Triplet. These superconducting quadrupoles are the main contribution from Fermilab for the LHC accelerator. The program at Fermilab is divided in two parts. The first one was used to find the best solution for mechanical, magnetic and quench protection problems building superconducting quadrupoles 2m long tested in a vertical dewar (VMTF) and it was finished completely in February 2000. The second part is still in progress and consists in building the cryogenic system positioned horizontally for tests on full scale magnets 5.5m long and, later, on the entire string of quadrupoles of the inner triplet (composed of four superconducting magnets).
Besides the general characteristics of these quadrupoles this thesis is focused on quench protection issue, which is one of the most important part in order to prevent magnets failure. The aim of this work is to analyze data from model magnets and extend the prediction of peak temperatures (maximum temperature reached in the magnet after a quench) and peak voltage to ground (maximum voltage developed in the winding) to the final system Q2a/Q2b (internal magnets of the triplet) used in the machine. In order to be protected in case of quench the peak temperatures have to be lower than **400K** and the peak voltage to ground lower than **400V**.

In the **first chapter** we describe general characteristics of the machine with particular attention to low-β insertions (strong focusing quadrupoles). We also introduced superconductivity with particular attention to Niobium Titanium (material used for magnets in the LHC).

The **second chapter** is dedicated to superconducting quadrupoles produced at Fermilab with a general overview of mechanics, cable design, field quality and set up for the tests. After these general aspects of the quadrupoles the attention is focused on quench protection problem, very important issue in big system as LHC.
In the **third chapter** we introduce quench protection and different kinds of protection systems with particular attention for the one used for quadrupoles of inner triplet in the LHC. These quadrupoles use quench protection system based on strip heaters. Strip heaters are simply long strips made of stainless steel alternate with copper covered by sheet of kapton (insulation). They are connected to a

capacitor bank and this bank is discharged upon detection of voltage imbalance in the magnet due to resistive voltage from a quench. Once the heaters are fired (they develop resistance) they help to spread quickly the heat reducing the hot spot temperature and big imbalance in voltage between quadrants.

In **chapter 4** we describe different tools used for analysis (parameters used, calculation of volumetric specific heat and resistivity in function of temperature for these quadrupoles). We also discuss different methods used to estimate the main properties of quadrupoles related to quench protection (such as peak temperature). Three methods are used to estimate this quantity.
The actual measurement taken gives the total resistance developed by different parts of magnets. Of particular interest is the resistance of the segment where the quench starts. From this value of resistance one can estimate the peak temperature reached from that segment by knowing its room temperature resistance.
The second method is an adiabatic one (it does not consider the beneficial contribute given by liquid helium) and it uses the relation between MIITs values and temperature in order to find the peak temperature. Being an adiabatic method the temperature is overestimated. This method is used for predictions for the final system Q2a/Q2b.
The third method (so-called inductance method) was used only for preliminary comparison since it was not useful for our final aim.

In **chapter 5** we analyze data taken during the tests of model magnets and with the tools before introduced we study all the parameters which characterize them. The data helped to make a comparison between different model magnets and find out necessary improvements, mechanical limits of the magnets and the best choice of strip heaters to use in the final design.

With more attention we discuss the main properties related to quench protection such as:

- peak voltage (maximum voltage developed across one quadrant),
- peak temperature (maximum temperature reached from the point where quench develops or other part of the magnet),
- quench velocity (velocity of the heat in propagating across turns and different quadrants),
- MIITs values (this quantity is the integral of current square times an interval of time and it is easily related to temperature and resistance).

In this chapter we consider different kinds of studies to focus the attention on each critical factor.
For each model magnet there were three possible kinds of study besides spontaneous quenches.

These studies are:

1. Spot heater induced quenches. In this case the heaters are fired at t=0 ms. The quench is induced from a spot heater, which is a little stainless steel segment that can be in low field position or high field position on the magnet and can be fired to simulate a quench. This kind of study is used to estimate the peak temperature in critical positions such as “high field” position (the most suitable for a natural quench since closer to critical surface) and “low field” position (quite uncommon but very dangerous for peak temperature reached).
2. Strip heaters induced quenches (and Manual trip). In this case the strip heaters are fired before t=0 ms (and at t=0ms). These studies permit to analyze the efficiency of the heaters.

3. $\underline{V_{min}}$. In this case the heaters are fired before t=0ms. With these studies one wants to find the minimum energy necessary to quench the magnet with the only heaters (lower the energy more effective is the heater).

In **chapter 6** the final design of the inner triplet is described and we make simulations for the final system Q2a and Q2b (Q2a/Q2b bussed in series and 5.5m each). In these predictions we use an adiabatic model to calculate peak temperatures and build voltage profiles across each coil of the two magnets. The aim of these calculations is to verify safety condition of the magnets even in their final design (**peak temperatures<400K**; **peak voltage to ground<400V**).
Initially we use data of model magnets to estimate quantities such as quench velocity (to estimate the time necessary to reach adjacent turns and other quadrant), window of time between a quench occurs and heaters to become effective. In particular with these data we observe "quench back" effect, which permits us to state that the magnets after a certain amount of time quench entirely even if the quench has not travel all along the magnet.
Then we consider particular events with different configuration of heaters for model magnets HGQ08 and HGQ09 and we build a model using parameters estimated with data analysis in order to compare directly the real signals of resistance and voltage profile with the calculation. The model supposes a starting current and divides the magnets in different quadrants and each quadrant is divided in more parts in order to consider different magnetic field. Each part has a different starting time to collect MIITs in function of time chosen appropriately in relation with the model magnets. From the relation between MIITs and temperature and field the temperature profile in function of time can be calculated and consequently the resistivity and resistance profile. From resistance then it is possible to find the resistive voltage profile and estimate the total voltage considering a constant inductance of the magnet and the current change in time.
This model works in circular way in fact a current at t_1 gives MIITs, temperature, resistivity, resistance and voltage at that time then the total resistance is used to calculate the next current at t_2 (there is an exponential decay once a quench occurs).
This model is used to predict peak temperature and peak voltage to ground for the system Q2a/Q2b of two full-scale magnets.
These quantities are predicted both for standard conditions and for particular events in which some failures in protection system is simulated. In fact in ideal conditions the two magnets in series should be exactly the same and the quench protection system should work in symmetric way.

In reality the magnets can have different residual resistance ratio (RRR) and heaters can be effective at slightly different time or one of them can not work so that imbalance between quadrants can be produced and create unexpected conditions.

It is verified that in **standard condition** the quadrupoles do not develop temperature higher than 400K and voltage imbalance higher than 400V and the quadrupoles of inner triplet are well protected in case of quench.

Another topic discussed in this thesis (**Appendix A**) is the project and the test of a capacitance probe to measure helium liquid level. Usually to read the liquid level a superconducting wire, which turns resistive if not covered by liquid, is used. The main use for this new capacitance probe will be for the tests in the cryostat where the string Q2a/Q2b will be installed.
With model magnets tested in a vertical dewar, knowing the actual level of liquid helium was a real problem because the conventional strain gauge probe fails around the λ-point. This problem with the standard liquid level gauge was seen not only during the tests of model magnets but also during the test of the capacitance probe (where we had a standard liquid level gauge in order to compare the

two reading methods and this conventional probe was not able to read the level in region of temperatures around λ-point). The choice of a capacitance probe is due to the fact that this device is not sensitive to temperature and at least can help in the reading of liquid level in that region of temperature. Due to space constrain (the pipe is horizontal and narrow) the capacitance probe was not a conventional one (usually coaxial sensing electrodes) but was a capacitance probe made with parallel plates in order to use all the space available in the pipe.
This probe was built and tested in Nitrogen and Helium in vertical dewar. This choice of environment should not effect the final results because the overall change in capacitance depends on the area of the capacitor, which is the same vertically and horizontally. Repeating two different cool down we verified the reliability of measurements even if we noticed a loose in preload of the plates once the capacitance probe was covered completely by helium. This affects directly the sensitivity of the probe since a bigger distance between plates reduce the overall change of capacitance. Changes in design will be probably made to reduce this effect and improve the sensitivity.
This device will be used during the tests in combination with a standard liquid level probe.

Chapter 1

LHC INTERACTION REGION QUADRUPOLES [1)]

1.1 Introduction and general aspects of HEP

High Energy Physics (HEP) or particle physics is the branch of science dedicated to the pursuit of the fundamental nature of matter. In order to study the structure of matter experimental HEP employs energetic particles analogous to the light source of a microscope; the performance of the particle "microscope" however, is dependent on the energy of the particles.
Most of these searches are carried out by smashing particles of very high energy into each other, and by analyzing the nature and the characteristics of the new particles produced at the expense of the collision energy. These interactions are obtained either by blasting high momentum particles onto a fixed target or by making them collide head-on among themselves. In head-on colliders, in order to achieve high event rates, the particles are bunched together and the bunches are formatted into high intensity beams.
From the well known quantum physical relationship ([2]),

$$l = \frac{h}{p} \qquad (1.1)$$

Where λ is the wavelength of the particle, p is the particle momentum, and h is the Plank constant (6.63×10^{-34} J·s), it follows that in order to achieve shorter and shorter distances, the energy (or momentum) of the particles has to increase.
For example, for proton beams with particle of 1TeV (such as Tevatron at Fermilab) we have a corresponding particle wavelength $\sim 1.2\times10^{-18}$ m.
In addition to this, since the strong interaction acts only at very short distances, the collision cross-section of high-energy particles is usually small and requires a high luminosity of colliding particles in order to study these interactions.
HEP was and still is the main driving force pushing particle accelerator development to the technological limit, thereby providing the incentive for the accelerator community to build higher and higher energy accelerators with higher particle luminosity.
Achieving such high energies and luminosity is not a trivial task.
Charged particles gain 1eV of energy when accelerated between two electroplates having a potential difference of 1V. In the beginning accelerators utilized static electric fields such as this for acceleration but this worked well up to the point where high voltage breakdown of the materials set the upper limit of the accelerating potential. This limit was on the order of a few tens of millions of volts, which was still five orders of magnitude farther away from the desired TeV energy range.

[1)] Reference for this chapter can be found in [1], [2], [3], [4], [7], [28]

Such a method to accelerate particles is the basic idea for a Linear Accelerator where charged particles travel along a straight trajectory and go through a number of accelerating stations. Usually this kind of accelerators are now used to pre-accelerate particles that then go through a Circular Accelerator which is the favorite structure.
The basic idea of a circular accelerator is to keep charged particles circulating around in a ring. At short straight sections of the ring the particles are accelerated by specially tuned cavities in which a radio-frequency (RF) wave is applied. The component of this wave closest to the beam has an electric field aligned such that the charged particles get a boost in the right direction at that time. This type of acceleration works like a swing that is periodically given a push at the proper phase of its harmonic cycle. After many revolutions, the particles will gain significant amounts of energy. A limiting factor is to achieve many revolutions of the particles without losing them.
The particles can be kept in a horizontal plane by bending the beam with a homogeneous magnetic field that is perpendicular to the direction of the beam. This is only possible if the beam has no vertical momentum spread. If the particle gets any small impulse (kick) in the vertical direction, it will spiral away from the beam orbit. Therefore, since all beams have some non-zero momentum spread, keeping the particles on a circular orbit requires both bending and focusing forces, which can be generated by electromagnetic field.
The Lorentz force is given by:

$$\mathbf{F} = e \cdot (\mathbf{E} + \mathbf{v} \times \mathbf{B}) \qquad (1.2)$$

Where "*e*" is the electric charge, **E** and **B** are the electric and magnetic field, and **v** is the particle velocity. Since the second term of the equation is proportional to $|\mathbf{v}|$, at high energies, even with a moderate magnetic field of 1T, it would generate the same force as an electric field of 3×10^8 V/m.
Furthermore, since

$$\frac{dE}{dt} = \mathbf{v} \cdot \mathbf{F} \qquad (1.3)$$

and

$$\mathbf{v} \cdot (\mathbf{v} \times \mathbf{B}) = 0 \qquad (1.4)$$

the energy *E* and the relativistic mass of the particle are unchanged in a static magnetic field. This is the reason why magnetic field are used for bending and focusing particle beams, since they do not affect the beam energy.
The most successful arrangement of focusing and bending elements of a circular accelerator or storage ring is the so-called FODO lattice. The accelerator is split into a series of magnetic sectors. Each sector contains an alternating series of focusing and defocusing magnets and between them are the bending magnets. The appropriate spacing and field gradient orientation of the magnetic lenses, however, leads to an overall focusing of the particles.
This arrangement in accelerator physics is usually referred to as "alternating gradient" or "strong focusing" type of accelerator. Although bending and focusing in theory can be achieved in many different ways, in practice pure dipole and quadrupole fields are used to model and design the FODO lattice o the accelerator. Therefore, the majority of modern HEP accelerator magnets are dipoles and quadrupoles.
The following magnet performance parameters are very important in the design of the next generation hadron collider:

1. Field strength. The general rule is the higher the field strength the better. The process of focusing and deflecting the particles is more efficient with higher fields. For a given ring size, higher magnetic fields yield higher final particle energy. But at very high energies synchrotron radiation

rapidly increases with energy, and the particles may loose more energy than they can gain in each revolution. This phenomenon may set an upper limit of 10-12T in field strength for the dipoles of 30-100TeV accelerators.

2. Field quality. Since the beam has to survive many revolutions, small imperfections of the magnetic field can be detrimental. This sets stringent design requirements for the field quality of these magnets.
3. Bore size. A larger bore size is, in general, better but it can not be smaller than 3-5 cm in diameter in fact at very high energies the beam size is small, however other factors like beam screens, alignment tolerances, beam tube size, etc., lead to a larger cross-sectional area.
4. Excellent AC-DC behavior. To keep the particle in orbit during acceleration the magnet current should be ramped up relatively quickly. At “flat top”, or final beam energy magnet operation should be very stable.
5. Radiation hardness. It must survive in a high radiation environment for the expected life of the accelerator.
6. Reliability. Losing a store of particles due to magnet failures can be very costly, both in financial terms and in lost research opportunities.
7. Cost. Both production and operation cost should be kept low.

To satisfy these things, magnet builders realized that they needed something more than the usual magnet so it started the development of superconducting magnets. Although most of these requirements can be more easily met using conventional magnets, the goal of reaching extremely high fields and keeping the operating cost low is impossible to accomplish with them.
On the other hand, superconducting magnets are much more delicate and complicated objects than conventional magnets. The complex material properties of the superconductors make them more interesting and difficult to deal with. The following lists some of these issues:

1. Persistent eddy currents. Eddy currents induced in the filaments of the superconductor during a magnet current ramp do not decay exponentially as in normal magnets due to the vanishing resistance of the superconductor. These currents are bipolar in each filament and generate higher order multipole fields. This effect is time dependent. Correction of these persistent current effects requires careful attention.
2. Quench behavior. If the temperature, magnetic field or current density exceeds a critical value, the superconductor will quench (transition from the superconducting state to the normal state). The problem is that sometimes magnets can quench spontaneously well below their critical current due to limitations or deficiencies in their design. Refining the magnet design to avoid these low current quenches and protecting the magnet if quenches occur, are very important issues.
3. Cryogenics. Low heat leak cryostats are desirable; otherwise a high cost for refrigeration will be incurred. This requires a large initial capital investment in order to build the refrigeration plan. For the LHC (see below), the estimated cooling power will be on the order of 144kW at 4.4K, which means operation of the cryoplant will require 36MW of power.

1.2 The project Large Hadron Collider (LHC)

The Large Hadron Collider (LHC) is a project settled at CERN in Geneva and it is the most important European project for particles accelerator with the international collaboration from USA and Japan. This project has the aim to build a synchrotron for collisions of proton beams with energy and luminosity (probability of collision) much higher than the ones reach up to now ([7]).

As already told before we use accelerators in order to make collisions between particles and obtain shorter and shorter wavelength and produce particles heavier and heavier. LHC will reach resolution of the order of 10^{-16} mm.
Another parameter very important, as mentioned, is the beam luminosity, which determines the number of events per second for each interaction and the goal for the LHC is $10^{34}cm^{-2}s^{-1}$. To reach such a luminosity the beam dimension has to be reduced in the points of collision (IP intersecting point), by using quadrupoles which act on the beam as focusing lenses (inner triplet quadrupoles commisioned to Fermilab and KEK).
The efficiency of a quadrupole is due to its focusing power and the field quality (the best would be to have a pure quadrupole).
These properties are obtained by choosing materials extremely sophisticated and putting great attention to construction. Between materials the ones which get the best performance are low temperatures superconductors and in particular NbTi.

1.2a General aspects of LHC

LHC is the main project for HEP in the world and it is the logic development for accelerators at CERN starting from the ISR (Intersecting Storage Ring), a synchrotron for collisions between proton beams of 60GeV in the center of mass. Then SPS (Super Proton Synchrotron) originally born as fixed target accelerator and then converted to a collider between proton and antiproton (SP**P**S), up to 600GeV in the center of mass. At last it comes LEP (Large Electron Positron storage ring) a collider for electron-positron, which reaches energy of the order of 100Gev in the center of mass. LHC will be a synchrotron for head-on collisions of proton beams of 14Tev in the center of mass.
The choice of a collider instead of a fixed target accelerator is due to the advantage of the former to convert all the energy of the particles in new particles while in the second case the momentum conservation says that part of the energy has to be converted in kinetic energy of the produced particles so that that energy is impossible to use to product other particles. The choice for proton beams is mainly due to the need to use heavy particles, in order to reduce to minimum the loss of energy by radiation. In fact for example the maximum energy for light accelerated particles (leptons) in circular machine is limited to 100GeV because these particles emit synchrotron radiation while they are moving on a circular orbit (as reached with LEP). When LEP was built it was clear that there was not enough space to build a bigger ring for new machine so space, upon LEP ring, to build an additional magnetic ring was left thinking of a possible proton-antiproton collider for the future.
At CERN there is already a system, which produce antiproton but the low efficiency of these systems pulled for proton-proton collisions.
LHC will provide proton-proton collisions with a center of mass energy up to 14TeV with a nominal luminosity of $10^{34}cm^{-2}s^{-1}$ and heavy ion (Pb-Pb) collisions with a luminosity of up to $10^{27}cm^{-2}s^{-1}$.
In the view of the fact that the machine is installed in the existing 27Km circumference LEP tunnel, considerable technological innovation is needed to fit the two rings (the presence of two beams of the same charge is a constrain to build two separated magnetic channels) into the tunnel cross section whilst leaving enough space for an eventual lepton ring.
So the solution proposed was to use magnets (dipoles) with a double bore (called twin-bore), which are two separated magnetic channels and each of them has its own coils but in the same mechanic and cryogenic environment.
The kinetic energy of a relativistic particle with charge q, which moves on a circular orbit with radius r under the effect of a magnetic field B_0, is:

$$E_p = qB_0 r \cdot c \qquad (1.5)$$

Where *c* is light velocity. As already told LHC will be installed in the existing 27Km circumference LEP tunnel so it has a fixed radius of ~ 4.243Km. So to reach the requested high energy one has to act on the intensity of B_0, which maintains protons on their orbits. Using superconducting magnets should allow B_0 up to 8.4T, and so proton beams of 7TeV and collision energy up to 14TeV.

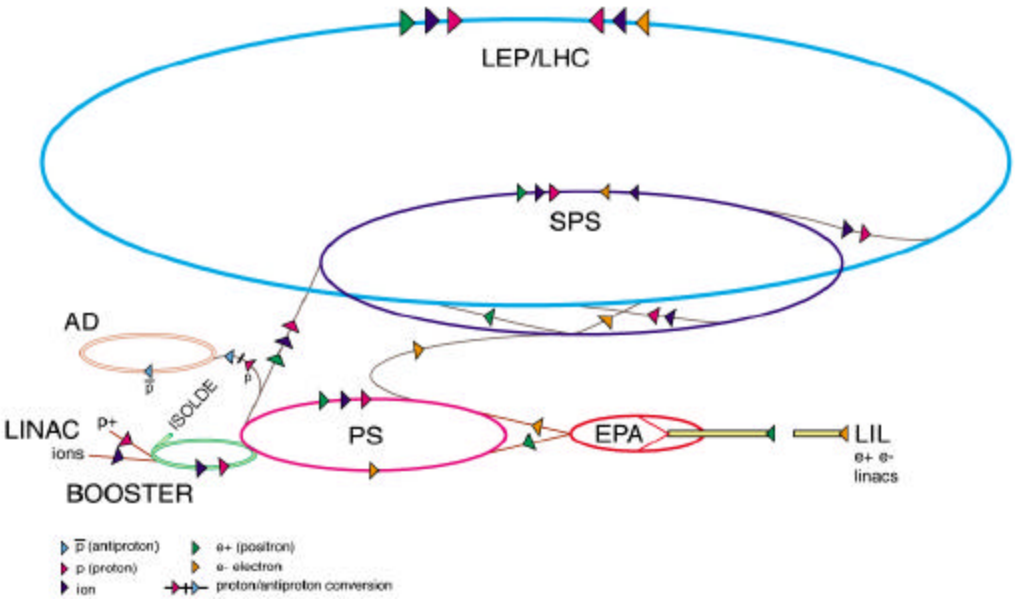

Fig. 1.1 Schematic of accelerators used for LHC.

Table 1.1 Specifics of LHC.

Energy	E	[TeV]	7.0
Dipole Field	B	[T]	8.33
Coil inner diameter	d	[mm]	56
Distance between aperture axis (1.9K)	δ	[mm]	194
Luminosity	L	$[cm^{-2}s^{-1}]$	10^{34}
Injection energy	E_i	[GeV]	450
Circulating current/beam	I_{beam}	[A]	0.56
Number of bunches	k_b		2835
Bunch spacing	l	[m]	7.48
Bunch separation	τ_b	[ns]	24.95
Particles per bunch	n_b		$1.05 \cdot 10^{11}$
Stored beam energy	E_s	[MJ]	350
Collisions			
Beta-value at I.P.	β^*	[m]	0.5
r.m.s. beam radius at I.P.	σ^*	[µm]	16
r.m.s. divergence at I.P.	σ'^*	[µrad]	32
Luminosity per bunch collisions	L_b	$[cm^{-2}s^{-1}]$	$3.2 \cdot 10^{26}$
Total crossing angle	ϕ	[µrad]	300
Number of events per crossing	n_c		19
Beam lifetime	τ_{beam}	[h]	22
Luminosity lifetime	τ_L	[h]	10
Energy loss per turn	E_l	[keV]	6.7

Beam separation in arcs (1.9K)	s	[mm]	194
Critical photon energy	E_p	[eV]	44.1
Total radiated power per beam	P	[kW]	3.8

In order to reach the desired luminosity several parameters have to be as close as possible to their limits. For examples when two bunches cross in the center of the detector only a tiny part of the particles collide head-on and all the others are deflected by the strong electromagnetic field of the opposite bunch. It has been showed that these deflections are stronger for denser bunches and accumulate turn after turn and may lead to particle loss. In the LHC one wants very dense bunches but has to put limits in order to maintain the beam for a sufficient amount of time to do experiments. Other parameters that have to be controlled are:

- collective instabilities due to the electromagnetic wake-field left behind by each bunch,
- stability of the beam over its life-time,
- beam losses which should not quench superconducting magnets (energy is converted in heat) and to avoid this particular collimation system is needed,
- synchrotron radiation which is not critical for the masses of particles, which are heavy ($P_s \div 1/m^4$), but because the energy has to be absorbed at cryogenic temperature.

1.2b Structure of LHC

The basic layout of the LHC mirrors LEP's one, with eight long straight sections each approximately 500m in length available for experimental insertions or utilities. Two high luminosity proton-proton experiments are located at diametrically opposite straight sections, Point 1 (ATLAS) and Point 5 (CMS). Two more low-beta insertions are located at Point 2 (ALICE, Pb ions) and Point 8 (B-physics), which also contain the two injection systems. The beams cross from one ring to the other at these four locations. The remaining four long straight sections do not have beam crossing. Point 3 and 7 are used for "cleaning" and collimation. The beam abort system is located at Point 6 and Point 4 remains spare.

In each of the first four locations the beams cross from one ring to another so that both of them travel the same length on the circumference. This is necessary to maintain the bunches synchronism (a bunch is a dense groups of particles which compose the beam).

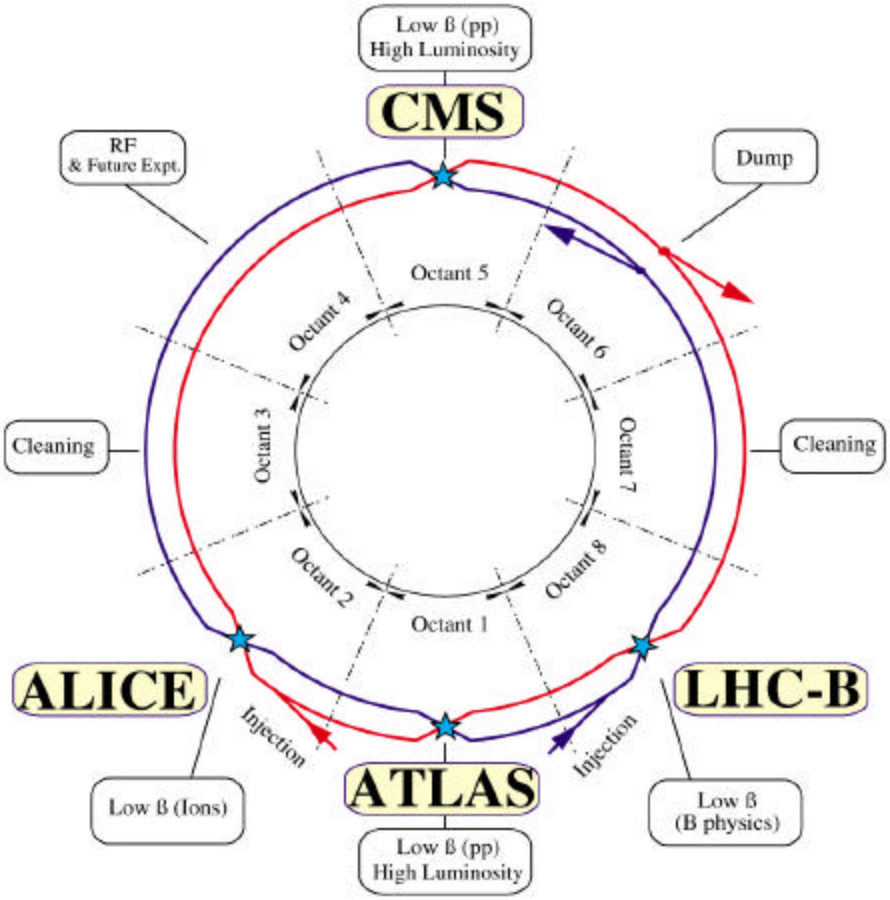

Fig. 1.2 Structure of LHC. There are four low-β insertions (two of them are High Luminosity Interaction Regions, two are Low Luminosity Interaction Regions).

Machine Layout

1. The regular arcs

The arcs contain 23 regular lattice period (FODO) per octant. Each lattice period, 106.9 meters in length, is made up of six twin-bore dipoles, each with a magnetic length of 14.2 meters. Each dipole contains short sextupole and decapole correctors in order to compensate for unwanted field harmonics. The lattice quadrupoles are 3 meters long with a maximum gradient of 250T/m and are separated from the dipoles. The coil aperture is the same as in the dipoles (56mm). The quadrupoles are integrated into “short straight sections” which also contain a closed orbit correction dipole, chromaticity correction sextupoles and some free space for either an octupole or a skew quadrupole. The short straight section also contains a beam pick-up monitor and a cryogenic service unit for the production of the primary superfluid helium needed to cool each half-cell.

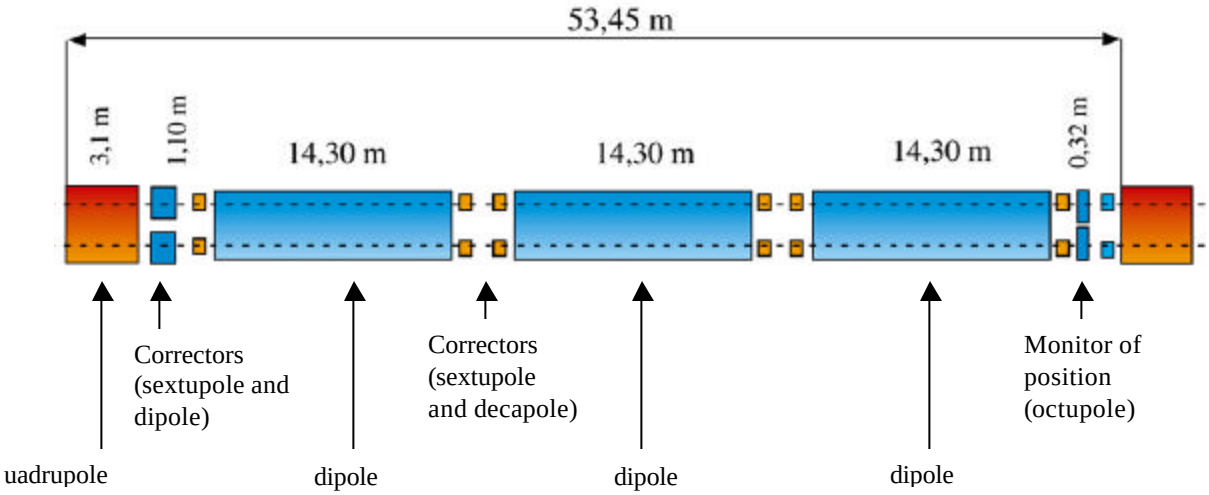

Fig. 1.3 Half lattice period.

1. The low-β insertions (points of collision in the machine)

The layout of a low-β insertion is shown in figures 1.4 and 1.5 together with the optical functions during collisions (β=0.5m) in figure 1.6. The insertion is antisymmetric and consists of a matching section (the outer triplet) for detuning the optics, and an inner triplet focusing the beams to the interaction point. Between the two, a pair of recombination dipoles brings the beams into a common channel with a small crossing angle (± 100μrad) at the interaction point. The outer triplet quadrupoles are twin-bore magnets with the same cross section as the regular lattice quadrupoles whereas the inner triplet quadrupoles are single bore with the aperture increased from 56 to 70 mm (gradient 215 T/m). In the two high luminosity insertions, a free space of ± 23 meters between the two inner triplets is available for the experiments, whereas for the other two insertions this space is reduced to ± 21 meters to allow more room for injection. During injection and acceleration, the insertion is "detuned", bringing the maximum β value down from its collision value of about 4500m to below 400m.

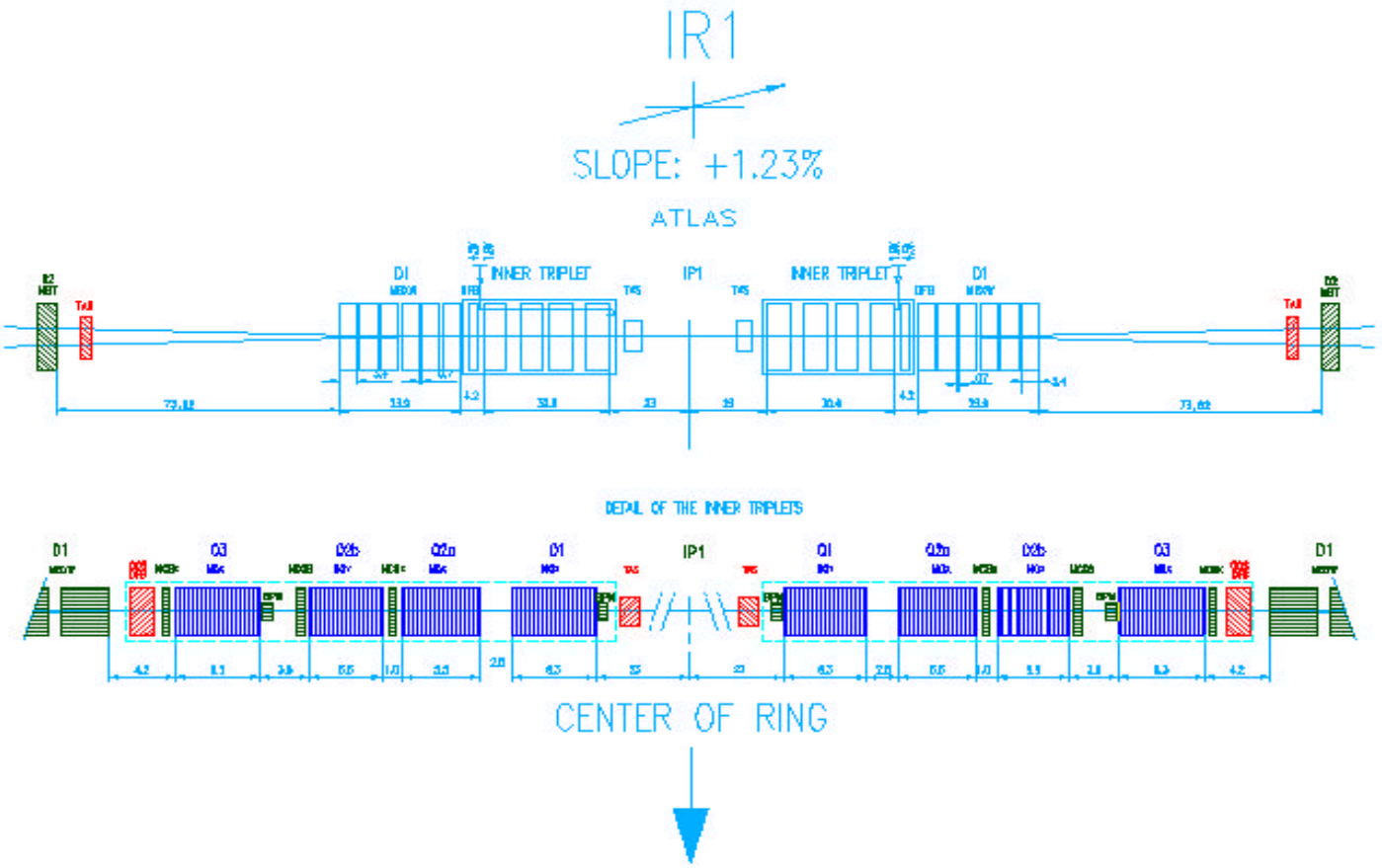

Fig. 1.4 Low-β insertion in point 1 (ATLAS).

In particular the inner triplet schematic is composed of four quadrupoles. The outer ones are from KEK while the inner ones are from Fermilab and they are the main topic of this thesis. Despite other quadrupoles in LHC the inner ones in the inner triplet are very critical because they have to maintain an operational gradient of 215T/m. So they have a peak field similar to the dipoles but they have more inductance (more poles) so that the extraction is much more difficult than in dipoles (higher energy stored).

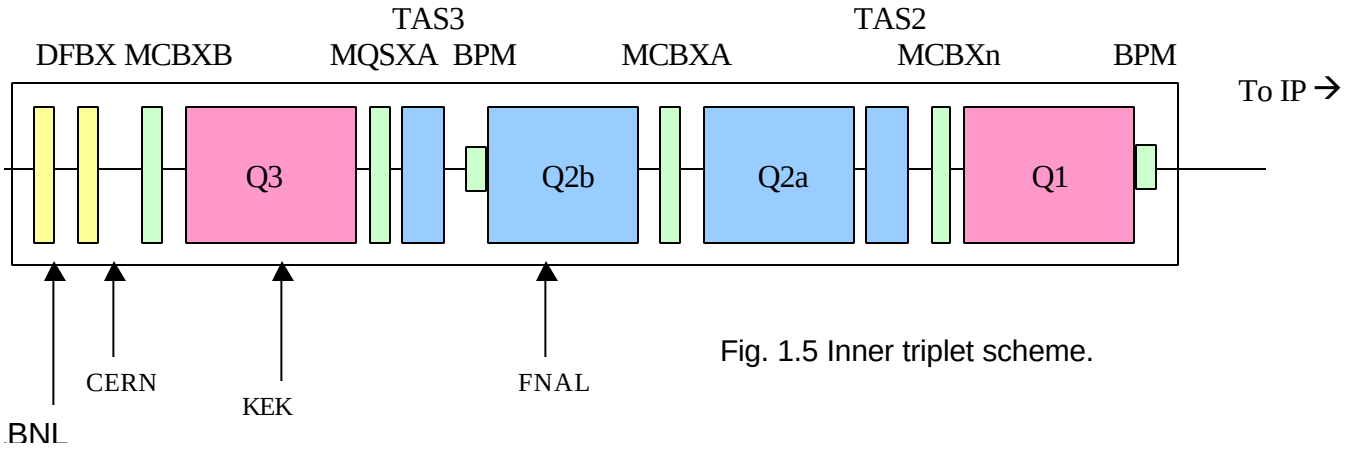

Fig. 1.5 Inner triplet scheme.

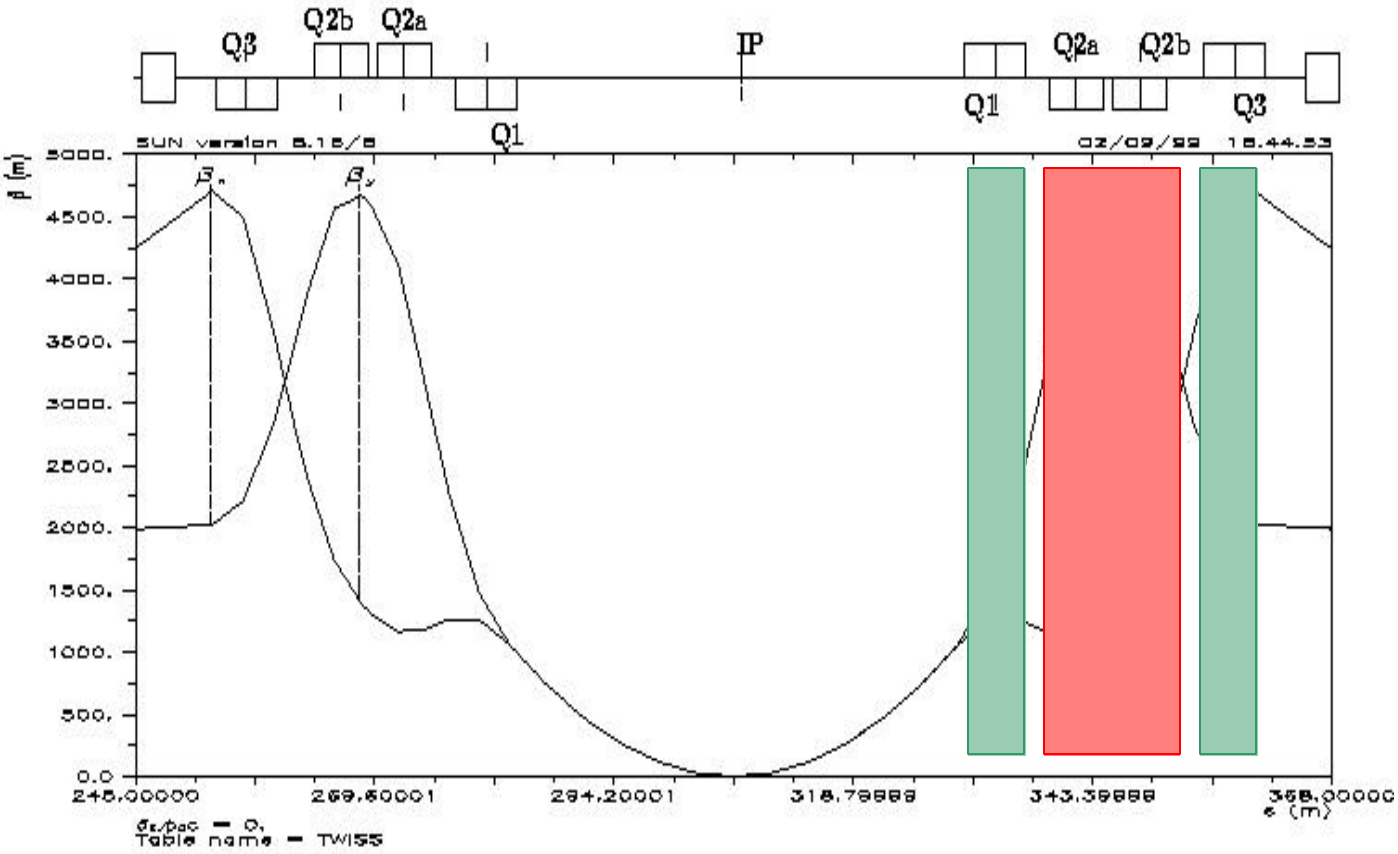

Fig. 1.6 Optical functions for the low-β insertions (as one can see the function β reaches its minimum value at the interaction point).

3. The cleaning insertions

The role of the cleaning insertion is to allow for collimation and cleaning of the beam halo in order to minimize the background in the experimental detectors as well as the beam losses in the cryogenic parts of the machine. The insertion consists of a "pseudo FODO" structure containing only classical magnets.

4. The beam abort insertion

The purpose of the abort insertion is to dump the beams in a clean and safe way at the end of physics runs or to protect the machine in case of hardware failure or beam instability. The beam dump kickers located at the beginning of the straight section deflect the beams horizontally across the septum in which they are vertically extracted from the machine.

5. Cryogenics

The elementary LHC cooling loop matches the periodicity of the machine lattice and corresponds to the half-cell of 53m length. Static superfluid helium pressurized at 1 bar permeating the magnet laminations is cooled by heat exchange with saturated superfluid helium flowing through a tube running through the magnet chain over the whole length of the half-cell.

Fig. 1.7 Elementary cooling loop of LHC.

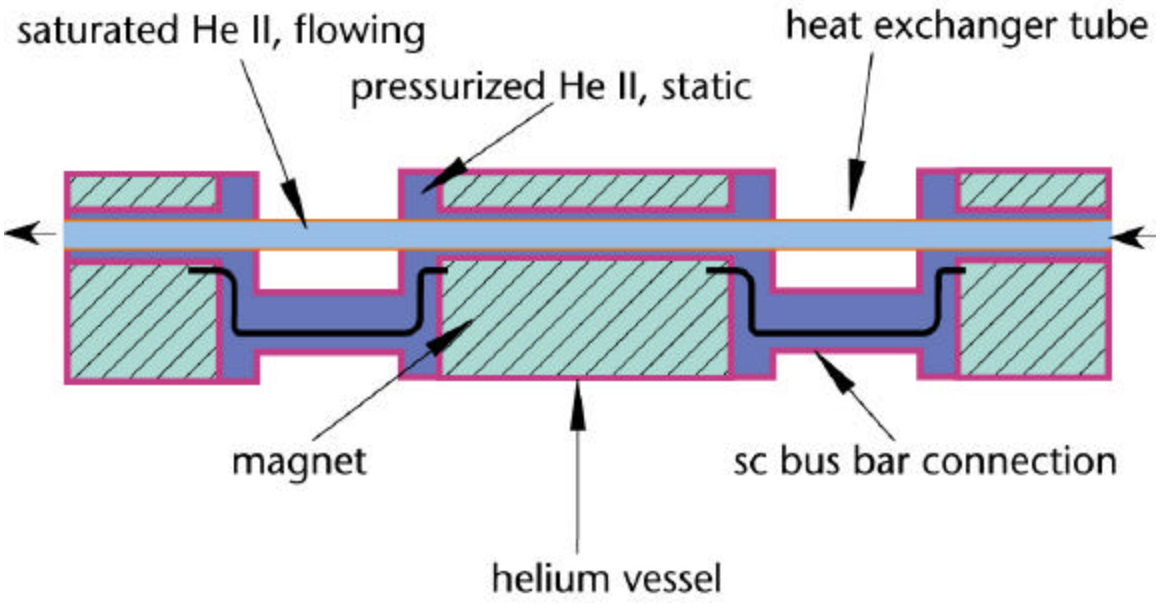

6. The RF system

The radio-frequency system will be installed at Point 8. In order to ensure sufficiently short bunches in collision and avoid RF noise diffusion. This will be ensured by a set of eight superconducting cavities. During acceleration, it is necessary to increase the bunch area from the SPS value of 1eV·s. to 2.5eV·s. in order to obtain a good infra-beam scattering lifetime at collision energy.

7. Vacuum

Due to the synchrotron radiation emitted by the protons (~4kW per ring at 7TeV) and the heating due to the image currents in the wall of the vacuum chamber, the magnet cold bore at 1.8K must be shielded from the beam, otherwise the required cryogenic power would become excessive (1 Watt at 2K needs approximately 1kW at room temperature).
An inner liner cooled to around 20K through tubes carrying high pressure gas will therefore be installed inside the cold bore in order to avoid pressures rise, which turns in temperature rise.

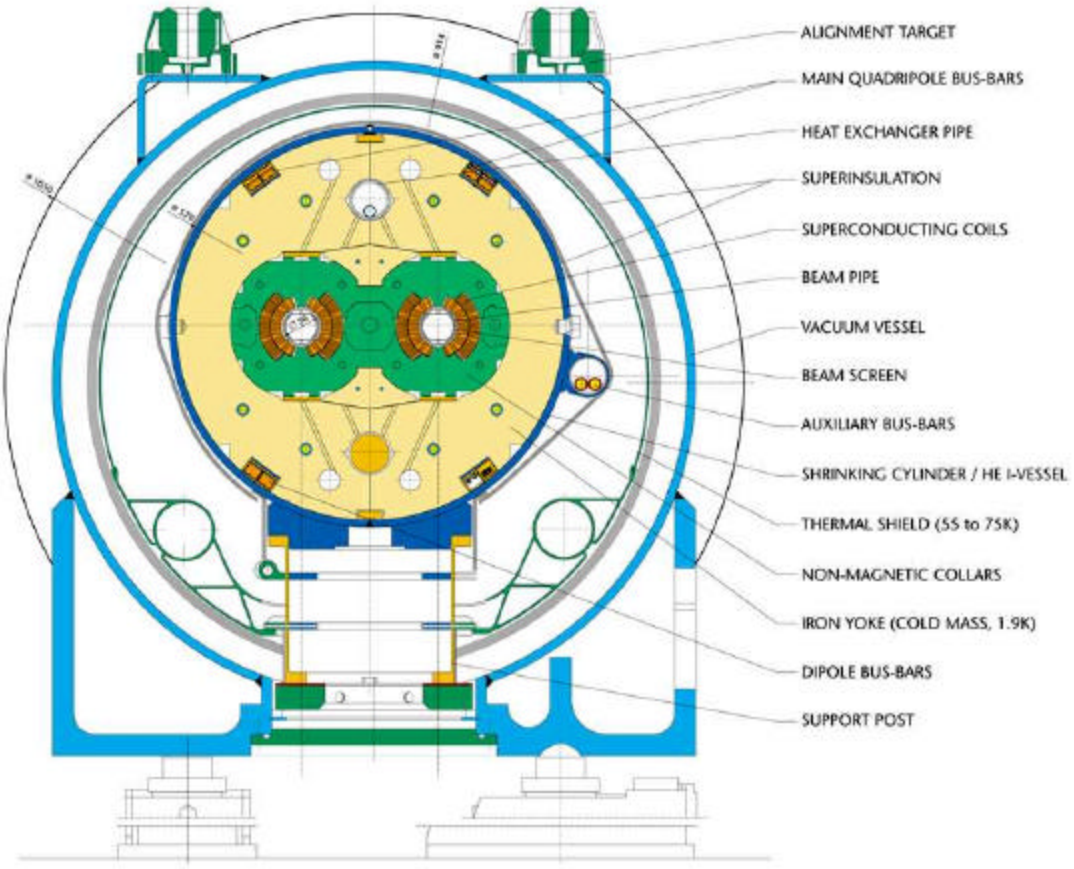

Fig. 1.8 Cross section of the machine and the main dipoles of LHC.

1.2c Critical factors of LHC

1. Operation temperature and superconducting magnets

Superconductivity is a property that some materials show at low temperatures: their resistance is zero or at least not measurable when a density of current (below a certain critical value J_c) flows through them. This allows to have currents very high in conductors of a small transverse cross section, so that one can build very compacted magnets with very high magnetic field because the current source can be positioned near to the central zone. To produce this magnetic field superconducting magnets requires the amount of energy needed to cool down the temperature and maintain the operation temperature. This is the principal cryogenic problem. Another crucial matter is the stability of a superconducting magnet. To prevent the irreversible transition from superconducting to normal state (called "quench") is then necessary to include a quench protection system.
The operating temperature for the LHC is below 2K in order to reach higher critical current of the superconductor used in dipoles and reach magnetic field of 8.4T needed to curve the beam.
The main heating source is the power released from synchrotron radiation. This power is valuable as ([4]):

$$P_s = Z_0 e^2 c N \cdot k \cdot f \cdot g^4 / 3r \qquad (1.6)$$

where Z_0 is impedance in vacuum, N is the number of protons in each of the k bunches that circulates in the machine, f is the frequency of revolution, g (= (E/m_0c^2)) is Lorenz factor and r is the bending

radius. The equation 1.6 shows that the beam current can not be increased without limits. For the LHC this power released is estimated to be 3.7kW, lower value than in the LEP but still critical because the operation temperature is also lower. It can be estimated that the power absorbed by cryogenics system to remove 1W released at 2K is the same to the one to remove 1000W at room temperature. This is particularly critical in intersection points where also all irradiated power of secondary products of collisions is released.
Moreover the electromagnetic forces on current conductors and the stored energy increase with B^2 so that in LHC conditions one has to compensate the former with a mechanical structure to contain materials, while the latter requires very complex and efficient systems of quench protection.
For all these restrictions superconducting magnets are technically the most demanding part in the LHC.

2. Luminosity (probability of collision)

The luminosity of an accelerated particles beam has to grow with the square of particles mass that one wants to create (in order to compensate the corresponding decrease in cross section values of the events of interest in the LHC). The luminosity is therefore an important parameter much as the energy. The final aim for the LHC is
$10^{-34}cm^{-2}s^{-1}$. The luminosity is defined as ([4]):

$$L = \frac{N^2 k f}{4p \cdot s^2} \qquad (1.7)$$

where N is the number of protons in each of the k bunches that circulates in the machine, f is the frequency of revolution and s is the radius r.m.s. of the beam (supposed circular) in the point of interaction.
Introducing the emittance ε_n:

$$e_n = \frac{g s^2}{b^*} \qquad (1.8)$$

where $g = (E/m_0c^2)$ is Lorenz factor and b^* is the value of betatron function at crossing points, luminosity can be expressed as:

$$L = \frac{N^2 k \cdot f \cdot g}{4p \cdot e_n b^*} \qquad (1.9)$$

The principal limitation to luminosity comes from the so-called interactions of beam-beam space charge (between two beams).
In fact at cross points there is the interaction between beams (head-on interaction) and plus an undesirable interaction in the region near collision points (spread is ~90m).

This is a long-range interaction due to the proximity of beams that are moving parallel in the same magnetic channel and then converge in the cross point and split apart after it. This long-range interaction limits the maximum value for *k* and *f*, and it imposes a specific distance (which depends on the crossing angle) between successive bunches to ensure that dynamic of a single bunch outer of the collision zone, is not related with the others. In the LHC case the distance is 25ns, i.e. 7.5m, while the angle is fixed to 200μrad (small enough to be contained in the small aperture of the common quadrupoles). Even if these conditions do not eliminate the electromagnetic interaction they ensure the reduction of parasite collisions.
Also *N* is limited in order to avoid the tune-shift effect ξ to be too big (above 0.006) compromising the "life" (duration) of the beam.
This tune-shift effect is due to the proximity of space charge between beams and is defined as (r_p is the classical radius of a proton):

$$x = \frac{N \cdot r_p}{4p \cdot e_n} \qquad (1.10)$$

From 1.9 we can conclude that to maximize luminosity the function b^*, in the crossing points with focusing quadrupoles, has to be minimized. But also here there are some limitations: the crossing angle f (superiorly limited by the physical aperture of the common magnetic channel of the two beams) has to be bigger than the divergence of the involution of the beam in the crossing region.
If we consider an involution of the beam at ns:

$$f \geq n\left[\frac{e_n}{g \cdot b^*}\right]^{1/2} \qquad (1.11)$$

And this creates minimum limit to b^*.

1.3 Interactions and quadrupoles low-β

Reduction of b^* to reach maximum value of luminosity in intersection points is obtained with a special insertion 300m long called low-β, which is added to dispersion suppressor at the end of each arc. In these insertions there are two triplets of quadrupoles which can reach b=0.5m both in vertical and horizontal plane. The fundamental role of these low-β insertions make these quadrupoles important components,. Their performances are aspects very decisive for efficiency of the LHC.
The outer triplet (further from the collision zone) has the goal to link optic functions of dispersion suppressor with the ones of inner triplet.
In the length between the two triplets (more than 200m) the two beams are made adjacent with action of a couple of dipoles: the beams see the same magnetic field and are curved in opposite directions, until they are far apart only few millimeters at the entrance of the inner triplet, which in this way can be single bore.
The inner triplet is exposed to an intense flux of secondary products because it is very closed (less than 20m) to the collision point. To protect the triplet is foreseen a collimator in copper and tungsten 2m long, with an internal aperture of 30mm. In any case quadrupoles have a large bore (70mm) and so only a little part (estimated as 130W) of flux, which goes beyond the collimator, deposits on them.
In reality every triplet is composed of four different quadrupoles but the two in the center focus on the same plane so the system is optically equivalent to a triplet.

To represent the focusing action of a quadrupole one can use the similarity with a thin lens in optic (see appendix B).
The focal distance in a quadrupole is at the first approximation:

$$F = \frac{p}{q}\frac{a}{B_{\max}L} = B_0 r \frac{1}{GL} \qquad (1.12)$$

where G is the field gradient, "a" the aperture radius, B_{max} the maximum field (on the coils $B_{max}=Ga$), and L the length ($p/q=B_0 r$ is the magnetic rigidity).
The characteristics requested for low-β quadrupoles are:

- single bore of 70mm (instead of 56mm for quadrupoles in the machine), to limit the secondary radiation which is deposited on quadrupoles
- gradient of 215 T/m, to have enough focusing power
- 5.5m length
- high linearity of the quadrupolar field on a extended radius to avoid the beams to be affected by different harmonics. The non-quadrupolar components of field harmonics are requested to be less than 10^{-5} T for multipoles until dodecapole and 10^{-6} T for the ones of higher order (the values are considered to a referent radius of 1cm).

These requests are much stronger than the ones for quadrupoles of the machine.

1.4 Superconducting material: NbTi

Before entering in details in the material used for magnets we would like to spend few words to recall different types of superconductors and their peculiar characteristics.
As already said the superconductivity is a phenomenon in which the material becomes resistless after a given temperature (at fixed field and current density). It is not uncommon in fact most of the metals become superconductors even if the temperatures to reach are very low. The parameters used to describe the superconductivity are temperature (T), field (B) and current density (J, or current I) which lie on a tri-dimensional critical surface so that we can not increase one of them without decreasing the other two (Fig. 1.9) ([1]).

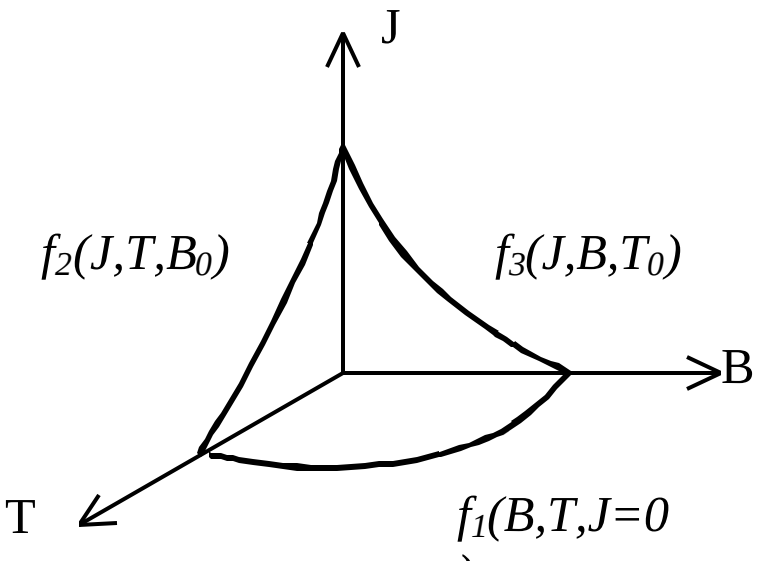

Fig. 1.9 Critical surface of a superconductor ([3]).

There are two different kinds of superconductors:

1. Type I superconductors: usually they are pure metals (for example Al, Sn) they have a sharp transition, very low critical values (T_c between 1 and 7K) so that they are not very useful because the critical current density is of the same order of the density in usual wires of copper (~5A/mm^2).

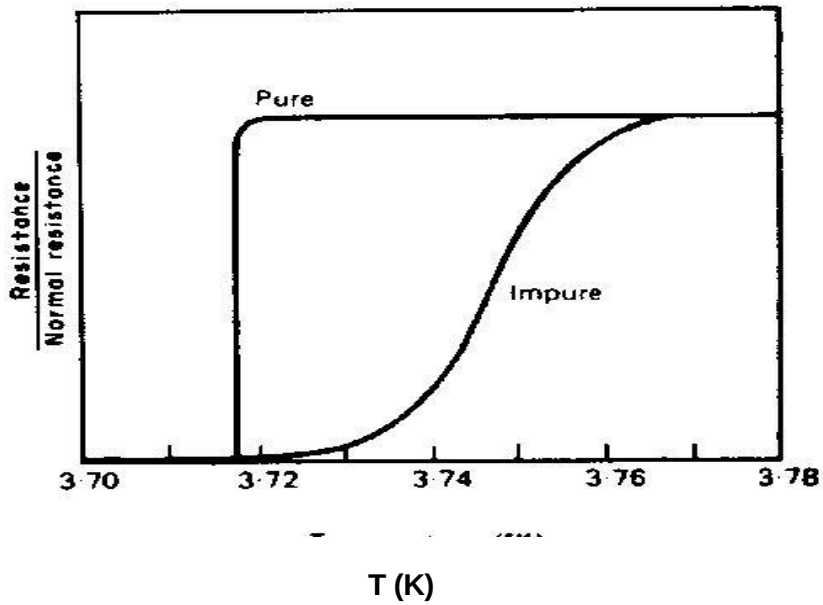

Fig. 1.10 Type I superconductor ([3]).

2. Type II superconductors: they are usually composites based on Nb (for example Nb itself, NbTi, Nb_3Sn, Nb_3Al). They have a quite large transition and higher critical temperature (8-20K) as well as higher critical field and current density. They are characterized from two different critical field: for $B<B_{c1}$ the material is a superconductor for $B_{c1}<B<B_{c2}$ the material is not completely superconductive but the field can penetrate under forms of fluxoids around which the current can flow (Fig. 1.11-1.12).

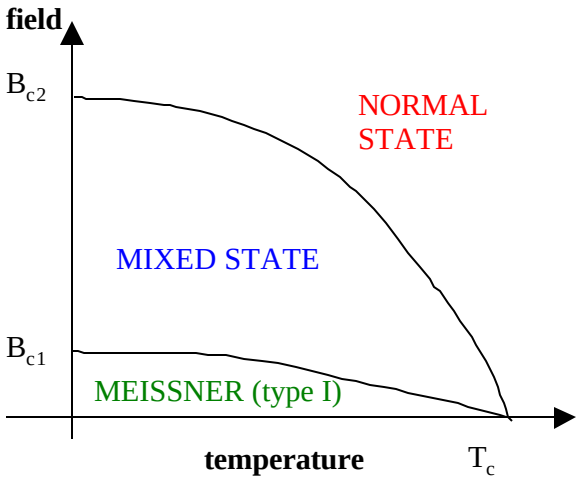

Fig. 1.11 Critical surface at constant current density for a type II superconductor ([3]).

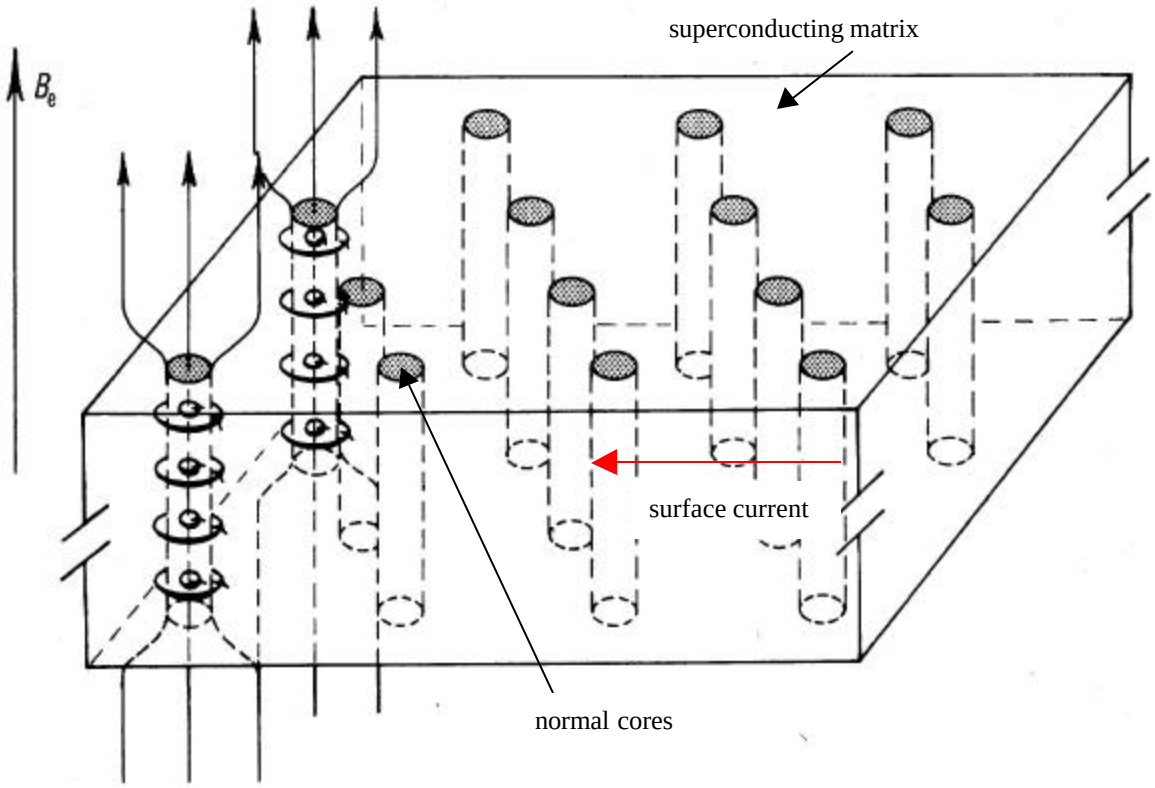

Fig. 1.12 Fluxoids in type II superconductor ([3]).

For magnets in LHC and in common superconducting magnets the material used is the composite NbTi.
As already said it is a Type II superconductor and as known in this kind of superconductors, in their pure uniform annealed form, the current does not flow in the bulk, but only on their surface. The magnetic field penetrates these superconductors in the form of quantized fluxoids. For a uniform

material, the fluxoids arrange themselves into a regular lattice and this means that there is a uniform field and so, from

$$\mathbf{curlB} = m_0\mathbf{J} \ , \qquad (1.13)$$

the current density is zero.
In order to promote the flow of currents within the bulk material, it is necessary to produce a non-uniform fluxoid lattice that can be created with the so-called “pinning centers”, i.e. non-uniformities in the microstructure of the material. These “pinning centers” can create a variation in energy of fluxoids with position, thereby giving rise to minimum energy configurations.
Niobium and titanium are mutually soluble to form ductile alloys over a wide range of compositions. The one used usually for magnets is Nb-46.5w/oTi in order to obtain the best performances for critical field. In fact one has to notice that the optimum critical field and critical temperature do not occur at the same composition because the normal state resistivity increase with titanium content. The principle source of flux pinning in NbTi is provided by finely divided deposits of the “α-phase”, a titanium-rich phase which is precipitated on the dislocation cell boundaries as a result of the heat treatments which are applied during manufacture. So for optimum pinning the precipitate cell size should be matched to the fluxoid spacing. A recent development in the technology of NbTi has been the use of Artificial Pinning Centers APC. These pinning centers are produced by incorporating fine fibers of a different metal, such as copper or niobium, into NbTi and then drawing down until the APC fibers have a size and spacing comparable with the fluxoid lattice spacing ([1]; chapter 12]).
As one can see we can gain a lot in critical field if we reduce the operation temperature. This gain can be easily seen simply by plotting critical current densities for different field at different fixed

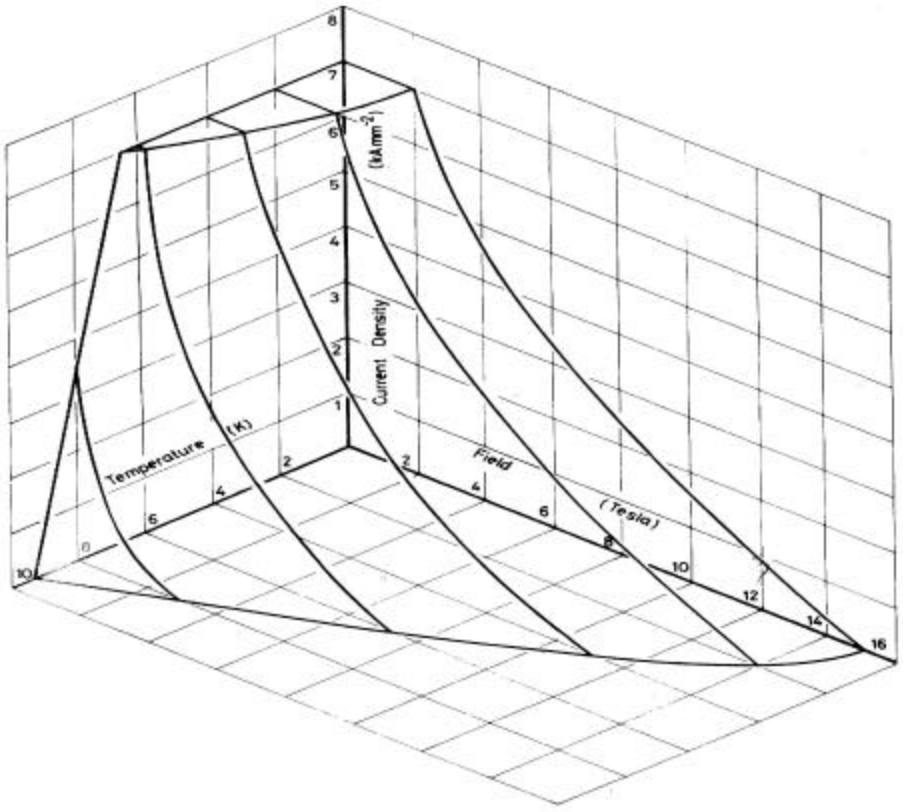

Fig. 1.13 Critical surface of NbTi ([3])

temperatures. In particular we would like to show liquid helium at 4.2K and superfluid helium at 2.17K (Fig. 1.14). The gain in field is around 3T at low current densities and it is crucial in order to obtain the luminosity and energy wanted even if it is much more difficult to deal with superfluid.

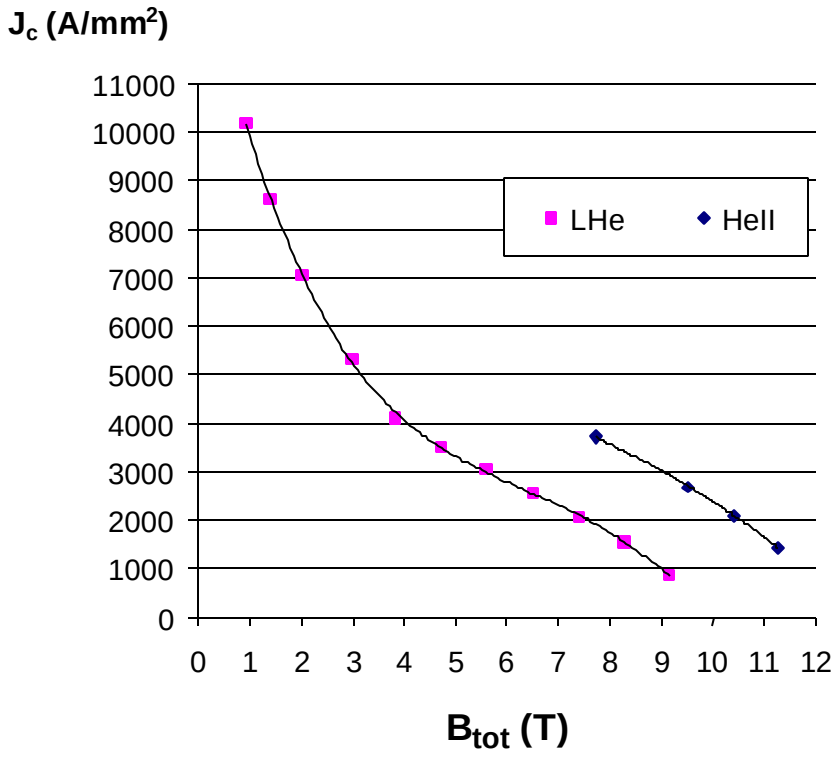

Fig. 1.14 Current densities for helium at 4.2K and 2.17K as a function of the field.

The production of filamentary NbTi composite wire has different steps. The cylindrical starting billet of NbTi is prepared by consumable arc vacuum melting and it is important the alloy composition to be as homogeneous as possible over the entire billet. The NbTi billet is machined to size, cleaned and fitted inside a copper extrusion can. If the composite is designed to have very fine filaments, a thin pure Nb diffusion barrier can be interposed between the NbTi and copper in order to prevent the formation of a CuTi intermetallic phase during the heat treatments. The problem is that the intermetallic is hard and brittle and does not draw down with the filament but instead breaks up into hard particles. At the later stages of drawing, when the filament size becomes comparable with these particles, the filament is broken by the particle. It may be better to make the can of copper doped for example with Mn, to suppress proximity effect coupling at final size.
Assembly of the billet should be carried out in clean conditions, after which it is evacuated, sealed by electron beam welding, heated and extruded. After cold drawing to size, the rod is drawn through a hexagonal die and then cut in many lengths. After cleaning, these lengths are stacked into another copper can, which is again sealed, extruded and drawn down to final size. For accelerator magnets, which may have up to 10^4 filaments, a double stack process is often used in which the rods are again drawn into hexagonal sections and stacked in another can. In wires intended for cabling, it has been found that a central core of pure copper is beneficial in helping the wire to resist the deformation of the cabling process. Multiple heat treatments are applied throughout the process in a defined sequence of alternating cold work and heat treatment, which has been found to produce the best configuration of α-Ti precipitate and hence best flux pinning. After reaching final size, the wire is twisted with typical twist pitch of 10-25mm.

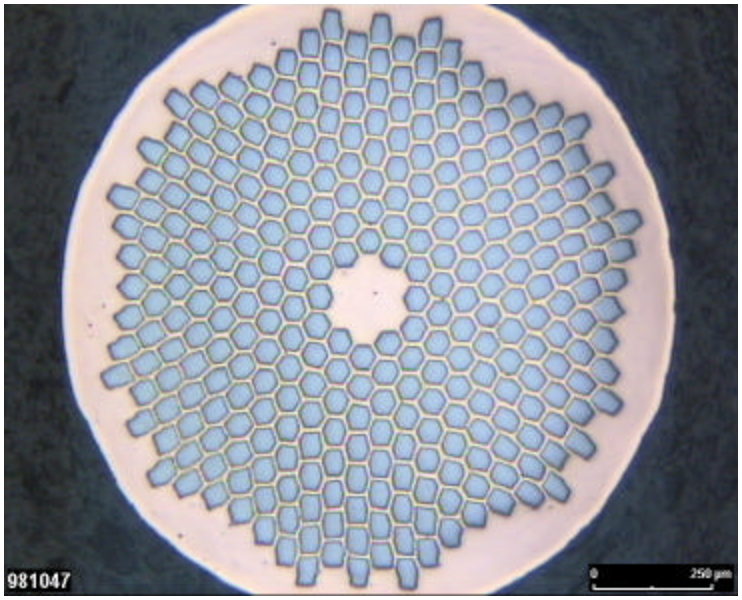

(a)

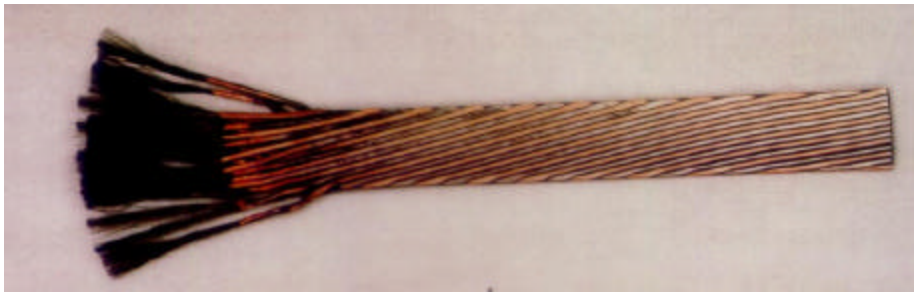

(b)

Fig. 1.15 (a)Cross section of a NbTi/Cu wire; (b) Rutheford cable ([3]).

1.5 Stability in superconducting magnets

Even if superconducting magnets are the best solution to achieve high energies required by accelerator they are very difficult to treat.
The major problem to deal with is instability of magnets and the consequent possibility of sudden transition from superconducting to resistive state (phenomenon called QUENCH) ([1]; chapter 5).

Due to this the conductors often failed to achieve the same performance reached in short samples (pieces of cable) when they are assembled in magnets. Quenching at lower currents than the critical ones is generally known as *degradation*. It is often accompanied by a related behavior known as *training*. Degradation and training are undesirable in any magnet, but are particularly to be avoided in an accelerator system, where many magnets have to be connected in series such that a single magnet quenching will bring the whole system down. Strategies to avoid or at least reduce degradation are called “stabilization” (see later).

If , for a problem of the magnet, an accidental transition of a zone of a magnet from superconducting to resistive state happens, the stored energy of the magnetic field is released as heat.
This heat can quench the zones next to the first one and probably quench the entire magnet. This process can be very dangerous:

- the dissipation of heat in a little zone of the winding can break or even fuse the interested zone
- superconducting magnets bring high current density so when a zone becomes resistive, to the ends of it a huge difference potential can be developed and it can break the insulation and cause a short
- the heat developed is dissipated into helium bath. But as well known helium is characterized by a little value of heat of vaporization (r =2.68 kJ/l) so that helium evaporates very easily causing an increasing of pressure in the cryostat. This increasing in pressure reduces again the value of r and so the production of gaseous helium is bigger and bigger and if not controlled it can be very dangerous

So it is necessary to know the causes which can induce a quench in order to prevent them or at least to have a protection system for the magnet if transitions occur.

We can divide the types of transitions from a temporal and spatial point of view.
In particular we can have (from a spatial point of view) punctual or distributed disturbs and (from a temporal point of view) transient or continuous disturbs.
Continuous disturbs are due to reproducible causes such as bad wiring or eddy currents effects and they can cause degradation but not training and they can be avoided with precise job in assembling and curing magnets.
Transient disturbs (causes for training and degradation) are not easy to prevent.
Two main problems were found to be related with these kind of disturbs. One of them (flux jumping, sudden rearrangement of magnetic field inside a superconductor) has been resolved by dividing the cable in filaments embedded in a copper matrix.
The other (mechanical movements) is not so easy to solve even if a lot of things can be done to prevent at least the worst cases.
Several stabilization criteria were studied during the last 40 years at they brought the development on superconducting magnets to very high level. Now the major cause of quench in a magnet is due to mechanical problems (things not yet well predictable).

1.6 Stabilization criteria

1. Cryogenic stabilization

Cryogenic stabilization was the earliest successful technique and the general principle is that the superconductor is joined along its entire length to a conductor of low resistivity (usually copper) with a much greater cross sectional area. If for any reason the superconductor stops conducting, current

switches to the copper, where it generates heat. By means of cooling channels in the magnet, the copper is sufficiently well cooled for the ohmic heating to be dissipated without excessive temperature rise. If this temperature is below a certain value, the superconductor can recovers its fully superconducting state and current transfers back to it from the copper and the ohmic heating ceases ([1]; chapter 6).

For most Type II materials (as NbTi) at fixed field, the critical current density falls off linearly with temperature so the current carrying capacity of the superconductor is reducing with increasing temperature and the excess current is transferring to the copper.

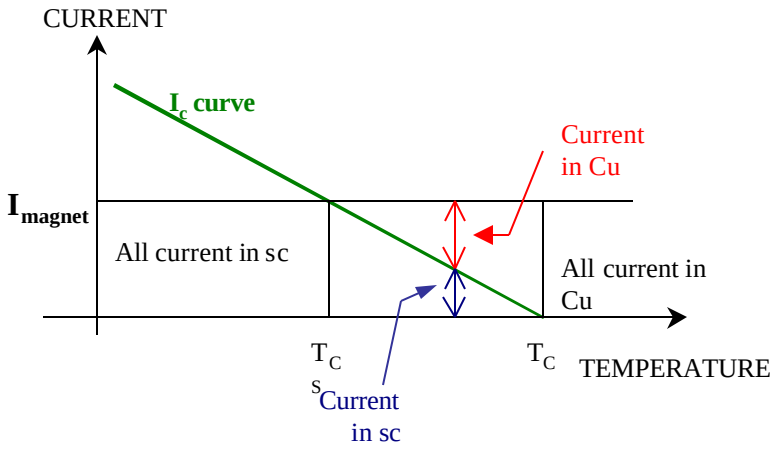

Fig. 1.16 Current sharing in NbTi/Cu cable ([3]).

When all the current is transferred to the copper, further increases in temperature do not change the power generation. The variation of power generation with temperature is thus ([1]):

$$G(T) = \frac{l^2 J_c^2 r (T - T_0)}{(1 - l)(T_c - T_0)} \qquad (1.14)$$

where λ is the proportion of superconductor in the conductor cross section (the rest is copper and does not change *G*), J_c is the critical current density, *T* is the conductor temperature, T_0 is the temperature of the cryogenic bath and T_c is the superconductor critical temperature. The variation of cooling with temperature is:

$$H(q) = h(T - T_0) \qquad (1.15)$$

where *h* is the heat transfer coefficient. *G(T)* is defined per unit volume and *H(q)* per unit cooled area so we need a factor *A/P* where *A* is the area of cross section and *P* is the cooled perimeter and the stability condition can be expressed as:

$$a = \frac{l^2 J_c^{\,2} r \cdot A}{(1 - l) P h (T - T_c)} \le 1 \qquad (1.16)$$

i.e. the variation of power generation does not exceed the power of cooling, which make possible the recover of the superconductor.

Cryogenics stabilization works well and indeed has made possible all the large superconducting magnets in operation today. Its big drawback is the large amount of copper and cooling channel required satisfying the equation despite the considerable reduction in ρ which pure metals show when cooled to low temperature. But this is possible for detector magnets while for accelerator magnet we need a way to reduce degradation without diluting J_c (to satisfy the criterion) too much.

2. Adiabatic stabilization (against "flux jumping" effect)

Early attempts to use hard superconductors for shielding or trapping of magnetic fields faced the difficulty that under certain conditions the supercurrents suddenly broke down. The underlying effect has become known under the name of flux jumping. Let us consider a slab of superconductor exposed to an external field B_0 in y direction, which is considerably larger than the penetrating field B_p (the transition is not sharp). Let us choose the x axis as the normal of the slab and call 2a its thickness so that it extends from x = -a to x = +a and its height h is assumed to be much larger than the width 2a ([1]; chapter 7). Applying the Maxwell equation

$$\oint \mathbf{B} \cdot d\mathbf{s} = m_0 I \qquad (1.17)$$

and with no variation in the y and z directions, we can easily find

$$B(x) = B_0 - m_0 J_c (a - x) h \qquad (1.18)$$

where J_c is the critical current density at the given field B_0 and initial temperature T_0. Now if we assume that an amount of heat DQ per unit volume is put into the slab the temperature will rise by an unknown amount ΔT and at the same time the critical current density will decrease by DJ_c. The effect of decreasing the current density is to increase the field inside the slab, and the resulting magnetic flux is associated with a longitudinal voltage. This voltage leads to Joule heat generation because a current with density J_c is flowing in the slab. The time integral of the voltage is equal to the change in magnetic flux through the slab.

The magnetic flux between 0 and x (the slab is symmetric) is:

$$f(x) = \int_0^x B(x)dx = B_0 \cdot x - \int_0^x m_0 \Delta J_c (a - x)dx = B_0 \cdot x - m_0 J_c (ax - \frac{x^2}{2})h \qquad (1.19)$$

and its change due to the change in J_c is

$$\Delta f(x) = m_0 \Delta J_c (ax - \frac{x^2}{2})h \qquad (1.20)$$

The Joule heat produced in a slice of thickness dx and height h is $DF(x)J_c dxh$. Integrating over x and dividing by the volume ah of the half-slab we obtain the Joule heat generation per unit volume

$$\Delta q = J_c \int_0^a \Delta f(x)dx = m_0 J_c \Delta J_c \frac{a^2}{3} \qquad (1.21)$$

In first order one can write for the reduction in critical current as

$$\Delta J_c = J_c \frac{\Delta T}{(T_c - T_0)} \tag{1.22}$$

Then the total energy balance is:

$$\Delta Q + \Delta q = c_s \Delta T \Rightarrow \Delta Q = \left[c_s - m_0 \frac{J_c^{\,2} a^2}{3(T_c - T_0)} \right] \Delta T \tag{1.23}$$

where c_s is the specific heat per unit of volume. From 1.23 we can see that the additional energy input Dq due to Joule heating is equivalent to a reduction in heat capacity. If we define an effective specific heat by:

$$c_s^{'} = c_s - \frac{m_0 J_c^{\,2} a^2}{3(T_c - T_0)} \tag{1.24}$$

Instability is then reached when this quantity vanishes or becomes negative. In that case the slightest disturbance will cause the superconductor to reduce its critical current and expel part of the captured magnetic flux. This process is called flux jumping. Not necessarily it brings a quench since the specific heat increases with the third power of temperature.
From the equation 1.24 the condition for flux jumps to be avoided is:

$$\frac{m_0 J_c^{\,2} a^2}{c_s (T_c - T_0)} \le 3 \tag{1.25}$$

$$a \le \sqrt{\frac{3 c_s (T_c - T_0)}{m_0 J_c^{\,2}}} \tag{1.26}$$

It can be shown that a flux jump is to be expected when the external field reaches B_{FJ} given by:

$$B_{FJ} = m_0 J_c p = (3 m_0 c_s (q_c - q_0))^{1/2} \tag{1.27}$$

A similar theory such as above gives a maximum stable radius for a superconducting cylinder filament as:

$$r_{\max} = \frac{p}{4} \sqrt{\frac{c_s (T_c - T_0)}{m_0 J_c^{\,2}}} \tag{1.28}$$

For example for NbTi with T_0=4.2K B_0=5T $J_c \approx 3 \cdot 10^9 A/m^2$ $T_c \approx 7.2K$ and $c_s \approx 5.6 \cdot 10^3 J(Km^3)$ we get r_{max}=30μm.

Hence wires made from pure superconductor are becoming unstable against flux jumping if their diameter exceeds about 0.1mm in this adiabatic model (we did not consider the effect of cooling). This is the main motivation for using composite wires, made of many thin NbTi filaments which are embedded in a matrix of high-conductivity normal metal, usually copper.

If this conductor has low resistivity it can provide an additional stabilization against flux jumping by slowing down the motion of flux and by conducting away the resulting heat (dynamic stabilization).

3. Filaments coupling

Now days filamentary NbTi superconductors are composed as follow: the matrix material is copper, which is easy to process with NbTi and contributes towards dynamic stabilization of flux jumping by virtue of its low resistivity and high thermal conductivity (both of which improves at low temperatures). However, the use of a high conductivity matrix does create one significant problem, it couples the filaments together magnetically. The result of coupling is to make the composite behave as a single large filament, the advantage of subdivision are lost and the whole composite once again becomes unstable to flux jumping. Fortunately by twisting the composite a changing field still induces screening currents to flow, but they must now cross the matrix twice per twist pitch, thereby encountering sufficient resistance to limit their amplitudes. The screening currents flow along a filament and vertically down (parallel to the field) through the matrix. The effect of these currents is to reduce the field inside the composite:

$$B_e - B_i = \dot{B}_i t \qquad (1.29)$$

Where B_e and B_i are the external and internal field, $\dot{B}$ is the rate of change of the internal field and

$$t = \frac{m_0}{2 r_t}\left(\frac{l_{twist}}{2p}\right)^2 \qquad (1.30)$$

where r_t is the effective transverse resistivity across the matrix and l_{twist} is the twist pitch.
If the screened field (B_e-B_i) is less than B_{FJ}, coupling between the filaments will not cause flux jumping.

4. Stability against mechanical movement

Another source of degradation in magnets is the possibility of sudden release of mechanical energy within the magnet as the current and field are increased. The problem is to minimize the possible movements of the magnet under electromagnetic stress ([1]; chapter 5).
An easy way to have an idea on how to deal with these problems is to use the concepts of Minimum Propagating Zone MPZ and Minimum Quench Energy MQE.
It is assumed that a sudden localized energy input has created a resistive zone of length l in a conductor of cross sectional area A carrying current density J in the superconductor which occupies a fraction λ of the cross section area A, the remainder being copper of thermal conductivity k and resistivity r (see Fig. 1.17).

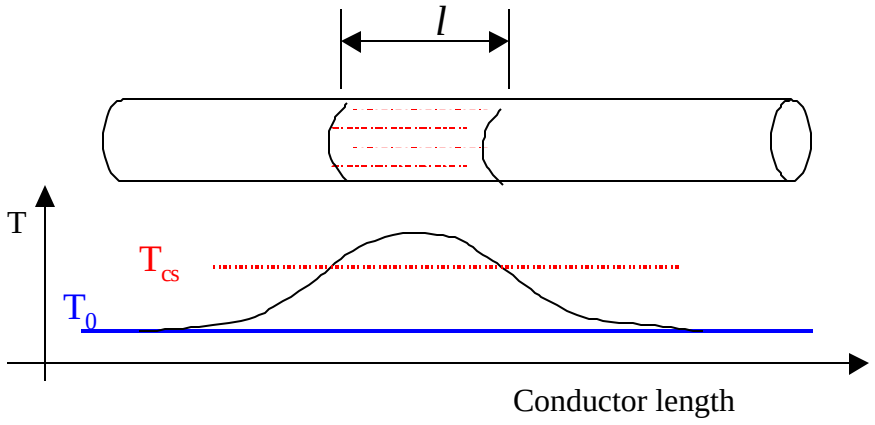

Fig. 1.17 Propagation of a normal zone ([3]).

Equating the heat generated to the heat conducted supposing a steady state condition:

$$\frac{2kA(1-l)(T_c - T_0)}{l} \approx \frac{l^2 J^2 r \cdot A \cdot l}{(1-l)} \qquad (1.31)$$

So we get the length l of a normal zone as:

$$l \approx \left(\frac{2k(1-l)^2 (T_c - T_0)}{l^2 J^2 r} \right)^{1/2} \qquad (1.32)$$

This l is the length of a normal zone in which the ohmic heat generated is just equal to the heat conducted out. For a length smaller than l we can recover the superconducting state while for length bigger than l the quenched zone will grow without limit and the entire magnet will quench. The energy needed to set up the MPZ is the MQE:

$$MQE = Alc_s (T_c - T_0) = Ac_s (T_c - T_0)^{3/2} \frac{1-l}{l \cdot J} \left(\frac{2k}{r} \right)^{1/2} \qquad (1.33)$$

where c_s is the volumetric specific heat of the composite.
To optimize the value of MQE (larger is preferred) we should have big volumetric specific heat (c_s) by making the winding porous to liquid helium, that has the highest heat capacity at this temperature, and reduce r, J, l even if these last two are not for sure the things which one wants to reduce. The solution is once again NbTi embedded in a matrix of copper (higher c_s, k and lower r).

Summary of requirements

1. critical field and temperature: depend on the material chemistry, it's important to get the optimum composition for alloys and the correct stoichiometry for compounds
2. critical current: depends on the microstructure, α-Ti precipitates on dislocation cell boundaries in NbTi
3. mechanical properties: NbTi is ductile and it is better when supported by matrix
4. for cryogenic stability, the superconductor has to be combined with large quantities of copper
5. for stability against flux jumping, one must take a filamentary composite wire with filament diameters < 50 mm
6. to decouple the filaments, the wire must be twisted
7. for low magnetization (field distortion), the filament must be 5-10 mm diameter
8. to provide dynamic stability against flux jumping and also to maximize MQE, the conductor must have a low resistivity and high thermal conductivity (NbTi plus copper matrix)

Chapter 2

HGQ PROGRAM AT FERMILAB

2.1 Introduction and general aspects of superconducting magnets

Before considering High Gradient Quadrupoles tested at Fermilab we would like to discuss some peculiar features of superconducting magnets such as cable, mechanical design and field quality.

2.1a Cable Design

Existing accelerators use NbTi as a superconductor material, due to its ductile property and insensitivity to stress. Magnets built with NbTi have a maximum field value limited to ~10T at operating temperature of 1.9K. Newer magnet designs utilize Nb_3Sn or Nb_3Al conductor to be able to achieve higher field values ([2]).
The basic constituent of superconducting magnet cable is a strand which is a multi-filamentary composite of NbTi filaments in a low resistivity copper matrix. Typically, strand diameters are around a millimeter. The filament size is generally <100μm in diameter, which is required to prevent flux jumps, the mechanism responsible for quenches in the early days of superconducting magnet development. The strand is also twisted to reduce intrastrand filament coupling, which would lead to energy losses during a current ramp. The main parameters in strand design are:

1. Critical current. The higher the critical current density at a given high B-field the better, as less conductor is needed to reach the target field, or a higher field is possible for a given volume of conductor.
2. Copper to superconductor ratio. A greater copper fraction lowers the peak temperature during a quench, but leads to lower achievable current for a given conductor cross-section.
3. Filament size. In addition to avoiding the flux jump mechanism, there is another requirement that leads to reduce the filament size, since field quality degradation due to superconductor

magnetization effects are inversely proportional to filament size. On the other hand lowering the filament size may result in a conductor cost increase.

4. Inter-filament spacing. Filaments should be kept as close as possible. However, sub-micron inter-filaments spacing can introduce detrimental proximity couplings of filaments.

Strands are bundled together to form a rectangular cross section cable called a Rutherford cable. The cable typically has 20-50 strands twisted and formed in a flat and keystoned (tapered) shape. This taper allows the cable to be arranged into an arched coil, which has beneficial mechanics, aspects. Multistrand cable is more flexible than a monolithic cable, and has several advantages relative to winding a single wire itself:

1. Winding a magnet coil using an n-strand cable means that single-piece strand lengths can be 1/n times as long as if the coils were wound from individual strand: this eliminates the need to produce uniform strand in multi kilometer lengths and the need for strand splice.
2. Smaller inductance due to fewer turns which results in lower coil to ground voltages during a quench.

Cable design and fabrication should address the following issues:

1. Compaction, which is the ratio of the conductor relative to voids. Higher compaction leads to greater mechanical stability and coil winding ability. If compaction is too high, however, less helium can penetrate into voids and this might affect the cable thermo-dynamical properties, in addition to possibly degrading the J_c of the cable at the highly compacted inner edge.
2. Control of the cable dimensions in order to ensure accurate coil geometry and mechanical properties.
3. Minimization of filament damage in the cable which could result in critical current degradation due to a sharp strand bending.
4. Control of interstrand resistance in order to minimize eddy current losses due to interstrand couplings while not restricting current re-distribution among strands.

Finally, the cable must be insulated with a thin insulation with good dielectric strength in a liquid helium environment and under high pressure (up to 100MPa). The insulating material requires good mechanical properties over a wide temperature range and also has to be radiation resistance. For example, Fermilab designed HGQ cables are insulated with two wraps of Kapton (polyimide) film, which have gaps while wounded and these gaps increase the wetted perimeter and allow for HeII penetration. Kapton is usually coated with epoxy or polyimide adhesive to keep the coils mechanically solid during furthers manufacturing procedures.

2.1b Mechanical design

In high field magnets Lorentz forces in the form:

$$\mathbf{F} = \mathit{Л}\mathbf{l} \times \mathbf{B} \qquad (2.1)$$

(where |**I**| is the direction of cable length) are extremely high due to the high current and high B field in the conductor. For example the operating current and the average field in the HGQ conductor are 12000A and ~8T respectively, so the Lorentz force on a 1m-length cable is ~96000N. This enormous force can move the cable or just a strand in the cable, resulting in premature quenching of the magnet. Furthermore, distortions of the magnet under Lorentz forces can result in poor field quality. All successful accelerator magnet mechanical designs have kept the conductor well constrained within a rigid mechanical structure ([23]).
The cos(nθ) design (see later section on field quality) approximated by current shells is the preferred design since it uses less conductor. An added benefit to use a current shell arrangement around a cylinder is that the coil behaves as a "Roman arch" (see Fig 2.1). In this cable configuration the external structure applies a radial inward compression which, as in a Roman arches, is transferred into azimuthal compression inside the coil, which counteracts the formation of tensile stresses that would otherwise appear under the action of the Lorentz forces. Therefore the coil tensile stress properties are not an issue. The coil needs only to be held together for the installation, then constrained in the roman arch structure ([3]).

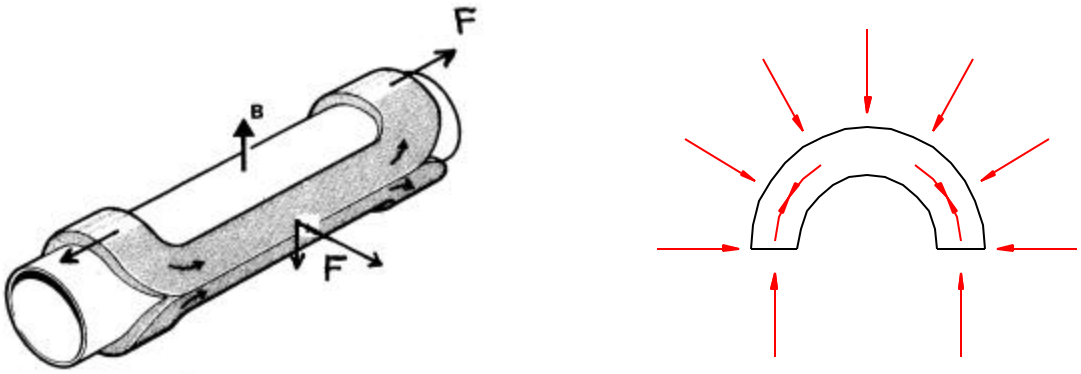

Fig. 2.1 Curved saddle coil and forces on roman arch structure.

For example (and we will explain in detail later) the HGQ mechanical structure is a common arrangement in existing superconducting accelerator magnets. The coil is surrounded with stainless steel collar laminations. The collared coil structure is contained in an iron yoke, and the yoke is held together with a stainless steel skin.
The horizontal component of the Lorentz forces points toward the midplane of the coil, which means that under excitation the coil may move away from the pole of the magnet collar and become unsupported. To prevent this from happening, the coils have to be pre-compressed (preloaded) in the collar laminations. The collar cavity size is designed to match the compressed coil size, so installing the collars is only possible by applying high radial pressure on them in order to compress the coil azimuthally. This procedure requires that the collar laminations cover about half of the coil and every other lamination is rotated by 90 degrees so that by applying a single key they can be locked together after the coils are preloaded ([22], [23]).

2.1c Field quality and current shell design

Field quality is of great importance to the accelerator designer as it directly affects beam optics and stability of the beam ([2]).
Superconducting magnets are current dominated magnets. The iron yoke is only used to shield the field and to prevent large stray fields around the magnet. The field contribution from the iron is usually less than 30%. In the absence of the iron yoke the vector potential **A** generated by a line current has

only a component parallel to the beam direction. Let us choose z to be the beam direction. From Biot-Savart's law the particular solution for A_z is:

$$A_z = \int_S -\frac{m_0 J_z}{2p} \ln R dS = -\frac{m_0 I}{2p} \ln R \qquad (2.2)$$

Where R=|**R**|=|**r**-**r**$_0$|, r is the current source vector and r_0 is the field observation point. In a cylindrical coordinate system **r** = (r,θ) and **r**$_0$ = (r_0,φ) we get

$$A_z = -\frac{m_0 I}{2p} \ln r + \frac{m_0 I}{2p} \sum_{n=1}^{\infty} \frac{1}{n} \left(\frac{r_0}{r} \right)^n \cos(n(j - q)) \qquad (2.3)$$

The r and φ components of the magnetic fields are given by Maxwell's equation **B**=curl**A**, so

$$B_{r_0} = \frac{1}{r_0} \frac{dA_z}{dj} = -\frac{m_0 I}{2p} \sum_{n=1}^{\infty} \frac{1}{n} \left(\frac{r_0^{n-1}}{r^n} \right) \cos(n(j - q)) \qquad (2.4)$$

$$B_j = -\frac{dA_z}{dr_0} = \frac{m_0 I}{2p} \sum_{n=1}^{\infty} \frac{1}{n} \left(\frac{r_0^{n-1}}{r^n} \right) \cos(n(j - q)) \qquad (2.5)$$

In order to generate pure dipole and quadrupoles field let us apply the following current distribution on a cylinder of radius r:

$$I(q) = I_0 \cos(mq) \qquad (2.6)$$

We get A_z, B_{r_0} and B_j :

$$A_z = -\frac{m_0 I_0}{2p} \ln r \int_0^{2p} \cos(mq) dq + \frac{m_0 I}{2p} \frac{1}{m} \left(\frac{r_0}{r} \right)^m \cos(mj) \qquad (2.7)$$

$$B_{r_0} = -\frac{m_0 I_0}{2} \left(\frac{r_0^{m-1}}{r^m} \right) \sin(mj) \qquad (2.8)$$

$$B_j = -\frac{m_0 I_0}{2} \left(\frac{r_0^{m-1}}{r^m} \right) \cos(mj) \qquad (2.9)$$

For **m=1**

$$B_x = B_{r_0} \cos j - B_j \sin j = 0$$

$$B_y = B_{r_0} \sin j + B_j \cos j = -\frac{m_0 I_0}{2pr} = const \qquad (2.10)$$

This is a homogeneous field pointing in the y direction, i.e., a **pure dipole field**.

For **m=2** and introducing

$$g = -\frac{m_0 I_0}{2p \cdot r^2} \tag{2.11}$$

We find

$$\begin{aligned} B_x &= gr_0(\sin 2j \cos j - \cos 2j \sin j) = gr_0 \sin j = gy \\ B_y &= gr_0(\sin 2j \cos j + \cos 2j \cos j) = gr_0 \cos j = gx \end{aligned} \tag{2.12}$$

And this is a **pure quadrupole field**. In general if the current density at a given radius follows a cos(mφ) distribution, it will generate a m^{th} order harmonic field.

Re-writing the equations 2.8, 2.9 using these identities

$$\begin{aligned} B_n &= -\frac{m_0 I_0}{2p} \frac{r_0^{n-1}}{r^n} \cos nq \\ A_n &= -\frac{m_0 I_0}{2p} \frac{r_0^{n-1}}{r^n} \sin nq \end{aligned} \tag{2.13}$$

We obtain

$$B_{r_0} = \sum_{n=1}^{\infty} (B_n \sin nj + A_n \cos nj) = B_N \sum_{n=1}^{\infty} (b_n \sin nj + a_n \cos nj) \left(\frac{r_0}{r_{ref}} \right)^{n-1} \tag{2.14}$$

Where b_n and a_n are the normal and the skew multipoles related to the main field B_N, with the B_n (A_n) given in unit of Tesla and b_n (a_n) are dimensionless and usually are given in units of 10^{-4} at a given reference radius (r_{ref}).
Reference table for HGQ magnets gives the values of normal and skew multipoles in unit of 10^{-4} related to tests done on quadrupoles with a reference radius of 17mm.
Ideally a quadrupole should have as only main multipole the quadrupolar component but in practice one can not produce a perfect cos(mθ) current distribution at a given radius, since the conductor cross section restricts the current density. If one could build winding coils with a cable whose cross section is changing then we could have perfect dipole with a cross section of conductor formed by intersection of two ellipses while the intersection of two crossed ellipses would produce a perfect quadrupole. But practically this is impossible and in multilayer coil designs the cable width within a layer must be constant.
The solution is to use a fixed conductor cross section and try to move blocks of conductor around by introducing “wedges” with zero current density. This approximates the cos(mθ) distribution of current density and minimizes higher order field harmonics and the amount of the conductor used.
Of course, it is not practical to introduce too many wedges, since wedges are voids, which reduce the amount of the conductor close to the beam, reducing the central magnetic field value. The use of a limited number of wedges can result in excellent field quality if the spacing and the angle of the wedges are chosen correctly.

After the final design is chosen it is necessary to measure the multipole coefficients in order to know the limit of the magnets one uses.

As introduced the reduced normal (b_n) and skew (a_n) multipole coefficients are used to describe the field quality since the values of b_n and a_n (with $n \neq N$ where N corresponds to the main multipole) are directly related to the field errors. Accelerator designers use an error table in their particle tracking studies to evaluate the accelerator performance.

The main sources of field errors are:

1. Geometrical errors. The field errors originating from misalignment of the conductor and iron yoke relative to the design values are called geometrical errors. These errors which can affect allowed and not-allowed a_n and b_n are usually related to fabrication and installation imperfections.
2. Iron saturation. When the field exceeds 2T, the contribution from the iron yoke to the central field is no longer increasing linearly with the transport current, but starts to saturate. Non-uniformity of the saturation leads to increase of the multipoles. This effect is undesirable since it leads to a current dependent field error, however by shaping the inner region of the iron lamination; saturation effects can be minimized.
3. Coil deformation under Lorentz forces. Once the mechanical analysis of the magnet is performed this current depend error can be easily calculated. Since Δb_n and Δa_n may not be corrected with design modifications, they should be minimized.
4. Superconductor magnetization. Ramping the magnet current changes the magnetic field in the superconductor as a function of time. In response, currents in superconductor are re-distributed in order to shield the interior of the conductor. This produces a changing magnetic moment affecting the field quality. Since these currents flow without resistance they do not decay quickly but very slowly only as a result of flux creep. These long lasting eddy currents are also called persistent currents. The bipolar nature of these currents can lead to non-uniform field distortions. The peak magnetization of a filament is proportional to the filament diameter a and critical current J_c as given by:

$$M_p = \frac{4}{3p} m_0 J_c a \qquad (2.15)$$

   Since the field distortion is proportional to M_p, the filament size is usually kept small (between 5-15μm in diameter) to control this effect.
5. Eddy currents. The copper matrix between the superconductor has low resistivity allowing eddy currents loops to develop between filaments and strands. These currents are temporary, and therefore they generate temporary magnetization and field distortions. In a twisted filament the time decay is given by:

$$t = \frac{m_0}{2 r_t} \left(\frac{l_{twist}}{2p} \right)^2 \qquad (2.16)$$

   where r_t is the effective resistivity of the copper-superconducting matrix and l_{twist} is the twist pitch. This time constant for practical NbTi strands is on the order of few tens of milliseconds, but for untwisted multifilamentary strands it can be quite large. In a Rutherford cable current loops can also be generated between strands through contact resistance. In a two-layer cable the resistance between crossing strands can be quite small, due to the large contact area and high pressure. They are usually referred to as interstrand coupling currents.

2.2 HGQ magnets: mechanical structure, design of magnets

Fermilab, as part of the international collaboration for the LHC project, has to provide the quadrupoles for interaction regions, which are high gradient quadrupoles. These magnets are key components to provide strongly focused high-energy proton beams and to realize high luminosity beam collisions for physics experiments. The inner triplet is composed by four high gradient quadrupoles and KEK will provide the external ones while Fermilab will provide the inner ones ([22], [23])
The four magnets are bussed together in series even if the power supplies 8kA, which run in every magnet, plus 6kA, which run only in the inner ones. As shown in Fig 2.2 the magnets are grounded so that the inner ones are decoupled from the outer ones (peak voltage to ground is related to one pair of magnets).
The connections between magnets consist of superconducting bus bars.
There are different parameters to be satisfied for the USA magnets and KEK ones and they have also rather different characteristics.

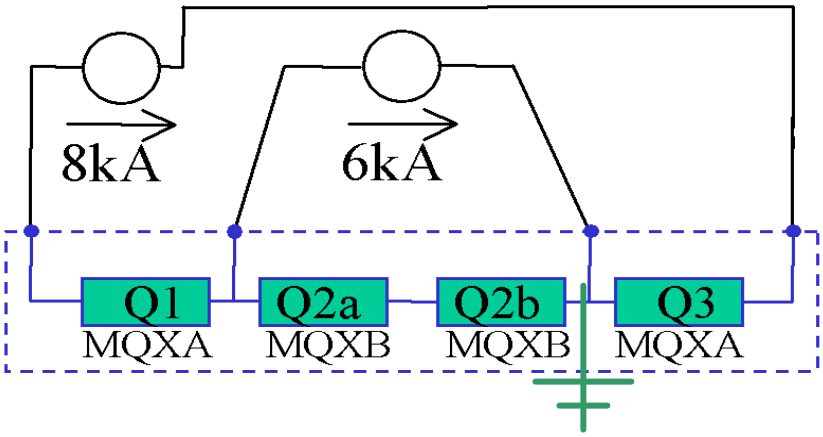

Fig. 2.2 Electrical schematic of the inner triplet the magnets are grounded so that the inner ones are decoupled from the outer ones.

HGQ model magnets

At Fermilab a series of model magnets has been produced to optimize design and details to ensure adequate performance, which is strongly determined by mechanical design.
Optimization of the magnet mechanical design is being pursued through comparison of results obtained from analytical calculations, finite-element method models, short mechanical assemblies and fully instrumented magnets.
Finally, short (~2m) fully instrumented model magnets (HGQ01-HGQ09) were fabricated utilizing the latest design and materials choices and tested at the Fermilab Vertical Magnet Test Facility (VMTF), where their mechanical, quench, and magnetic performance were extensively studied.

The mechanical design of the Fermilab HGQ magnet consists of a 2-layer cos(2θ) coil structure supported by stainless steel collars, which are surrounded by a cold iron yoke and stainless steel skin capped with steel end plates. The collars provide coil azimuthal and radial support. The iron yoke is magnetically aligned to the coils but does not provide any additional support. Longitudinal support

and restraint of the coils is provided by end loading screws (bullets) which apply an axial load to the coils that is reacted via the end plates by the stainless steel outer shell (see figure 2.3).

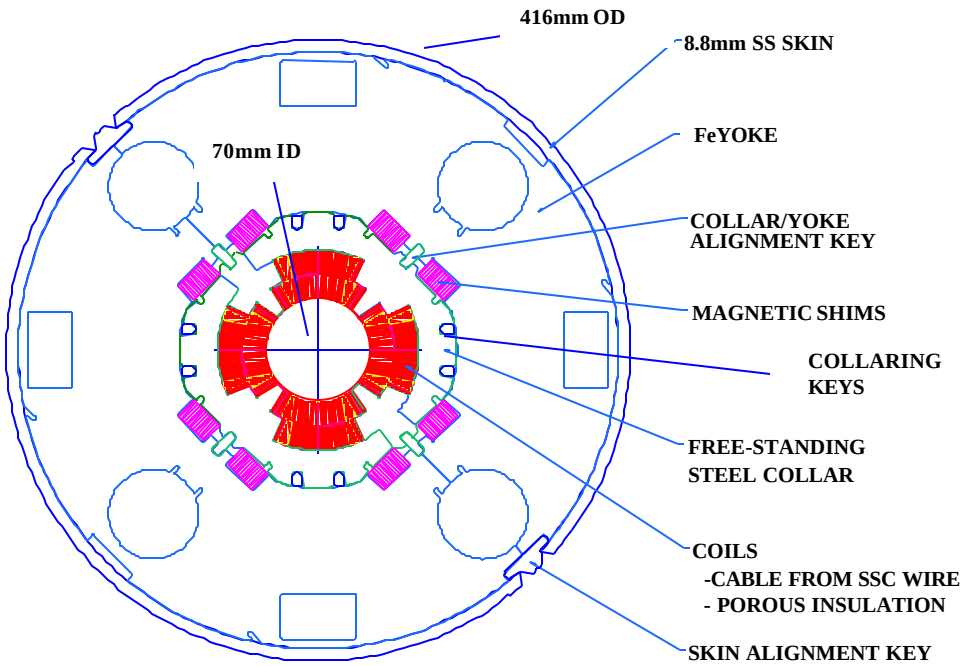

Fig. 2.3 Cross section of Fermilab HGQ short model.

The coils are wound using Rutherford-type NbTi cable, insulated with Kapton film with a polyimide adhesive (Epoxy). The end spacers of the coil were fabricated using G-10. The collared coil assembly is surrounded by a laminated two-piece iron yoke that is aligned to the coils using bronze keys. The iron yoke provide magnetic field tuning and flux return, and acts as a spacer for the outer shell. The iron yoke is constrained by an 8mm thick stainless steel shell that is aligned to the yoke using full-length stainless steel keys, which also provide the optimal geometry for the shell weld joint. The two halves of the skin are welded simultaneously from both sides, using multiple passes.

Radial support and azimuthal compression of the coil ends is provided by an aluminum end can and G-11 collets. The profiles of the end can and collets are tapered so that as they are installed longitudinally, they provide radial compression and support. Longitudinal support of the coils is provided by 50mm thick stainless steel end plates that are welded to the outer shell. Loading screws (bullets) mounted into the end plates apply a longitudinal load to the coils. The end cans are bolted to the end plates in an effort to minimize coil displacement away from the end plates during cool down. Longitudinal expansion towards the end plates during excitation is reacted only by the bullets.

2.3 Winding and structures of coils

The general design of the Fermilab HGQ magnet, as already said before, consists of a 2-layer cos(2θ) coil structure and often we will refer to the inner and outer layer as inner and outer coil. The main properties of the coils are ([19]):

- the inner (outer) coils for these magnets are wound under 36kG of tension, from 38 (46) strands NbTi Rutherford cable (the only exception was for magnet 7 with 37 strands in the inner layer).
- the inner layer cable consists of 38 0.808mm (diameter) strands and has a cross section with a minor edge of 1.326mm, a major edge of 1.587mm and a width of 15.4mm.
- the outer layer cable consists of 46 0.648mm (diameter) strands and has a 1.054mm minor edge, a 1.238mm major edge and the same width of 15.4mm.
- both cables have a packing factor of 91%. The NbTi filament size in the strands of both layers is 6μm, and the Cu:Sc ratio is 1.3:1 for inner strand and 1.8:1 for the outer strand.
- the strand critical current density at 5T and 4.2K is greater than 2.75kA/mm^2.
- the cables are insulated with Kapton tape and polyimide or epoxy adhesive. In particular they are insulated using two wraps. The inner wrap for both cables is made of Kapton film 25μm thick and 9.5mm wide wound with 50% overlap. The outer wrap of inner cable is made of 50μm thick Kapton film wound with a 2mm gap, while the outer cable outer wrap consists of Kapton film 25μm thick and 9.5mm wide with 50% overlap. The gaps in the outer wrap of the inner cable significantly increase the wetted perimeter and allow for HeII penetration, enhancing the removal of energy deposited in the inner coil.
- copper wedges are used to separate current blocks and yield the proper current density distribution. The end parts of these coils, made from G-10 or Ultem, are designed and machined to provide least-strain paths for the individual cable turn.

After winding, the coil assemblies are cured at 130°C or 190°C (depending on the adhesive used) with sufficient pressure and mold cavity shimming to yield a finished coil with the required azimuthal size and mechanical properties.

The cured coils are supported by collar laminations made of Nitronic 40 stainless steel. The coils are assembled, covered with several layers of Kapton film to provide electrical insulation, and enclosed by the collar laminations. The collars are then compressed radially, providing mechanical support for the coils and the proper conductor alignment, and they are held in place using stainless steel keys inserted under pressure.

The collared coil is enclosed by a two piece iron yoke, which is radially supported by an 8mm thick stainless steel skin. The yoke is aligned with the collared coil using alignment keys, which also maintain a gap of about 350μm between the collar and yoke laminations.

The HGQ magnet mechanical constraint system was designed to provide a coil stress of approximately 80MPa in the inner and outer coils when assembled at room temperature. This stress was chosen so that upon cool down to liquid helium temperatures and under the effect of Lorentz forces, the coils are still fully supported by the collar structure.

Table 2.1 Strand Parameters.

Parameter	Unit	Inner cable		Outer cable	
		Value	Tolerance	Value	Tolerance
Diameter	mm	0.808	± 0.0025	0.6505	± 0.0025
Cu/SC ratio		1.3 : 1	± 0.1	1.8 : 1	± 0.1
Surface coating		None	-	None	-
Anneal		None	-	None	-
Minimum critical current	A	378	-	185	-
Minimum RRR		70		70	
Twist direction		Left		Right	
Twist pitch	mm	13	± 1.5	13	± 1.5

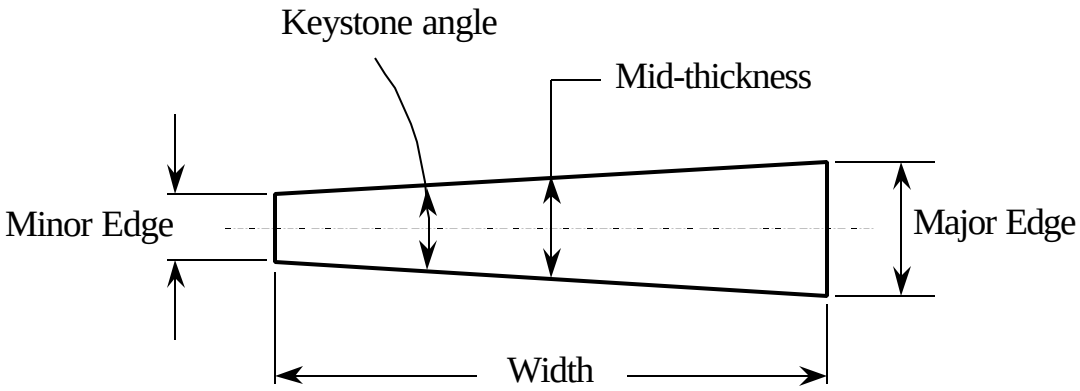

Fig. 2.4 Cross section of the cable.

Table 2.2 Cable Parameters.

Parameter	Unit	Inner cable		Outer cable	
		Value	Tolerance	Value	Tolerance
Number of strands		37	-	46	-
Cable width	mm	15.40	± 0.025	15.40	± 0.025
Minor edge	mm	1.320		1.051	
Cable Mid-thickness	mm	1.465	± 0.006	1.146	± 0.006
Major edge	mm	1.610		1.241	
Keystone angle	degree	1.079	± 0.05	0.707	± 0.05
Transposition length	mm	114	± 5	102	± 5
Lay direction		Right	-	Left	-

Minimum critical current	kA	14.0	-	8.5	-
Minimum unit length	m	180	-	200	-
Residual twist	degree	0 - 90		0 - 90	
Minimum bending radius	mm	7		15	

Starting from HGQ05 a set of design and manufacturing modifications were made to eliminate issues considered the causes of poor quench performance in previous model magnets. The most important mechanical changes, relative to the base line design were:

- use of G10/G11 as end part material
- cure of inner coil at higher pressure, resulting in a higher inner layer elasticity modulus and more uniform inner/outer coil mechanical properties
- welded 75mm collar packs with pole filler pieces to increase the out of plane rigidity of the collar laminations relative to the coils and the insensitivity of quench performance to the presence or absence of end restraint
- aluminum end can assemblies over both ends
- attachment of the end cans to the end plate, which ensures contact between the coil ends and the end plates and stretches the coil straight section after cool-down
- reduction of shim from 0 to 25μm at the pole to achieve the required pre-stress

Other changes were made starting from magnet HGQ06 to study their effect on the stability of magnet. These include a 5-block end design and variations on cable parameter and coil fabrication to study the effect of interstrand resistance.
As we can see from table 2.3 the high ramp rate quenches originated in the midplane turns (see Fig.3.7), are related to the low cable interstrand resistance (high eddy current effect). This is a result of the 190 °C high pressure cure used on HGQ06-07 and stabrite coated cable (with cable cores of unalloyed Ti (ST-TI), stainless steel (ST-SS), and kapton (ST-KA) ribbons) in HGQ08 (to avoid oxidation of Cu and reduce interstrand resistance).

Table 2.3 Curing cycle for coils and critical currents with ramp rate 300A/s.

	coil curing cycle		**I_c (ramp rate 300A/s)**
model	**temperature**	**Pressure (MPa)**	**(A)**
HGQ01	135°	20	10965
HGQ02	190°	20	11335
HGQ03	195°	20	11298
HGQ05	130°	20	10519
HGQ06	190°	80	6433
HGQ07	190°	80	4487
HGQ08	190°	80	3941
HGQ09	190°/135°	20/80	12946

Table 2.4 Applied stress on the coils.

model	Azimuthal pre-stress 300K		Longitudinal end-stress 300K	
	Inner layer (MPa)	Outer layer (MPa)	Lead end (kN)	Return end (kN)
HGQ05	99	55	10.5	10.2
HGQ06	59	61	9.4	9.4
HGQ07	65	66	11	8
HGQ08	90	93	8.4	9.1
HGQ09	58	68	11	9

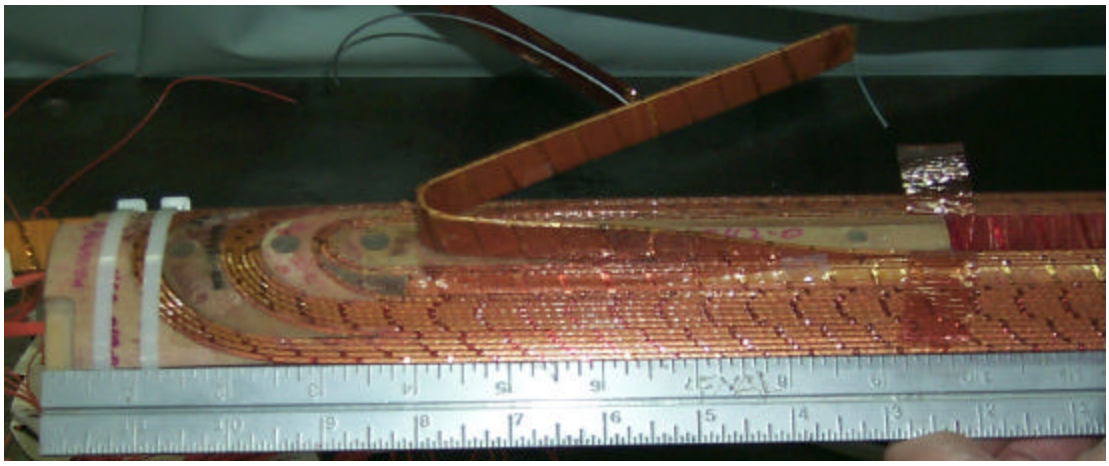

(a)

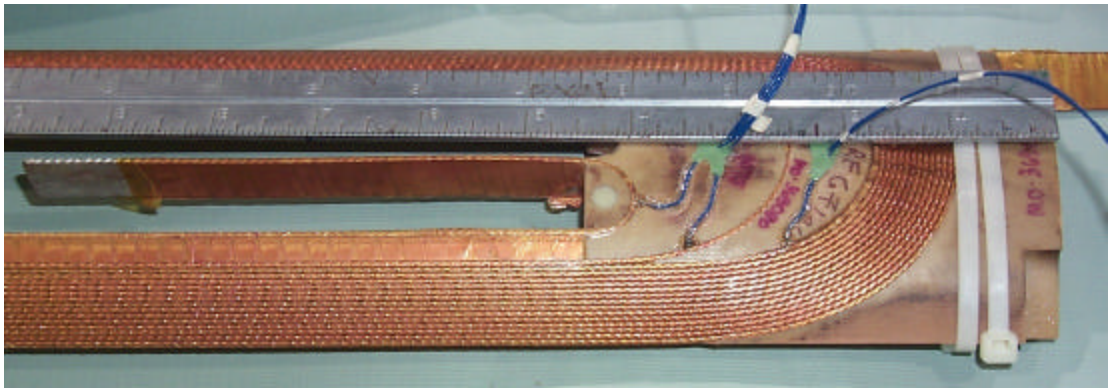

(b)

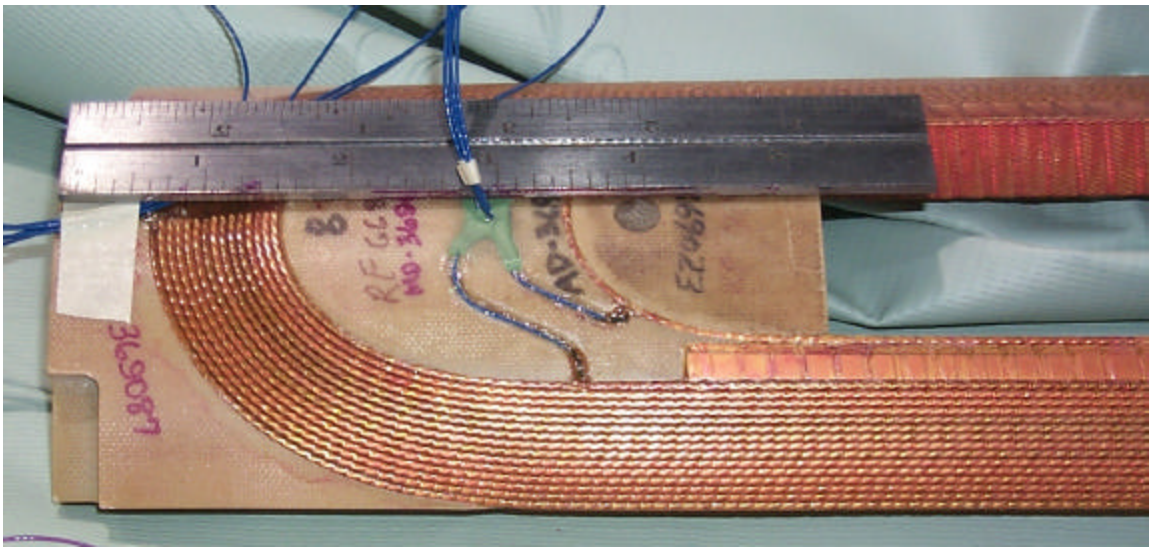

(c)

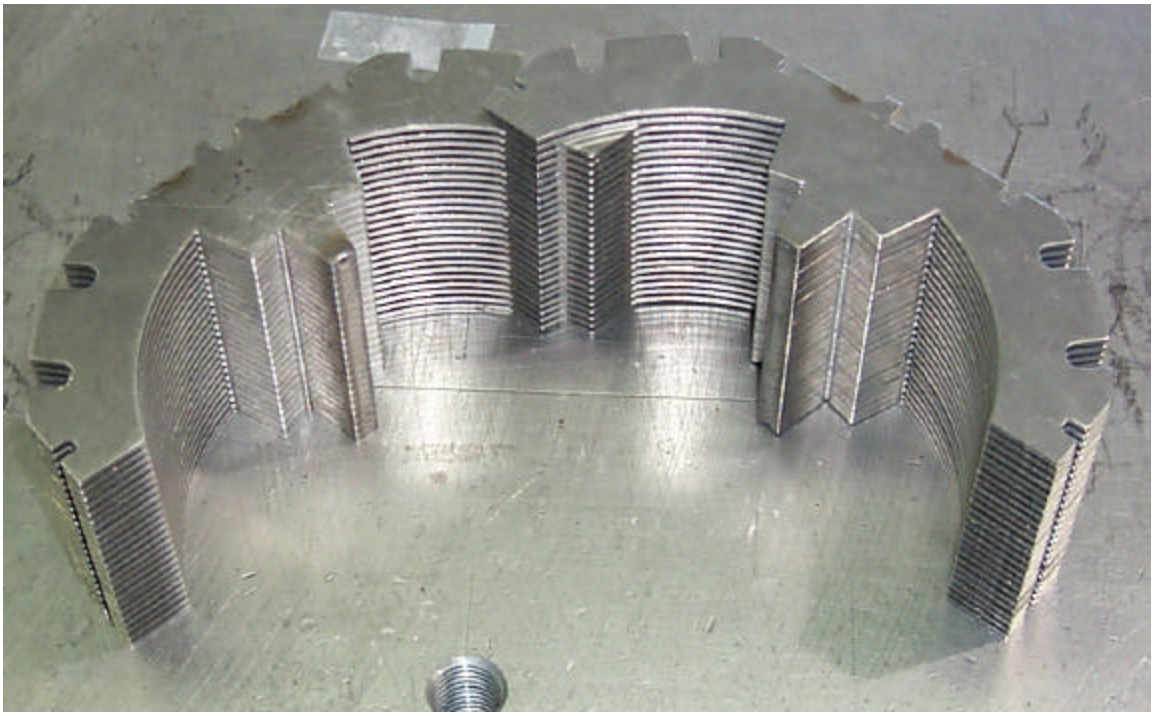

(d)

Fig. 2.5 (a) inner cable lead end, (b) outer cable lead end and spot heater position, (c) outer cable return end and spot heater position, (d) welded collar packs. A spot heater is a stainless steel segment which is used to induce quenches.

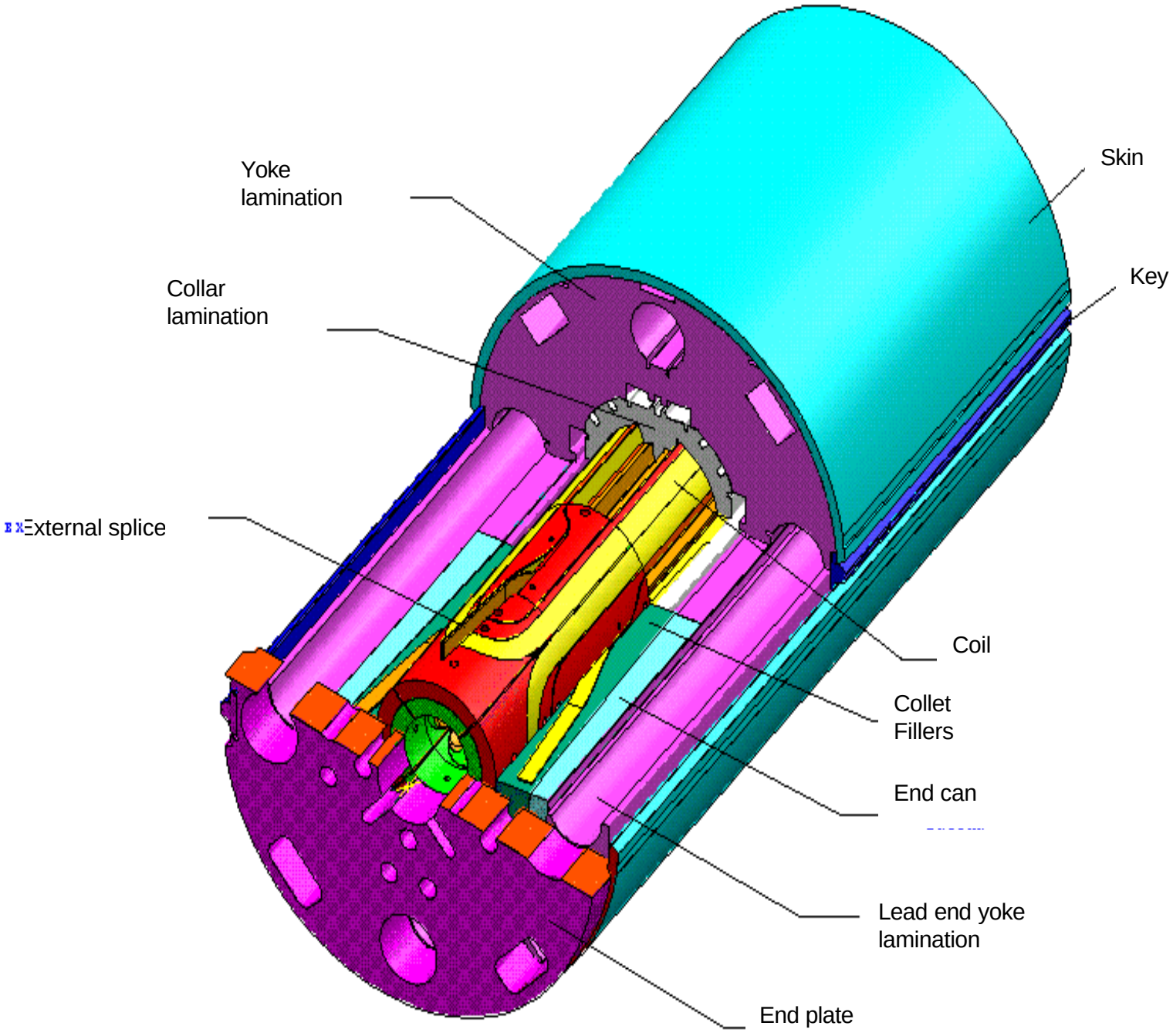

Fig. 2.6 Lead end structure.

2.4 Field map and field quality

As already said before the HGQ magnets have to provide a field gradient of 215T/m over a 70mm bore with good field quality due to large and rapidly varying values of the β-function in the interaction region ([11]).
The choice for the magnetic structure for the coils was changed through the HGQ program. The first short samples up to magnet 5 had a 4-block design where both the outer coil and inner coil were split in two blocks. The last four magnets had a 5-block design in which one of the two blocks in the inner coil was split again in two. The peak field in the inner coil is unchanged while the peak field in the outer coil was reduced by about 2%. This change brought a big improvement in the quality of the field and reduced the values of multipoles.
Another big difference between tested magnets is that while in magnets HGQ01-HGQ03 tuning shims were used to correct field errors from HGQ05 to HGQ08 they were eliminated and the missing iron from the shims reduced the gradient by 1%, but produced not noticeable change in harmonics. HGQ09 was built with yoke laminations incorporating the iron of the nominal shim returning the gradient to the design value. Magnetic measurements were performed using a vertical drive, rotating coil system. Probes used have a tangential winding for measurement of higher order harmonics as well as dedicated dipole and quadrupole windings measuring the lowest order components of the field.

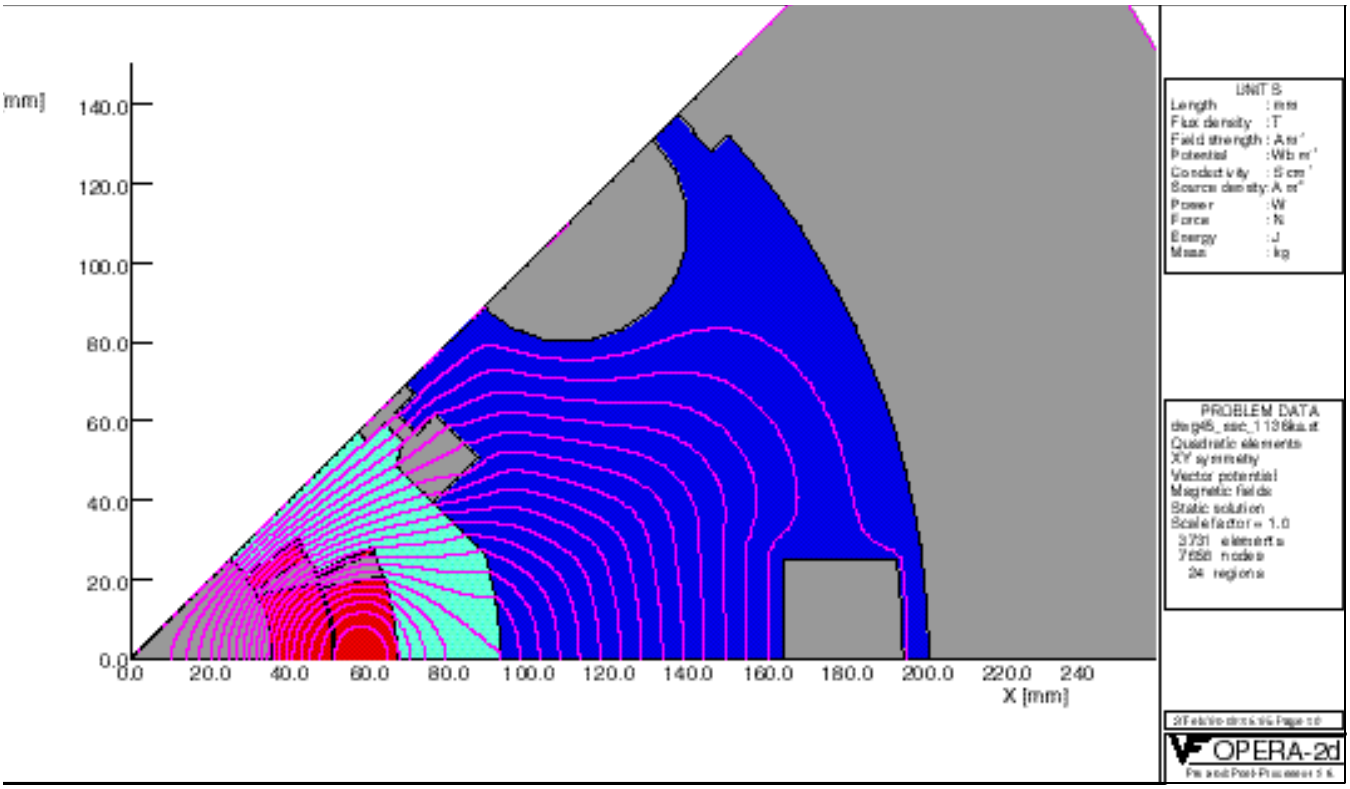

Fig. 2.7 Field map of an octant of a HGQ quadrupole.

As presented before the field is defined as series expansion with coefficients a_n, b_n which are used conventionally to define field quality.
Results for tested models are presented in tables 2.5 in units of 10^{-4} of the quadrupole field.

Table 2.5 Measured harmonics in the magnet straight section (6kA) in units of 10^{-4}.

n	HGQ							
	01	**02**	**03**	**05**	**06**	**07**	**08**	**09**
b_3	0.36	-0.70	1.04	0.72	0.25	0.18	0.61	0.71
b_4	0.26	0.18	0.14	0.00	0.09	0.01	-0.12	-0.05
b_5	-0.29	0.09	-0.34	-0.04	-0.11	-0.04	-0.01	0.08
b_6	-3.91	-1.54	-1.02	-0.30	-0.05	-0.45	-0.06	-0.28
b_7	-0.08	-0.01	-0.06	0.01	-0.03	0.02	-0.01	0.06
b_8	0.06	0.01	0.00	0.00	0.00	0.00	0.00	-0.01
b_9	0.04	0.00	0.00	0.00	0.00	-0.01	0.00	0.00
b_{10}	-0.10	-0.10	-0.04	0.01	0.00	-0.02	-0.01	-0.01
a_3	0.27	0.55	-0.30	0.12	-0.27	0.41	-0.01	0.35
a_4	2.00	0.53	0.32	0.19	-0.31	-0.50	-0.43	0.31
a_5	0.02	-0.17	0.26	0.05	-0.07	-0.24	0.12	-0.14
a_6	-0.08	0.03	0.07	-0.03	-0.05	-0.10	-0.03	0.04
a_7	-0.05	0.00	-0.03	0.01	0.00	0.07	0.00	0.02
a_8	0.02	0.02	0.03	0.00	0.00	0.01	-0.01	0.01
a_9	0.01	-0.01	0.01	0.00	0.00	0.01	-0.01	0.00
a_{10}	0.02	0.00	-0.01	0.00	0.00	0.00	0.00	0.00

Table 2.6 Measured harmonics in the magnet end regions in units of 10^{-4}.

	HGQ							
	lead end							
n	**01**	**02**	**03**	**05**	**06**	**07**	**08**	**09**
$b_{6,}$calc	3.1	5.5	5.4	5.4	3.5	3.5	3.5	3.5
$b_{6,}$meas	2.9	4.2	3.8	8.0	3.1	3.1	3.1	3.0
$b_{10,}$calc	-0.3	-0.3	-0.4	-0.4	-0.1	-0.1	-0.1	-0.1
$b_{10,}$meas	-0.3	-0.2	-0.4	-0.2	-0.1	-0.1	-0.0	-0.1
$a_{6,}$calc	0.5	0.4	-0.1	-0.1	-0.7	-0.7	-0.7	-0.7
$a_{6,}$meas	0.1	0.2	-0.3	-0.3	-0.4	-0.3	-0.4	-0.4
$a_{10,}$calc	-0.1	0.0	0.0	0.0	0.0	0.0	0.0	0.0
$a_{10,}$meas	-0.1	0.0	0.0	0.0	0.0	0.0	0.0	0.0

We have also to consider that injection takes place at fields ranging from 12.3-14.1T/m (B_2) due to the different β^* in the different interaction regions. At these low levels of excitation (670-700 A) persistent currents result in an additional component of the allowed harmonics (b_i). But these effects decay rapidly at a given constant current so that they have a negligible impact on machine performance.

2.5 VMTF and set up of the tests

Each model magnet in the HGQ project was tested in a vertical dewar and was seated in a HeII bath. The dewar is more or less 6m tall and the magnet seats in the bottom part of it.

Fig. 2.8 HGQ model ready to be inserted in the vertical dewar.

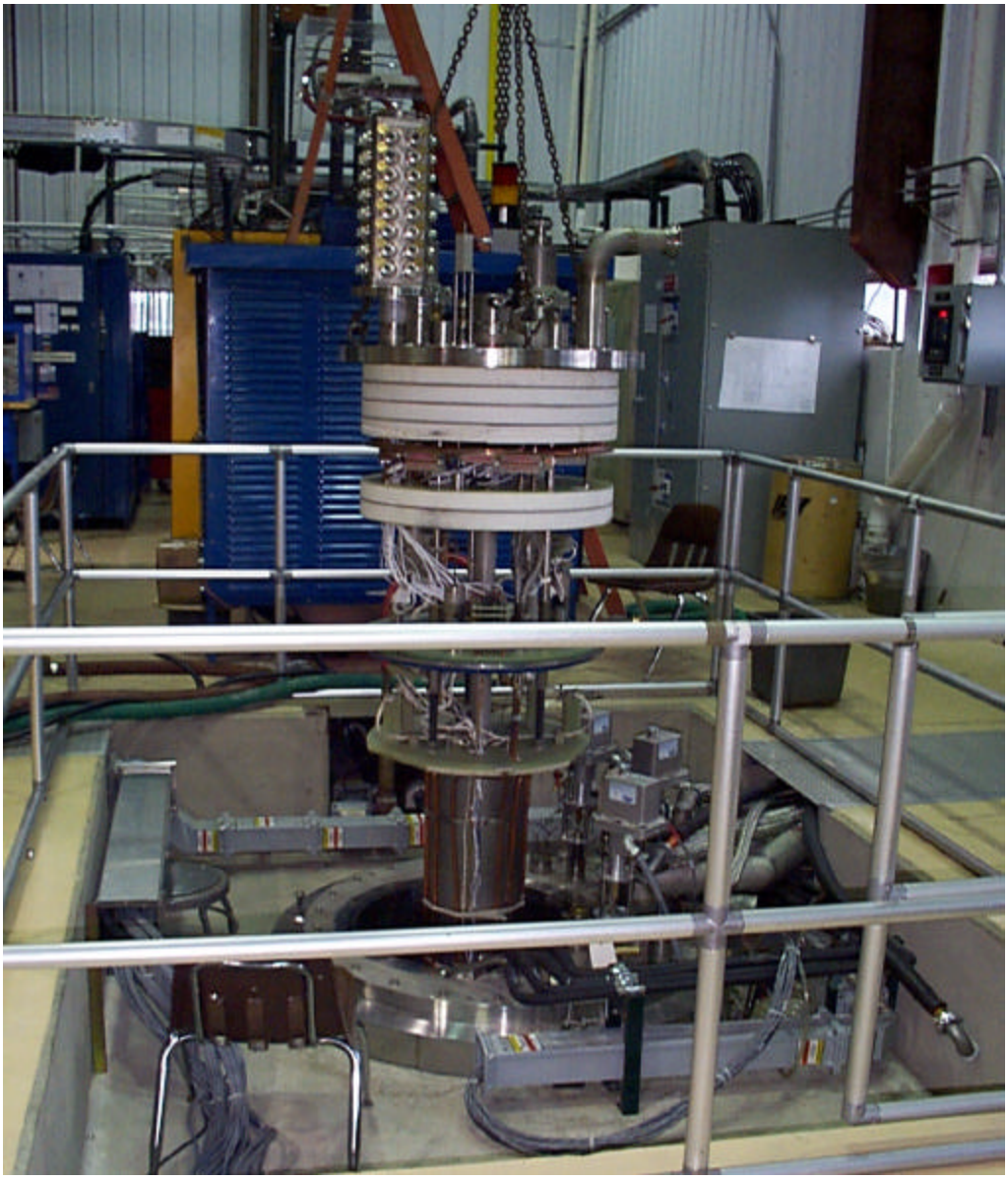

Fig. 2.9 Assembling for the test (instrumentation tree+top plate+HGQ model).

VMTF has a “double bath” dewar which is capable of testing a 4m long × 60cm diameter magnet. The leads can bring 15000A and the temperature environment is between 4.5K and 1.8K. The capability of pumping HeII is 2.5g/s at 16mbar.

In figure 2.10 we reported the usual window to control all the critical parameters in the dewar during the test. In particular several temperature sensors are in the dewar itself at the top and bottom of the magnet and pressure sensors are across the pipes where the helium flows. In case of quench the temperatures increase and by controlling the flow across the pipes one can recover the operating temperature of the magnet in a short period of time.

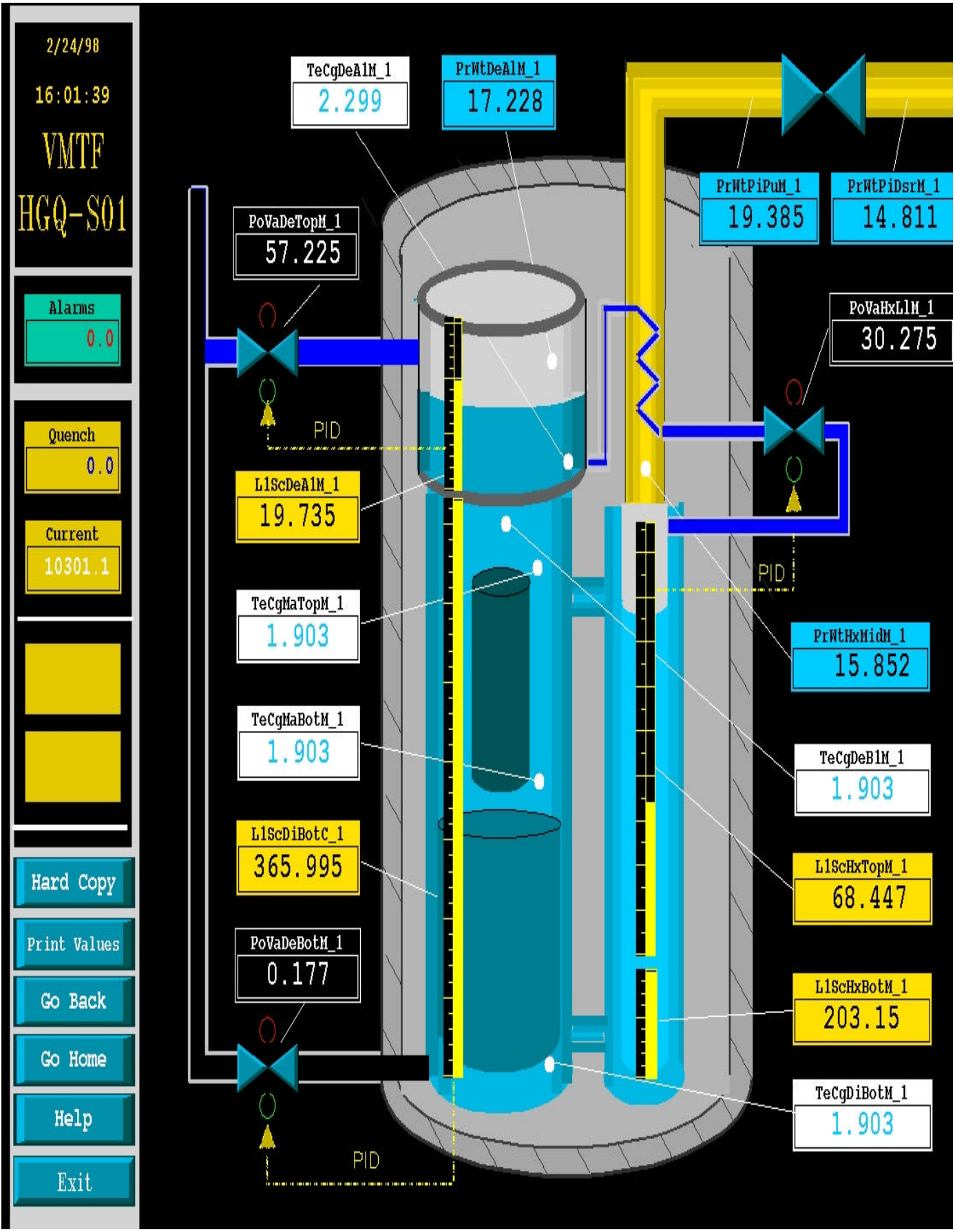

Fig. 2.10 Schematic view of the dewar during a test (control window of pressures in the pipes and temperatures inside the dewar).

Before entering in detail on measurements it is necessary to show the schematic system of a magnet and all the points where the actual measurements are taken.

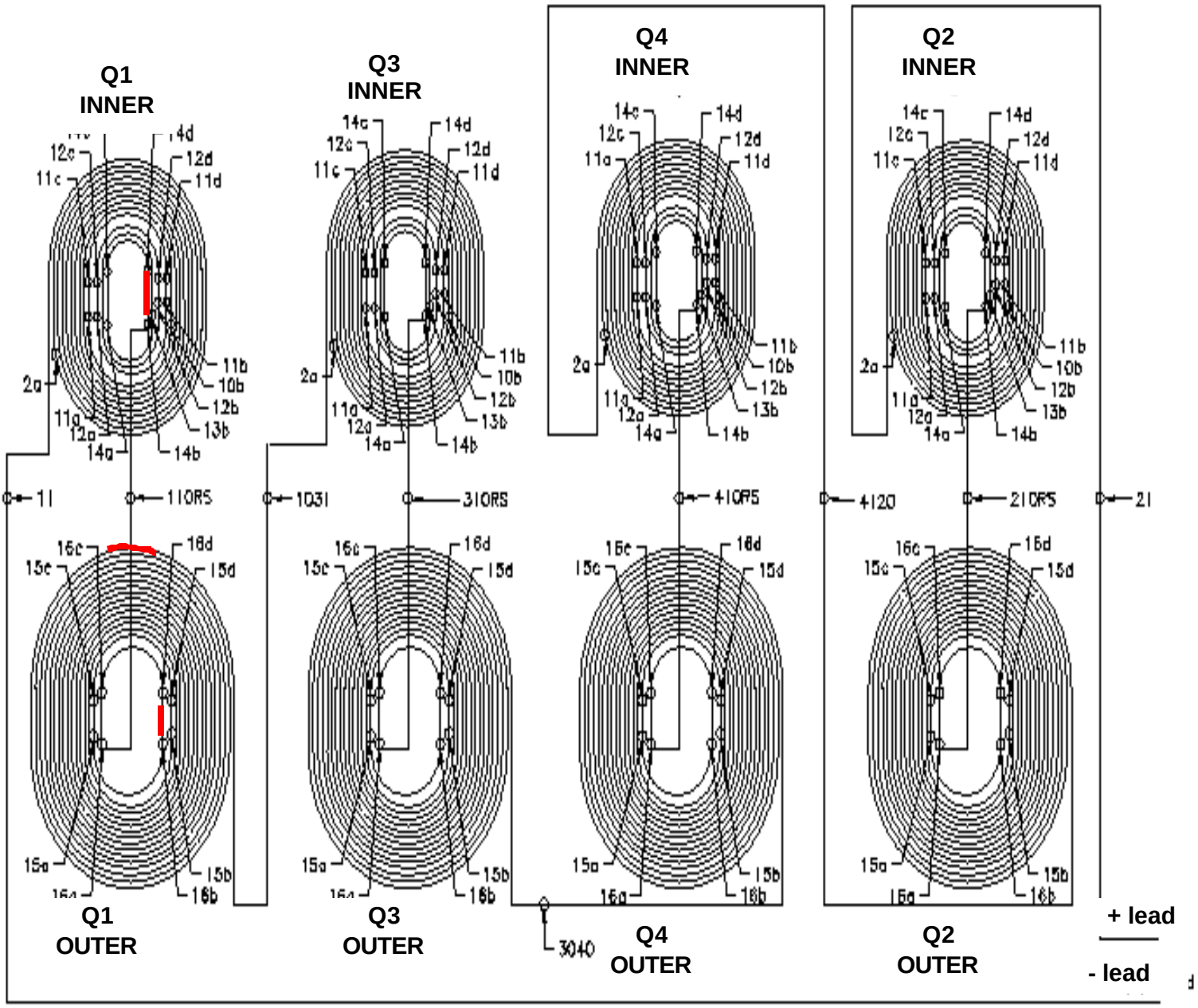

Fig. 2.11 Schematic voltage taps position (following electrical connection between different coils and different quadrants).

INNER COIL 14 turns, voltage taps from 11a to 14b
OUTER COIL 16 turns, voltage taps from 15a to 16d plus voltage tap 01m-01n on the end

As one can see the magnet has 128 voltage taps disseminated on **pole turns** (most internal turns) and **midplane turns** (external turns). Starting from inside the dewar the wires come out from the magnet. Then the voltage taps split in two blocks and enter in two different hypertronics connectors and exit in-groups of eight voltage taps. They cross the same resistor board and split again in two separate hypertronics connectors at 80K shield. Then they enter in the instrumentation tree and exit at room temperature. So the wires from every single voltage taps, which is on the magnet, follow a long path arriving at room temperature outside the dewar. Once outside the dewar they reach the patch panel and they are again split at the exit of it. They reach different isolation amplifiers and different pentek ADC where the signals are read out from software analysis system.

More important channels to analyze for our purpose are:

- magnet current I
- I_{dot} signal (change of current with time)
- whole coil signal (voltage of the entire magnet)
- half-half coil signal that is the difference in voltage between coils 2+4 and 1+3 and it helps to see where the quench starts
- half coils signal (1&3 and 2&4)
- quarter coil signals (Q1,Q2,Q3,Q4)
- eight coil signals (Q1 inner and outer, Q2 inner and outer, Q3 inner and outer, Q4 inner and outer)
- strip heater signals (usually not all of them are fired)
- voltage signal of the segment that quenches after the spot heater is fired, since the heater does not lye directly on the cable
- voltage taps signal of segments on the coils (for different studies we are interested in different channels)

In chapter 3 and 4 we will give more details about read out system, quench protection system and how data analysis was made.

Chapter 3

QUENCH PROTECTION SYSTEM FOR SUPERCONDUCTING MAGNETS

3.1 Introduction

As already defined a quench is the sudden transition from superconducting to resistive state (we cross the critical surface f(B,T,J)=0 in a point) and the basic process of a quench is the conversion of stored electromagnetic energy into heat. One of the first steps in the design of a superconducting accelerator is the choice of the cooling system and the liquid helium temperature in order to set the operational conditions well below the critical values of the magnet. If by some disturbance part of the magnet coil is heated beyond the critical temperature the cable becomes normal-conducting in this region. Depending on the size of the normal zone, the available cooling can be sufficient to recover the superconductivity (the current passes in copper until NbTi recovers its superconducting state) otherwise the heating is so violent that the transition is irreversible and the magnet quenches. In such a case if this heat could be distributed uniformly throughout the magnet winding, there would not be any problem but unfortunately the stored electromagnetic energy will never spread uniformly around the magnet winding. The quench always begins in a point and then spreads through the winding through ohmic heating and thermal conduction processes. The resistance of this normal zone will grow and will force the current to decay but during this process the starting point will always suffer the highest temperature rise because it is subjected to ohmic heating for the longest time. We can have two kinds of problems:

- the local temperature rise may be sufficient to char the insulation or even melt the conductor and destroying the magnet
- even if we can control temperature rise, very large potentials will be developed across the normal zone and may cause arcing between turns

There are several kinds of protection system for a magnet and they can be divided in two categories: active and passive techniques. These methods work for a single magnet but for a string of magnets as in LHC it is necessary to introduce a different protection system, as we will see later in this chapter.

3.2 Protection of a single magnet

The minimum response necessary to prevent conductor burnout when a quench occurs is the disconnection of the power supply. This requires the detection of the quench. Several signals can be used to sense a quench. For example acoustic emissions precede a quench and follow it. This is not a very accurate method because noise emission is not always accompanied by a quench. The best way to see a quench is to observe the resistive voltage which builds up when a normal zone grows and expands. This rising resistance leads to a change in current that induces also an inductive voltage. An inductive voltage can be present even if there is not a quench (for example during magnet charging) so one should be able to subtract this contribute to the voltage (to isolate the resistive contribution). In some cases one can measure the inductive voltage from additional devices and subtract it from the coil voltage electronically or estimate the inductive part with another identical magnet.
After quench detection the stored energy has to be dumped. For a single magnet two different techniques exist [28; “Quench Protection” lecture K.H. Mess]:

1. Active techniques (see fig 3.1), using a dump resistor which, reduces rapidly J because, after the quench is detected, the current is switched on a different path with a big resistance that will dominate the current decay (which is exponential). In a similar circuit a diode can be installed inside the cryostat (the so-called cold diode). The current will commute partially into the diode branch once the diode threshold is reached (at room temperature is few tens of a volt at 4.2K is few volts). These techniques have the advantage of extracting most of the stored energy from the cryogenic environment, thus avoiding the high pressures, which might result from explosive boiling of helium. Their main disadvantages are that they totally depend on the reliable operation of detectors and switches and that they can generate large external voltage. Moreover the diodes have a fixed polarity and a threshold which has to be passed only in case of real quench.

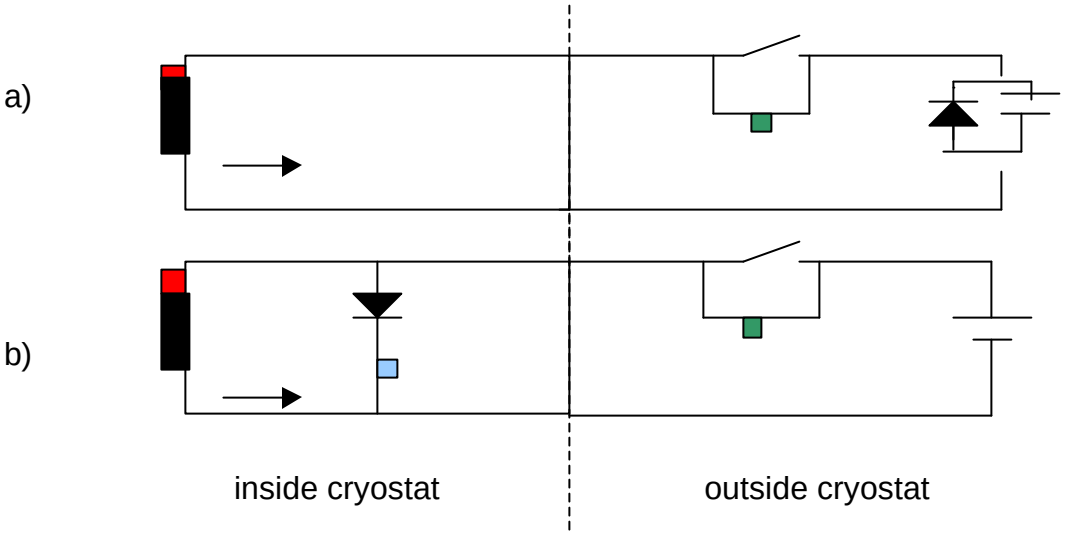

Fig. 3.1 Active techniques: a) external resistor, b) internal diode and resistor plus external resistor.

resistance quenching part — external resistance — added resistor

2. Passive techniques (see figure 3.2), using the coupling of the magnet with a secondary winding which will receive a fraction of stored energy after the quench so that temperature and voltage of the first will be reduced. They are usually cheaper, simpler and more reliable. They can also

reduce significantly the internal voltage without producing more external voltage. Another useful function that can be performed by a coupled secondary magnet, is the enhancement of the rate of propagation of the normal zone. As quench proceeds, the secondary will heat up and if it is in good thermal contact with the magnet winding, it will initiate further quenching (quench-back effect) increasing quench velocity and reducing the peak temperature. Another passive technique (that is preferable because more effective) is the subdivision. In this case the current can be driven to a different path by connecting shunt resistors across the magnet sections so that the heat is spread more easily in the entire magnet and the reached peak temperature is lowered. The main disadvantages of these techniques are that one has to set the energy dissipation when the magnet is charged and that all the magnet energy will be dumped in the cryostat at quench. Both these factors will waste liquid helium. Also, unbalance between windings could be a big risk.

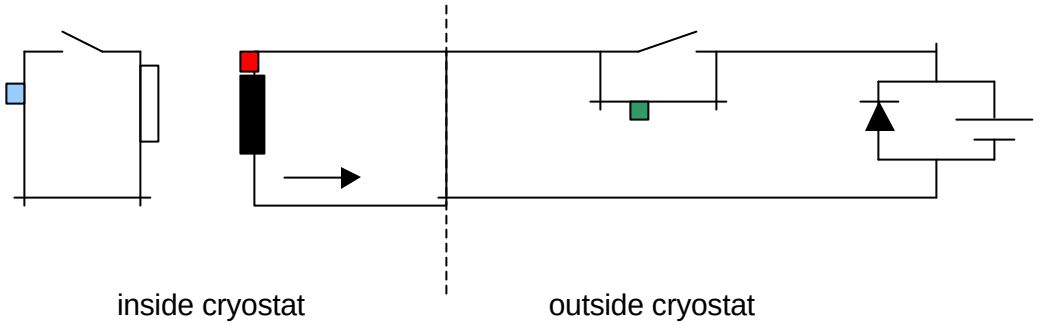

Fig. 3.2 magnetically-coupled resistor.

resistance quenching part — external resistance — coupled resistor

3.3 Protection of a string of magnets

Unfortunately, a simple switch, as in the case of a single magnet, cannot work in a case where more magnets are bussed in series. In fact simple switching-off dumps almost all stored energy into the quenching magnet and destroys it. On the other hand, energy extraction with external resistors would require an enormous resistance and hence a huge voltage to support them.
So the best way to protect a string of magnets is:

- detect the quench as fast as possible
- isolate the quenching magnet
- spread energy over a big region to prevent high peak temperature and voltage
- subdivide the inductance

For example let us consider the case of TEVATRON. The quench detection system is based on the measurement of voltage differences. Average voltage differences are calculated, including the inductive voltages during ramps, and compared with measured values. A significant discrepancy indicates a quench. The large values for the resistors, chosen for safety reasons, together with the cable capacity introduce a sizeable signal distortion to be corrected. Then the power supply of the quenching magnet has to be switched off without interrupting the magnet current and the stored energy has to be stored in suitable devices.
After this the energy of the unquenched magnets has to be kept away from the quenching magnet basically guiding the main current around the magnet through an external resistance R_b. In fact the total inductance L of the magnet string is much larger than the inductance L_q of a single magnet

hence the main current I decays with a much larger time constant than the current I_q in the quenching magnet. The differential equation for I_q is:

$$L_q \frac{dI_q}{dt} + I_q R_q(t) = (I - I_q) R_b \qquad (3.1)$$

Once the whole coil has become resistive one arrives at a steady state solution:

$$I_q = I \frac{R_b}{R_b + R_q} \approx I \frac{R_b}{R_q} \qquad (3.2)$$

So to minimize the current inside the quenching magnet the resistor R_b in the bypass line should be made as small as possible.
Two basic solution exist:

- thyristors, which act as fast switches at fast ramping machines. They have to be mounted outside the cryostat so one has to look carefully for low electrical resistance (main contribution to R_b) but high thermal resistance to avoid a heat load on the liquid helium system.
- bypass diodes, which act as fast switches at low ramp rate machines and can be mounted inside the cryostat. This solution brings lower resistance and each magnet can have its own bypass diode avoiding external supply needed for thyristors. Diodes have to be chosen carefully with low dynamic resistance and with a proper backward voltage (if it is too high it can produce high resistance and also it can make the non-quenched magnets to exceed the backward voltage of the diode itself).

To spread the heat very quick quench heaters are needed. But they need energy storage, some firing electronics, and feed-through into the cryostat. The heater band has to be in close thermal contact with the coil, because the heat must reach the coil as fast as possible. Good heat conduction means also little electrical insulation and hence the risk of shorts in the coil so that quench heaters are costly and dangerous themselves but essential in some case.
Finally, it is necessary to subdivide the machine into as many independent current-circuits as possible in order to be able to separate the quenching part from the others. For example for LHC it was proposed to divide the accelerator into 16 independent units with an equal number of breakers and dump resistors.

In this thesis we speak about the short sample for inner triplet quadrupoles for LHC and the final magnets for the inner triplet. It has to be noted that during the test of a single HGQ besides the protection system of quench heaters (which will be used in the final inner triplet) a dump resistor was added to increase protection and save some liquid helium. In the final design the inner triplet of LHC will be equipped only with strip heaters.

3.4 Protection system in LHC quadrupoles

As already said the USA magnets in the interaction region, will be combined into a cryogenic element (see figure 3.3) consisting of two 5.5m quadrupoles connected in series, operating at a peak field gradient of 215T/m and corresponding excitation current of approximately 12kA ([9], [15]).
The quench protection goals for these magnets are to limit the peak voltage to ground at **400V** and the peak temperature at **400K**, in a case of a spontaneous quench of a full scale magnet during LHC operation.
In fact, as already said, after a quench the energy is dissipated in the normal zones heating the coil and generating turn to turn and coil to ground voltage drop. The propagation velocity of the normal

zones is usually low relative to the heating rate of the cable so quench heaters are used to protect by greatly increasing the coil normal zones thus allowing the energy to be dissipated over a larger conductor volume.

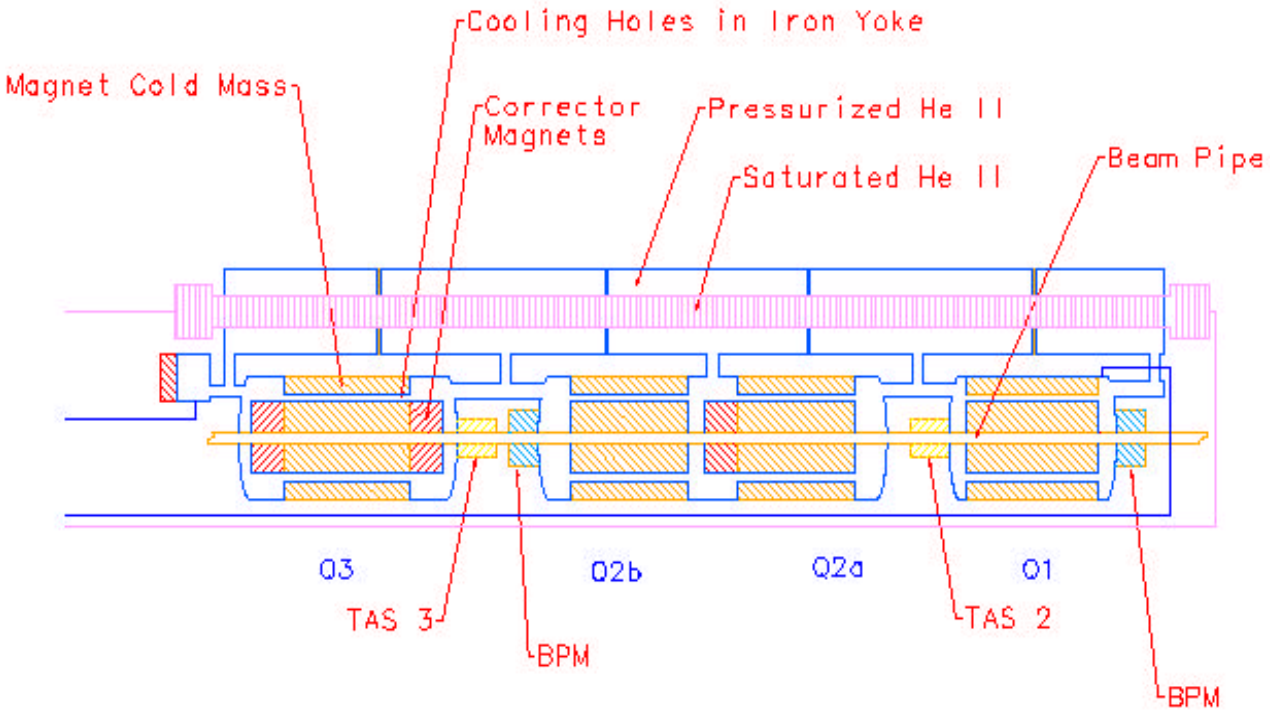

Fig. 3.3 Cryogenic element for inner triplet.

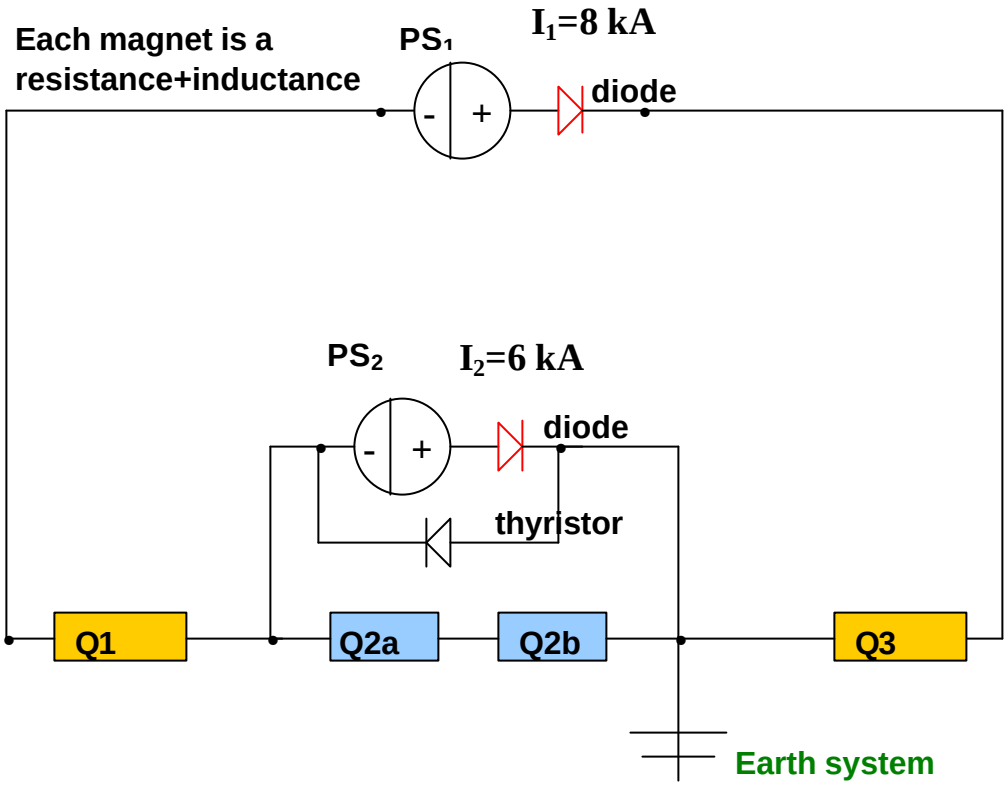

Fig. 3.4 Electrical system for the inner triplet.

Figure 3.4 shows the proposed power circuit for the inner triplet. As we can see, the maximum current for Q1 and Q3 is 8kA, while Q2a-b has a maximum current of 6kA + 8 kA.
When a quench occurs anywhere in the system, the power supplies are promptly turned off and all of the quench protection heaters are energized.
The placement of the earth system and the location of thyristors and diodes were chosen to minimize the voltage to ground and decouple the peak voltage and temperature characteristics of the Q2a-b vs Q1 and Q3 magnets.
The thyristor acts as a "current bypass" ,in the case when the inner loop I_2 current decays more quickly than the outer I_1 loop. This can easily occur since the L/R time constants of the inner and outer current loops will in general be different. The difference is due to the differences in magnet inductances between Fermilab and KEK magnets (Q1+Q3 has 5 times the inductance of the Q2a-b pair) and the expected variations in resistance growth due to heater efficiencies and quench origin. The combination of diode and thyristor in the inner loop assures that the voltage across the Q2a-b pair can never exceed the thryistor threshold voltage of 20 V. The system ground between Q2a-b and Q3 assures that one of the terminal of each magnet can be no more than 20 volts from ground. Hence, the voltage growth in the Q2 system with respect to ground does not depend significantly on the Q1 and Q3 voltage characteristics (and vice versa).
The quench protection strategy for LHC quadrupoles is to utilize strip heaters energized by external heater power supplies.

During the tests of model magnets we tested one magnet at the time. Also in this case the quench protection is based on strip heaters even if in order to save time and helium a dump resistor was added in the circuit. The dump resistor is disabled for events of induced quenches. In this case upon quench detection the leads of the magnet element are effectively shorted together and the stored energy dissipated within the magnet. The prompt and symmetric on set of resistive voltage due to the heaters is essential to minimize the peak coil temperature and minimizing the resistive-inductive voltage imbalances, which can generate large voltages to ground.
In fact these cold iron superconducting quadrupoles consist of eight coils positioned in a two- layer cos(2θ) geometry. The coils are electrically connected in series through inner coil pole turn to outer coil pole turn splices in each quadrant and through midplane turn quadrant to quadrant splices (see figure 2.11). In an ideal magnet and if the resistance of the region where the quench started is negligible with respects to the total coil resistance after firing the heaters, the voltage should be symmetric at every quarter coil. Any peak voltage would be generated from the differences in inductive and resistive voltage growth from inner to outer coil. But, in a real magnet, there are several factors to take in consideration because they can increase this voltage.

For examples

- **spontaneous quench origin**. The quench occurs in a particular place in the magnet so one coil starts to develop resistance voltage first.
- **variations in strip heater efficiency**. If resistance is not started at the same time on each quadrant, the resistance will not be the same quadrant to quadrant even if measurements seem to show that the difference in starting time is less than 10ms at operating current of 12 kA. Anyway it is important to consider the possibility that the heater firing units could introduce similar delay.
- **variation in RRR**. There can be variation in RRR both between inner and outer coils, between quadrant to quadrant and also magnet to magnet. The inner to outer coil RRR variation is usually

large but it is not a problem because the outer coil develops most of the resistance due to the heater position. The other two kinds of variation are more important and need to be studied.

- **failure modes**. In the normal LHC operation, Q2a Q2b will both have two circuits of heaters in operation in series. We should consider a possible simulation of the system Q2a/Q2b where one magnet has only one operational circuit, which should be safe from the point of peak temperature but it creates a resistance imbalance (voltage imbalance).

3.4a Strip heater: geometry and characteristics

Every model of HGQ test program was disseminated with 120 voltage taps. Every voltage taps reads a voltage between two different points on a coil and all the coils have the same scheme of voltage taps. The voltage taps are in turns near to the pole turns in inner and outer coils and in between them and then there are some voltage taps on outer midplane turn (most dangerous place for a quench). In these turns the field is very low and so the time to reach the critical surface is longer and it permits to reach higher peak temperature and higher voltage to ground values.
Magnets have been equipped with two possible layers of protection heaters. Inter layer heaters are located between the inner and outer coils (used in HGQ01-HGQ05), while the outer layers are placed between the collars and the outer layer. Each layer consists of four heaters. The geometry of the heater is that of a “race track” covering approximately 10 turns of one side of two azimuthally adjacent coils.
Thus the parallel or series connection of two “diametrically opposite heaters” (H1&H3 or H2&H4) in a given layer provide protection for all four magnet quadrants (see Fig. 3.5b). It is envisioned in the LHC quench protection system that independent power supplies (for protection redundancy) will power the two heaters strings. Strip heaters are connected to a capacitor bank constituted of 4 capacitors in parallel of 4.8mF each. The capacitor bank is discharged upon detection of voltage imbalance in the magnet due to resistive voltage from a quench ([15]).
The geometry of heaters was changed among the magnets in order to find out which one is the best in minimizing peak temperature and voltage to ground (see table 3.1 and figure 3.5a-c).

Magnet	Position	Element (all 25μm thick)	Insulation
HGQ01	Inter	stainless steel 15.9mm wide	325μm
	Outer	none	N/A
HGQ02	Inter	stainless steel 15.9mm wide	325μm
	Outer	stainless steel 15.9mm wide	350μm
HGQ03 & HGQ05	Inter	stainless steel 15.9mm wide	325μm
	Outer	15.9mm wide with copper plating 38mm etched areas at 114mm intervals	350μm
HGQ06	Inter	none	N/A
	Outer	12.7mm wide with copper plating 610mm etched areas at 1930mm intervals	250μm
HGQ07	Inter	none	N/A
	Outer	22.2mm wide with copper plating 610mm etched areas at 1930mm intervals	250μm
HGQ08	Inter	none	N/A

	Outer	15mm wide with copper plating 120mm etched areas at 360mm intervals	250μm
HGQ09	Inter	none	N/A
	Outer	15mm wide with copper plating 102mm etched areas at 204mm intervals	225μm

Table 3.1 Specifications for HGQ heaters (reported insulation is heater+cable insulation).

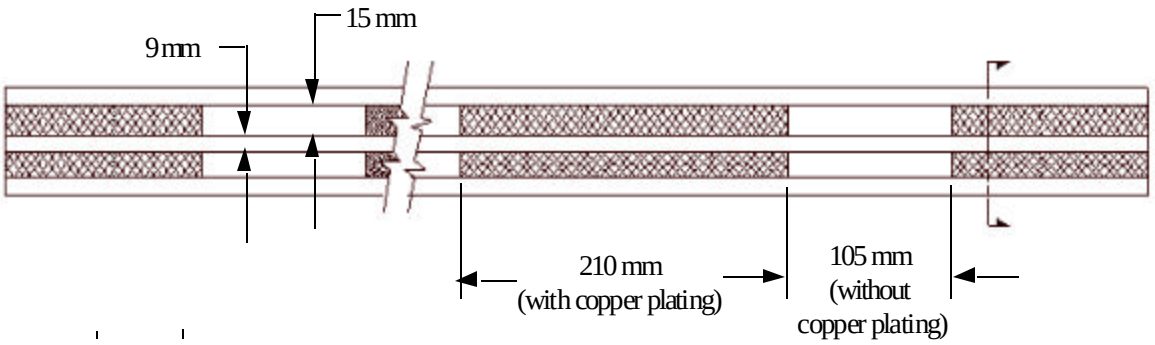

Fig. 3.5a Strip heater geometry for HGQ09.

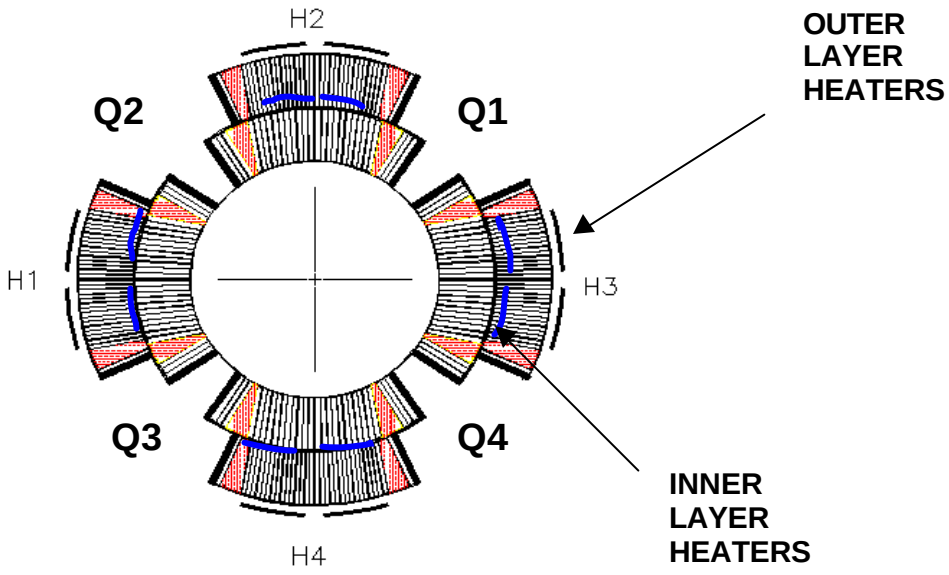

Fig.3.5b Cross section of a quadrupole of inner triplet and strip heater position.

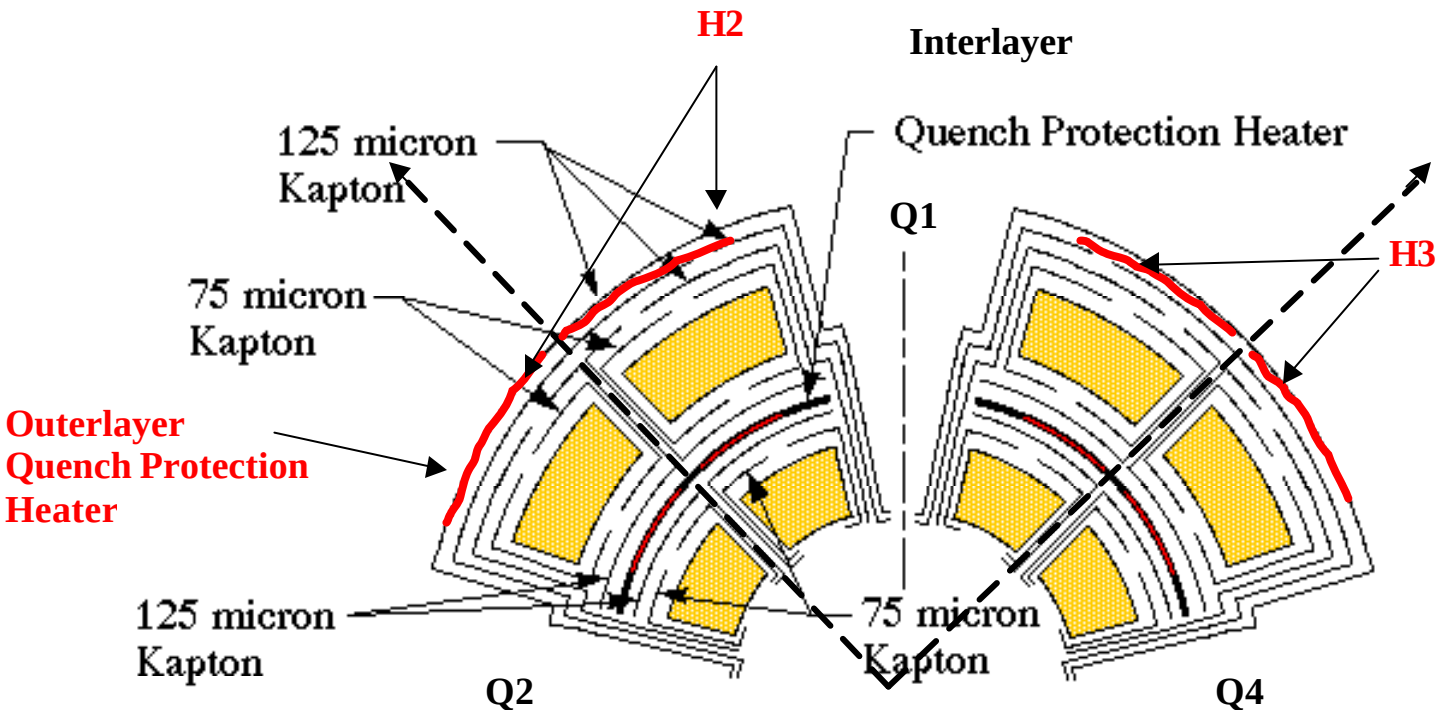

Fig. 3.5c Cross section of a quadrant of a quadrupole of inner triplet and strip heater positions. As one can see clearly if we hook up all the heaters circuits (H1+H2+H3+H4) each quadrant is "double" covered. For example in Q1 in covered by half heater circuit of H2 and half heater circuit of H3. If we hook up two heater circuits diametrically opposite we still covered all the quadrants but only half of it is covered by the heater. For example if we hook up H1&H3 then Q1 is "half" covered by H3 only on its right part while if we hook up H2&H4 then Q1 is "half" covered by H2 only on its left part.

There are several important parameters, which characterize heaters performance in particular:

- **V_{min}**, the minimum voltage (or energy) required to initiate a quench. It determines the voltage requirements for the heater power supplies.

- **t_{fn}**, the time between quench heater firing and resistive voltage initiation. It is a good measure of heater efficiency and low values of t_{fn} result in lower quench integral, which in turn translates into lower coil peak temperature.

- **MIITs**, the time integral from quench initiation of the square of the current (expressed in kA). This is actually related to the peak temperature reached in the coil and it is also defined as quench integral *QI*.

From the efficiency of heaters depends three other important characteristics of a magnet:

- **peak voltage**, the highest voltage measured from any of the eight coil leads relative to the magnet leads. This voltage develops because of the coil to coil variation in t_{fn} and coil to coil RRR.

- **peak coil temperature**, the highest temperature reached in the magnet (which usually occurs where the quench is started). It is estimated in two different ways. First the temperature can be simply related to the time integral of the square of the excitation current (quench integral), using an adiabatic temperature model. The other method is to measure directly the cable resistance adjacent to a spot heater. The measured resistivity, dominated by the resistance of the copper is then directly related to the cable's local temperature. We will see the details for these methods later (chapter 4).

- **quench propagation velocity** determined with the "time of flight" technique in which we determine the time needed for the quench to propagate between voltage taps separated by a known distance.

3.5 Eddy currents and quench back phenomenon

The operation of a synchrotron generally includes an acceleration phase during which the magnets are ramped from a low field (injection mode) to a high field (extraction or collider mode). While ramping, the varying field induces eddy currents in various components of the magnets, which result in heat dissipation and field distortions. The heat dissipation raises the magnet temperature and can lead to quenching. The field distortions perturb the beam circulation and can result in beam losses. Faster the acceleration, more serious the potential for ramp-related problems.
When the collider mode is reached and current is constant, in case of quench there is a sudden change in current and in field that can creates again eddy currents effects. This could also enhance protection properties because eddy currents can cause other quenches (quench back) and dissipate the heat faster along the magnet reducing the peak temperature and resistance.

The possible source of eddy currents in supeconducting magnets can create two different types of current:

1. intra-strand eddy currents: magnet coils are wound with Rutherford-type conductors, which consist of a few tens of strands twisted together and shaped into a flat, two-layer, keystoned cable. The strands themselves consist of thousands of filaments twisted and embedded in a matrix of copper. At liquid helium temperature the resistivity of copper becomes very low eventually resulting in filament coupling (reduced by twisting the strands but still visible when the field changes). In this multifilamentary twisted superconducting wire, the eddy currents run in a zig-zag path along the wire. The path is partly superconductive (inside the cable) and in part normal (in the copper matrix). For a case in which there is a constant ramp rate it can be found that the time constant of decay for these currents is related to the twist pitch length l_{twist} of the strand and the effective transverse resistivity ρ_t of the copper-NbTi composite ([1; chapter 7]):

$$t = \frac{m_0}{2r_t}\left(\frac{l_{twist}}{2p}\right)^2 \qquad (3.3)$$

2. inter-strand eddy currents: the mid-thickness of the two-layer cable is smaller than twice the strand diameter and contact surfaces at the crossovers between the strands of the two layers can be large. Also, during curing cycles the coils are pre-compressed azimuthally. Large contact surfaces and high pressure can dramatically reduce contact resistances at the strand crossovers that couple the cable strands so that loops are created and when the cable is subjected to a varying field eddy currents effect can be seen. The time constant of the current decay is ([27]):

$$t_{is,cable} = C\frac{l_{transp}(N_s^2 - 4N_s)}{R_{is}} \qquad (3.4)$$

where l_{transp} (~100mm) is the transposition pitch length of the strand, N_S is the number of strands in the cable and C varies between $1.6 \cdot 10^{-8}$ / $1.7 \cdot 10^{-8}$ $\Omega m^{-1}s$.

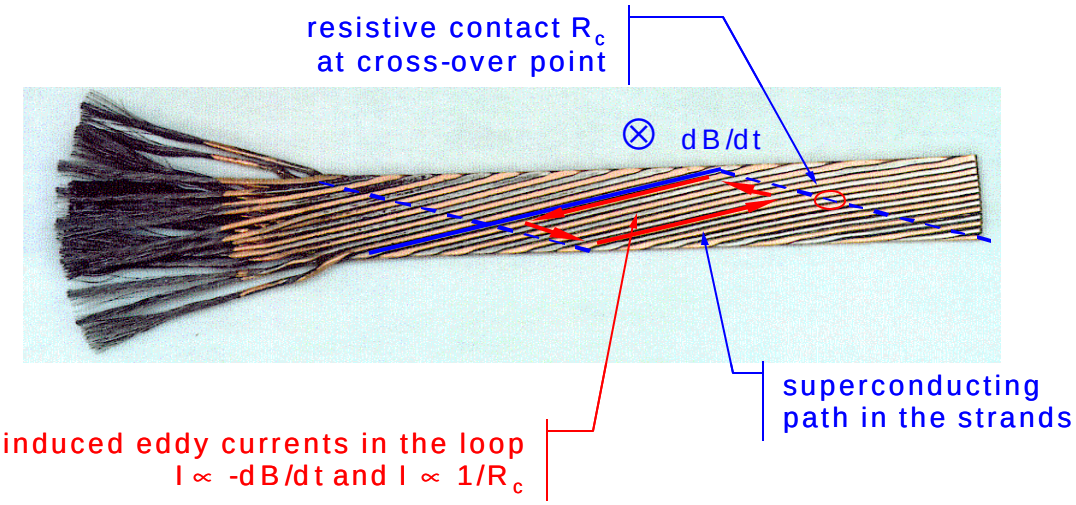

Fig. 3.6 Induced eddy currents in a Rutherford cable ([3]).

In addition, eddy currents are generated in all the other conductive components of the magnet (copper wedges and iron-yoke laminations) but these provide minor contributions. For example in HGQ program **HGQ06-HGQ08** had different curing cycle for their coils resulting in an effective reduction of inter-strand resistance which enhanced eddy current effect very visible during ramp-rate studies (τ is proportional to $1/R_{interstrand}$). In fact for these samples the critical current at high ramp rate was really low compared to magnet as **HGQ09** where the inter-strand resistance was much higher and eddy current effect was not visible.

To better compare the results for different magnets let us report the results on ramp rate studies made for all the models which can provide important information about heat deposition (eddy current effects in the cable) and coil cooling condition ([12]).
In particular at 1.9K we have:

Table 3.2 Critical current as a function of ramp rate for each short model.

model magnet	**dI/dt (A/s)**	**I_c (A)**
HGQ05	50	13542
	100	13504
	150	13531
	200	12469
	300	10519
HGQ06	300	6433
	200	10327
	100	13346
HGQ07	300	4487
	250	4738
	200	8326

	150	10419
	100	13172
	75	13934
HGQ08	150	4842
	135	7565
	120	9903
	100	10914
	80	12620
	300	3850
	200	3868
HGQ09	300	12946
	250	13046
	200	13183
	150	13310

From figure 3.7 one can see two regions on this curve: flat, ramp rate independent region at low ramp rates and region with monotonic decrease of quench current with the increase of current ramp rate.
As we can notice there is not visible degradation for critical current values at low ramp rate (nominal ramp rate is 10A/s) and for ramp rates below 100 A/s, the magnet quench current is well above the nominal operating current of 12kA corresponding to a field gradient of 215 T/m.
It is interesting to see where the quenches occurred for different ramp rates values. All quenches at lower ramp rates took place in the coil pole regions exposed to the highest field. At higher ramp rates we have to consider the magnets separately.
For HGQ05 at higher ramp rates the quenches occurred in the splice region (where joint between outer and inner layers is made). Since the high ramp rate quenches are observed near the inter layer splices, and this is due probably to the combination of AC losses and cooling conditions in the solder-filled splice cable (20% change in current between the case at 150A/s and the one at 300A/s).
For HGQ06-HGQ08, the high ramp rate quenches originated in the midplane turns, related to the low cable inter-strand resistance and AC loss measurements confirmed the presence of this large eddy current component. The low cable inter-strand resistance is produced by the particular cycle used for models HGQ06-07, which is a 190°C, high-pressure cycle necessitated for the use of polyimide adhesive on the cable insulation and to reach the desired size of the coils. Also magnet HGQ08 showed this ramp rate dependence and this is due to the use of stabrite cable, which again lowers the inter-strand resistance and enhances the eddy current effect (there can be 50% change in current between the case at 150A/s and the one at 300A/s).
For HGQ09, the high ramp rate quenches originated in the pole turns (highest field region). In this model we used uncoated and unannealed cable and a two step cure cycle was used which enhances inter-strand resistance value. The first is 190°C/low-pressure cycle to fix the adhesive the second 135°C/high-pressure cycle to fix the coil size (see table 2.3). In this model we observe the best performance since there is not visible degradation for critical current values for all ramp rate values used (3% change in current between the case at 150A/s and the one at 300A/s).

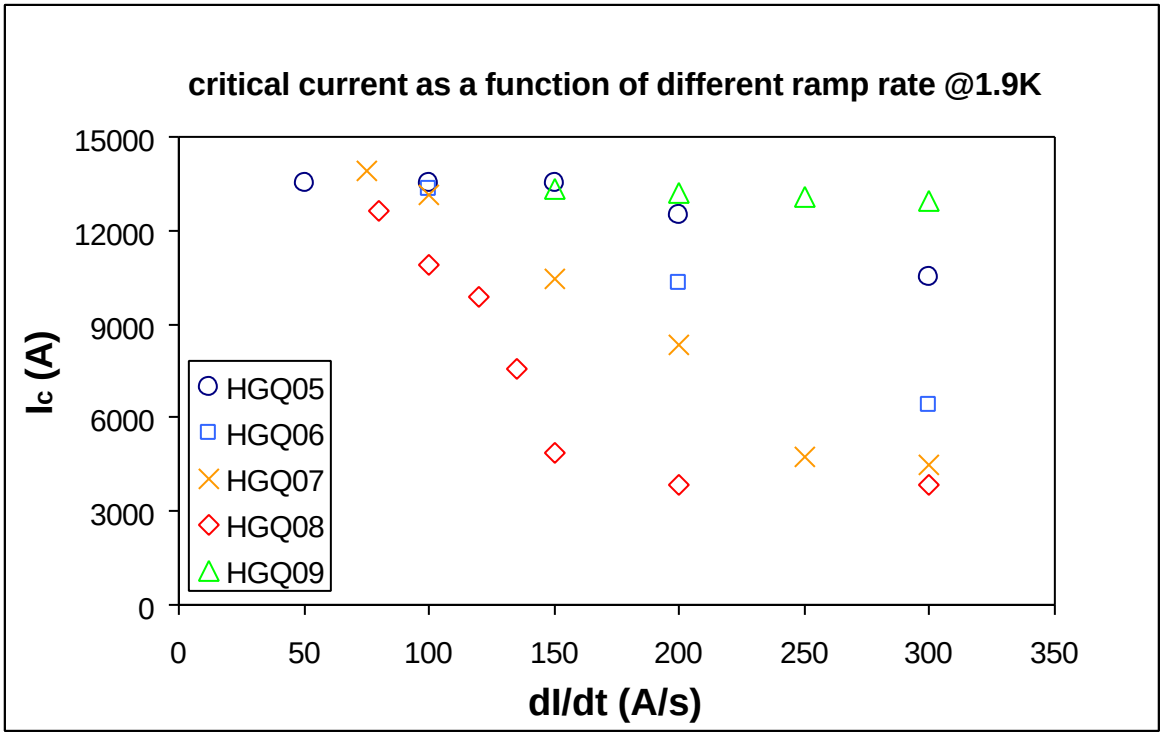

Fig. 3.7 Critical current as a function of different ramp rate at 1.9K for model magnets HGQ05-HGQ09. The different trends are due to different curing cycles for the coils of the model magnets (see table 2.3) which enhance or reduce the interstrand resistance of the cable.

Chapter 4

DATA ANALYSIS

4.1 Introduction

To analyze data taken during tests we needed several tools in order to estimate all the parameters necessary to characterize superconducting magnets in particular parameters linked to quench protection (main feature in this thesis).
First of all we needed to calculate the volumetric specific heat and resistivity for the cable used so that we could estimate parameters such as peak temperature and peak voltage to ground. These two parameters have to be limited because they can create serious problems to magnets and even destroy them. To evaluate peak temperature in particular there are three different methods described later in this chapter. They are:

1. Resistance method
2. MIITs method
3. Inductance method

All the arguments treated in this chapter will be used not only for data analysis of measurements taken in HGQ models (chapter 5) but also to predict critical parameters for the system Q2a/Q2b in the final design of the inner triplet (chapter 6).

4.1a Volumetric specific heat calculation

c_p(T) calculation (volumetric specific heat)

To estimate this quantity we had to consider two different sources (Dresner-Erold-Miller and Zong-Ping Zhao-Wilson-B.C.G.D.H.) and after comparing them we decided to take in consideration the average values for $c_p(T)$.
Following the hypothesis made to calculate $c_p(T)$ for inner and outer cables are shown.

1. Zong-Ping Zhao-Wilson-B.C.G.D.H.

Table 4.1 Parameters used for calculation of volumetric specific heat (method1).

Critical field of NbTi	B_{c0NbTi}	T	14
Critical temperature of NbTi	T_{c0NbTi}	K	9.09
Bath temperature	T_b	K	1.9
Applied field	B	T	1
γ_{Cu}	γ_{Cu}	J/K^2kg	0.011
β_{Cu}	β_{Cu}	J/K^4kg	0.000744
Density of copper	δ_{Cu}	Kg/m^3	8960
Residual resistance ratio	RRR		100
Specific heat of Cu at 300K	$c_{pCu300K}$	J/Km^3	$3.454 \cdot 10^6$
γ_{NbTiSC}	γ_{NbTiSC}	J/K^2kg	0.1338843
γ_{NbTiNC}	γ_{NbTiNC}	J/K^2kg	0.192
β_{NbTiSC}	β_{NbTi}	J/K^4kg	0.00705785
β_{NbTiNC}	β_{NbTiNC}	J/K^4kg	0.00274
Density of NbTi	δ_{NbTi}	Kg/m^3	6050
Inner cable			
Number of strands			38
Diameter of strand	d	m	0.000808
copper/superconductor ratio	λ		1.3
Outer cable			
Number of strands			46
Diameter of strand	d	m	0.000648
copper/superconductor ratio	λ		1.8

We have to consider that:

$$
\begin{aligned}
T_{cNbTi} &= T_{c0NbTi}\left(1-\frac{B}{B_{c0NbTi}}\right)^{0.59} \\
A_{tot} &= (d^2)\frac{p}{4}N \\
A_{Cu} &= \frac{1}{1+l}\cdot A_{tot} \\
a &= \frac{1}{1+l}
\end{aligned}
\qquad (4.1)
$$

In particular for copper:

$$c_{oCulow}(T) = (g_{Cu}\cdot d_{Cu}T + b_{Cu}\cdot d_{Cu}\cdot T^3)$$

$$c_{pCu}(T) = \frac{1}{\left[\left(\frac{1}{c_{pCu300K}}\right)+\left(\frac{1}{c_{pCulow}(T)}\right)\right]} \qquad (4.2)$$

While for NbTi:

$$c_{pNbTiSC}(T,B) = g_{NbTiSC} \cdot d_{NbTi} \cdot \frac{B}{10.5T} \cdot T + b_{NbTiSC} \cdot d_{NbTi} \cdot T^3$$
$$c_{pNbTiNC}(T) = l\,\mathrm{int}\, erp(\Theta, C_p, T) \tag{4.3}$$

Where the linear interpolation is done on these experimental values in table 4.2:

Table 4.2 Data of specific heat of NbTi for linear interpolation.

Θ(K)	C_p(J/K·kg) specific heat	$c_p=C_P\cdot\delta_{NbTi}$ volumetric specific heat
10	4.68	28314
12	7.18	43439
14	10.4	62920
16	14.1	85305
18	18.4	111320
20	23.2	140360
25	37.9	229295
30	61.6	372680
35	89.9	543895
40	121	732050
50	167	1010350
60	208	1258400
70	242	1464100
80	270	1633500
90	297	1796850
100	320	1936000
125	362	2190100
150	390	2359500
175	407	2462350
200	416	2516800
250	429	2595450
300	437	2643850
310	439	2655950

Finally the volumetric specific heat for NbTi is calculated with different values in different temperature range:

$$c_{pNbTilow}(T,B,T_{cNbTi}) = \begin{cases} c_{pNbTiSC}(T,B) & if\ (T \le (T_{cNbTi} - dT) \\ c_{pNbTiNc}(T,B,T_{cNbTi}) & if\ (T > (T_{cNbTi} + dT) \end{cases} \tag{4.4a}$$

and the total volumetric specific heat for NbTi as a function of T, B, T_c is:

$$c_{pNbTi}(T,B,T_{cNbTi}) = \frac{1}{\left(\frac{1}{c_{pNbTi300K}}\right)+\left(\frac{1}{c_{pNbTilow}(T,B,T_{cNbTi})}\right)} \qquad (4.4b)$$

2. Dresner-Erold-Miller

Table 4.3 Parameters used for calculation of volumetric specific heat (method 2).

Critical field of NbTi	B_{c0NbTi}	T	14
Critical temperature of NbTi	T_{c0NbTi}	K	9.09
Bath temperature	T_b	K	1.9
Applied field	B	T	1
γ_{Cu}	γ_{Cu}	J/K^2kg	0.011
β_{Cu}	β_{Cu}	J/K^4kg	0.000744
Density of copper	δ_{Cu}	Kg/m^3	8960
Residual resistance ratio	RRR		100
Specific heat of Cu at 300K	$c_{pCu300K}$	J/Km^3	$3.454 \cdot 10^6$
γ_{NbTi}	γ_{NbTi}	J/K^2kg	0.145
β_{NbTi}	β_{NbTi}	J/K^4kg	0.0023
Density of NbTi	δ_{NbTi}	Kg/m^3	6000

The other quantities are the same as 1.
For copper we have the same law, as before and there is no difference between the two methods.

While for NbTi we have:

$$c_{pNbTiSc}(T,B) = g_{NbTiSC} \cdot d_{NbTi} \cdot \frac{B}{Bc_{0NbTi}} \cdot T + \left(b_{NbTiSC} + 3 \cdot \frac{g_{NbTi}}{T_{c0\,NbTi}^{\,2}} \right) d_{NbTi} T^3 \qquad (4.5)$$

$$c_{pNbTiNc}(T,B) = g_{NbTiSC} \cdot d_{NbTi} \cdot T + b_{NbTiSC} \cdot d_{NbTi} T^3$$

Between superconducting and normal state we have:

$$c_{pNbTilow}(T,B,T_{cNbTi}) = \begin{cases} c_{pNbTiSC}(T,B) & if\ (T \le (T_{cNbTi} - dT) \\ c_{pNbTiNc}(T,B,T_{cNbTi}) & if\ (T > (T_{cNbTi} + dT) \end{cases} \qquad (4.6a)$$

The volumetric specific heat of NbTi (using the right expressions 4.6 depending on temperatures) is:

$$c_{pNbTi}(T,B,T_{cNbTi}) = \frac{1}{\left(\frac{1}{c_{pNbTi300K}}\right)+\left(\frac{1}{c_{pNbTilow}(T,B,T_{cNbTi})}\right)} \qquad (4.6b)$$

So for **both** the methods the composite will have a volumetric heat capacity given by:

$$c_{pcomp}(T) = a \cdot c_{pNbTi}(T,B) + (1-a) \cdot c_{pCu}(T) \qquad (4.7)$$

Results for these calculation for inner and outer coils used for inner triplet quadrupoles are show in figures 4.1 and 4.2:

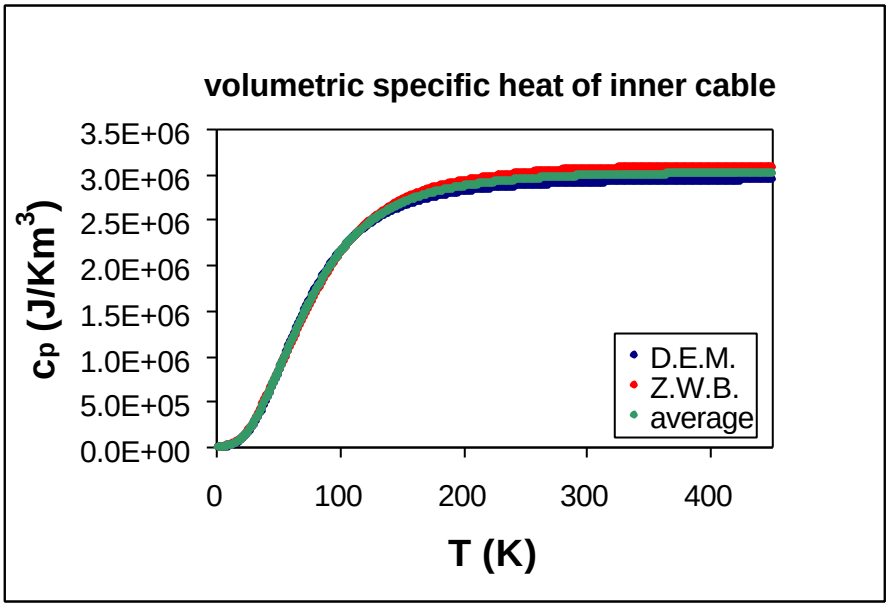

Fig. 4.1 Volumetric specific heat for **inner** cable of superconducting quadrupole for the two methods and their average.

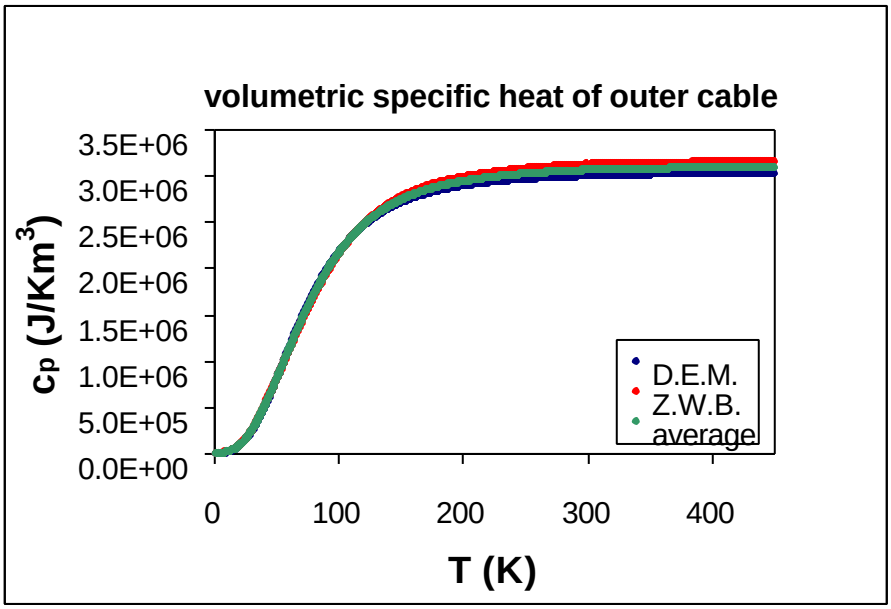

Fig. 4.2 Volumetric specific heat for **outer** cable of superconducting quadrupole for the two methods and their average.

As we can see the difference between the two methods is not crucial (less than 4% of difference) and we verified that the results of simulations in chapter 6 are not affected by the choice of this parameter.

4.1b Resistivity of copper (ρ_{Cu}(T) calculation)

For ρ_{Cu}(T) calculation several parameters have to be considered.
First of all we have to consider that resistivity of copper is not only a function of temperature but it depends also on the magnetic field (magneto resistance contribute) and on residual resistivity ratio (RRR). The RRR value, which depends on kind of copper used and thermal curing applied to coils, is defined as R_{Cu300K}/R_{10K}.[1)]
The contribute from magnetic field is easily calculated because it is simply the product between a constant value and the field applied (Kohler rule) i.e.

$$r_{magnetores} = B \cdot c \qquad \text{where} \quad \chi = 4.5 \cdot 10^{-11}\,\Omega\text{m/T} \qquad (4.8)$$

To find the total resistivity of copper we considered a series of curves, which depend on RRR values and we found the scale factors to consider for different range of temperature. In particular beyond ~70K resistivity is not longer dependent on the field and on RRR value so that for every value of RRR we have the same value for resistivity and in particular ρ_{Cu}(300K) is a constant value of $1.7 \cdot 10^{-8}\Omega$m.
Knowing the RRR value we can find the starting value for ρ_{Cu}(T,RRR) and summing $\rho_{magnetores}$(B) we obtain the total value of resistivity for the copper ([1; 6.3, 6.4]).

$$r_{total}(T, RRR, B) = r_{magnetores}(B) + r_{Cu}(RRR, T) \qquad (4.9)$$

In particular the data used for the analysis are listed in table 4.4 and figure 4.3a shows resistivity as a function of temperature for different RRR values while 4.3b shows resistivity for a fixed RRR but different field.

Table 4.4 Input table for calculation of resistivity as a function of temperature.

	ρ_{Cu}(300K)	$1.7 \cdot 10^{-8}$				
RRR	85	100	120	150	175	200
T(K)	ρ_{Cu}(Ωm)	ρ_{Cu}(Ωm)	ρ_{Cu}(Ωm)	ρ_{Cu}(Ωm)	ρ_{Cu}(Ωm)	ρ_{Cu}(Ωm)
1	2.00E-10	1.70E-10	1.417E-10	1.13E-10	9.71E-11	8.50E-11
10	2.00E-10	1.70E-10	1.417E-10	1.13E-10	9.71E-11	8.50E-11
25	2.10E-10	1.85E-10	1.50E-10	1.30E-10	1.00E-10	9.50E-11
30	2.50E-10	2.00E-10	1.88E-10	1.70E-10	1.55E-10	1.40E-10
40	3.80E-10	3.25E-10	3.10E-10	2.80E-10	2.80E-10	2.80E-10
60	1.00E-09	1.00E-09	1.00E-09	1.00E-09	1.00E-09	1.00E-09
70	1.70E-09	1.70E-09	1.70E-09	1.70E-09	1.70E-09	1.70E-09
80	2.30E-09	2.30E-09	2.30E-09	2.30E-09	2.30E-09	2.30E-09
90	3.00E-09	3.00E-09	3.00E-09	3.00E-09	3.00E-09	3.00E-09
100	3.70E-09	3.70E-09	3.70E-09	3.70E-09	3.70E-09	3.70E-09
150	7.00E-09	7.00E-09	7.00E-09	7.00E-09	7.00E-09	7.00E-09
200	1.00E-08	1.00E-08	1.00E-08	1.00E-08	1.00E-08	1.00E-08
300	1.70E-08	1.70E-08	1.70E-08	1.70E-08	1.70E-08	1.70E-08

[1)] Note that this definition, although more practical is different from the reference one RRR=$\rho_{273.15K}/\rho_{4.2K}$

400	2.30E-08	2.30E-08	2.30E-08	2.30E-08	2.30E-08	2.30E-08
500	3.00E-08	3.00E-08	3.00E-08	3.00E-08	3.00E-08	3.00E-08
600	3.90E-08	3.90E-08	3.90E-08	3.90E-08	3.90E-08	3.90E-08

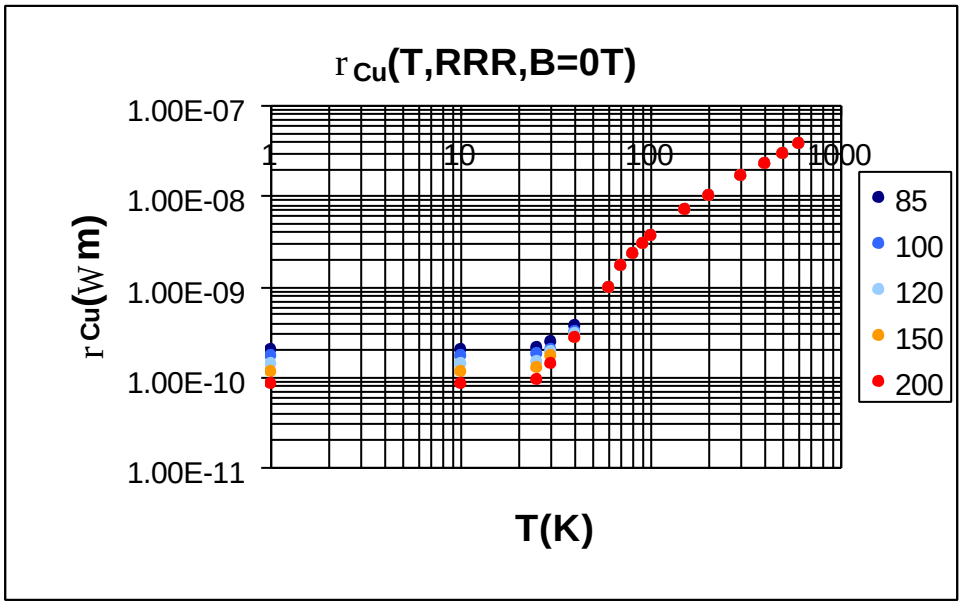

Fig. 4.3a Resistivity of copper as a function of temperature for different RRR and B=0T.

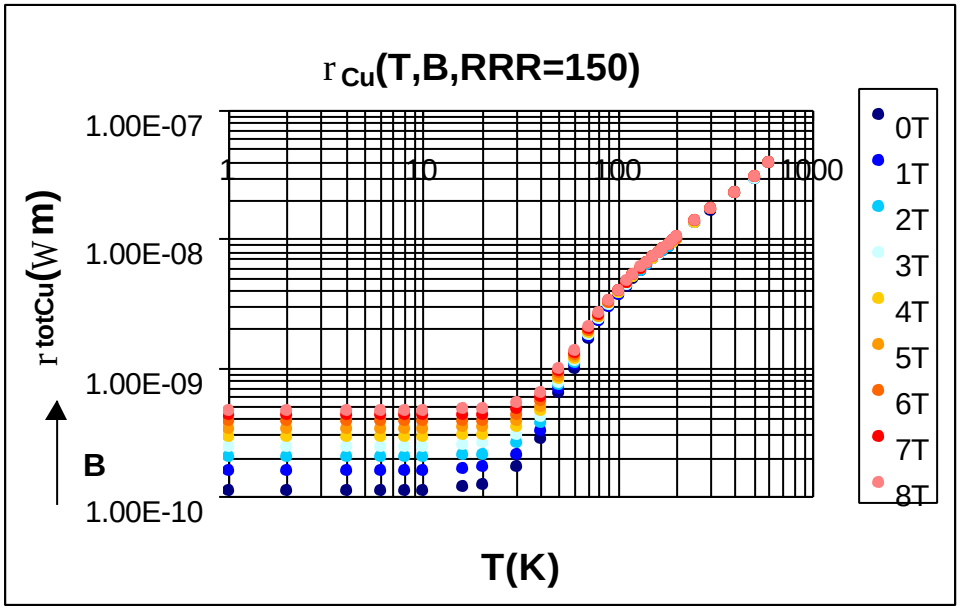

Fig. 4.3b Resistivity as a function of temperature for different field and fixed RRR.

From figure 4.3a we can observe that the difference in RRR can be important between 0K and 70K while later on there is not visible difference in resistivity due to RRR values.
From figure 4.3b we can conclude that also the magnetoresitance contribution is important between 0K and 70K. Moreover we can observe that this contribute is important if the field is sufficient high and it can double the value of resistivity reducing the difference due to RRR values. We can conclude

that at high field values the difference in RRR is not so evident because the magnetoresistance contribution is of the same order of magnitude of resistivity due to the residual resistivity ratio.

4.1c Parameters used in analysis

Several constants were introduced in data analysis and we would like to summarize them to have a better view of all the parameters used.

Table 4.5 Constant values used in analysis.

Temperature of the bath	T [K]	1.9
Resistivity of copper at 300K	ρ_{Cu} [Ωm]	$1.7 \cdot 10^{-8}$
Resistance per length inner cable	R/l_{300K} [mΩ/m]	1.6
Resistance per length outer cable	R/l_{300K} [mΩ/m]	1.8
Diameter inner cable	d_{inn} [mm]	0.808
Diameter outer cable	d_{out} [mm]	0.648
Cu:Sc inner cable	λ	1.3
Cu:Sc outer cable	λ	1.8
Copper area inner cable	A_{Cu} [mm^2]	10.63
Copper area outer cable	A_{Cu} [mm^2]	9.44
NbTi area inner cable	A_{NbTi} [mm^2]	8.17
NbTi area outer cable	A_{NbTi} [mm^2]	5.25
Number of strands inner cable	N	38
Number of strands outer cable	N	46
Magneto resistance coefficient	χ [Ωm/T]	$4.5 \cdot 10^{-11}$

The area of the cable i.e. the metal cross section can be calculated as:

$$A_{tot} = Np\left(\frac{d_{strand}}{2}\right)^2 \tag{4.10}$$

from this value we can estimate A_{Cu} and A_{NbTi} as:

$$\begin{aligned} A_{Cu} &= \frac{l}{l+1} A_{tot} \\ A_{NbTi} &= \frac{A_{tot}}{l+1} \end{aligned} \tag{4.11}$$

or we can estimate the same quantities from R/l_{300K} value (we used this in order to consider also the packing factor because strands are not perfectly circular) in fact:

$$R_{300K} = R_{Cu\,300K} = \frac{r_{Cu\,300K} \cdot l}{A_{Cu}} \tag{4.12}$$

so we get the value of A_{Cu} and then we can estimate A_{Nbti} dividing by l with 1-5% accurancy.

4.2 Resistance method

The first method used to estimate peak temperatures is very simple and it is based on the assumption that in superconducting state the only contribution to resistivity is from copper and in normal state (usually temperatures reached are of the same order of room temperature) the copper is again the main contribute because the current goes only in the copper part of the cable. So we have:

$$\frac{R_{cold}}{r_{cold}} = \frac{R_{coldCu}}{r_{coldCu}} = \frac{R_{300K}}{r_{300K}} = \frac{R_{Cu\,300K}}{r_{Cu\,300K}} \qquad (4.13)$$

In particular we can record directly the resistance of a particular segment at low temperatures (the spot heater is a little stainless steel segment which can induce a quench in the part of cable, of known length, under it) and we can measure its room temperature value. So we can estimate ρ_{cold} :

$$r_{coldCu} = \frac{R_{coldCu} \cdot r_{Cu\,300K}}{R_{Cu\,300K}} \qquad (4.14)$$

Then we know how r of copper varies with temperature so we can find temperature. This method works because we have a lot of voltage taps in model magnets and we can read easily the voltage across the segment where the quench occurs which is effectively only resistive since inductive voltage of this segment is negligible.

4.3 MIITs method

This method is an adiabatic one and it does not take in account the beneficial contribution of helium. As one could expect this method overestimates the temperature values but it permits to have the order of magnitude these quantities.
MIITs are defined also as the quench integral and it is calculated as:

$$MIITs = 10^{-6} \cdot \int_{t_0}^{t} I^2(t)dt \qquad (4.15)$$

Where *I(t)* is magnet and t_0 is the time when we first see resistive voltage growth.
We show that this quantity can be related to the heat released in the coil, which can be calculated knowing the heat capacity of the coil. In fact we can write ([1]):

$$Q = \int_{T_0}^{T} mC_p(T)dT = \int_{T_0}^{T} d \cdot VC_p(T)dT = \int_{T_0}^{T} Vc_p(T)dT \qquad (4.16)$$

Where $C_p(T)$ is the specific heat, T_0 the temperature of the bath (1.9K), m the mass of the cable, d and V the density and volume of the cable, $c_p(T)$ the volumetric specific heat. If we divide everything by the resistance of the cable R we get:

$$\frac{Q}{R(T)} = \int_{T_0}^{T} \frac{V}{R(T)} c_p(T)dT \qquad (4.17)$$

But $V=A_{tot}l$ and R is mainly due to the copper part of the cable so that $R=r_{Cu}l/A_{Cu}$ in fact once the quench starts the current goes in the copper part because $R_{NbTi}>>R_{Cu}$ so that copper is the only contribute to resistance.

Another thing to notice is that in our calculation we did not consider the contribution from helium bath (this method is adiabatic) and we did not include the contribution from insulation of the cable. This last contribution can be disregarded because the amount of insulation is very small (the cables are coated and not impregnated) and the resistivity of kapton and epoxy is much higher than copper resistivity.
So we can write:

$$\frac{Q}{R(T)}=\int_{T_0}^{T}\frac{A_{tot}lA_{Cu}}{r_{Cu}(T)l}c_p(T)dT=\int_{T_0}^{T}\frac{A_{tot}A_{Cu}}{r_{Cu}(T)}c_p(T)dT=\int_{t_0}^{t}\frac{I^2(t)R(T)}{R(T)}dt \tag{4.18}$$

$$\int_{t_0}^{t}\frac{I^2(t)R(T)}{R(T)}dt=\int_{t_0}^{t}I^2(t)dt=10^6\,MIITs$$

So measuring MIITs and knowing c_p and r_{Cu} as a function of temperature we can relate MIITs value to the heat developed in the coil (using regression sum of intervals) and so to temperature.
The main results and calculation made are discussed later in chapter 6 in particular several steps were made to arrive at the final possibility to estimate some parameters for the final design of the inner triplet and in particular the system Q2a/Q2b.
We started by analyzing data of models and figure out the differences in estimation of peak temperature between the actual measurements and MIITs results (which make several strong assumptions besides the adiabatic one). After this we tried to simulate the system Q2a/Q2b and in particular try to estimate the total peak voltage to ground developed in several events.
Here we would like just to show in figures 4.4a and 4.4b the dependence of MIITs with temperature, RRR value and field for a typical magnet:

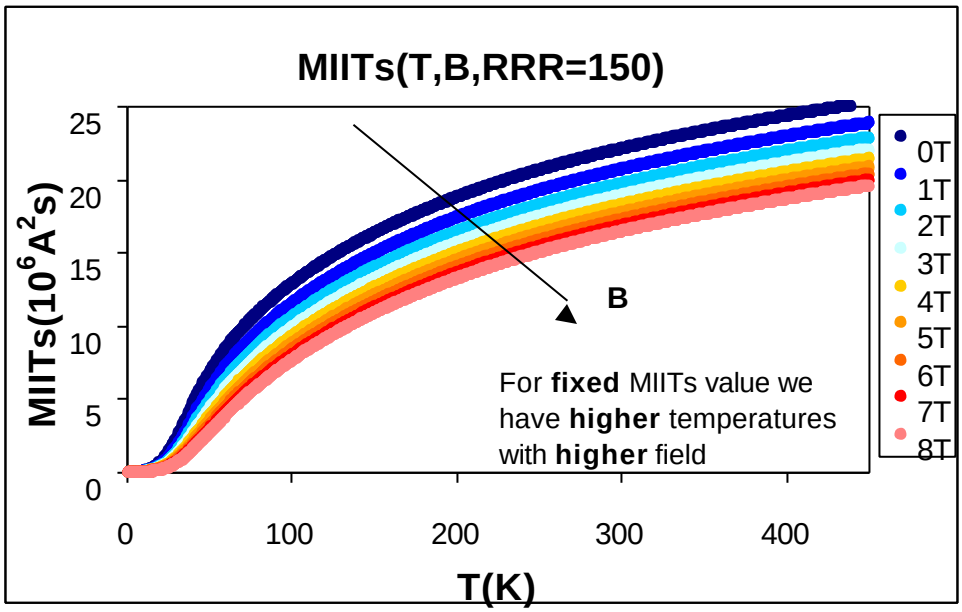

Fig. 4.4a MIITs curves as a function of temperature and field for fixed RRR=150.

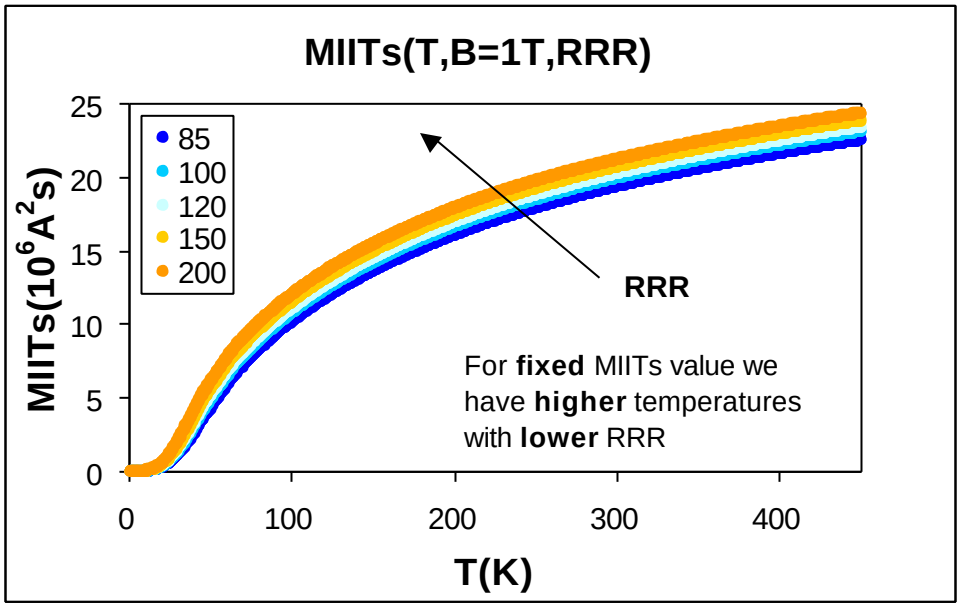

Fig. 4.4b MIITs curves as a function of temperature and RRR for fixed B=1T.

These curves are calculated with the specifics of a superconducting quadrupoles Q2a and Q2b of the inner triplet.

Before describing the third method used we would like to demonstrate that the assumption made in the model regarding the insulation is not so crucial. In particular to demonstrate this we can use the quantity *U(T)* (easily related to MIITs definition), coming from energy conservation (in adiabatic case) ([1]):

$$r(T)J^2(t)dt = d \cdot C_p(T)dT$$

$$U(T) = \int_0^{\infty} J^2(t)dt = \int_{T_i}^{T_f} \frac{d \cdot C_p(T)}{r(T)} dT \qquad (4.19)$$

where d is the density, $C_p(T)$ is the specific heat and $r(T)$ the resistivity. The three materials are in parallel so that we can write:

$$\frac{1}{r(T)} = \frac{1}{r_{Cu}} + \frac{1}{r_{kapton}} + \frac{1}{r_{epoxy}} \approx \frac{1}{r_{Cu}} \qquad (4.20)$$

in fact r_{Cu} is on the order of $(10^{-8}\text{-}10^{-7})\Omega$m while for kapton and epoxy we have order of magnitude of $10^{14}\Omega$m so that is reasonable to disregard them.
The quantity $d\chi C_p(T)$ can be write as the sum of the three contribution weighted by the amount of them in the cable so we have:

$$dC(T) = d_{Cu} f_1 C_{p,cable}(T) + d_{kapton} f_2 C_{p,kapton}(T) + d_{epoxy} f_3 C_{p,epoxy}(T) \qquad (4.21)$$

where

$$f_1 = \frac{1}{1+\frac{A_{kapton}}{A_{cable}}+\frac{A_{epoxy}}{A_{cable}}};\ f_2 = \frac{1}{1+\frac{A_{Cu}}{A_{kapton}}+\frac{A_{epoxy}}{A_{kapton}}};\ f_3 = \frac{1}{1+\frac{A_{Cu}}{A_{epoxy}}+\frac{A_{kapton}}{A_{epoxy}}} \qquad (4.22)$$

but the area of epoxy is so small that the ratio containing the area of epoxy at the numerator can be disregarded. Finally we can write:

$$U(T) = \int_{T_i}^{T_2} \frac{f_1 c_{p,cable}(T) + f_2 c_{p,kapton}(T)}{r_{Cu}} dT \qquad (4.23)$$

where c_p is now the volumetric specific heat (product between density and specific heat). Using the specifics from table 4.6 (for kapton we have sheet 15mm wide and 25µm thick) and supposing to divide the integral in sum of interval where the volumetric specific heat and resistivity are constant we obtain the plots below (Fig.5.a and 5.b), which show that the contribute to U(T) from kapton is seven order of magnitude less than the one from the cable itself. We can conclude then that this contribution does not affect the results of peak temperature and peak voltage.

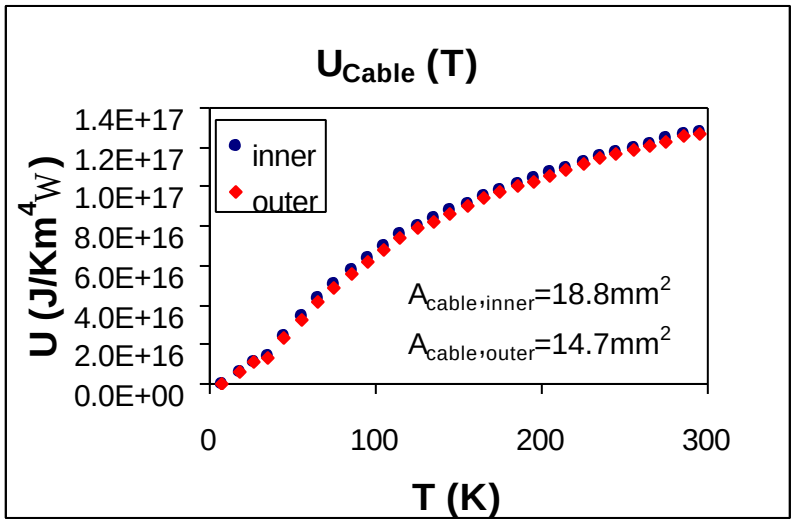

(a)

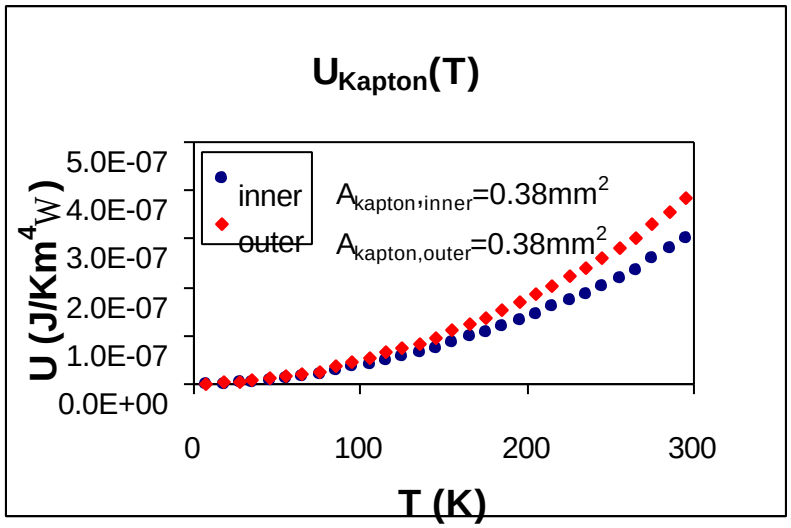

(b)

Fig. 4.5a, 4.5b Comparison of contribution to U(T) from cable and from kapton insulation. The contribute to U(T) from kapton is seven order of magnitude less than the one from the cable itself.

4.4 Inductance method

This last method was first used to do data analysis because it was already used at CERN for superconducting dipoles. Unluckily the signals recorded in our case were noisy and not very stable so that the analysis was much harder than expected. We made a lot of assumption and we achieved some results that were comparable with the two methods above. Finally we decide to use only the two first methods because they were easier to handle and more appropriate for our short models.
Anyway we would like to mention how this method works and which results we obtained for the cases we treated.

This method allows the evaluation of the dynamics of temperature development in different parts of superconducting coil and the localization of critical points in the magnet design at various powering conditions and assessment of the magnet protection system.
The basic idea and equations are now discussed ([5]; [6]).
For a non linear purely inductive circuit the differential inductance *L(I)* can be defined as the ratio of the infinitesimal changes of current *I* and flux F through the winding. In this case the energy equation which couples the infinitesimal changes of stored energy *E* and the square of current remains similar to that for a linear circuit i.e.

$$L(I) = \frac{d\Phi}{dI} \qquad (4.24)$$

So that

$$dE = \frac{L(I)}{2} d(I^2) \qquad (4.25)$$

For the integral equations this similarity disappears but we can define two different functions $L_F(I)$ such that $F = L_F(I) \cdot I$ and $L_E(I)$ such that $E = 1/2 \cdot L_E(I) I^2$ but these two functions are different in general:

$$L_\Phi(I) = \frac{1}{I}\int_0^I L(I')dI' \qquad (4.26)$$

$$L_E = \frac{2}{I^2}\int_0^I L(I')I'dI' \qquad (4.27)$$

The magnet equivalent circuit during a quench can be drawn as a serial connection of a non-linear inductance *L(I)* and a time dependent resistance *R(t)*. In general *R(t)* changes in a different way from quench to quench.

The energy equation which links the current *I* through the whole magnet, the voltage *V* on the whole magnet and Joule heat released in the magnet during a quench can be written as (4.28):

$$Q(t) = \int_{t_0}^{t} (V(t') - V_{inductive}) I(t')dt' = \int_{t_0}^{t} (V(t') - L(I)\frac{dI}{dt}) I(t')dt' = \int_{t_0}^{t} V(t')I(t')dt' + \frac{1}{2}(L_E[I(t_0)]I^2(t_0) - L_E[I(t)]I^2(t))$$

Where t_0 is chosen before the quench in the superconducting state (so in $t=t_0$ the resistive heat is equal to zero because we do not have resistance in superconducting state).

Now if we consider the case when V is not the total voltage on the magnet, but the voltage measured between two of the all voltage taps of the magnet coil (V_n) the inductive voltage across a single turn is proportional to the time derivative of the magnetic flux through that turn.

If we assume that during a quench the ratio of the flux through the turn to the whole flux through the whole magnet remain constant (in general it can change with the iron yoke saturation) the ratio of inductive voltage $V_{inductive}$ at any turn to the whole inductive voltage on the magnet remain constant although the magnet inductance may be not constant i.e. we suppose

$$\frac{\Phi_n}{\Phi_{whole}} = const \qquad (4.29)$$

so

$$\frac{d\Phi_n/dt}{d\Phi_{whole}/dt} = const \qquad (4.30)$$

then

$$\frac{V_{ind.n}}{V_{ind.whole}} = const \qquad (4.31)$$

At this condition the equation which is similar to the previous one for Joule heat released is applicable for a single turn or a single segment of the magnet coil:

$$Q_n(t) = \int_{t_0}^{t} V_n(t')I(t')dt' + \frac{L_n}{L_E(0)}\frac{1}{2}(L_E[I(t_0)]I(t_0)^2 - L_E[I(t)]I(t)^2) \qquad (4.32)$$

Where

$$L_n = \frac{V_{inductive}^{segment}}{V_{inductive}^{whole}} L_E(0) = \frac{\Phi_{segment}}{\Phi_{whole}} L_E(0) \qquad (4.33)$$

So with the constancy of the flux distribution in the coil region this equation can be used for any part of the winding, which can consist of non-integer number of turns.
We should notice that the way in which the inductive voltage changes during the current decay is an important condition to apply the method. We noticed that the inductance of the whole coil changes with current and even if this change is small probably one has to take care of it.
In the coil region there is not essential distortion of the magnetic flux due to the iron yoke saturation.
The experimental way to do this analysis was to take data from magnet HGQ09 and estimate the inductance of every single segments by using data that we suppose purely inductive such as strip heater induced quenches at different current and evaluating the ratio between the voltage of the segment with the voltage of the inner layer *Q1I*, which is one eight of the whole magnet (we found the voltage signal of this layer more believable than the whole coil signal which seems to be deeply affected by every single little change in the system) i.e.:

$$L_n = \left(\frac{V_n}{V_{Q1I}} \right) \cdot L_{Q1I} \qquad (4.34)$$

Where L_{Q1I} is found by the ratio of the voltage of the whole coil and the signal of the change of current with time (dI/dt) which has to be scaled properly because the signal has some offset. Another problem, as told above, is that the inductance of the whole coil changes with the current and this is due to saturation of iron yoke so we have also to see if this problem is real or if the error for this can be ignored. To study this problem we considered these events at different current and we estimated a transfer function for inductance and we calculated also the two different integral inductances $L_F(I)$ and $L_E(I)$ in order to estimate the inductive part in the equation (4.23) before taking in account changes with current.

In practice the calculation of the ratio of inductances was not so easy because it turned out that the signal were not so clear to understand (because we have rather small signals) and it was quite difficult to choose where to consider this ratio even if we tried to suppose to have an error on this ratio of 15% and we found small changes in the results (peak temperature values) so it does not seem to be a big uncertainty not to know with deep accuracy this value.

When the partial inductance of the turn is known, the Joule heat, which is released in the turn, can be calculated because the voltage across two voltage taps is recorded during measurements. Then if the masses of the copper and the superconductor, and the dependencies of the specific heat versus temperature are known, the temperature of the coil segment can be calculated.

In particular for LHC quadrupoles the Cu:Sc ratio is 1.3:1 for inner strands and 1.8:1 for outer strands. The inner layer cable consists of 38 0.808mm strands and has a cross section with a minor edge of 1.326 mm, a major edge of 1.587 mm and a width of 15.4mm. The outer layer cable consists of 46 0.648mm strands and has a 1.054 mm minor edge, a 1.238 mm major edge and the same width of 15.4 mm. With these data we can calculate ΔT and then evaluate the temperature reached from the magnet during the quench.

We can express Q(t) as

$$Q(t) = m \int_{T_0}^{T} C_{pCuNbTi}(T)dT \cong \sum_i m \Delta C_{pCuNbTi,i} \Delta T_i \qquad (4.35)$$

We know the curve of C_p (specifc heat) as a function of T so we can divide the interval T-T_0 in many intervals of length DT_i and find the correspondent $Q(t)_i$. When we make the measurements we calculate $Q(t)_i$ from the difference between the integrated voltage of a segment and its inductive part and once known $Q(t)_i$ we can estimate DT_i and find the final T.

The advantage of this method is that one does not need to calculate the resistance of the turn while needs to know the variation of specific heat with temperature that is also quite complicate because we have a composite and range temperature in which the specific heat changes a lot. We have also to estimate the mass of the segment of which we want the temperature and so we need to know its length, area and density of the cable.

The peak temperature obtained by this method is by definition lower than the hot spot temperature extracted from the commonly used MIITs method because temperatures are averaged along the cable length bounded by two voltage taps.

For the analysis we start to calculate the different values as a function of current for the quantities $L(I)$, $L_F(I)$ and $L_E(I)$.

We suppose than the total inductance of Q1I (the coil used to calculate the ratio V_n/V) falls with current as the transfer function so we suppose that between 4000A and 12000A the change in inductance is 2% and below 4000A it is constant as L_{low} at 0A (0.586mH). We can express this quantity as:

$$L(I^{'}) = L_{low}\left(1-\frac{(I^{'}-4000)}{12000-4000}\cdot\frac{2}{100}\right) = L_{low}\left(1-\frac{(I^{'}-4000)}{8000}\cdot 0.02\right) \qquad (4.36)$$

From this we can easily find $L_F(I)$ and $L_E(I)$ in fact we have:

$$L_{\Phi}(I) = \frac{1}{I}\int_0^I L(I^{'})dI^{'} = \frac{4000}{I}L_{low} + \frac{L_{low}}{I}\left[(I-4000)\cdot 1.1 - \frac{0.02}{8000}\frac{1}{2}\left(I^2-4000^2\right)\right] \qquad (4.37)$$

$$L_E(I) = \left(\frac{4000}{I}\right)^2 L_{low} + \frac{2L_{low}}{I^2}\left(\frac{I^2-4000^2}{2}\cdot 1.1 - \frac{0.02}{8000}\frac{I^3-4000^3}{3}\right) \qquad (4.38)$$

By plotting the three equations 4.31-4.33 we get:

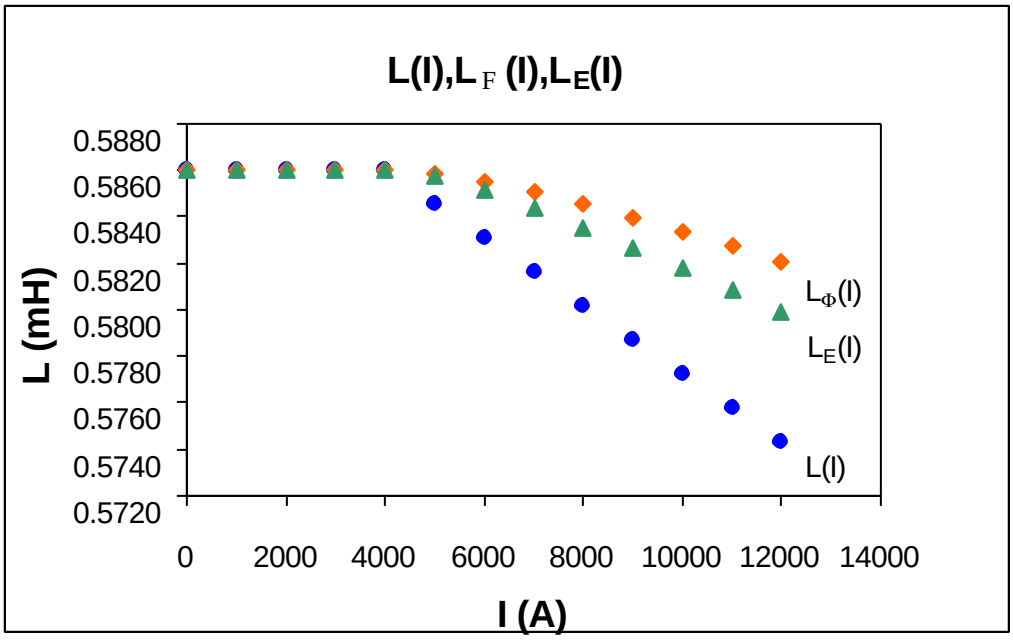

Fig. 4.6 Inductance as a function of current.

First of all using equation (4.32) we tried to calculate temperatures at different currents and in particular we used segments with pretty stable ratio V_n/V_{Q1I} (16^{th} turn of an outer coils and 12^{th} turn of inner coils a-c b-d segments see Fig. 2.11). Then we compare this method with the other two methods and as expected MIITs method is the one which predict the bigger temperatures. In fact in inductance method temperatures are averaged along the cable length bounded by two voltage taps.
We used manual trip events from magnet HGQ09, which was the magnet more suitable to estimate V_n/V_{Q1I} values because it had very little eddy current effect (low interstrand resistance). Here the results we obtained for strip heater events at different currents.

1. 10150A

Table 4.6a Peak temperatures for different methods for event at 10150A.

segment	T(K)$_{\text{inductance method}}$	T(K) $_{\text{MIITs method}}$	T(K) $_{\text{resistance method}}$
16a-16c Q1	73	93	74
16a-16c Q3	71	86	72
16b-16d Q2	74	92	74
16b-16d Q4	80	114	82
16a-16c Q2	64	86	54
16a-16c Q4	73	101	74
16b-16d Q1	71	107	72
16b-16d Q3	74	106	76
12a-12c Q1	37	33	43
12a-12c Q3	39	31	46
12b-12d Q2	40	36	45
12b-12d Q4	41	38	45
12a-12c Q2	32	33	41
12a-12c Q4	31	32	40
12b-12d Q1	33	38	41
12b-12d Q3	30	37	39

2. 12000A

Table 4.6b Peak temperatures for different methods for event at 12000A.

segment	T(K)$_{\text{inductance method}}$	T(K) $_{\text{MIITs method}}$	T(K) $_{\text{resistance method}}$
16a-16c Q1	87	108	90
16a-16c Q3	87	108	90
16b-16d Q2	87	108	90
16b-16d Q4	98	127	97
16a-16c Q2	79	101	81
16a-16c Q4	87	120	90
16b-16d Q1	84	111	86
16b-16d Q3	89	119	91
12a-12c Q1	51	51	53
12a-12c Q3	55	50	56
12b-12d Q2	52	51	54
12b-12d Q4	54	53	55
12a-12c Q2	49	50	52
12a-12c Q4	49	50	51
12b-12d Q1	50	52	52
12b-12d Q3	48	52	51

Plotting the results for these two cases in figure 4.7(a-b) we have:

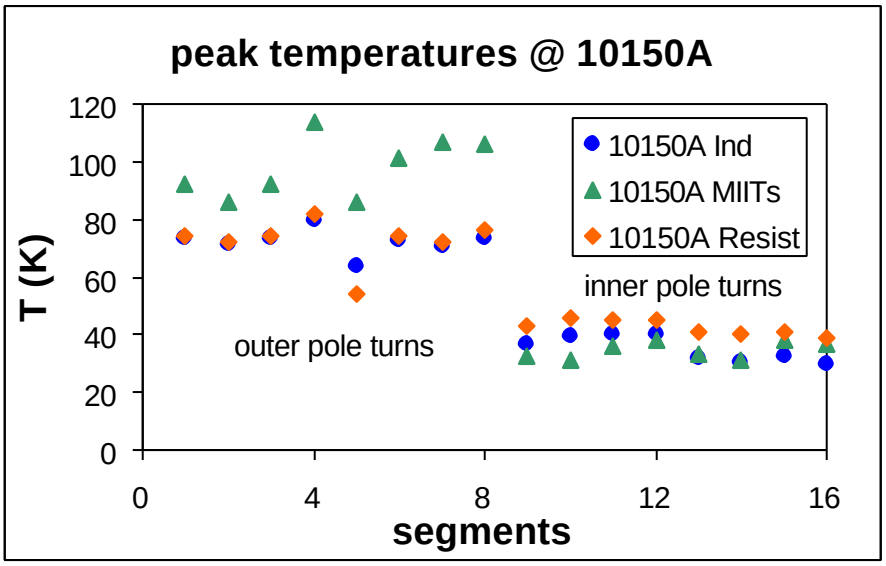

Fig 4.7a Different methods to estimate peak temperatures @10150A.

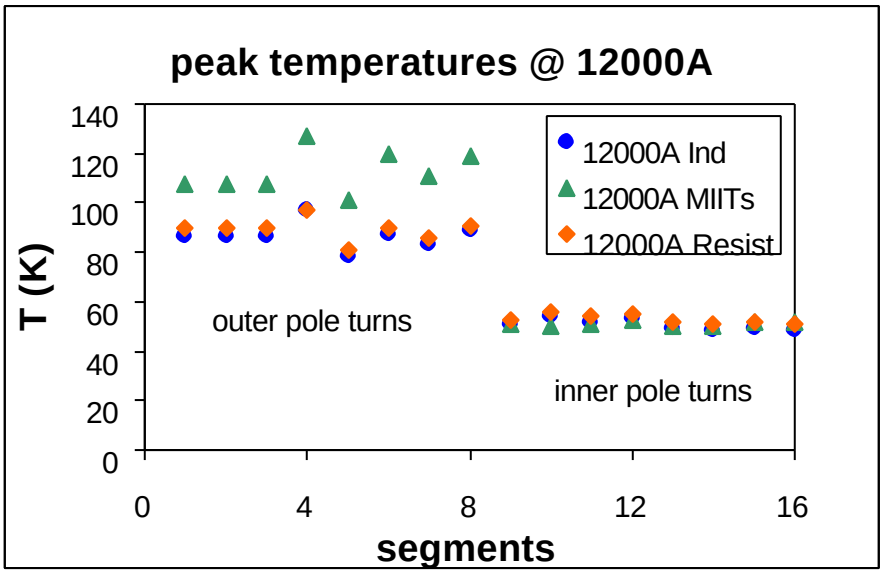

Fig 4.7b Different methods to estimate peak temperatures @12000A.

As one can observe MIITs method overestimates the temperatures at least for the outer pole turns and probably this is due to the fact that the outer coils have more area of contact with everything outside the magnet, so that the adiabatic assumption is very pessimistic. Besides inner coils do not reach very high temperature and cooling channels are more effective.
We had very much uncertainty L_n values mainly due to the fact that the assumption of V_n/V_{Q1I} =constant was not perfectly verified and what it appeared from our data was a change in this values with time in particular we noticed differences of the order of 15%. So we tried also to estimate peak temperatures introducing an error of 15% on L_n values and we did not notice a big change in results.

Other studies were made with this method in particular we calculated peak temperature for spot heater events for magnet HGQ08 and HGQ09 and we compared these calculations with the actual measurements (temperature measured with resistance method during tests) and we tried to have a temperature map for a spot heater event for magnet HGQ09 at 12000A.
We can summarize the spot heater events in table 4.7 and we plot results in figure 4.8 underlying also the different conditions in which we made measurements.

Table 4.7 Results for peak temperatures with two different methods for magnets HGQ08-09.

HGQ	I (A)	$T_{inductance}$ (K)	$T_{resistance}$ (T)
9 Q1(25W/cm^2)	3000	61	50
	5000	146	123
	7000	238	210
	8000	278	258
	9000	305	295
9 Q1(45W/cm^2)	7000	218	196
	9000	276	271
	10000	296	301
	12000	307	332
9 Q4(45W/cm^2)	7000	153	133
	10000	198	175
8 Q1 (50W/cm^2)	3000	56	46
	5000	105	94
	7000	168	148
	9000	235	219
	10000	256	245
	12000	264	271

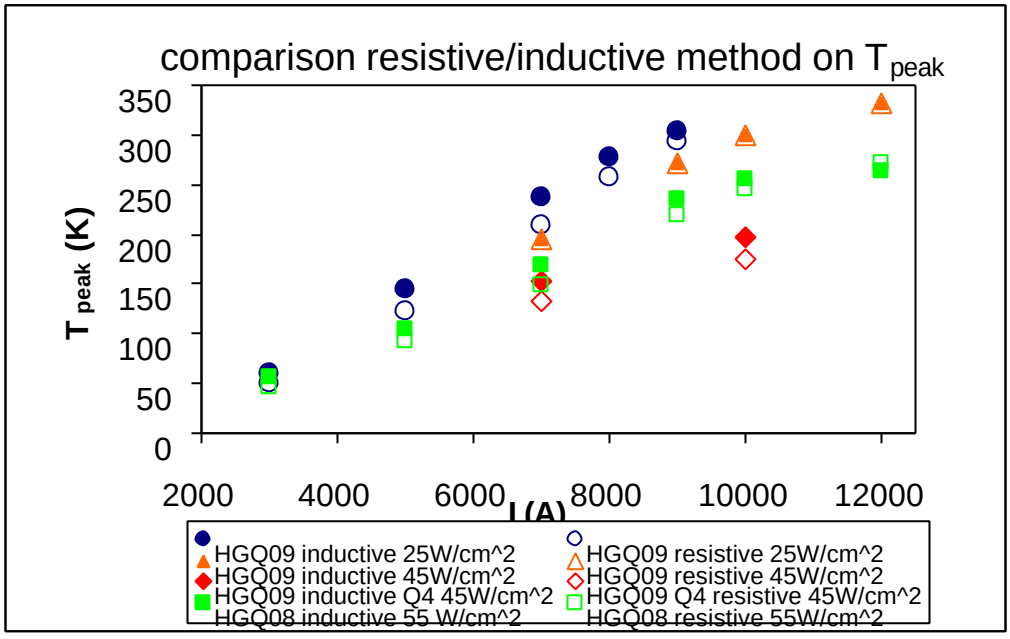

Fig. 4.8 Comparison between inductance method and resistance method (measured values).

As we can see from figure 4.8 the two methods seem to agree well even if the inductance one overestimates systematically peak temperatures.
Later we considered a spot heater event in the worst case of excitation current (12000A). We considered again magnet HGQ09 and in this magnet the spot heater fired was in the outer midplane position on coil 1. In particular to make this temperature map (as we already did for first comparisons between the three methods earlier this chapter) we had to use strip heater events at different current in order to estimate every single L_n for all the segments of the magnets. To estimate these quantities we used strip heater events because in this case the heaters are fired and resistance voltage develops only after 30ms so that initially the voltage in purely inductive. We considered these kinds of events at different currents in order to consider also the change with current of transfer function, which reduces the values of inductance.

In figure 4.9 we report the result for the spot heater events considered:

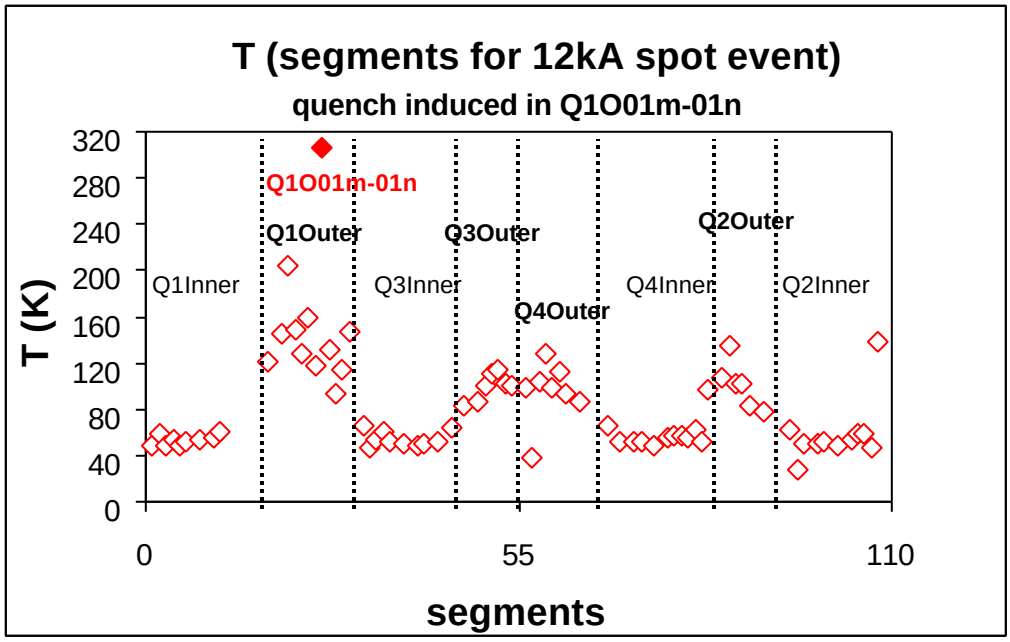

Fig. 4.9 Temperature map after a quench triggered by spot heater at 12000A.

From the pattern on the plot we can easily see where the quench is generated (highest temperature) and how the coil has higher temperatures where the quench is developed and in particular around the spot position as expected. It is interesting also to notice how the other outer coils have temperatures very similar not only in values but also in the pattern showing higher temperatures for longer turns. We can also observe that higher temperatures are developed in low field region because in this region quench velocity is slower so that the quench stays longer in a segment developing more heat (farther from critical surface) (see Fig. 2.11 to follow the wiring and positions of voltage taps).

We decided anyway to abandon this method because it was not useful for the analysis we want to make since with the adiabatic method we can obtain the same kind of results in an easier and more reliable way. On the other hand this method can be very useful to estimate temperatures of longer coils (they have a bigger inductance easier to extrapolate from data) for example the coils of main dipoles of LHC.

Chapter 5

TESTS OF HIGH GRADIENT QUADRUPOLES AT FERMILAB

5.1 Introduction

Test program

As already said for the tests of model magnets it was used a vertical dewar (VMTF) designed to operate with superfluid and normal He at 1.1 atmosphere. Magnet current is supplied by a 16kA DC power system with an energy extraction circuit (dump resistor). Every magnet was furnished with ~120 voltage taps and in particular positions spot heaters (that cover a ~5cm length of conductor and are installed in three positions, inner pole, outer pole, outer midplane, for studying quench propagation and peak temperature) were attached. Magnets have been equipped with two possible layers of protection heaters. “Inter” layer heaters are located between the inner and outer coils, while “outer” layer heaters are placed between the collars and the outer coil. Each layer consists of 4 heaters, which have a race track geometry covering ~10 turns of one side of two azimuthally adjacent coils. Thus connection of two “opposite heaters” (H1&H3 or H2&H4) in a given layer provides protection to all four magnet quadrants (see Fig. 3.5b).
The strip heaters and spot heaters are powered by a heater-firing unit (HFU), whose voltage can change. The capacitance of the system can be set in 4.8mF increments up to 19.2mF. The cold resistance of a stainless steel heater of width 15.9mm is about 5.5Ω. The system resistance is low relative to the strip heater resistance such as 92% of the HFU energy was deposited into the heaters. The stainless steel heaters were typically operated in parallel (heaters used from HGQ01 to HGQ05), while the distributed resistance heaters (HGQ06 to HGQ09) were operated in series. The RC time constant for the former tests was 40ms while for the latter tests the time constant was set to approximately 80ms. The 80ms time constant was chosen because this is the value in LHC operation, using a 7mF capacitor bank and two full length heaters connected in series with a stainless steel/copper longitudinal distribution of 1:2 ([15]).

Typical measurements on a HGQ model

Every model magnet of HGQ project follows a guideline run plane which was changed among the magnets only for choices of the setting parameters to test the performance of each magnet and make improvements for the next one. In fact the main characteristics, such as material for cable, winding system, collaring of coils were maintained always the same for all the magnets (see specifications chapter 2). But each magnet has particular differences from the others such as curing cycle for the cable to insulation, and as we said strip and spot heater position and geometry.
Let us now consider a typical guideline of a run plan for a test on a magnet and later we will consider in particular the last magnets (HGQ05-09) and their differences.

Usually a test on a magnet was divided in two or more thermal cycle in order to be able to have more sets of data and study the training effect on magnets.
For the first magnets (HGQ01-HGQ07) there was a thermal cycle at 4.5K in which all the typical study were done but for the latest magnets (HGQ08-HGQ09) only the 1.9K thermal cycle was made. At the beginning the 4.5K cycle was important to study mechanical properties of the magnet, which are the most critical for the magnet design and quench characteristics. In fact for the first five magnets several mechanic changes were made in order to obtain requested specifics.
Later, when the final mechanic design of the magnets was reached, it made more sense to concentrate studies at the operational temperature of 1.9K, in order to improve as much as possible the peculiar characteristics in the final layout.

Typical measurements during the cycles are:

- magnetic measurements at room temperature and at 1.9K where with a z-scan probe one measures multipoles at different excitation current at different positions (see chapter 2 for results)
- pre-test on the magnet at room temperature and during the cool down (between 4.5K and 1.9K) during which one has to check the strain gauge, voltage taps, thermometers and heaters
- quench training up to short sample limit (above 230T/m) if reached
- ramp rate studies (to see how the critical current changes with a different ramp rate see chapter 3 for results)
- temperature dependence studies (see later)
- heaters study (to see the efficiency of heaters in different situations)
- energy loss measurement (see chapter 3 for results)
- bus test (where the bus is the cable which links the magnets of the inner triplet region and since it is inside the same system with the magnets it was necessary to verify that this cable does not affect the properties of the system. This issue is not discussed in the thesis).

In particular we are interested in quench protection system so we will focus the attention on heater studies after a general view on other studies.

5.2 Quench training and thermal studies

Before going in details on quench protection we would like to speak about quench training for the different HGQ models. Other interesting things to show briefly are thermal studies done on all the

models to demonstrate the temperature margin of the models and justify the choice to work in superfluid to provide the appropriate cooling conditions for IRQ.

1. Quench training

All models have been tested in normal and superfluid liquid helium in the temperature range of 1.8K-4.5K. During training quenches about 70% of the stored energy was extracted and dissipated in an external dump resistor (disabled only for particular studies). Models HGQ05-HGQ07 were trained in normal and superfluid helium while HGQ08 and HGQ09 were trained only in superfluid helium. Only HGQ05 and HGQ07 went through three test cycles, the rest of the magnets were warmed up only once to room temperature and then cooled again in liquid helium ([10], [12])).

Table 5.1 Quench history of HGQ models.

thermal cycle	HGQ quench #	HGQ05 I_c (A)	HGQ06 I_c (A)	HGQ07 I_c (A)	HGQ08 I_c (A)	HGQ09 I_c (A)
4.5K (TCI)	1	9553	9056	10155		
	2	9942	9614	10681		
	3	9936	9701	10742		
	4	10001	9730	10753		
	5	10018	9814	10779		
	6	10031	9858	10867		
	7	10174	10043	10862		
	8	10159	10092	10898		
	9	10150	10146	10946		
	10	10095	10169	10917		
	11	9927	10199			
	12	10130	10212			
	13	10182	10310			
	14	10110	10340			
1.9K (TCI)	15	10896	12224	12101	11144	12760
	16	11656	12554	12468	11649	12650
	17	12228	12721	12993	12173	12898
	18	12316	12713	13072	13343	12992
	19	12541	12628	13077	12376	
	20	12556	12778	13144	12503	
	21	12553	12791	13220	12575	
	22	13038	12860	13464	12742	
	23	13198	12898	13358	12807	
	24	13152	12941	13521	12832	
	25	13240	13043	13499	12863	
	26	13290	13098	13555	12898	
	27	13362	13123	13635	12953	
	28	13284	13137	13696	13045	
	29	13367	13148	13722		
	30	13240	13172	13700		
	31	13457	13288	13855		
	32	13393	13291	13938		

	33	13437	13325	13836		
	34	13385	13285	13956		
	35	13515	13367			
	36	13585	13362			
	37	13578	13288			
	38	13482	13221			
	39		13327			
1.9K (TCII**)**	40	13316	12044	12855	12938	12688
	41	13549	12971	13204	12885	12781
	42	13243	13012	13430	12956	12910
	43	13656	13038	13604	12998	12969
	44	13486	13177	13869	13020	13005
	45	13614	13263	13955	13107	13022
	46	13542	13343		13120	13144
	47	13504	13342		13207	13272
	48	13531	13353		13301	13316
	49	12417	13428			13320
	50	13000				13332
	51	13202				
	52	13283				
	53	13332				
1.9K (TCIII**)**	54	12276		12842		
	55	12399		12934		
	56	13048		13857		
	57	13070		13898		
	58	13171		13981		
	59	13267		13791		
	60	13334				
	61	13401				
	62	13475				
	63	13505				
	64	13296				
	65	13315				

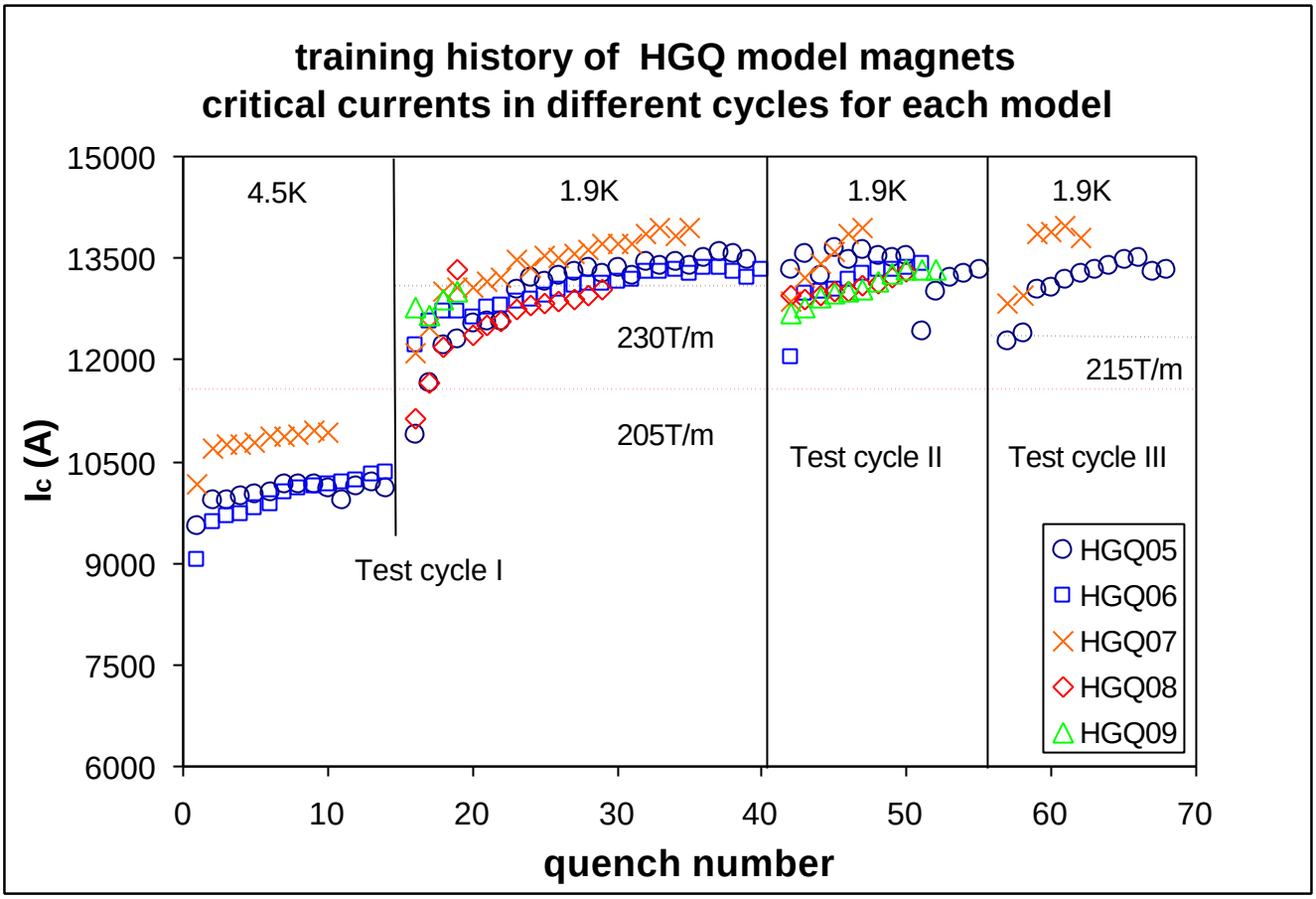

Fig. 5.1 Quench training history for HGQ05-HGQ09.

At normal helium temperature, after short training, HGQ05 and HGQ07 reached the estimated critical current value of the conductor based on critical current measurements of a short sample of the cable (short sample limit), while was a little below this limit for magnet HGQ06.
The first quench at 1.9K for HGQ06, HGQ07 and HGQ09 and the second for HGQ05, HGQ08, was higher than the required nominal gradient of 205T/m (High Luminosity IR). All five magnets remembered their training after the first thermal cycle and had their first quench above 215T/m field gradient value (operation field gradient).
During the measurements taken all the models were quenched several times using spot heaters to initiate the quench and no external resistor was used to extract the stored energy. The magnets were protected by strip heaters only so the magnet dissipated the stored energy. After these heater induced quenches we quenched few time each magnet and no quench current degradation was observed.

2. Temperature dependence of critical current

This kind of study gives information about the critical current short sample limit and temperature margin for these magnets. All the models reached their short sample limit at around 4.5K (see Fig. 5.2).
The temperature expected in cryogenic system for the inner triplet quadrupoles is in the range of 1.9K and 2.0K. It has to be noticed that the inner coil is cooled by convection directly to superfluid on the coil inner radius. The outer coil is cooled by conduction through the collar laminations and through the inner coil. Heat is removed from the magnet via superfluid heat transport through the four, round, iron yoke holes. Heat in the superfluid in the annular space between the beam tube and the inner coils is removed via heat transport through channels in the collars and yoke to the yoke holes. The operating

point for the High Luminosity Interaction Region magnets is 205T/m and the temperature margin is calculated to be 2.4K for inner layer (higher field) and 3.7K for the outer layer (lower field). But cooling conditions for the inner cable are better so that the actual peak temperature in case of quench is higher in the outer layer ([10], [12], [13]).

Table 5.2 Thermal studies for HGQ models.

HGQ model	T(K)	I_c (A)
HGQ05	1.90	13444
	2.00	13579
	2.10	12705
	2.20	12448
	2.35	12293
	2.75	11978
	3.30	11567
	3.80	10952
	4.20	10478
	4.40	10164
HGQ06	1.90	13288
	2.10	13221
	2.20	13327
	4.00	11337
	4.30	11095
	3.50	11929
	3.00	12442
	2.50	12869
HGQ07	1.90	13851
	1.87	13907
	2.10	13684
	2.60	13344
	3.30	12430
	3.73	11690
	4.20	11057
HGQ08	1.90	13301
	1.95	13191
	2.00	13335
	2.05	13315
	2.10	13301
	4.50	10557
	4.20	10661
	3.70	11333
	3.20	12020
	2.72	12567
	2.20	13129
HGQ09	1.90	13357
	4.20	10564
	3.50	11565
	3.10	12338

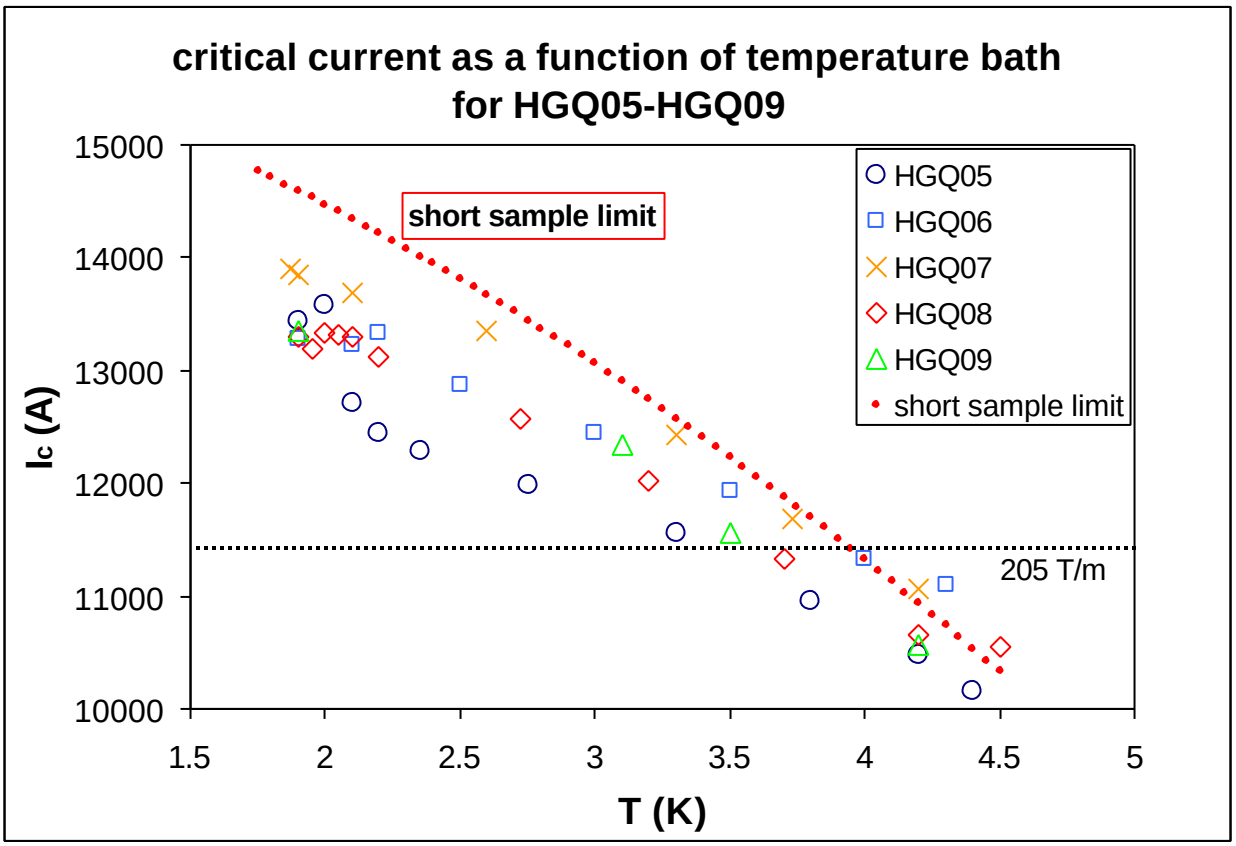

Fig. 5.2 Critical current as a function of the temperature bath for different HGQ models.

As we can see from figure 4.2 all the models reached the short sample limit (*ssl* line plotted) at 4.2K while at lower temperatures all the magnets seems to be at 90-95% of their short sample limits probably for some mechanical limitations. Some points between 4K and 4.5K are above the line of short sample limit due to the natural uncertainty on the estimate of this quantity.

3. Thermal studies on HGQ08

The model **HGQ08** was very interesting from the point of view of thermal studies.
This model was wound with stabrite coated cable so that the resulting low interstrand resistance and high AC losses allowed us to measure magnet performance in superfluid as a function of helium temperature ([13]).

Table 5.3 Critical current as a function of ramp rate and temperature for HGQ08.

dI/dt (A/s)	T (K)	I_c (A)
20	1.900	13207
135	1.900	8150
80	1.900	12653
150	1.950	4842
135	1.950	7565
120	1.950	9903
100	1.950	10914
80	1.950	12620
300	1.950	3850
200	1.950	3868

20	1.950	13191
150	2.005	4568
135	2.005	6861
120	2.005	9587
100	2.005	10761
80	2.005	12399
300	2.005	3777
200	2.005	3792
20	2.005	13335
150	2.050	4142
135	2.050	4671
120	2.050	8767
100	2.050	10552
80	2.050	12157
300	2.050	3697
200	2.050	3625
20	2.050	13315
150	2.200	3464
135	2.200	3676
120	2.200	4654
100	2.200	7767
80	2.200	10312
65	2.200	11045
300	2.200	3345
200	2.200	3324
20	2.200	13129

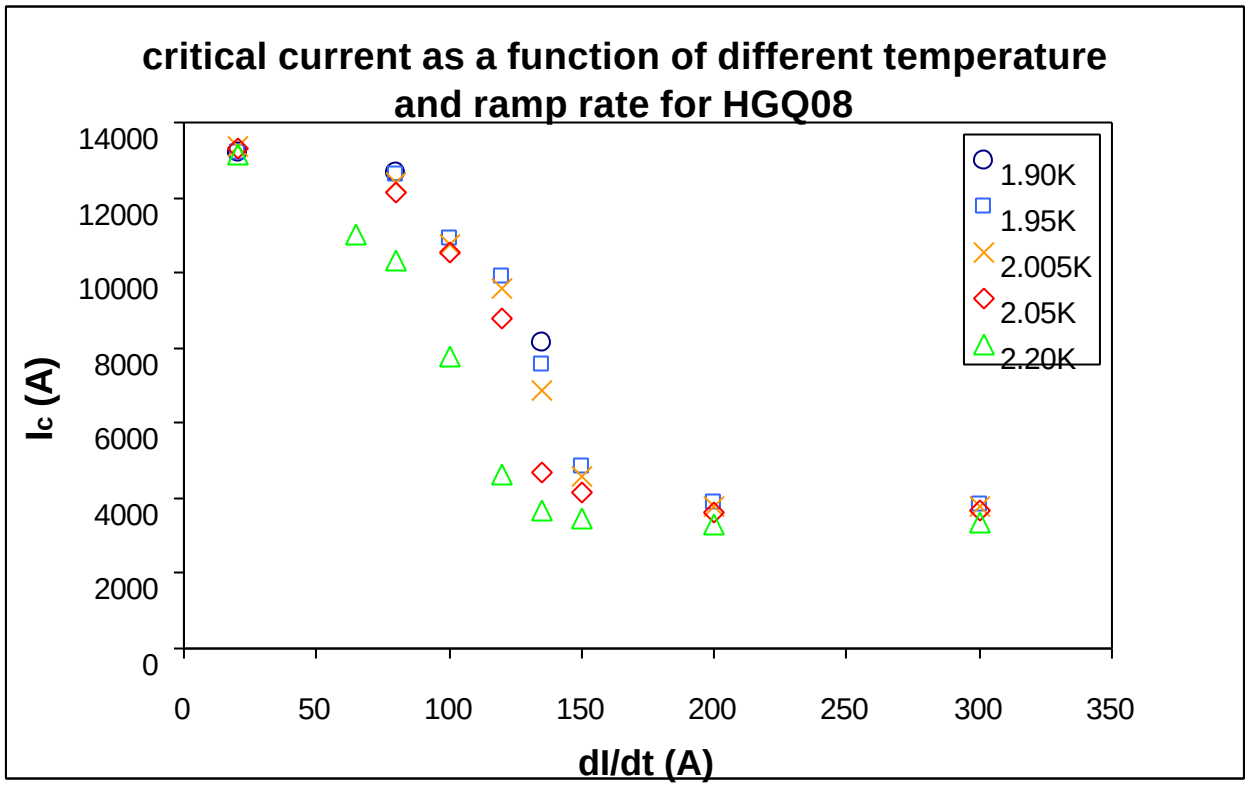

Fig. 5.3 Critical current as a function of different ramp rate and temperature for HGQ08.

As one can notice from figure 5.3 the temperature (lower than 2.05K i.e. below λ-point), has little effect on quench current. This is due to the fact the superfluid helium is able to remove the heat better than normal liquid helium even if above a certain value of ramp rate (200A/s) they behave similarly since superfluid helium can not remove heat as fast as it develops.

5.3 Determination of main values to characterize heaters

The heaters are characterized by several parameters, which can be obtained directly from data acquisition or data analysis.
During the tests there were four heater parameters studied:

1. heater location, either inner or outer layer
2. the amount of heater insulation between the coil and the heater
3. heater width
4. longitudinal distribution of the stainless steel (SS) heater centers by masking the stainless steel with a thin layer of copper (Cu)

The first heaters were stainless steel strips located between inner and outer coil while at the end they were moved to the outer layer (easier position to install them) and contained distributed resistance centers and less insulation between coil and the heater. The heater width varied from 12.7mm to 22.2mm (higher protection).

Table 5.4 Specifications for heaters of HGQ models (insulation is heater+cable insulation).

Magnet	Position	Element (all 25mm thick)	Insulation
HGQ01	Inter	stainless steel 15.9mm wide	325μm
	Outer	none	N/A
HGQ02	Inter	stainless steel 15.9mm wide	325μm
	Outer	stainless steel 15.9mm wide	350μm
HGQ03 &05	Inter	stainless steel 15.9mm wide	325μm
	Outer	15.9mm wide with copper plating 38mm etched areas at 114mm intervals	350μm
HGQ06	Inter	none	N/A
	Outer	12.7mm wide with copper plating 610mm etched areas at 1930mm intervals	250μm
HGQ07	Inter	none	N/A
	Outer	22.2mm wide with copper plating 610mm etched areas at 1930mm intervals	250μm
HGQ08 (CERN heater)	Inter	none	N/A
	Outer	15mm wide with copper plating 120mm etched areas at 360mm intervals	250μm
HGQ09 (CERN heater)	Inter	none	N/A
	Outer	15mm wide with copper plating 102mm etched areas at 204mm intervals	225μm

To compare heaters it is necessary to study their performance and compare results on the same kind of tests.

Heater performance is characterized by:

1. **V_{min}**, the minimum voltage (or energy) required to initiate a quench. It determines the voltage requirements for the heater power supplies. This quantity is changed by hand in the tests set up so that one charged the capacitor banks for the heaters at different voltage until it reaches the one which quenches the magnet by firing the heaters. To verify that the actual inserted value is the value applied the voltage signal of the strip heaters has to be checked and verify they were fired and they had the voltage expected.

2. **t_{fn}**, the time between quench heater firing and resistive voltage initiation. It is a good measure of the heaters efficiency and low values of t_{fn} result in lower quench integral which in turn translates into a lower coil peak temperature. This measurement is done by analyzing the channels related to the position where the quench occurred and where one can see resistive voltage. Later on describing the different studies done we will define better this quantity.

3. **MIITs**, the time integral, from quench initiation, of the square of the current, normalized to 10^6. This quantity is calculated directly with a C-shell called script. MIITs which calculates MIITs value knowing the current profile and integrating from a certain time introduced as parameter dependent on the particular study considered.

The studies used to characterized heaters of each HGQ magnet were:

- **V_{min} study**. In this kind of study the dump delay (time when the dump resistor is fired) is set to 25ms and the magnet is excited at different currents and for every current one has to determine the minimum voltage in order to have a quench by firing the strip heaters. In this case the heaters are fired at $t=t_{st}$ before 0s. (1)

- **Spot heater study**. In this kind of study the quench is induced from the spot heater, which is in different position for different magnets in order to check the protection system under the more different possible cases. The spot heater is fired at different current and one calculates MIITs values to see the correspondence with peak temperature. In this case the heaters are fired at $t_{st}=0ms$ while the spot heater is fired before $t=0ms$ and the energy is completely deposited in the magnet (dump is fired after 1000ms).

- **Strip heaters induced quenches and manual trips**. In these two studies the heaters are fired at $t=t_{st}$ before 0ms and $t_{st}=0ms$ respectively so that in the first case the heaters are fired when the current is still on the flat top while in the second case they are fired when the current is decaying.

For each study t_{fn} is always the difference between the time when the heaters are fired and the time when the first segment becomes resistive.
MIITs are calculated in different ways for the different study. In particular we have:

- **V_{min}**: in this case the heaters are fired before $t=0ms$ and t_{fn} is again the difference in time between t_{st} (time where the heaters are fired) and a time t_r after where one can see resistance growth due to the strip heaters. In this case is not useful to measure MIITs because the dump resistor is

(1) t_{st} = time when Strip Heaters are fired, t_r = time when we see Resistive growth, t_{sp} = time when SPot heater is fired

activated at 25 ms and so heat is spread fast everywhere and the current decays so fast that MIITs collected are very small.

- **Spot heater induced quenches**: In this case t_{fn} is the difference in time between t_{st} (time where the heaters are fired) and a time t_r when one can detect resistance growth due to the strip heaters. But is interesting also to collect the time t_{sp} when, after the spot heater is fired, the segment develops resistance voltage and calculate the resistance of this little segment. For every time is calculated MIITs even if the most important value here is the one which starts from t_{sp} (time where one can see resistance growth of the segment below the spot heater).

- **Strip heaters induced quenches**: in this case t_{fn} is again the difference in time between t_{st} (time where the heaters are fired) and a time t_r after where one can see resistance growth due to the strip heaters. Sometimes the quench can start far away from heaters due to mechanical stress or movements of the magnet and one could measure this time too and calculate two different MIITs values. But it was not our case where the time used to calculate Mitts was always t_r.

- **Manual trip**: in this case t_{fn} is again the difference in time between t_{st} (time where the heaters are fired) and a time t_r after where one can see resistance growth due to the strip heaters. In this case we calculate two different MIITs values, one from $t_{st}=0ms$ and one from t_r.

We have to notice that every time where the dump is activated after 25 ms it is not easy to see real resistance growth because heat is spread fast everywhere and the current decays so fast that MIITs collected are very small so that the temperatures reached are well below dangerous values.
In case of a spot heater event with the full deposition of energy in the magnet (dump is fired after 1s) it is also interesting to measure the resistance of the segment underneath the spot heater itself which is a little segment seated in different positions in the coil and it can be plotted as a function of time with another C-shell called script.resistance.

Three other important characteristics of a magnet depend on the efficiency of heaters:

- **peak voltage**, the highest voltage measured across any of the eight coil leads relative to the magnet leads. This voltage develops because of the coil to coil variation in t_{fn} and coil to coil RRR.
- **peak coil temperature**, the highest temperature reached in the magnet (which usually occurs where the quench is started). It is estimated in two different ways. First the temperature can be simply related to the time integral of the square of the excitation current (quench integral), using an adiabatic temperature model. The other method is to measure directly the cable resistance adjacent to the spot heater where quench was originated. The measured resistivity, dominated by the resistance of the copper is then directly related to the cable's local temperature. We will see the details for these methods later.

- **quench propagation velocity** determined with the "time of flight" technique in which we determine the time needed for a quench to propagate between voltage taps separated by a known distance.

For magnet HGQ08 and HGQ09 we tried to simulate CERN condition and to have for the two different configurations of heaters the same peak power density in order to compare efficiency of two different heaters geometry. To estimate the conditions we had to set in tests we consider two heaters in series for a full-scale magnet. We have that the resistance for one heater is ~16Ω so for two heaters in series we have ~32Ω (for a stainless steel heater of 1.9m the resistance is ~5.5Ω). So for heaters with SS:Cu ratio 1:2 (as HGQ08) one interval has a resistance of ~10.8Ω (32/3) while for

heaters with SS:Cu ratio 1:1 (as HGQ09) one interval has a resistance of ~16Ω (32/2) so the RC constant for the two types is respectively ~75ms and ~110ms (considering $R=R_{system}+R_{heater}$ and $R_{system} \gg 1W$ and $C=7mF$ as at CERN). If we estimate the peak power in every interval we have:

$$P = I^2 R_{heater} = \left(\frac{V_{heaters}}{R_{system} + R_{heaters}} \right)^2 R_{heaters} \approx \left(\frac{V_{heaters}^{\ 2}}{R_{heaters}} \right) \qquad (5.1)$$

$$p = \frac{P}{S_{tainless} S_{teel} area} \qquad (5.2)$$

so we get ~55W/cm^2 (for 1:2 SS:Cu ratio) and ~25W/cm^2 (for 1:1 SS:Cu ratio) for the supposed 900V power supply at CERN. If we want to simulate a case in which both the configurations have a *RC* constant of 80ms and the same peak power density of 40/45W/cm^2 for the short samples used at Fermilab we have to choose different C for HGQ08 and HGQ09 (in particular 14.4mF for HGQ08 and 19.2mF for HGQ09) and different voltages (in particular 350V for HGQ08 and 450V for HGQ09). This power density was used also for magnets HGQ06 (350V events) and HGQ07 (400V events) so that we can better compare the different kinds of heaters.

5.4 Results of the tests and discussion

Now we would like to summarize the results of the tests and discuss them considering the differences between magnets. In particular we will consider HGQ05-HGQ09 more in detail because they gave better results at least from quench behavior point of view and they are more similar to the final design which was achieved with magnet HGQ09 ([9], [15], [25]).

5.4a Vmin

First measurements related to heater performances is V_{min}, the minimum voltage needed to initiate a quench. This minimum voltage level determines the voltage requirements for the heater power supplies (it is the voltage across the sum of the heaters).
Here there is a summary of results for different magnets:

Table 5.5 V_{min} results for HGQ05-HGQ09.

HGQ	I (A)	I/Ic	V_{min}(V) per heater circuit	position
5	2800	0.20	353	inter layer, parallel connection
	5600	0.40	195	“
	9800	0.70	120	“
	9800	0.70	156	inter layer, series connection
	5600	0.40	292	“
6	2900	0.20	168	outer layer, parallel connection
	5800	0.40	145	“
	10150	0.70	84	“
	2900	0.20	184	outer layer, series connection
	2900	0.20	176	“
	5800	0.40	152	“
	10150	0.70	92	“
	2900	0.20	156	“
7	2900	0.20	196	outer layer, series connection
	5800	0.40	160	“
	10150	0.70	88	“
8	2900	0.20	174	outer layer, series connection
	5800	0.40	146	“
	10150	0.70	108	“
	12000	0.83	92	“
	800	0.06	194	“
9	2900	0.20	210	outer layer, series connection
	5800	0.40	184	“
	10150	0.70	132	“
	12000	0.83	108	“
	800	0.06	270	“

We have to notice we compare the minimum voltage across a heater circuit. It is necessary then, to consider the difference between heaters hooked up in parallel (HGQ01-HGQ06) and in series (HGQ06-HGQ09).

In fact for two heaters in **parallel** we have:

$$\begin{aligned} V_1 &= R_{heater1} I_1 \\ V_2 &= R_{heater2} I_2 \\ V_{\min} &= V_1 = V_2 \end{aligned} \qquad (5.3)$$

but $I_{tot}=I_1+I_2$, $I_1=I_2$ $V_1=V_2$ and $R_1=R_2$ so the voltage signal seen across one heater is the actual V_{min} of the circuit.

For two heaters in **series** we have:

$$\begin{aligned} V_1 &= R_{heater1} I = V_{\min 1} \\ V_2 &= R_{heater2} I \ = V_{\min 2} \\ V_1 + V_2 &= 2V_{\min 1} = V_{\min} \end{aligned} \qquad (5.4)$$

so the actual V_{min} of the heater circuit is twice the voltage read in the signal of one single heater.

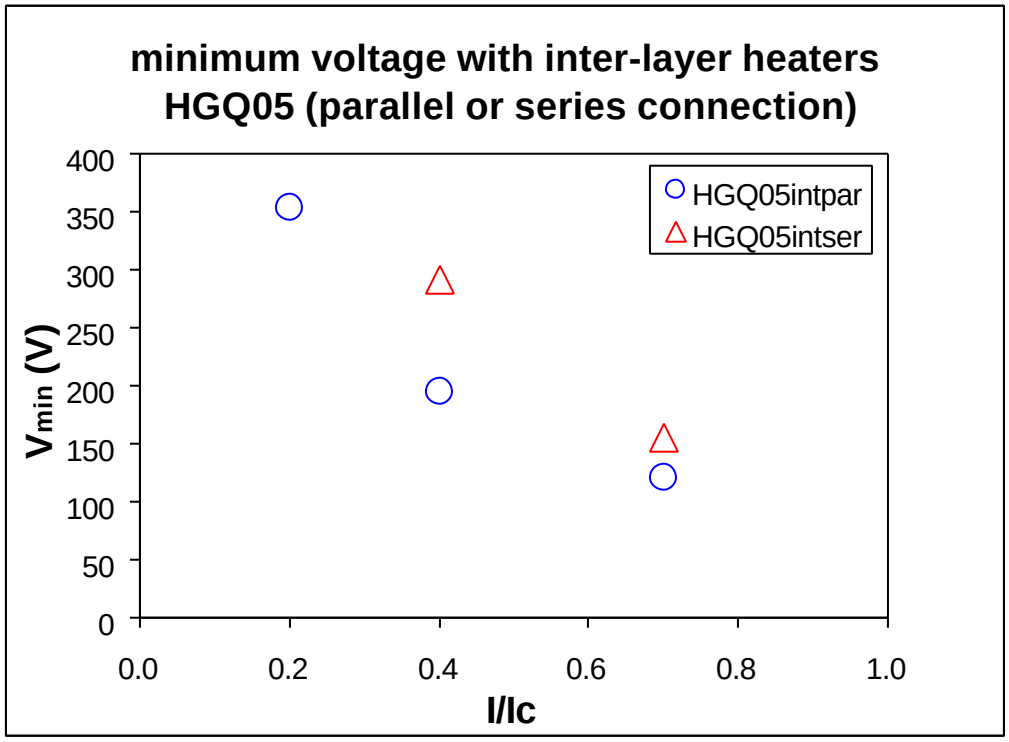

Fig. 5.4 V_{min} results for interlayer heaters (stainless steel heaters). The minimum voltage is for a heater circuit. We can see that interlayer heaters in parallel needs less voltage to quench the magnet.

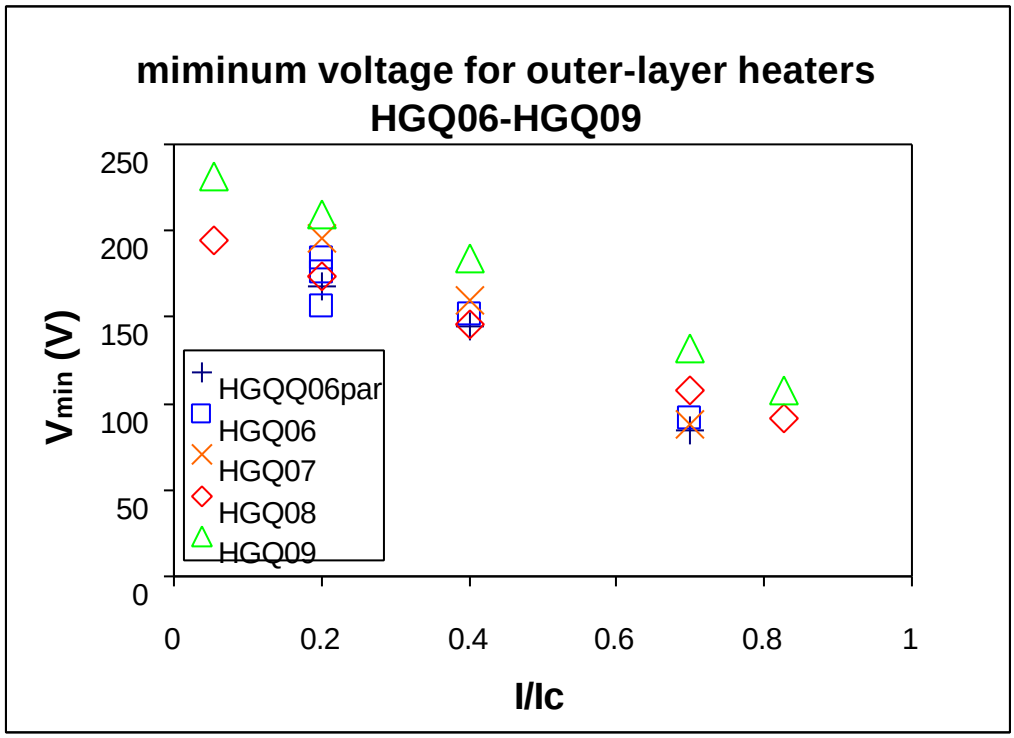

Fig. 5.5 V_{min} results for outer layer heaters (resistance distributed heaters). The minimum voltage is for a heater circuit. The voltage for the distributed heaters is reduced relative to that for SS heaters because copper plating enhances heaters performance.

From the plots for results for different magnets we can observe several things:

- interlayer heaters are effective as outer layer heater at quenching the outer coil (heat has to cross the same amount of insulation). Interlayer heaters also quench the inner layer but a delayed time (better cooling condition so that the temperature margin fro these layers is higher). Since they have the same performance regarding quench protection the choice to use outer layer heaters was made for practical reason (heaters are easier to install on outer layer position)
- outer layer heaters hooked up in series have slightly higher minimum voltage than the ones in parallel
- the voltage for the distributed heaters is reduced relative to that for SS heaters because copper plating enhances heaters performance
- the voltage savings (with reduced peak power density) are not as one would expect for the narrower heaters (HGQ06, 08, 09) probably because these heaters cover turns in low region field (so farther from critical surface)
- in magnet HGQ06 the measurements at *I/Ic=0.2* were made with different conditions of peak power density (V_{min} is less for less peak power density i.e. higher *RC* constant)
- for HGQ08 and HGQ09 we took measurements at 800A, which is the operating current of the LHC injection. The required voltage for quench initiation is less than 250V, that scaled to full length magnet is approximately 750V (well below the power supply setting of 900V).

5.4b t_{fn} studies

The value of t_{fn} is very important to determine the efficiency of the heaters. In particular it is the difference in time from when the heaters are fired to when one can see the first resistance voltage growth.
In HGQ01-HGQ05 heaters were between inner and outer layer but since there is not difference in the initiation of the resistive voltage from the configuration with the heaters on outer layer, the latter was preferred because easier to install.
Here the results for HGQ06-HGQ09:

Table 5.6 t_{fn} studies for models HGQ06-HGQ09.

model magnet	I/I_c	V_{shfu}(V)	$t_{stripheater}$ (ms)	$t_{Resistive}$ (ms)	t_{fn} (ms)
HGQ06	0.2	300	-258	-150	108
	0.2	400	-228	-141	87
	0.4	400	-69	-8	61
	0.7	400	-39	-4	36
	0.8	400	-36	-11	25
	0.7	400	0	35	35
	0.2	220	-337	-158	179
	0.4	220	-129	-11	118
	0.6	220	-96	-7	89
	0.7	220	-75	-28	47
	0.8	220	-52	-18	34

	0.2	220	-355	-181	174
	0.4	220	-120	4	124
	0.6	220	-92	0	92
	0.7	220	-73	-20	53
	0.8	220	-49	-10	39
HGQ07	0.2	400	-121	-33	88
	0.4	400	-77	-28	49
	0.7	400	-36	-14	22
	0.8	400	0	20	20
HGQ08	0.2	350	-130	-50	80
	0.4	350	0	60	60
	0.7	350	0	30	30
	0.8	350	0	25	25
	0.8	350	0	22	22
	0.4	225	0	65	65
	0.7	225	0	45	45
	0.4	300	0	60	60
	0.7	300	0	37	37
HGQ09	0.2	330	0	125	125
	0.4	330	0	75	75
	0.7	330	0	45	45
	0.8	330	0	37	37
	0.2	330	-165	-40	125
	0.4	330	-91	-10	81
	0.7	330	-49	-11	38
	0.8	330	-38	-9	29
	0.2	450	-128	-35	93
	0.4	450	-72	-12	60
	0.7	450	-40	-6	34
	0.8	450	-32	-7	25
	0.2	450	0	100	100
	0.4	450	0	67	67
	0.7	450	0	38	38
	0.8	450	0	31	31

We have to notice that the studies made are different in particular we used strip heater induced quenches and manual trip events already presented earlier.
It can be helpful to show two different plots for magnets HGQ06-HGQ07 and HGQ08-HGQ09 to understand better the differences.
Several patterns emerge from Fig. 5.6 and 5.7:

- for a given heater and power density the t_{fn} decreases with excitation currents
- there is a considerable spread at low current while at high current all the values converge to a t_{fn} of 20-30ms because we are closer to critical surface
- in general the larger the power supplied (higher energy) the smaller the t_{fn} for a given magnet current (heaters are more efficient)
- the wider the strip the smaller the t_{fn} and it should be like this because for all the heaters, one edge is placed between the first two midplane turns (16th and 15th). So wider heaters cover more turns and cover more turns in higher field region where there is a lower temperature margin and a faster response to heater energy pulse

As we explained the quench integral is directly linked to peak temperature. By plotting this quantity as a function of the normalized current I/I_c (Fig 5.8) using different power density for the two different kinds of heaters we can see that as expected the quench integral decreases with increasing power of the heaters. The different power densities, as already explained earlier, were chosen in order to simulate the final conditions at CERN with these two different heaters. In this case heaters of HGQ08 performed better than heaters for HGQ09.

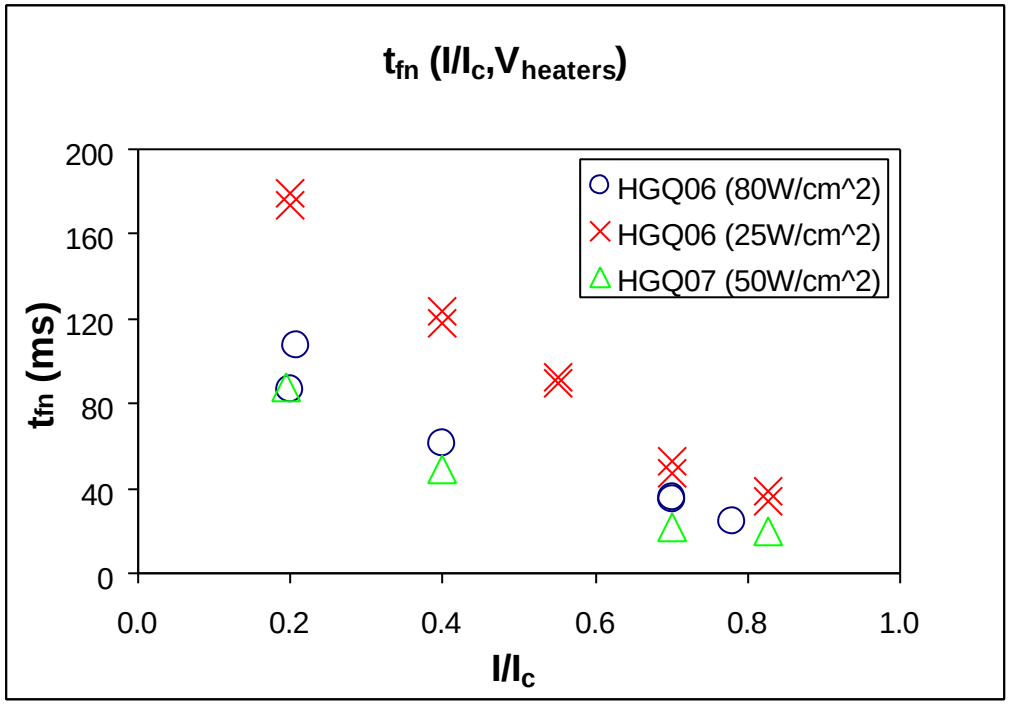

Fig. 5.6 t_{fn} studies for HGQ06-HGQ07
For HGQ06 we have two sets of measurements at different peak power density. In the case of 25W/cm^2 two sets of measurements were taken. HGQ07 is wider so that t_{fn} values are lower.

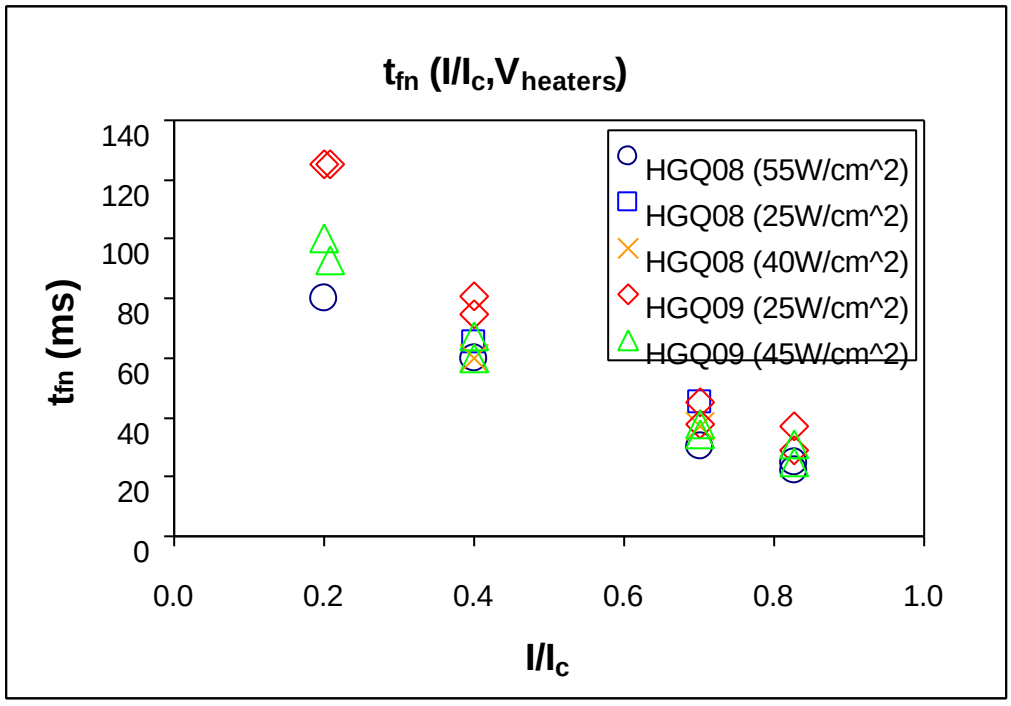

Fig. 5.7 t_{fn} studies for HGQ08-HGQ09 at different peak power density condition. Larger power supplied produce a lower t_{fn} values since the heaters deposit more energy.

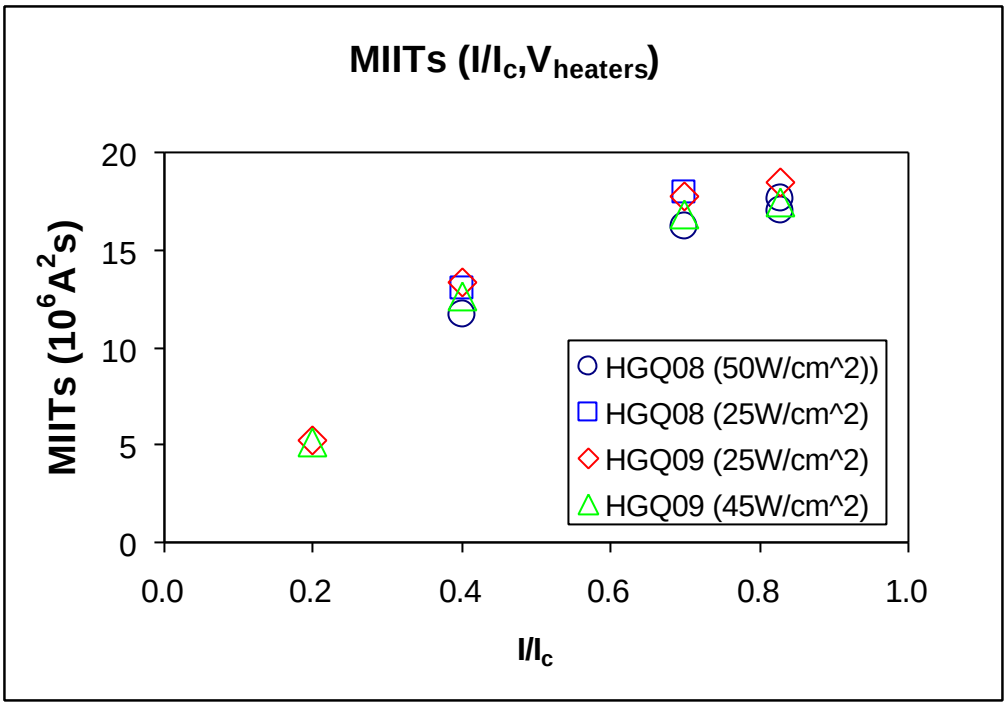

Fig. 5.8 Quench integral for HGQ08-HGQ09 at different peak power density condition. As we can see MIITs collected with these two different strip heater geometries are comparable even if HGQ08 performs better.

5.4c MIITs

MIITs are defined also as the quench integral and it is calculated as:

$$MIITs = 10^{-6} \cdot \int_{t_0}^{t} I^2(t)dt \qquad (5.5)$$

Where *I(t)* is magnet current that usually is constant before t=0ms but after it can changes, and t_0 is the time when we start to collect MIITs and it corresponds at the time when we first see resistive voltage growth.
This quantity can be related to the heat released in the coil, which can be calculated knowing the heat capacity of the coil. We will use this method to estimate the peak temperature and peak voltage to ground for the final system of two 5.5-meter long quadrupoles as we will explain in chapter 6.
In this chapter we would like to show only some measurements taken which linked MIITs with peak temperature or as before MIITs and current.

5.4d Peak voltage

The peak voltage is defined as the highest voltage measured across any of the eight coil leads relative to the magnet leads. This voltage develops because there is variation in t_{fn} between coils and coil to coil difference in RRR (that is not an easy measurement to do). It is very common to have difference in RRR values. The measured voltage to ground measured in our models is less than 60V under standard conditions. Extrapolating to a full-scale magnet with two heater circuits the voltage should not exceed 250V (in standard conditions). Using these data one can model the effects of having two 5.5-meter long magnets connected in series, using as input the measured resistance and inductive voltage growth from the heater induced quenches. In this model (described in detail in chapter 6) we can consider also difference in efficiency of heaters and also difference in RRR between magnets and between coils of the same magnet. Again the peak voltage to ground should be less than 250/300 V as we will show later.

Table 5.7 Measured peak voltage to ground.

model magnet	heaters	I (A)	V_{peak} (V)
HGQ05	stainless steel	3000	0.57
		5000	3.15
		6000	5.85
		7000	8.72
		8000	11.60
		3000	0.65
		5000	3.18
		5000	3.08
		9000	19.30
		10000	32.20
		11000	48.80
		12000	65.80
HGQ06	distributed heaters	2900	0.82
		5800	4.78
		8000	11.73
		10150	20.60
		12000	33.20
	Q4uncovered	2900	1.33
	Q4uncovered	5800	14.20
	Q4uncovered	8000	34.70
	Q4uncovered	10150	58.20
	Q4uncovered	12000	70.00
HGQ07		3000	0.48
		5000	4.56
		6000	8.45
		7500	17.09
		8500	22.86
		10000	31.00
		12000	47.52

HGQ08		3000	0.45
		5000	3.85
		7000	12.60
		9000	27.40
		10000	36.13
		12000	63.70
	Q3uncovered	12000	79.80
HGQ09		3000	0.36
		5000	4.22
		7000	13.94
		8000	21.75
		9000	33.50
		7000	12.60
		9000	29.10
		10000	38.63
		12000	59.45
		7000	14.83
		10000	45.07

As reported in this table in HGQ05 we utilized stainless steel heaters in parallel while foe model magnets HGQ06-HGQ09 we utilized distributed resistance heaters hooked up in parallel (some events of HGQ06) and in series (all the other events of HGQ07-HGQ09).
In magnets HGQ06 and HGQ08 we had events in which the heaters were hooked up such as one quadrant was completely uncovered (situation of asymmetry of the system). To obtain this particular configuration one has to hook up two adjacent heaters (see Fig. 3.5b). For example if we use H2&H3 the quadrant Q1 is covered in both halves of the coil while quadrant Q3 is completely without heaters protection.

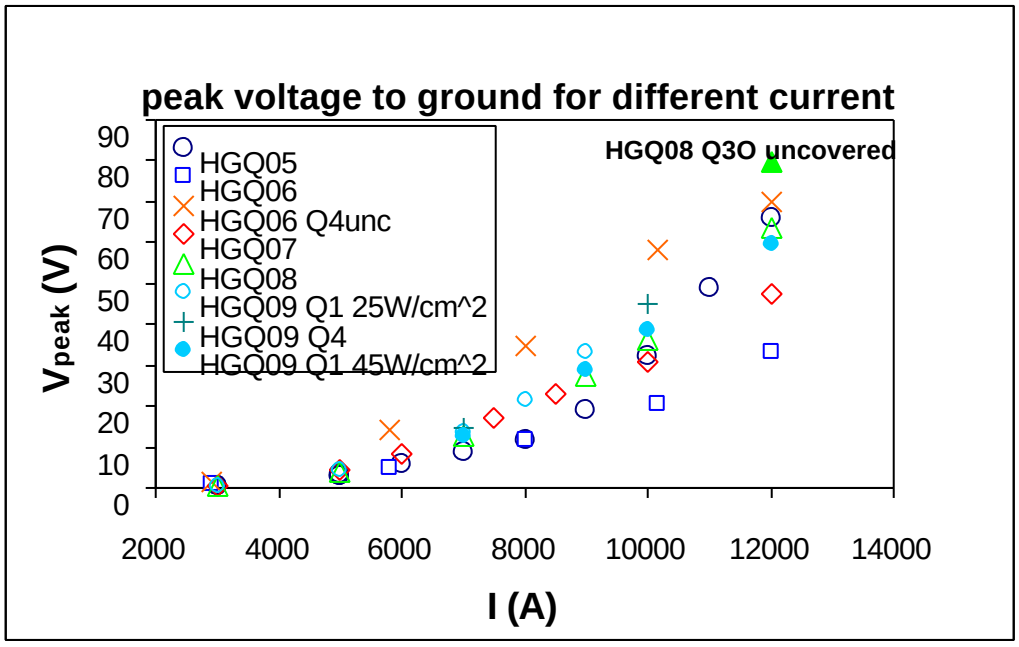

Fig. 5.9 Peak voltage to ground as a function of current fro model magnets HGQ05-HGQ09

For HGQ09 we have three different sets of measurements: in two of them the spot heater is fired in Q1 and the heaters have different peak power density while in the third one the spot is fired in Q4. Cases in which one quadrant is completely uncovered by heaters were studied in HGQ08 and HGQ06.

Several things can be noticed from figure 5.9:

- as expected the peak voltage increases with excitation current
- there is not visible difference in using stainless steel strip heaters in parallel (HGQ05) or distributed heaters in series (HGQ06-HGQ09)
- for HGQ09 we have open dots at a power density of 25W/cm^2 while solid dots are at 45W/cm^2 and as we can notice for higher power density we have lower peak voltage (as peak temperatures are lower for higher power densities as we will show)
- for HGQ06 and for one point of HGQ08 (solid triangle) we considered a case where there is not heater protection in one quadrant. This situation creates higher peak voltage (higher imbalance in heat distribution) but still the values are not higher than 90V

Even if the heaters for HGQ07-HGQ09 were wider than HGQ06 this does not help in reducing the peak voltage probably because wider heaters cover higher field region which develop higher resistance.

5.4e Peak temperature

Special events are used to estimate this quantity. In particular we use the so-called spot heater induced quenches, which as already mentioned, are events where a spot heater is fired in particular positions and the dump resistor is disabled so that all the stored energy is discharged inside the magnet.
The peak coil temperature is assumed to be in the origin of a spontaneous quench is estimated in two ways. First, the temperature can be simply related to the MIITs, using an adiabatic temperature model. The other method is to measure directly the cable resistance adjacent to a spot heater. The measured resistivity, dominated by the resistance of the copper is then directly related to the cable's local temperature. We presented these two methods and a third one in chapter 4 where we compared all of them. The adiabatic one will be use in chapter 6 for the simulation of the final system. Table 4.8 shows some measured results for peak temperature with the resistance method (used during measurements) and the measured values of MIITs:

Table 5.8 Measured peak temperature for HGQ models.

HGQ	I (A)	R (mΩ)	T (K)	MIITs (10^6A^2s)
2	3000	5.51	40	12.01
	3000	5.74	41	11.68
	5000	22.86	71	15.66
	6000	38.18	89	16.79
	7000	52.78	103	17.68
	8000	66.31	116	18.24
	9000	79.11	128	18.78
	3000	5.65	40	11.53
	5000	22.98	71	15.24
	7000	49.06	99	17.09
	9000	74.33	123	18.22
	10000	84.07	133	18.24

5	5000	19.80	98	12.27
	5000	20.16	99	12.30
	9000	56.72	204	15.86
	10000	62.11	219	16.24
	11000	64.96	226	16.38
	12000	67.55	232	16.36
7	3000	5.00	60	10.98
	5000	28.56	132	16.51
	6000	41.60	174	17.70
	7500	62.47	239	20.42
	8500	69.51	259	21.17
	10000	79.25	288	21.69
	12000	86.83	312	21.81
8	3000	3.36	50	10.88
	5000	16.45	95	16.24
	7000	38.13	162	19.45
	9000	62.58	239	20.98
	10000	70.83	263	21.68
	12000	79.29	288	22.03
9	3000	4.44	57	13.48
	5000	30.00	137	19.92
	7000	63.79	243	22.50
	8000	80.34	291	23.37
	9000	92.83	332	23.77
	7000	58.89	228	22.02
	9000	84.66	304	22.67
	10000	94.82	339	23.28
	12000	106.60	379	23.14
	7000	34.19	149	19.62
	10000	51.89	208	20.87

Figure 5.10 shows the measured peak temperature as a function of quench integral for HGQ models, which have spot heaters in different positions. In these tests in particular we considered three different positions:

- the pole turn of the inner coil (straight section)
- the pole turn of the outer coil (straight section)
- the outer coil midplane turn (end)

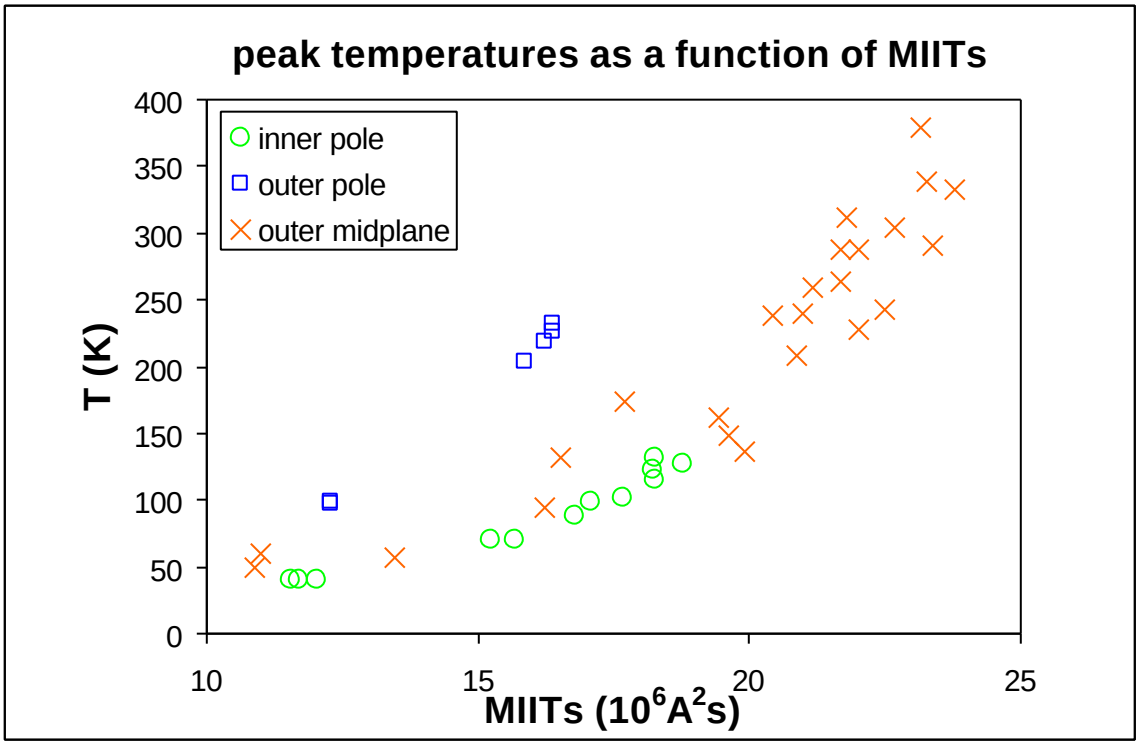

Fig. 5.10 Measured peak temperatures as a function of measured quench integral. For a fixed current if the spot heater is fired in a low field position the MIITs collected are higher so that peak temperatures are higher.

In all cases, increasing quench integral represent higher excitation currents and therefore high magneto-resistance (proportional to the current) at the onset of the quench. In general the inner cable has a lower peak temperature versus quench integral curve because the inner cable has better cooling channels. For the outer cable the pole turn temperature is higher than the midplane temperature because the pole turn is in a higher field region. The shape of these curves is well predicted by an adiabatic model which since adiabatic is more pessimistic.

In figures 5.11 and 5.12 we plotted the peak temperature as a function of current. Figure 5.11 shows this relationship for spot heater quenches originating in the high field region (pole turns) of the inner and outer coils. For quenches originating in the inner coil, the peak temperature is approximately 150K, while for the outer coil is less than 220K.

Quenches in the outer coil (midplane turn) have the highest peak temperature (because it is a low field position we are farther from critical surface so that we need more time to develop enough voltage to detect the quench) so the studies on the last three magnets were concentrated on these worst cases. These studies are shown in figure 5.12. The power densities for HGQ07and HGQ08 were chosen to fit LHC conditions and even if the heaters for HGQ07 were wider the peak temperatures were higher.

For HGQ09 there were two heaters one in coil 1 and the other in coil 4. One heater produced peak temperatures comparable to the ones of HGQ07 and HGQ08 the other heater produced temperatures 100K higher at the highest excitation currents.

The difference in temperatures can be attributed to a variation in turn to turn propagation in the coil ends near the spot heater. Lower turn to turn propagation would result in the observed increase in quench detection time, which increases the MIITs and so peak temperature.

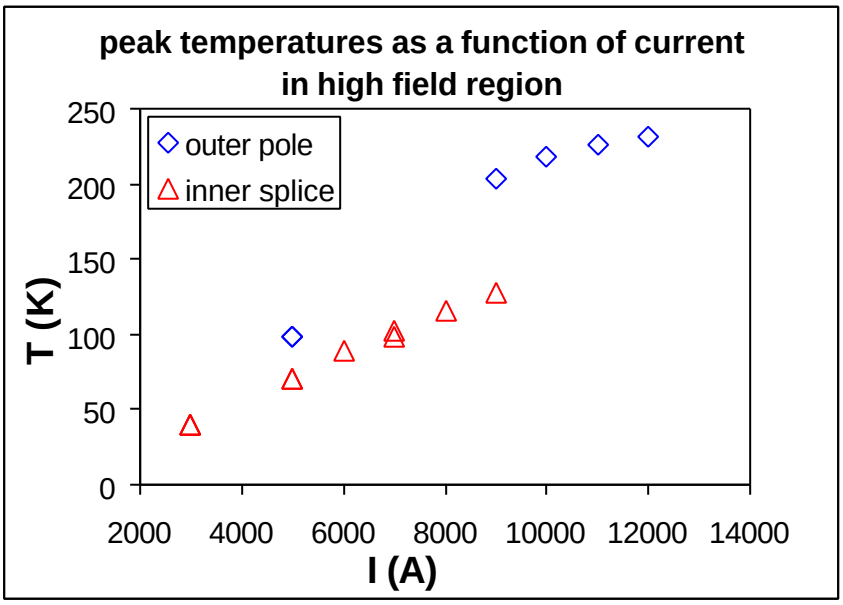

Fig. 5.11 Measured peak temperature for quenches in high field region (inner splice is the part of cable which joints the inner and outer layers in high field region).

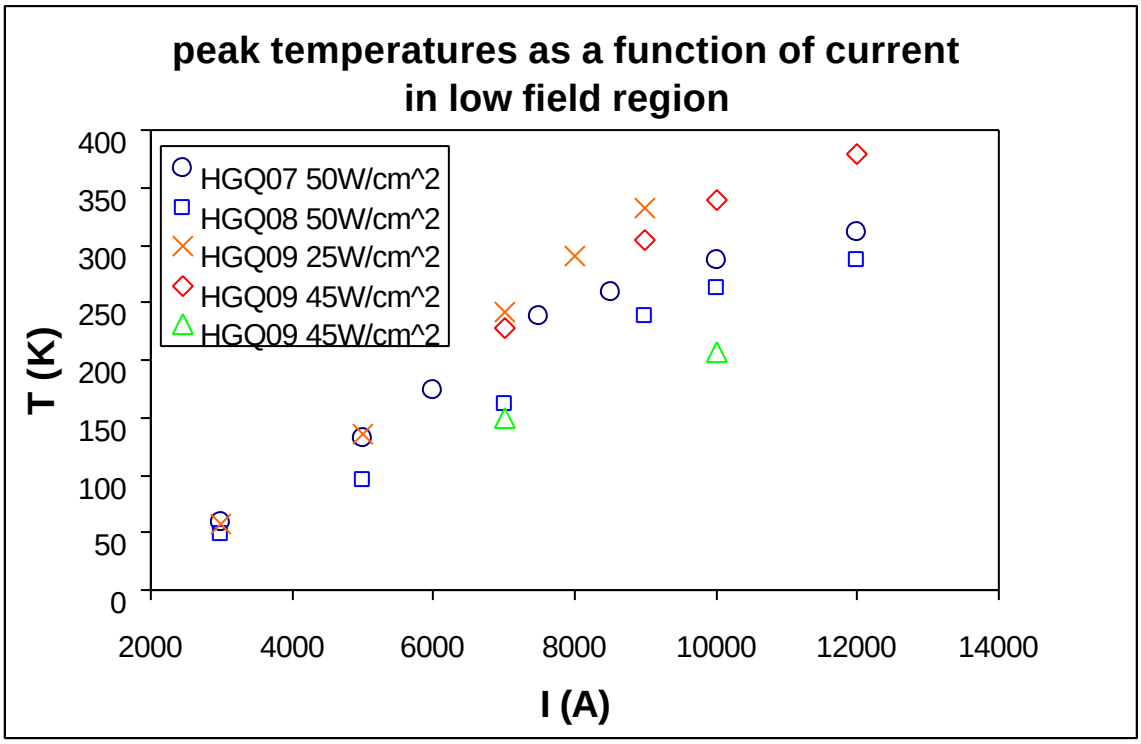

Fig. 5.12 Measured peak temperatures for quenches in low field region. In general lower peak power densities gives higher temperatures. For HGQ09 we have three sets of measurements: the first two differ for the value of peak power density with the spot hater fired in Q1; the third set is with the spot heater fired in Q4. The difference in temperatures can be attributed to a variation in turn to turn propagation in the coil ends near the spot heater.

Chapter 6

COMPUTATION OF THE PEAK TEMPERATURE AND PEAK VOLTAGE FOR Q2a/Q2b QUADRUPOLE SYSTEM

6.1 LHC inner triplet final design

Fermilab, as already said, is commissioned for the production of the quadrupoles Q2a/Q2b (5.5meter long superconducting magnets) and it is responsible for the cryogenic environment of the entire inner triplet.
In this chapter we wanted to simulate the expected variations in cable parameters and quench heater performance for the final system Q2a/Q2b using the data from the model magnets. We even considered the case where the system has a failure in the heater firing circuits.
The model used was based on adiabatic assumption and in particular we wanted to find not only the values for these critical parameters but also simulate voltage, current and resistance profiles. The model used is based on the so-called “MIITs method” already introduced in chapter 4. As shown this quantity can be easily related to temperature, which is then related to resistance (via resistivity) and finally to voltage.
The model divides the magnets in different quadrants (a magnet is simply a resistance+inductance). Each quadrant is divided in more sections in order to consider different magnetic field. Each part is subdivided again in subsections which become resistive at different times chosen appropriately in relation with data analysis from model magnets in order to consider quench propagation once the quench started from a single section. In each sections the resistive growth begins in a particular subsection at a time t_1 (chosen considering quench propagation and again using data) related to a particular current and so to a value of MIITs related to this current. From the relation between MIITs, temperature and field, we can calculate the constant temperature, resistivity and resistance in each time step considering small increment of time. With this resistance we can solve the differential equation of a L/R system and calculate a new current (next time step). With this new current we numerically integrate the MIITs to arrive a new MIITs value which leads to a new resistance and

temperature. For example we can try to explain the process with a schematic diagram of half a layer (top view).

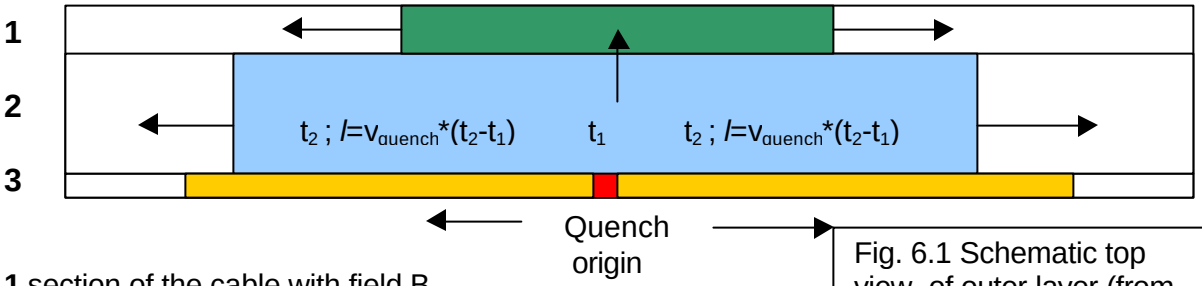

1 section of the cable with field B_1
2 section of the cable covered by heaters with field B_2
3 section where the quench occurs with field B_3

Fig. 6.1 Schematic top view of outer layer (from the external heater part) in order to explain quench propagation.

The quench is originated in the section 3 (red rectangle) and at each time step we collect MIITs depending on current, which is changing as the resistance and temperature are growing. For the amount of time necessary for the quench to propagate only this little segment develop resistance. Once the quench arrives in the two adjacent subsections (the quench propagates in both directions) another part of the cable starts to develop resistance so that the total resistance of this section is the sum of the resistance. The part of cable which is turned resistive has a length estimated from the product of quench velocity time the interval of time it passed since the first subsection quenched. In the meanwhile quench detection circuit detects the quench and heaters are fired so that a big part of section 2 becomes resistive at the same time (light blue rectangle) and the heat starts to propagate in this section and with transversal propagation also in section 1. The main idea is to simulate quench propagation by breaking the layer in little sections which turn resistive as soon as the quench arrives there and they increase resistance at each little time step necessary to simulate the exponential current decay and numerically integrate MIITs value.
This model was used to predict peak temperature and peak voltage to ground for the system Q2a/Q2b of two full-scale magnets. These quantities are predicted both for standard conditions and for particular events in which some failures in protection system is simulated. In fact in ideal conditions the two magnets in series should be exactly the same and the quench protection system should work in symmetric way. In reality the magnets can have different residual resistance ratio (RRR) and heaters can be effective at slightly different time or one of them can not work so that imbalance between quadrants can be produced and create unexpected conditions.
Before going in details in the analysis we would like to introduce terminology used in this chapter regarding strip heaters and how they covered different quadrants.
Each magnet has two circuits of strip heaters diametrically opposite (H1&H3 and H2&H4). To cover all the quadrants it would be sufficient to have only one of the two circuits because under this condition half heater would cover each quadrant. This condition was the standard condition used for the test of the short models. In this chapter we will often refer to a quadrant as two coils (inner coil and outer coil) and we will refer to “single covered coil” if it is half covered by the heater or “double covered coil” if it is totally covered by the heater (as explained in Fig. 6.2).

In figure 6.2 we recall heaters position and these definitions (see also fig. 3.5c).

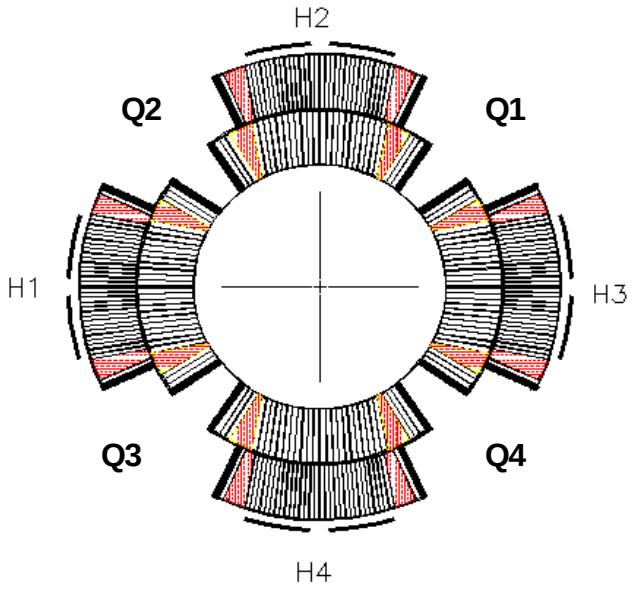

Fig. 6.2 Coil cross section and azimuthal position of protection heaters. If all the heaters are hooked up each quadrant is covered in both sides of the winding (double covered coil). If only azimuthally opposite heaters are hooked up (H1&H3 or H2&H4) each quadrant has only one side of the winding covered (single covered coil).

6.2 Set up and conditions used to simulate different events in inner triplet

To arrive to our final goal and estimate the quantities of interest we used data taken for HGQ program in order to see if we could simulate real events from tested magnets and then develop a further model adapted for long magnets. As already introduced in chapter 4 several parameters and constant were used for data analysis. We used again the results obtained in chapter 4 for the calculation of resistivity and specific heat. In particular we would like to recall here all the constant used and remind all the assumptions made:

Table 6.1 Constants used in analysis.

Temperature of the bath	T [K]	1.9
Resistivity of copper at 300K	ρ_{Cu} [Ωm]	$1.7 \cdot 10^{-8}$
Resistance per length inner cable	R/l_{300K} [mΩ/m]	1.6
Resistance per length outer cable	R/l_{300K} [mΩ/m]	1.8
Diameter inner cable	d_{inn} [mm]	0.808
Diameter outer cable	d_{out} [mm]	0.648
Cu:Sc inner cable	λ	1.3
Cu:Sc outer cable	λ	1.8
Copper area inner cable	A_{Cu} [mm^2]	10.63
Copper area outer cable	A_{Cu} [mm^2]	0.944
NbTi area inner cable	A_{NbTi} [mm^2]	0.817
NbTi area outer cable	A_{NbTi} [mm^2]	0.525
Number of strands inner cable	N	38
Number of strands outer cable	N	46
Magneto resistance coefficient	χ [Ωm/T]	$4.5 \cdot 10^{-11}$

To estimate peak temperature and peak voltage we used the adiabatic model based on calculation of current and voltage profiles. The main assumption made in this model is (besides the ones for calculation of resistivity and volumetric specific heat see chapter 4):

- for MIITs calculations it was neglected the contribution of helium (adiabatic assumption). The adiabatic model is useful to estimate the quantities of interest since as shown MIITS is easily related to them. By analyzing data from model magnets we were able to build this adiabatic model and we took in consideration the help of helium by scaling of a factor 1.25 (EMPIRICAL STEP BASED ON DATA ANALYSI) the temperatures calculated with the adiabatic model (we will se later that with this method the peak temperatures are overestimate of at least a factor 20-25%).

The simulation started with the analysis of real data and then continued with the simulation for the entire system of two 5.5m long magnets.

6.2a Pre-analysis on real data from short models

Once we had all the tools necessary to develop our model we wanted first to try to use it for a simulation of the real data we have from the different model magnets tested at Fermilab.
Our data analysis started considering spot heater events for different magnets from the HGQ program (data already mentioned in chapter 5).
A spot heater is a little segment of stainless steel inserted in different position in the coil and it can be fired in order to induce a quench in a particular point and test the protection system. The spot heater is in different positions for different magnets. In magnet 5 it was on the outer coil number 1 on a pole turn in between the voltage taps 16n-16m, in magnet 7 it was again on the outer coil number two on a midplane turn between the voltage taps 01n-01m. The same position used for magnet 7 was used for magnet 8 and 9 but on coil number 1 (see Fig. 2.11).
The positions were chosen in order to simulate the worst cases where a quench can happen. In fact the cooling channels of outer coils are less effective because the outer cable itself is smaller. In particular the midplane turns were chosen because the field is very low so that the critical surface is farther from operating point and the quench velocity is low. Therefore in these cases temperature can grow and reach the highest values. The pole turn, on the other hand, has higher field so that we are very closed to the critical surface and the risk of quench is bigger and it is the most likely position for a quench to occur.
As previously said, the model divides the magnet in different parts to consider the difference in field in the quadrupole so it was necessary to estimate an average field for these different sections of the magnet. To estimate the field we used some calculations of field map made with Roxie.
In particular we took the field map for 1kA and then we scaled our averaged values with current without considering iron saturation (so that the transfer function T_f [1)] is considered constant and we have different constants for different positions).
In fact
In fact

[1)] It has to be noticed that in this case the transfer function is considered on a layer and not on the entire magnet.

$$\frac{dB}{dt} = T_f \frac{dI}{dt} \qquad (6.1)$$

so that for steady state we can consider

$$B = T_f I \qquad (6.2a)$$

Now if we consider two different currents I_1 (as reference is 1000A) and I_2 for the same position and we know B_1 we can estimate the correspondent B_2 in fact:

$$\begin{aligned} B_1 &= T_f I_1 \\ B_2 &= T_f I_2 \end{aligned} \quad \Rightarrow \quad B_2 = \frac{I_2}{I_1} B_1 \qquad (6.2b)$$

In figure 6.3 it is shown the field map for the case of 1kA and in table 6.2 we reported the range of values for the field in the different positions in correspondence to the color legend in the figure ([16], [17], [18]).

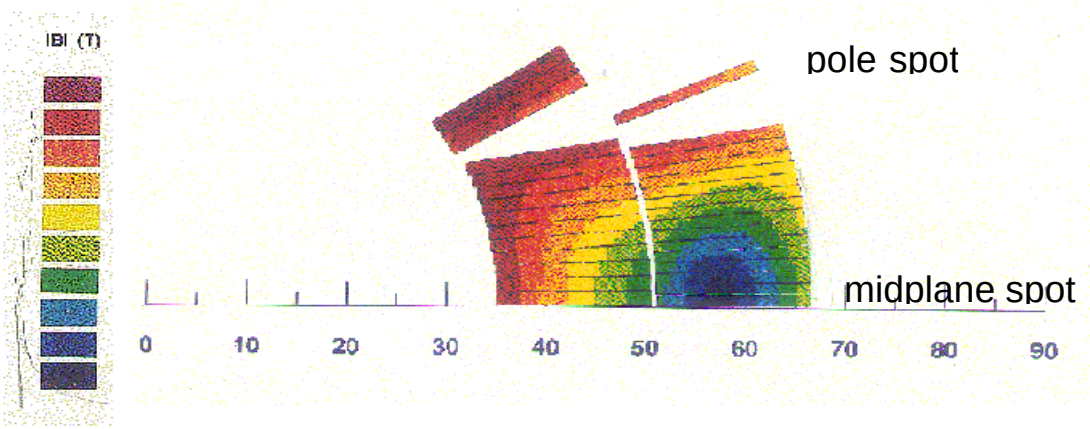

Fig. 6.3 Field map for HGQ model at 1kA.

Table 6.2 Field values in different positions of the coil at 1kA ([16]).

	B (T)	B (T)
Dark red	0.64664	0.71673
Red	0.57656	0.64664
Orange	0.50648	0.57656
Dark yellow	0.43639	0.50648
Yellow	0.36631	0.43639
Light green	0.29622	0.36631
Green	0.22614	0.29622
Light blue	0.15605	0.22614
Blue	0.08597	0.15605
Dark blue	0.01589	0.08597

In figure 6.3 we reported also the possible positions of the spot heater. One is the region at high field (straight section in high field region) while the other one is in the low field position (midplane position on the end section). For magnet HGQ05 we used the outer pole spot heater (high field) on coil Q1, for magnet HGQ07-8-9 we used outer midplane spot heaters (low field) in coil Q2, Q1 or Q4.
In table 6.3 we reported the averaged field for different currents for these two cases.
In figure 6.4 we can see the difference in slope and field in the two positions while the third curve reported data analysis made on magnet HGQ05 as explained later.

Table 6.3 Calculated field values as a function of current and position.

	Outer pole	Outer midplane
I (A)	B (T)	B (T)
1000	0.53	0.10
2000	1.07	0.21
3000	1.60	0.31
4000	2.14	0.41
5000	2.67	0.52
6000	3.21	0.62
7000	3.74	0.72
8000	4.28	0.83
9000	4.81	0.93
10000	5.35	1.03
11000	5.88	1.14
12000	6.42	1.24

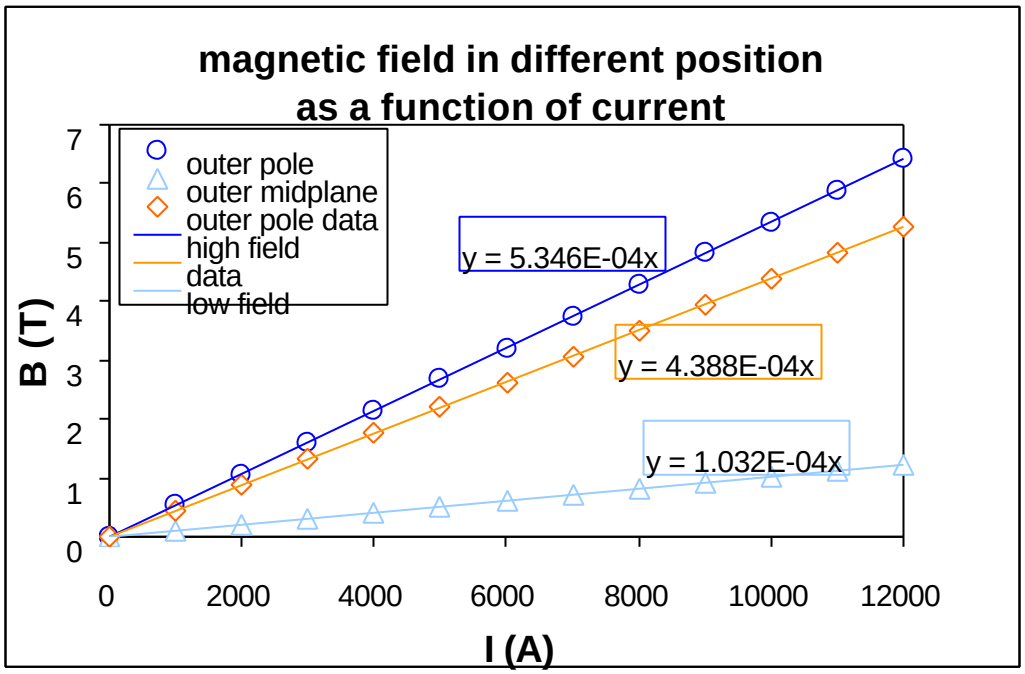

Fig. 6.4 Field calculation for different position in the magnet. In the plot we have three different curves. We analyzed the two different positions for a spot heater: outer pole, in which we calculated the field as a function of current in high field position; outer midplane, in which we calculated the field as a function of current in low field position. The third curve is based on data analysis for HGQ05 in which, via resistivity of a segment quenched at different currents, we estimated the transfer function (used for field calculation).

Another way to estimate the field is to calculate directly from the data the transfer function. In fact we can look from data at the resistance profiles of the segment where the spot heater is seated and

estimate the total resistance, which is the sum of the magneto resistance contribute and the resistance of the cable itself. In the case of a spot heater in the pole turn, where the field is higher (quench velocity is higher because proportional to the field), a sudden change in resistance can be seen and one can extrapolate the value of resistance when both contributions are important. With this value at different current one can extrapolate a line, which has as intercept the value of magneto resistance and so estimate the RRR.
In particular we have ([1; chapter 6]):

$$\frac{R_{300K}}{R_{1.9K}} = \frac{r_{300K}}{r_{1.9K}} \qquad (6.3)$$

but

$$R_{1.9K} = \frac{l}{A}(r_{RRR} + KI)$$
$$R_{300K} \cong \frac{l}{A} r_{300K} \qquad (6.4)$$

so

$$r_{RRR} = \frac{R_{1.9K}}{R_{300K}} r_{300K} - KI \qquad (6.5)$$

with

$$K = c \cdot T_f \qquad \text{where} \qquad c = 4.5 \cdot 10^{-11} \Omega \cdot m/T \quad ([1]) \qquad (6.6)$$

Unluckily we could use only the data from magnet HGQ05 because in other magnets the spot heaters are in a low field region and the signal is not clear enough to extrapolate the values of resistance because the contribute from magneto resistance is much lower.

For magnet 5 the measurements are reported in table 6.4:

Table 6.4 Resistance measurements for spot events for HGQ05.

I (A)	**$R_{1.9K}$ (Ω)**	**$r_{1.9K}$ (mΩ)**
5000	1.3777E-06	2.5458E-10
5000	1.4369E-06	2.6551E-10
9000	1.8305E-06	3.3824E-10
10000	1.9815E-06	3.6614E-10
11000	2.0742E-06	3.8328E-10
12000	2.1174E-06	3.9125E-10

With

R_{300K}=92μΩ (directly measured)
ρ_{300K}=1.7·10^{-8}Ωm

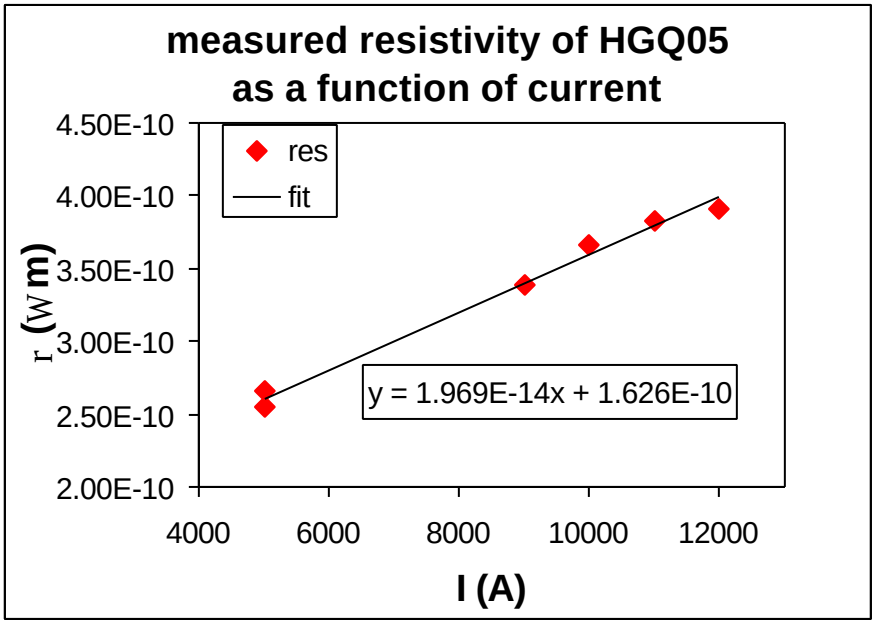

Fig. 6.5 Measured resistivity of a segment quenched at different currents in HGQ05. These data enable to calculate the transfer function necessary to calculate the field as a function of current.

We can conclude that

$K=1.969\cdot10^{-14}\ \Omega/A$
$T_f=0.0004388T/A$

Extrapolating the line to I=0A we can find ρ_{RRR} and we can estimate the RRR value for our magnet

$$RRR = \frac{r_{300K}}{r_{RRR}} = 105 \qquad (6.7)$$

With this transfer functionwe calculated again the field as a function of the current (eq. 6.2a) and we plotted it with the other two cases in figure 6.3.
We should observe that the value of RRR is not the one found experimentally, which is around 90. The uncertainty on estimation of this quantity is due to the fact that the measurements to do are not easy and an unknown difference in temperatures in the magnet during this test can change the value of RRR. We have to observe also that the RRR value for the magnet is a value known in 15-20% and this parameter was not reproducible in test of short models (see table 6.5) because different curing cycles were used but in production this uncertainty should be much less. We will simulate cases with magnets with different RRR values in order to see how is crucial this parameter.
In table 6.5 we reported the measured values of RRR for the different coils of different magnets (*I* inner layer, *O* outer layer):

Table 6.5 RRR values for inner and outer layers for different HGQ models. For HGQ07 two sets of measurements were taken.

magnet	RRR_{Q1I}	RRR_{Q2I}	RRR_{Q3I}	RRR_{Q4I}	RRR_{Q1O}	RRR_{Q2O}	RRR_{Q3O}	RRR_{Q4O}
HGQ05	143	158	134	153	90	92	89	87
HGQ06	151	147	157	150	154	155	160.5	158
HGQ07	133	149	137	149	158	143	156	143
	133	149	137	150	159	144	157	144
HGQ08	Data scatter between 3 values					116 128 140		
HGQ09	155	157	153	156	194	195	192	195

After developing the calculation of MIITs (as a function of RRR and field as shown in chapter 4) we used data from all the magnets in order to see if our calculation could estimate peak temperature which match with data. During the test the peak temperature is estimated by comparing the measured resistance of the segment with its room temperature values as we already explained in chapter 4.
The results obtained for the spot heater events in various model magnets (supposing for each of them the RRR values reported in table 6.5) are summarize in table 6.6 where we compared peak temperatures predicted with adiabatic method and measurements taken during tests:

Table 6.6 Calculated and measured peak temperatures for different HGQ and RRR (we used different RRR values of table 6.5 for different model magnets in order to calculate this peak temperatures). For HGQ09 we used different peak power density and position of spot heater. The difference in temperatures for the two positions Q1O and Q4O (at the same current values) can be attributed to a variation in turn to turn quench propagation in the coil ends near the spot heater. Slower propagation increases MIITs and temperatures.

magnet	I (A)	MIIts ($10^6 A^2 s$)	T_{calc} (K)	R (mW)	T_{meas} (K)
HGQ05	3000	8.30	75	3.80	47
	6000	13.60	165	30.40	127
Q1O pole	7000	14.60	186	40.00	154
R_{300K} (mW)	8000	15.40	205	50.00	184
92.0	5000	12.27	131	19.80	98
	5000	12.30	131	20.16	99
	9000	15.86	231	56.72	204
	10000	16.24	242	62.11	219
	11000	16.38	247	64.96	226
	12000	16.36	261	67.55	232
HGQ07	3000	10.98	80	5.00	60
	5000	16.51	153	28.56	132
Q2O mid	6000	17.70	207	41.60	174
R_{300K} (mW)	7500	20.42	289	62.47	239
83.2	8500	21.17	319	69.51	259
	10000	21.69	340	79.25	288
	12000	21.81	346	86.83	312
HGQ08	3000	10.88	86	3.36	50
	5000	16.24	160	16.45	95
Q1O mid	7000	19.45	271	38.13	162
R_{300K} (mW)	9000	20.98	329	62.58	239
83.2	10000	21.68	360	70.83	263
	12000	22.03	376	79.29	288
HGQ09	3000	13.48	97	4.44	57
	5000	19.92	205	30.00	137
Q1O mid	7000	22.50	355	63.79	243
R_{300K} (mW)	8000	23.37	397	80.34	291
83.2	9000	23.77	418	92.83	332
	7000	22.02	334	58.89	228
	9000	22.67	363	84.66	304
	10000	23.28	392	94.82	339
	12000	23.14	385	106.60	379
Q4O mid	7000	19.62	246	34.19	149
	10000	20.87	288	51.89	208

In figure 6.6a we reported the peak temperature values estimated and measured.

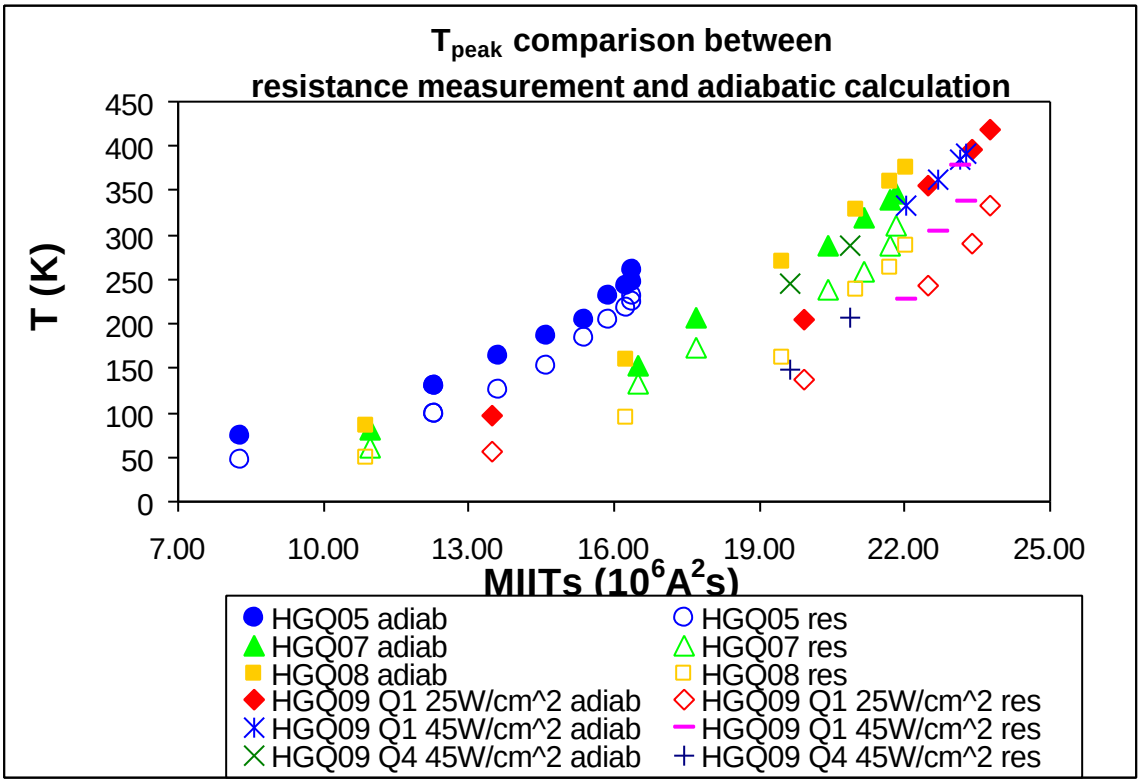

Fig. 6.6a Comparison between peak temperature values calculated with adiabatic method (solid symbols) and values measured (open symbol). For HGQ09 three different series are reported (one with quench induced in Q1 with peak power density 25W/cm^2, one with quench induced in Q1 with peak power density 45W/cm^2, one with quench induced in Q4 with peak power density 45W/cm^2. For measurements higher the peak power, higher the peak temperature (higher energy deposited) but in the adiabatic model this parameter is not included since it considers only the total amount of MIITs collected independently from the energy released from the heaters.

From this plot one can clearly see that the highest temperatures are reached in low field position where the quench ha a slower quench velocity (in fact the MIITs values collected are higher since current decay is slower).
From this figure we can see that the adiabatic method, as expected, overestimates systematically peak temperatures values even if each group of estimated temperatures has the same trend of its correspondent measured group. From this data analysis we can conclude that adiabatic method overestimates the peak temperature values of a factor 20-25%.

We can also report the calculated values and the measured ones on the same plot where we reported also MIITs curves for different field for a fixed RRR (the estimated value for magnet 5 is 100) (figure 6.6b). The set of measurements is peak temperature values of spot heater events for magnet HGQ05 (blue triangles) and the calculation made with MIITs method (red dots).
Clearly the calculated values lay on a specific MIITs curve depending on the field (which change with current) so that for lower current (lower MIITs collected because the heat developed is less) the red dots lay on low field curve while for higher current the lay on high field curve (the highest field reached in this position is ~6T).
We can observe that the measured values follow exactly the same trend, except that they have systematically lower values of at least 20-25%.
In order to follow the same trend the data had to change the scale by 25%.

This scale factor will be introduced as **EMPIRICAL STEP** (based on data analysis) in our simulation so that from a MITTs value we calculate a temperature and we scale it by 25% in order to reproduce a real situation.

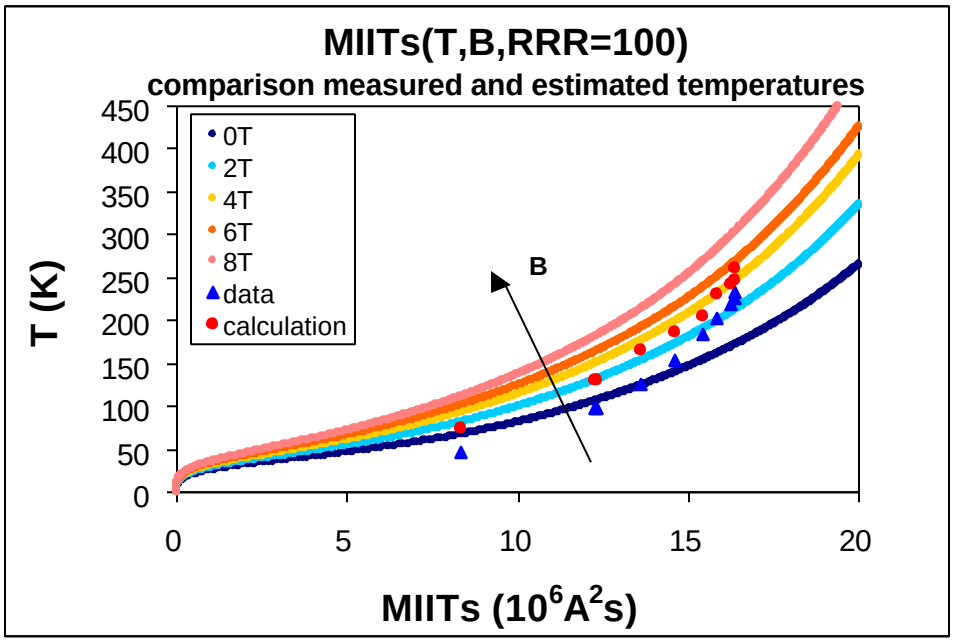

Fig. 6.6b MIITs curves as a function of field and temperature at fixed RRR=100 (similar to RRR of HGQ05). In this plot are reported the actual measurements taken in HGQ05 (blue triangles) and its corresponding calculation from MIITs(T) (red dots) . MIITs calculations and measured values would overlap if we scale down the temperatures calculated from MIITs method by 1.25. The curves reported are the same curves of fig. 4.4 with the axes inverted.

As one can see the temperatures in the real data are less than the ones expected with MIITs calculations.

This is due to several things:

- MIITs method is an adiabatic method and does not consider the effect of the cooling channels and the beneficial effect of liquid helium so the temperatures are overestimated
- heat capacity is an average between two methods and still probably is underestimated
- in these calculations we considered current and field constant but in a real test once a quench occurs the current decays exponentially and the field reduces with the current. In the estimation of peak voltage and temperature for the system Q2a/Q2b we will consider the change in time of these quantities
- the field is an averaged value calculated without considering any saturation effect that can help to reduce the field and consequently the peak temperature

The aim of the simulation is to predict peak temperatures and peak voltages in within 15/20% so that after this preliminary analysis we decided to apply a scale factor on the temperature values of **1.25** in order to better match the real results using an adiabatic method.
Another tool we needed for our analysis is the quench velocity so that we could estimate the different starting time in the different position of the magnet and the length covered from a quench in a certain interval of time.
Once again we used data from magnet 5 to estimate quench velocity because it has the spot heater in the position more probable for a quench to occur (pole position).

In particular we used the spot heater events for magnet 5 at different currents. The quench starts in the segment 16m-16n in outer coil 1 and we considered the time when it reaches the segment 16d-16c and knowing the distance between these two points and the interval of time we calculated the velocity i.e. ([21]):

$$v_{quench}(I) = \frac{l_{16m-16d}}{(t_{spot} - t_{16d-16c})(I)} \qquad (6.8)$$

Table 6.7 Measured quench velocity estimated with induced quenches at different current in HGQ05.

I (A)	$t_{16n-16m}$ (ms)	$t_{16d-16c}$ (ms)	v_q (m/s)
5000	-134.4	202.0	4.71
5000	-135.8	204.8	4.66
9000	-31.5	40.6	22.00
10000	-22.7	25.8	32.70
11000	-16.3	17.9	46.37
12000	-11.9	14.4	60.30
3000	-406.2	372.0	2.04
5000	-134.6	200.0	4.74
6000	-88.9	151.4	6.60
7000	-62.0	107.1	9.38
8000	-44.8	66.6	14.24

From these data points we extrapolated values for all the other currents as shown in figure 6.7.

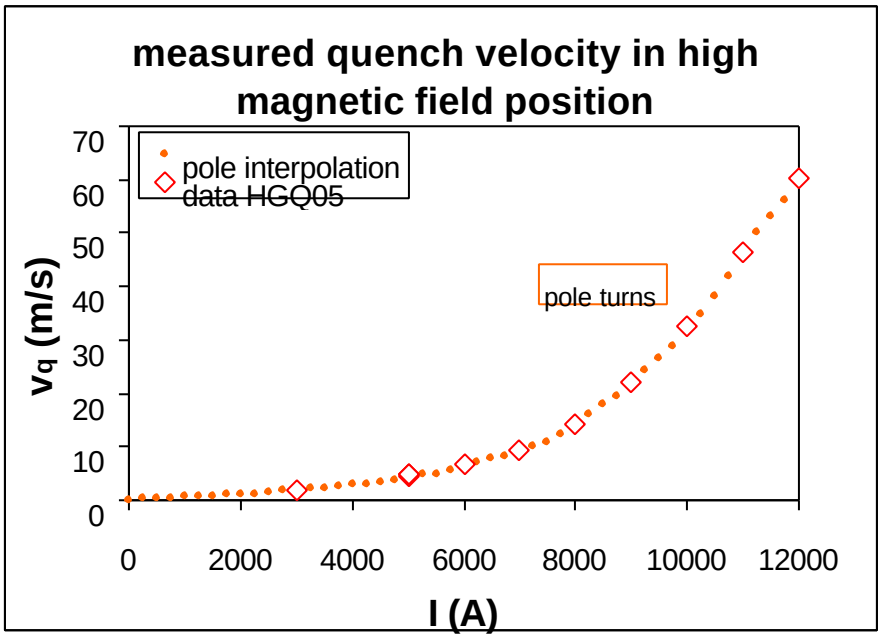

Fig. 6.7 Measured quench velocity and estimated quench velocity for high magnetic field position as a function of current. The velocities were measured with model magnet HGQ05.

Another important thing which emerged from the data analysis of the short models and supposed in our simulation is the existence on **quench-back phenomenon**, which was visible for all the model magnets HGQ05-09 (we will show the analysis made for the last two). In particular we considered events called “manual trip”, which as explain already in chapter 5 are events where the heaters are fired at t=0ms even if they become effective after a certain amount of time. We analyzed several events in order to estimate the starting time for evidence of resistance growth for each segments in the magnet. In particular we considered:

- for HGQ08 we analyzed two events at 12000A. One is with the standard configuration for strip heaters (H1&H3 or H2&H4 hooked up) where each quadrant is half covered and the other one is an unusual case (H2&H3 hooked up) where the coil Q1 is fully covered while Q3 is without coverage
- for HGQ09 we analyzed manual trips with the standard configuration but at different currents (12000A, 10150A, 5800A, 2900A)

We measured the starting time in collecting resistance for all the segments in the magnets (each layer has several voltage taps used to measured voltage across two points). To calculate these times we take the voltage signal and I_{dot} signal. After subtracting off the offsets for both of them we subtract also the inductive part ($L*I_{dot}$) so we get only the resistive part and we can find the time when this resistive growth starts. In figure 6.8a,b,c we reported the actual measurements made on these model magnets.
First we reported (fig.6.8a) a manual trip event for magnet HGQ08 at 12000A with the standard configuration for strip heaters (H1&H3 or H2&H4 hooked up) where each quadrant is half covered

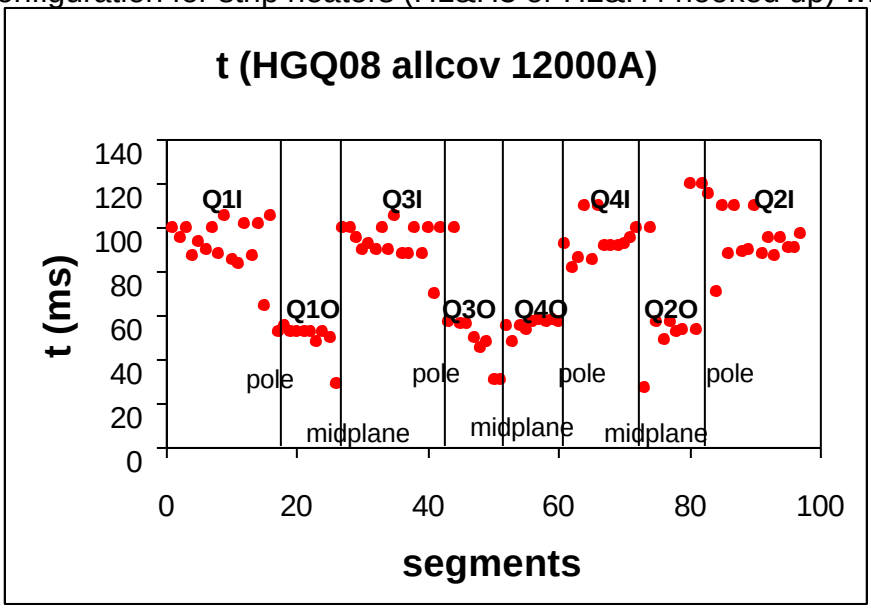

Fig. 6.8a Manual trip HGQ08 12kA all quadrants half covered (two opposite heaters are hooked up in series).

We can observe several things from this plot:

- the heaters are on the outer layer in fact the outer layer (Q1O-Q4O) start to quench around 30ms (time when heaters become effective) and the quench propagates all around one layer in 20-25ms.
- even if the inner layers (Q1I-Q4I) do not receive directly the heat from heaters after a certain amount of time (~85-120ms) we observe quenching also in these layers (the heat arrives in the inner layers by propagation of the quench and heat transfer through the helium).
- in outer coil segments we can see that heat propagation is faster in midplane segments (low field region) where the strip heaters are seated.

- we observe the same trends in all the layers even if they are not all directly coupled (all the layers respond in the same way to heat propagation)

If we report now the similar study made for HGQ09 (manual trip in standard condition at 12000A fig. 6.8b) we have:

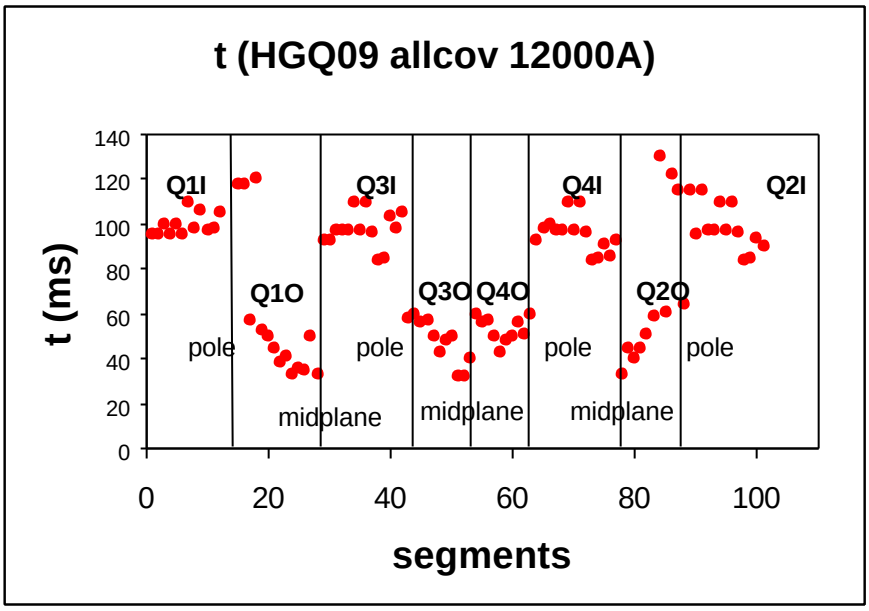

Fig. 6.8b Manual trip HGQ09 12kA all quadrants half covered.

The conclusions are the same as for plot 6.a (heaters effective from ~30ms, outer layers quench between 30ms and 60ms, inner layers between 85ms-120ms). We did similar studies for HGQ09 at different current and as expected for lower current the time to develop resistance grow but in all the events we observed similar trends (quenching of outer layers first and then inner layers).
In figure 6.8c we report a case for HGQ08 in which we hooked up two consequent heaters (H2&H3) so that Q3O is not covered by heaters and Q1O is completely covered (see fig. 6.2).

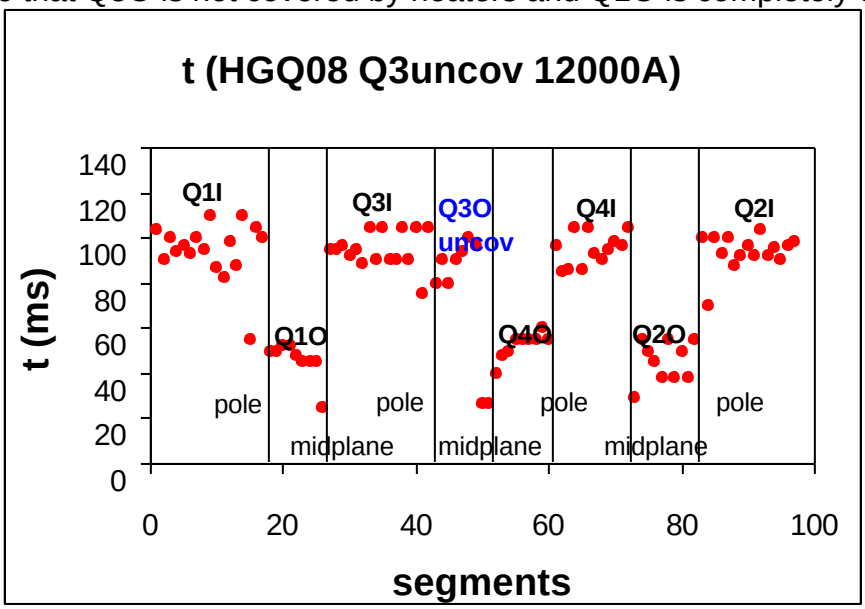

Fig. 6.8c Manual trip HGQ08 12kA Q3 uncovered.

Also in this case we can observe that:

- outer layers Q1O-Q2O-Q4O quench between 30ms and 60ms (Q1O develops heat faster because the heaters covered completely the layer)
- inner layers develop resistance between 85ms and 120ms
- outer layer Q3O develops resistance at the same time as inner layers even if the heaters do not cover this quadrant

It has to be notice that in these events the heaters were powered in such a way the time constant was the same for both of them (and to simulate the final condition of LHC). Furthermore, it was previously shown (see chapter 5) that the difference in geometry for heater does not effect the results regarding quench propagation, peak temperature and voltage. Since the heaters cover only outer layers one would expect to see resistive growth only in outer layers and not in inner layer (considering quench propagation, beneficial effect of helium and sheet of insulation between inner and outer layer we expected a resistive growth much later). Moreover in the case showed in 6.8c we did not expect Q3O to quench at time of the same order as inner layers.
There are two possible explanation to interpret these results:

1. **quench back phenomenon** due to eddy currents (quench back is a second quench, which develops after the first one and starts from other parts of the magnet (before the first quench with propagation arrives there).
   This effect is related to **intrastrand** resistance, which is the same in both models since the relevant length is the "twist pitch" ~10mm for both models.
   This resistance is directly linked to eddy current effect in particular to the time of decaying of these currents is [26]:

$$t_{\mathrm{int}rastrand} = \frac{m_0}{2r}\left(\frac{l_{twist}}{2p}\right)^2 \qquad (6.9a)$$

   where l_{twist} is the twist pitch length of the strand (~10mm), r is the transverse resistivity of the copper-NbTi composite ($\tau_{\mathrm{interstrand}}$ ~10ms). The power dissipation is proportional to square of the magnetic field time derivative ([26] 7.3).

   Another factor which develops eddy-currents is **interstrand** resistance (cable coupling) which is 70 times higher for HGQ09 ($R_{\mathrm{isHGQ08}} \approx 1.5\mu\Omega$, $R_{\mathrm{isHGQ09}} \approx 100\mu\Omega$). This difference is due to different coil curing cycles used for the construction of these two models as well other measures in HGQ08 to reduce the copper oxidation on the strand surface. This interstrand resistance is directly linked to eddy current effect in particular with the following steady state time constant ([27]):

$$t_{is,cable} = C\frac{l_{transp}(N_s^2 - 4N_s)}{R_{is}} \qquad (6.9b)$$

   where l_{transp} (~100mm) is the transposition pitch length of the strand, N_S is the number of strands in the cable and C varies between $1.6\cdot10^{-8}$ / $1.7\cdot10^{-8}$ $\Omega m^{-1}s$. The time constant τ_8 for HGQ08 is ~1400 ms while the τ_9 for HGQ009 is ~20ms. In the steady state , time is much higher than τ_9 ($t >> \tau_9$), the heat generation ([26] 7.3) is proportional to the square of the magnetic field time derivative and inversely proportional to the interstrand resistance. In chapter 3, the significant dependence of the quench currents in HGQ08 compared to HGQ09 can be understood in terms of this phenomena. Thus we might expect a large heat generation in the 50-100 ms after a

quench is detected due the sudden decay in transport current and magnetic field. In the steady state, HGQ08 heat generation would be larger than HGQ09, but in the time regime of ~100 ms, less than 10 percent of the 1400 ms time constant, the generation of heat could be comparable.
Neither interstand nor intrastrand eddy currents fully explain the phenomena that all parts of the magnet seem to quench after a certain time, since there is considerable spread in fields strengths and directions throughout the magnet.

2. **sudden jump of the pressure** in the dewar which could develop a global temperature rise in the dewar (the pressure is even higher inside the magnet) and turns resistive most part of the layer. In these measurements a jump of about $\Delta p \sim 0.41$atm has been observed at the same time when the entire magnet quenches but it was not possible to verify if this pressure change can produce this effect.

Since this effect was not well understood we decide to apply in our model the worse case from protection point of view developing quench back later but supposing this effect which turns resistive parts of the magnet before the first quench arrives there.
This second quench is not dangerous from the point of view of peak voltage or peak temperature because the current decays exponentially when the first quench begins so that when this second develops the current is well below its initial value. The quench-back phenomenon helps to spread the heat much faster reducing the danger of failure of the magnets and reducing the protection margin needed otherwise. This assumption is based on the fact that in all model magnets we see the same effect even if models have different protection system and different curing cycle for the cables.

6.2b Simulation of events from short models

As already mentioned among the parameters to be studied for quench protection there are the peak voltage to ground for the Q2a/Q2b system and the peak temperature in a magnet after a quench occurs.
We measured the peak temperature and the peak voltage to ground of many model magnets. The peak voltage is defined as the running sum of the eight coil voltages starting from one terminal (which one is not important since after a quench the terminals are effectively shorted together)
The peak voltage to ground is a parameter necessary to set the Hi-Pot test, applied to all the magnets. In particular the Hi-Pot voltage is estimated to be twice the peak voltage plus 500V. A big uncertainty on peak voltage or an overestimate of it set difficult conditions to run this part of this test.
The problem was, then, to predict these two parameters for Q2a/Q2b system during LHC operation.
The main idea was to use data from our model magnets and then figure out all the critical parameters and create a model in which we could have changed these parameters and predict all the possible cases.
In an ideal magnet this prediction would be very simple because the voltage should be symmetric at every quarter coil. Any peak voltage would be generated from the differences in inductive and resistive voltage growth from inner to outer coil.
But, in a real magnet there are several factors, which can increase this voltage, to take in consideration.

For examples:

- **Spontaneous quench origin**. The quench occurs in a particular place in the magnet so one coil starts to develop resistance voltage first.
- **Variations in strip heater efficiency**. If resistance is not started at the same time on each quadrant, the resistance will not be the same from quadrant to quadrant even if measurements seem to show that the difference in starting time is less than 5-10ms at operating current of 12 kA. It is important to consider the possibility that the heater firing units could introduce similar delay.
- **Variation in RRR**. There can be variation in RRR both between inner and outer coils, between quadrant to quadrant and also magnet to magnet. The inner to outer coil RRR variation is usually large but it is not a problem because the outer coil develops most of the resistance due to the heater position. The other two kinds of variation are more important and need to be studied.
- **Failure modes**. In the normal LHC operation, Q2a Q2b will both have two circuits of heaters in operation in series. We should consider a possible case where one magnet has only one operational circuit, which should be safe from the point of peak temperature but it creates a resistance imbalance. Unluckily we did not take any data with two complete circuits firing but we did take data with different combinations of heaters firing so we should be able to extrapolate the parameters necessary to set up a model.

On our magnet, the heaters were located beyond the outer coil, and cover ¾ of the outer turns. The geometry of heaters is discussed in chapter 3 but we can recall the fact that heaters have longitudinal gap of copper between stainless steel.
When they are fired we should consider that only half of the real length quenches immediately but since typical quench velocities are of the order of 60m/s the time necessary to spread the heat over the entire length of the heater is of the order of 1 or 2ms. We verified that this difference in time does not affect the final answer for peak voltage and temperature so that under this condition it is reasonable to consider that when the heaters are fired they develop heat over their entire length and width.

What we did is:

- to develop resistance vs. time profiles for the magnets
- to generate voltages, current decays, MIITs with the resistance vs. time profiles
- to compare these profiles directly with data used also to find quench velocities and heat propagation
- to simulate resistance growth using our knowledge of field maps, heater coverage and the empirical spread of the quench across the magnet (parameters that can be varied in the model).

To simplify our first approach to this kind of analysis and understand step by step all the necessary things to use we decided to start with simulation of only one quadrant (Q1) of short magnet tested so that we could have a real comparison with data taken. In particular we decided to use the real time scale and current profile taken during data acquisition of the events we simulated.
To simulate the event we divided the quadrant considering more sections divided by their field. The outer layer is divided in three sections while the inner one in two.
Each section in the outer layer is divided in subsections (as shown in fig. 6.1) which collect MIITs starting from different time estimated with data analysis.
The characteristics of each section is summarized in summarized in table 6.8:

Table 6.8 Sections used for simulation of short models and their characteristics.

COIL	SECTION	FIELD@12kA B (T)	starting time to collect MIITs	L (mH)
INNER LAYER	turn 1-11	5.66	95ms	0.53
	turn 12-14	7.34	95ms	
OUTER LAYER	turn 1-3	1.87	48ms	0.81
	turn 4-13	4.40	33ms **heaters position**	
	turn 14-16	6.50	48ms	

Total length per turn	3.8 m
Length covered by half heater	1.705 m
Total inductance of the magnet	5.35 mH

We reported only the field at 12kA because the cases simulated were manual trip at this particular current and also in the simulation for the system Q2a/Q2b we considered spot heater events and manual trips at this current. As already said the heaters are close to the outer layer and their width cover 10 turns of the outer layer.

There are two main reasons to use this current:

- 12kA is the current needed to obtain the peak nominal gradient of 215T/m
- as we noticed in chapter 5 for short models measurements of peak voltage showed that this quantity increases with current (fig. 5.9). In literature one can find studies that showed that the peak of this quantity is reached around 80% of sample limit (in our case the 80% is 12kA). With current beyond 80% of I_c the magnet is too close to critical surface in order to have problems in case of a quench (the time to collect MIITs is largely reduced). So the case of 12kA is the most dangerous and critical case to be considered (with our model we verified that at lower current we were well below dangerous values).

In the simulation, each section is subdivided in three subsections. The first one starts to collect MIITs at t_1 and in each interval time we numerically integrate MIITs value which increases with time until the current is not negligible. Once this subsection started it is independent from the other in collecting MIITs and resistance. After a certain amount of time evaluated with data another subsection turns resistive (an entire piece of cable with length equal to the distance covered by the quench from the position it started). So each subsection acts independently from the others and collects its MIITs and resistance. The sum of resistances of all the subsections is needs to calculate the total resistance of the magnet and the current decay (exponential decay with L/R equal to the total inductance and the total resistance of the magnet).
To explain in equations the process lets consider a particular subsection.
The MIITs increases at each time step with:

$$MIITs(t_2) = MIITs(t_1) + I^2(t_2)\Delta t \qquad (6.10)$$

where $I^2(t_2)Dt$ with current expressed in kA.
Once we have this values of MIITs as a function of time with our tables (they consider MIITs as a function of different RRR and field) we can calculate the temperatures related to every value of MIITs for every step so we get the temperature profiles in time (temperatures are scaled by a factor 1.25). With temperatures from tables of resistivity as a function of temperature, RRR and field we can find resistivity.

When a subsection starts to collect MIITs an entire piece of cable of known length (estimated considering quench propagation) turned resistive so that we can calculate resistance profiles (from resistivity) and so resistive voltage profiles and total voltage profiles of the coils (because inductive contribute is simply the product of the inductance of the coil times the time derivative of current). Supposing that at t_1 the magnet is still superconducting (MIITs(t_1)=0, T(t_1)=1.9K) and the first resistive segment of known length (equal to spot heater length) quenches at t_2 with a initial current $I(t_2)$ we have:

$$t_2 \Rightarrow I(t_2) \Rightarrow MIITs(t_2) = MIITs(t_1) + I^2(t_2)(t_2 - t_1) \Rightarrow T(t_2) \Rightarrow r(t_2) \Rightarrow R(t_2) \Rightarrow V_{resistive}(t_2)$$
$$t_3 \Rightarrow I(t_3) \Rightarrow MIITs(t_3) = MIITs(t_2) + I^2(t_3)(t_3 - t_2) \Rightarrow T(t_3) \Rightarrow r(t_3) \Rightarrow R(t_3) \Rightarrow V_{resistive}(t_3)$$

and so on until we arrive at 1 second (the standard window to collect data is between –1second to 1second) when the current is negligible and MIITs value stays constant.

The resistive voltage is the total resistive voltage across the outer layer and inner layer so we have:

$$\begin{aligned} V_{resistiveouter}(t) &= \sum_{sections=1}^{3} \sum_{subsec=1}^{3} R_{s,p} I(t) \\ V_{resistiveinner}(t) &= \sum_{sections=1}^{2} \sum_{subsec=1}^{3} R_{s,p} I(t) \end{aligned} \Rightarrow V_{totalresquadrant} = V_{resistiveouter}(t) + V_{resistiveinner}(t) \qquad (6.11)$$

The total voltage across one quadrant is then:

$$V_{quadrant}(t) = V_{resistivequadrant}(t) + V_{inductivequadrant}(t) \qquad (6.12)$$

where

$$V_{inductivequadrant}(t) = L_{innerlayer} \frac{dI}{dt}(t) + L_{outerlayer} \frac{dI}{dt}(t) \qquad (6.13)$$

where the inductance is the sum of mutual-inductance and self-inductance of the quadrant and it is considered constant. These values were measured for the short model and are reported in table 6.8. It has to be notice that while the outer layer was subdivided in small subsections in order to follow quench propagation; the inner layer was divided with less sections since this layer becomes resistive at a certain point but its main contribute is inductive (resistive part is ~80% less than outer contribution).
This division does not permit to simulate perfectly the inner layer resistance and resistance voltage as a function of time but we are interested more on effects on outer layer where a quench can be dangerous.

- The easiest case to simulate is the one with a coil completely covered by the heaters because in practice all the resistive part is coming from the block of heaters.

After the heaters are fired (they are fired at t=0ms but they become effective around 33ms as one can see from data acquisition) the quench quickly cover the entire coil.
In this first simulation we decided to use the real current and real current change in time (I_{dot}) recorded from data acquisition. This choice was made in order to understand better the limits of our model and overall, to see if we were able to predict resistance and voltage profile only from MIITs calculations.

This was the case of a manual trip (the heaters are fired and we simulated a quench induced by the heaters) in magnet **HGQ08** at the starting current of **12000A** in which Q3O was completely uncovered while Q1O was double covered (H2&H3 hooked up). As reported in table 6.8 the section covered by the heaters starts to develop heat at 33ms and the other section start 15ms later (time estimated from data). As seen the magnet quenches entirely in 110ms and in particular outer layer is quenched by 60ms and inner layer in 110ms. We used these intervals of time measured directly from data to better simulate the event. Our simulation for Q1O and Q1I gives results for resistance profile and resistive voltage shown in figure 6.9a and 6.9b where they are directly compared with the actual data.
As one can see the error between the simulated profile and the real one is of the order of 8% even if we scaled the temperature by a factor 1.25. In this case, we made the big assumption to use the real signal for the current and we simulated only one quadrant.

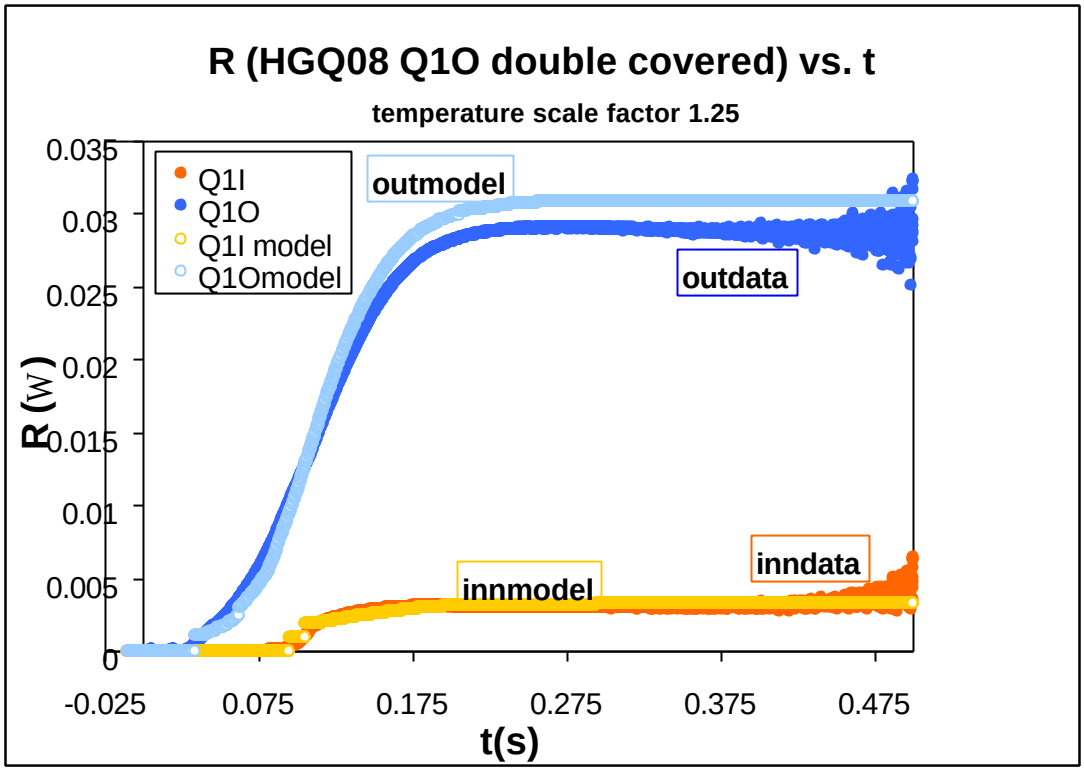

Fig. 6.9a Simulation and data of resistive profile for quadrant 1 (HGQ08). The scattering of data on resistance profile is probably due to the fact that the current is almost negligible and the voltage is comparable to noise.

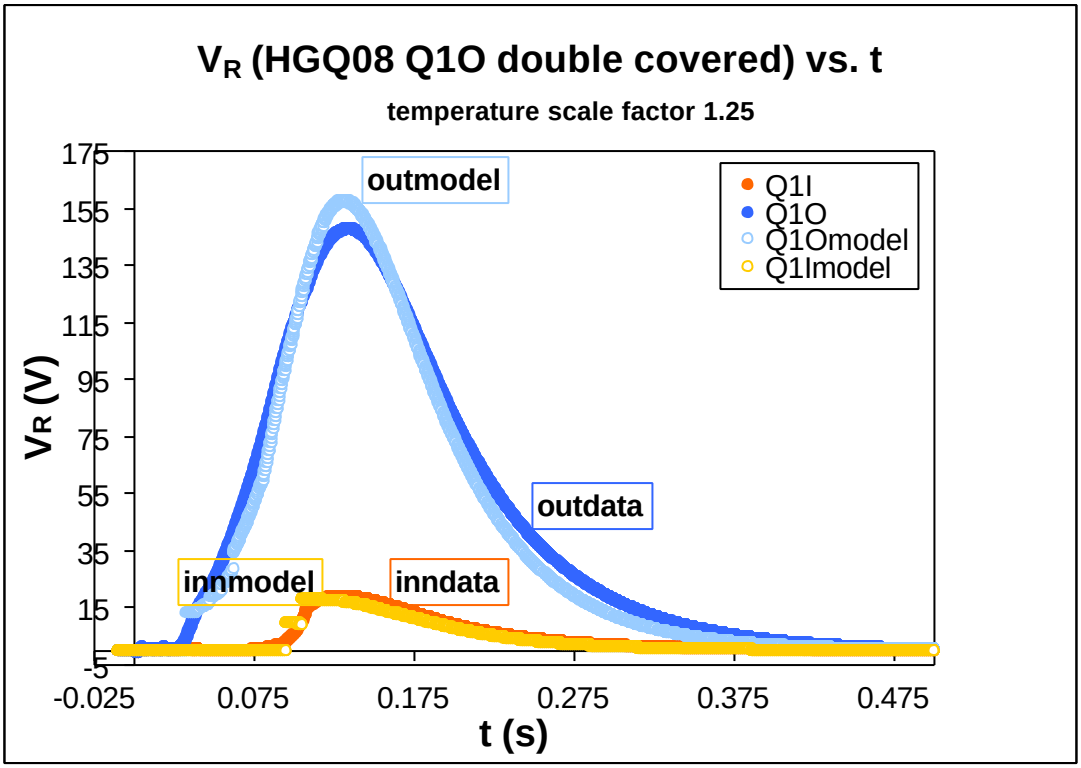

Fig. 6.9b Simulation and data of resistive voltage profile for quadrant 1 (HGQ08). The simulation of inner coil is not crucial for the final result so that the inner coil is divided in bigger subsections and the quench propagation has no need to be simulated with precision.

- The next step we made to improve our model was to simulate a standard situation of short model (in particular a manual trip at **12kA** for **HGQ09**) in which the heaters cover only half quadrant (H1&H3 hooked up). In this case we divided the magnet again in 5 sections but we considered a bigger window of time for the propagation of the quench because the length to cover is longer since the heaters quench only half coil. In this case each section in the outer coil is divided in 6 subsections (separated again by an interval of time of 7ms). As one can see from figure 6.8b in this event the time for the quench to develop entirely in an outer coil is higher than for HGQ08 so that in our simulation we supposed the outer coil is completely quenched around 70ms instead of 60ms as in the previous case. The propagation of a quench is not easy to simulate but with the help of data we could obtain the profile for quadrant Q1 of this event. The error, as one can see from figure 6.10a and 6.10b, is of the order of 15% (the final estimate of peak temperature and voltage is expected to be inside this error).

In this case we tried to simulate the current profile in fact we can suppose an exponential decay with the time of the current so we have:

$$I(t_2) = I(t_1)\exp((-\frac{L_{magnet}}{R(t_1)})(t_2 - t_1)) \qquad (6.14)$$

where L is the total resistance of the magnet while R is the resistance developed in the magnet (sum of all contributions of the subsections) during the time (so that $R(t_1)$ is needed to calculate $I(t_2)$).

In this simulation we considered the all the quadrants half covered and each quadrant is equal to the other so that $R(t)=4*R_{Q1}(t)$. Probably this affects the final result because the coils are not exactly equal and in particular they can have different reacting time in developing resistance.

In figure 6.10a and 6.10b we reported the resistive profile and resistive voltage compared to the data for this particular event for one quadrant.
As one can notice the trend simulated is similar to the real one and the difference as already said it can be due to the fact that the current profile is different. In fact if we report the real current and the one calculated with the model in figure 6.11 we can see that the real current is falling slower at the beginning, then faster and again slower. The voltage profile reflects the same pattern (the model for voltage first is below the real one, then it is higher and again lower).
In fact if the current decay is slower the resistance growth is slower and so we have more time to collect higher values of MIITs. If it is faster the resistance growth is faster but at the same time the value of MIITs added at each time step is lower so that the overall resistance is comparable.

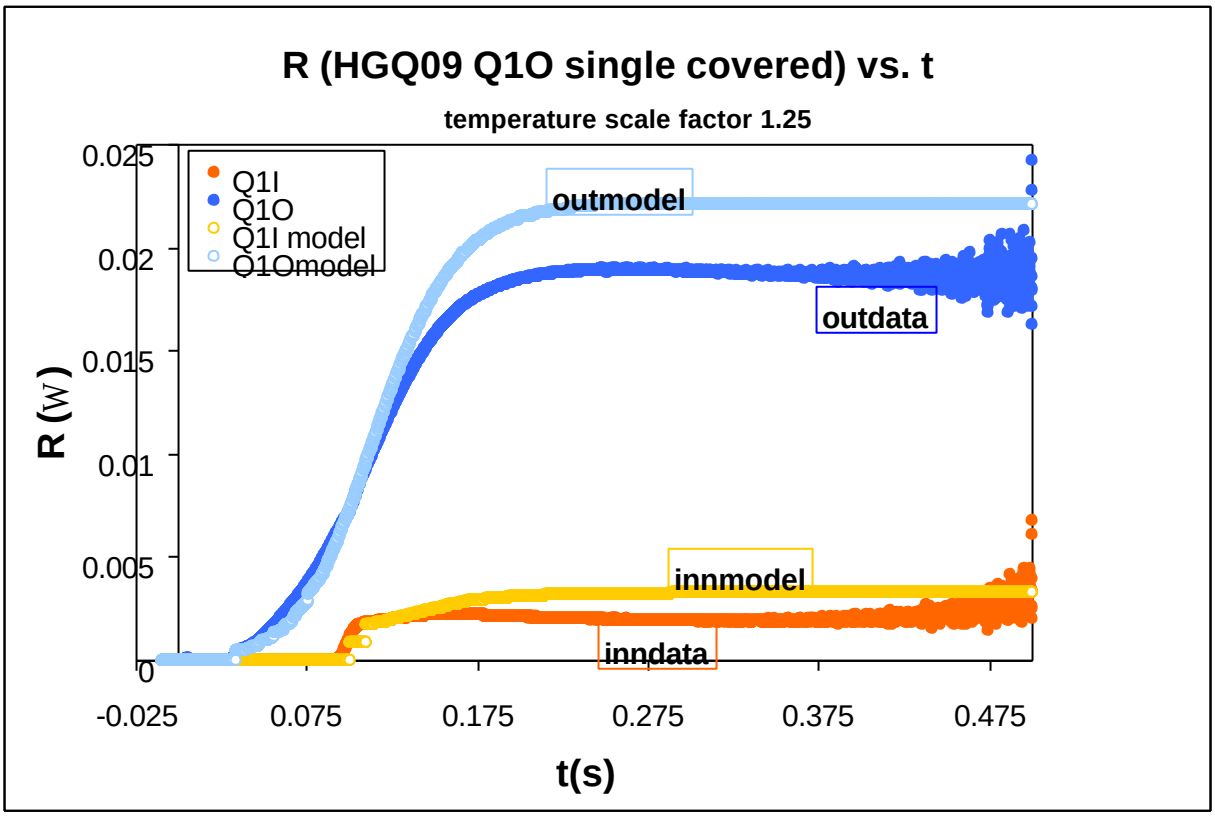

Fig. 6.10a Simulation and data of resistive profile for quadrant 1 (HGQ09). The scattering of data once the resistance reaches a plateau is due probably to the fact that current is negligible and the voltage is of the same order of magnitude of the noise.

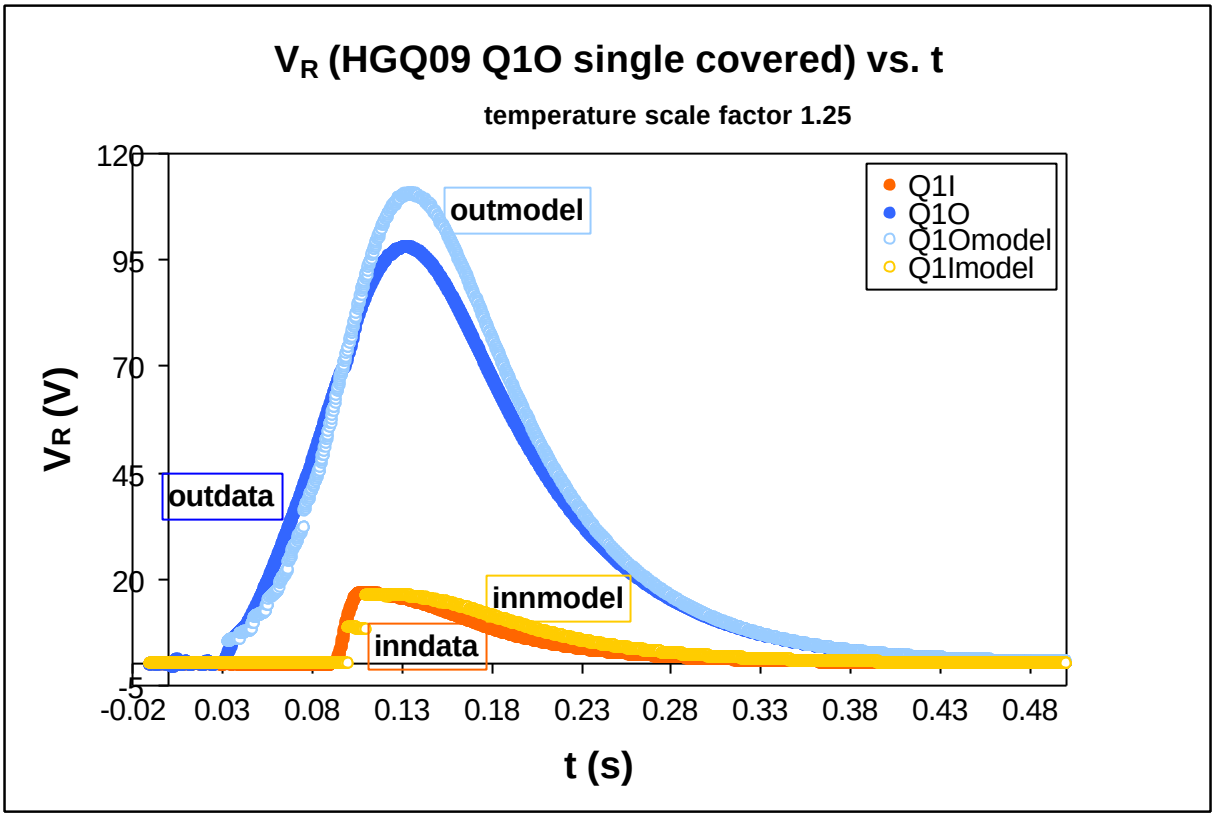

Fig. 6.10b Simulation and data of resistive voltage profile for quadrant 1(HGQ09). Also in this case the simulation of inner coil is not of great interest so that we did not use so many subdivisions in order to simulate quench propagation.

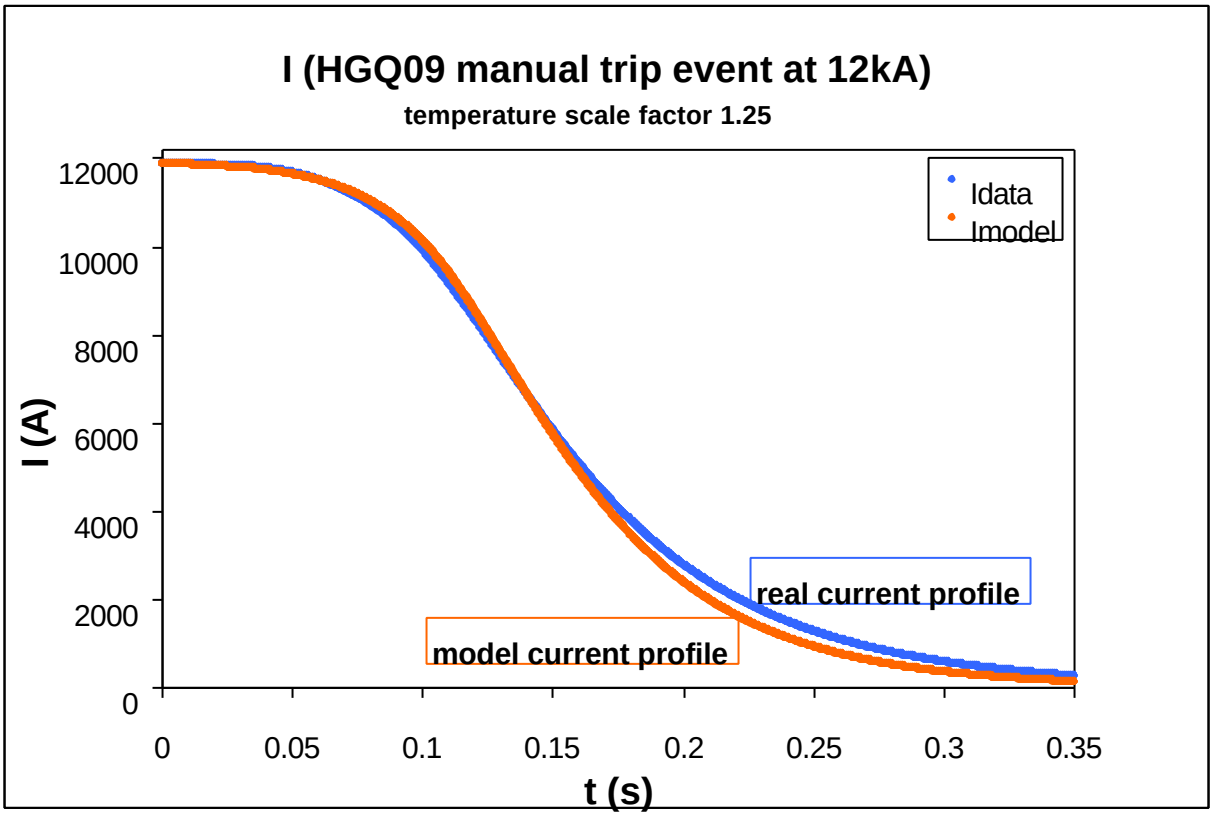

Fig. 6.11 Current profile from data and simulation (HGQ09).

Before going to simulation for the final system Q2a/Q2b we would like to summarizing the steps done up to this point:

- analyzing spot heater events of different model magnets we established a temperature scale factor in order to fit the overestimation of the adiabatic model (set to 1.25 for our simulation)
- we considered three manual trips events (from HGQ08 and HGQ09) and we calculated the time necessary for a quench to develop in every part of the magnet and we supposed the existence of quench-back effect (from data evidence)
- we developed the model simulating only one quadrant of two particular events of magnet HGQ08 (with one quadrant full covered by heater) and HGQ09 (with all the quadrant half covered) using appropriate parameters extracted from data analysis. We realized the necessity to simulate current profile and the entire system composed of four different quadrants but we could predict resistive voltage and resistance profiles inside the margin of error permitted on this simulations (the aim is to ESTIMATE peak voltage and peak temperature in a margin of 25% of error).

6.2c Parameters used for simulations in Q2a/Q2b system

Before entering in the details of simulation we would like to underline again why we need to do these analysis:

- first of all we want to verify that peak temperatures reached in the final system Q2a&Q2b do not reach dangerous values even under non standard conditions. The upper limit imposed for this quantity is **T<400K**.
- we want to build voltage profile in order to estimate the peak voltage to ground. The upper limit for this value is **V<400V** under standard condition. We have to underline that if this voltage is even higher when the magnets are at liquid helium temperatures it would not be a problem. The problem is that all magnets have to be tested at room temperature (Hi-pot test) at a voltage equal to 500V plus twice the value of peak voltage to ground in helium. If this value is too high the magnets have to be tested at room temperature at high voltage that can be dangerous for electronic instrumentation and for the magnets themselves (it is possible to create shorts before the magnets are cooled down).

In the final structure used for the simulation for the system Q2a/Q2b each section is subdivided in six further subsections (we tried to simulate better quench propagation subdividing the magnets in smaller but more parts) separated one to each other from an interval of time of 10ms to start to collect MIITs . We start to collect MIITs in the first subsection at t_1 (a length equal to the length of a spot heater becomes completely resistive). The process of colleting MIITs and then calculate temperature, resistivity, resistance is the same as in the previous section. The difference now is that we have two magnets 5.5m long each in series (the total inductance of one single magnet scale with length as the total resistance but the current decay depend on the total inductance and resistance of the system Q2a/Q2b).
The time step is now 1ms since its small enough to produce the profiles of interest. The process of quench evolution is the same used in the previous section, the only difference in this last simulation being that we produced step by step also the current profile and its derivative in time.
To calculate MIITs values and temperature profiles in time we used the same equations (from 6.11 to 6.14) of the previous section with the only difference that in this case the interval of time is 10ms and the magnet is divided in 5 section differently as reported in table 6.9.

Table 6.9 Sections used for simulation of full scale magnets and their characteristics

COIL	SECTION	FIELD@12kA B (T)	NOTE	L (mH)
INNER LAYER	turn 1-11	5.66	/	1.53
	turn 12-14	7.34	/	
OUTER LAYER	turn 1-5	1.87	/	2.33
	turn 6-15	4.4	heaters position	
	turn 16	6.5	/	

Total length per turn	11 m
Length covered by half heater	5.3 m
Total inductance of one magnet	15.44 mH
Total resistance of one magnet @300K	290 mΩ
Total resistance of one magnet @10K	9 mΩ

As previously said in this analysis we simulated also current and rate of change of the current as a function of time. In fact the current has again an exponential profile i.e:

$$I(t_2) = I(t_1)\exp((-\frac{L_{string}}{R_{string}(t_1)})(t_2 - t_1)) \qquad (6.15)$$

Where *L* is the total resistance of the string of two magnets (30.872mH) while *R* is the resistance developed in both the magnets during the time (so that $R(t_1)$ is needed to calculate $I(t_2)$). This resistance includes a constant resistance of the system, which drives the initial decay of the current. For our simulation we set this resistance as 1mΩ.

Now if we take the derivative of this expression we find:

$$\frac{dI}{dt}(t_2) = I(t_1)\left[\exp(-\frac{L_{string}}{R_{string}(t_1)}(t_2 - t_1))\right]\cdot(-\frac{L_{string}}{R_{string}(t_1)}) \qquad (6.16)$$

so that in equation 6.13 we can substitute this value to calculate the total inductive voltage in the string.

All our model works in this circular way starting from a fixed current and superconducting state and then developing resistance (used to calculate the new current) with a quench.

$$t_0 \Rightarrow I(t_0) = I_0 \Rightarrow MIITs(t_0) = 0 \Rightarrow T(t_0) \Rightarrow r(t_0) \Rightarrow R(t_0) = R_{system} \Rightarrow$$

$$I(t_1) = I_0\exp((-\frac{L_{string}}{R_{string}(t_0)})(t_1 - t_0)) \Rightarrow MIITs(t_1) = MIITs(t_0) + I^2(t_1)(t_1 - t_0)$$

$$\Rightarrow T(t_1) \Rightarrow r(t_1) \Rightarrow R(t_1) = R_{system} + R_{string}(t_1) \Rightarrow I(t_2)$$

In the next section we will summarize the results of our simulation.

Several conditions were tested in order to verify that the parameters concerning the protection were respected. We simulated two different kinds of events: manual trip events and spot heater event both at 12kA for reasons already mentioned.

Particular attention was posed on:

- different RRR values for the two magnets in the string
- different time efficiency of the heaters in different quadrants and between the two magnets
- different configurations of heaters in case of failure of the system
- calculation with a temperature scale factor 1.25 and with no scale factor for temperatures

Before computing the final results we tried to verify if the parameters set in our model were not affecting the results for the simulations:

- As already said in chapter 4 we decided to consider an average between two different sources for the specific heat and we verified that the difference in results for peak temperatures and voltages is well included in our margin of error and it does not affect significantly the results.
- We set the resistance of the system as 1mΩ. As said before this resistance drives the initial current decay but as soon as the magnet develops its own resistance this value can be disregarded. We verified that even if this value is doubled there is not significant change in results.
- In simulations of spot heater induced quench the length of the segment which quenches first is not well known. But, as said, the resistance in the system drives the initial decay and the resistance developed by this segment is very low in respect to the overall resistance so that the MIITs collected depend more on resistance developed by heaters than the spot itself. We can conclude that even a difference of 10mm in the estimate of this length does not affect results.
- We simulated a standard event (spot heater event with both magnets fully covered and same RRR value) at 9kA and we verified that under this case peak temperature and voltage values are well below condition of danger for the magnet.
- Even if we have an error on the estimation of the length of cable covered by the heater of 5/10% the results change by 1or 2% (in fact it changes the current profile so that the MIITs collected are the same).
- With a systematic error of 1T on the field in each part of the magnet the results change by 2/3%. Next step to improve the analysis done in this thesis should be to consider a changing field with current and not constant as considered in our model.

6.3 Simulations of different events and results

In these simulations several parameters were changed in order to study all the possible conditions in the real accelerator. In particular we considered two kinds of events:

1. **Manual trip events**, where the heaters are fired at t=0ms but become effective after a certain amount of time. In these simulations we are interested in peak voltage to ground developed in the string. We set different conditions in order to see how they affect the final results and in particular we studied:

- effect of difference in RRR between the magnets

2. **Spot heater events**, where a spot heater was fired in high field position next to the straight section of turn 16 (see Fig. 2.11) and the heater are fired after an interval of time chosen in relation to data taken with model magnets and considering that they should become effective after the voltage is above a set threshold of 500mV. In these simulations we are interested to peak temperature reached by the segment where the quench occurs and the peak voltage developed across the string. Also in this case we set different conditions to see their effect on results:

- effect of temperature scale factor
- effect of difference in RRR between the magnets
- effect of delay of the heaters
- complete failure of two circuit of heater in the same magnet
- earlier effect of quench back

LEGEND for plots reported in the next paragraphs

- **SC** coil half covered by heater
- **DC** coil full covered by heater
- **NC** coil NOT covered by heater
- the **number** reported in plots are the times when the heater circuits become effective

1. **Manual trip events**

- **effect of difference in RRR between the magnets**

In table 6.10 we report the results for simulation in which we studied the effect of RRR on peak voltage and in figure 6.12 we can visualize these results. In all these simulation the starting time for heaters to collect MIITs is 25ms. This value is estimated with data from model magnet HGQ05 even if the results do not change if this value is different because we would have only a constant shift in time scale.

Table 6.10 Peak voltage results as a function of RRR for manual trip events. Q2a/Q2b can have not only different RRR value but also the kind of coverage furnished by the heaters.

Q2a RRR	Q2b RRR	coverage Q2a	coverage Q2b	$MIITs_{heaters}$ (10^6 A^2s)	V_{peak} (V)
120	120	double	double	11.63	103
		single	single	12.69	94
		single	double	12.13	306

150	150	double	double	11.86	105
		single	single	12.92	95
		single	double	12.36	308
150	120	double	double	11.75	141
		single	single	12.81	132
		single	double	12.23	344
200	150	double	double	11.95	142
		single	single	13.02	127
		single	double	12.44	340

As one can see from figure 6.12 the difference in peak voltage due to difference of RRR value are not so evident. Even if for a fixed field and a fixed MIITs value lower RRR should give higher voltage, in our simulation we do not see this effect because the current decay is faster for lower RRR so that the final MIITs value is lower. So for RRR of 120 we get a lower voltage value because we have a lower amount of MIITs. The difference between Q2a=150;Q2b120 and Q2a=200;Q2b150 is once again not significant because in the second case the current decays slower so that the MIITs collected are higher but we have the same voltage because when RRR is higher the resistance is lower.
Also from figure 4.3 one can see that the effect of RRR is important between 0K and 60K. But in this range of temperature for a field of 4T (heater part) the magneto resistance dominates the resistivity value so that effectively there is no difference in resistance collected for different RRR. After 60K the resistivity is not longer dependent on RRR value.
The lowest value of peak voltage is for the configuration of heater half covered because we develop the lowest amount of resistance and imbalance between coils. But as we will see this configuration is worse for the peak temperature in a spot heater event.
The peak voltage, as expected, is much higher in the case the magnet are covered in different ways for examples one is half covered and the other one is double covered. In fact in this not symmetric case we have a big imbalance and the heat is spread more in one magnet than in the other.

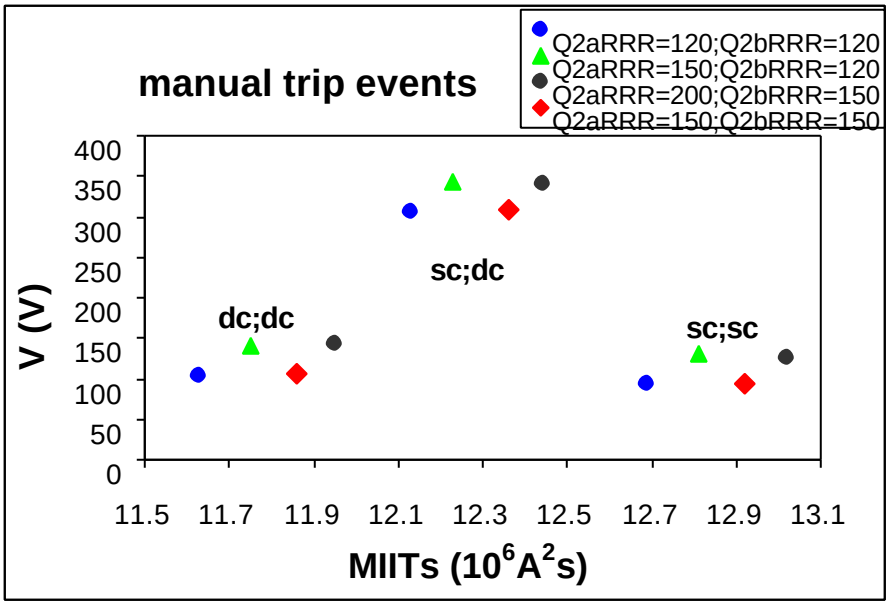

Fig. 6.12 Peak voltage as a function of RRR and coverage of the system Q2a/Q2b. The worst condition in these studies is when one of the two magnets has a failure in one of the heater circuits because this condition develops a high asymmetry of the system.

2. Spot heater events

Now we will consider cases of spot heater induced quench, which are more interesting from a point of view of peak temperature and peak voltage. These events are the more realistic situation of possible quench in the machine. In particular we simulated cases in which the quench starts in the **16th turn of Q2b outer layer 1** since it is a high field region (closer to critical surface) and the most probable part for a quench to occur.
We considered only cases at 12000A since is the current of operation in the machine and commonly the most dangerous for the peak values of temperature and voltage as already said before. We verified that the critical values were well below dangerous values simulating an event at 9000A.

- **effect of temperature scale factor**

In table 6.11 we report the results for peak voltages temperatures for spot heater events with different scale temperature factors. We considered both the magnets with a RRR = 120 and in each case we fired the heaters at 20ms. The quench starts in the **outer coil Q1 of magnet Q2b**.

Table 6.11 Scale temperature effect on peak temperatures and peak voltages (spot heater in coil Q1 outer of magnet Q2b).

temp scale	coverage Q2a	coverage Q2b	MIITs$_{spot}$(10^6 A^{2}s)	T$_{peak}$(K)	V$_{peak}$ (V)
1.25	double	double	17.03	236	128
1			15.50	244	155
1.25	single	single	18.10	271	128
1			16.57	278	149

As in the case of manual trip if we consider the complete adiabatic case (temperature scale factor is 1) the current falls much faster than if we scale the temperature so that the MIITs collected in the first case are lower and the temperatures differ only few percent. If we estimated the peak temperature with a fixed amount of MIITs we would reach much higher temperatures for the case completely adiabatic. This effect is clearly shown in figure 6.13 where we reported the current profiles for different scale factor for different RRR (see next simulation).

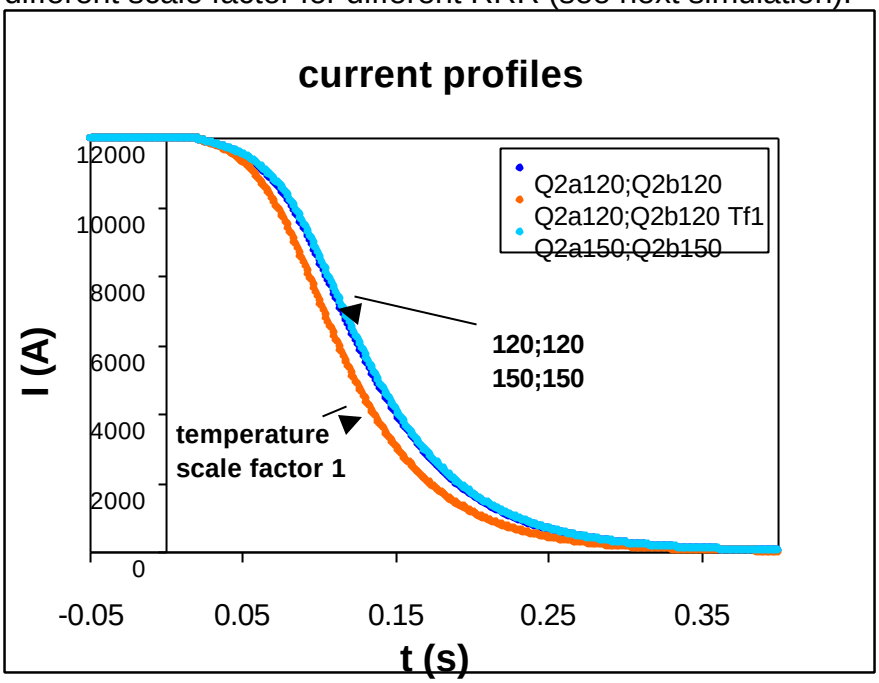

Fig. 6.13
Current profiles for different temperature scale factors and different RRR.
If the model is used without scaling temperatures (complete adiabatic condition) the current falls down faster because we develop more resistance. At the end, the MIITs collected without scale factor are reduced so that the peak temperatures of the two cases are comparable.

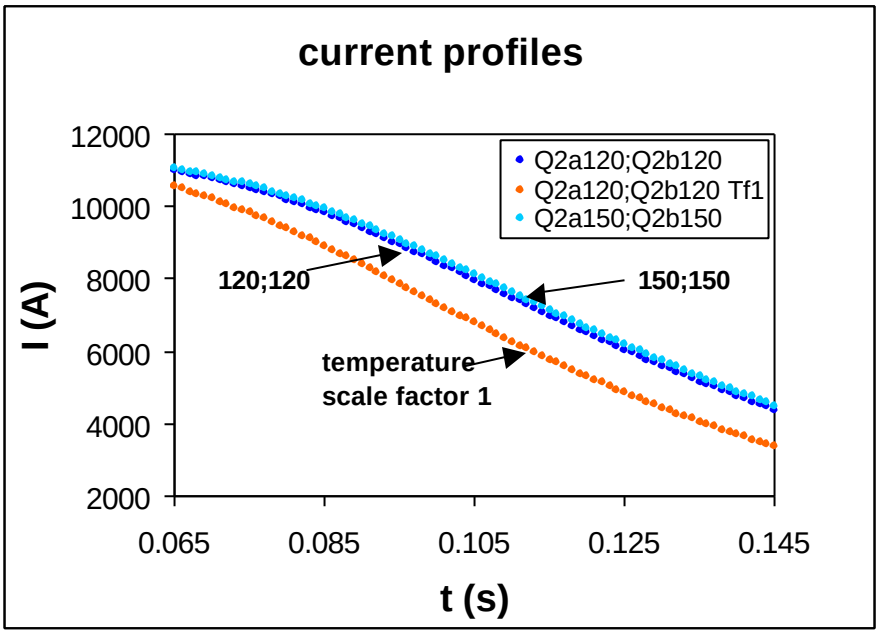

In fig 6.14a and 6.14b we reported peak temperatures and peak voltages summarized in table 6.11. We considered two different configurations for the heaters to see if this could affect the results. As expected the cases, in which both the magnets are half covered, have higher temperatures but lower voltage. In fact the peak temperature is driven by the spot placed in turn 16th and if both the magnets are fully covered they spread faster the heat but develop higher total resistance.

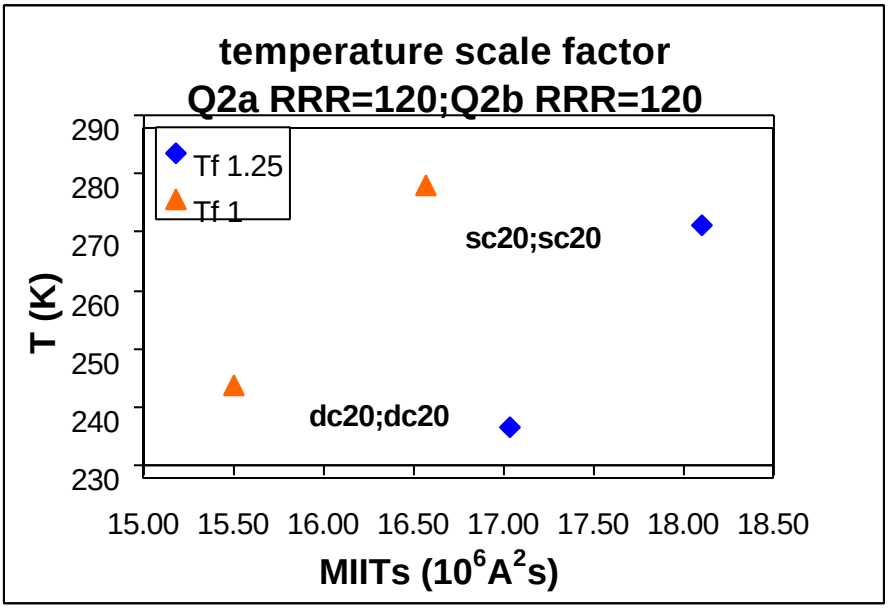

Fig. 6.14a Peak temperature as a function of different scale temperature factor. The most critical condition is when both the magnets are half covered.

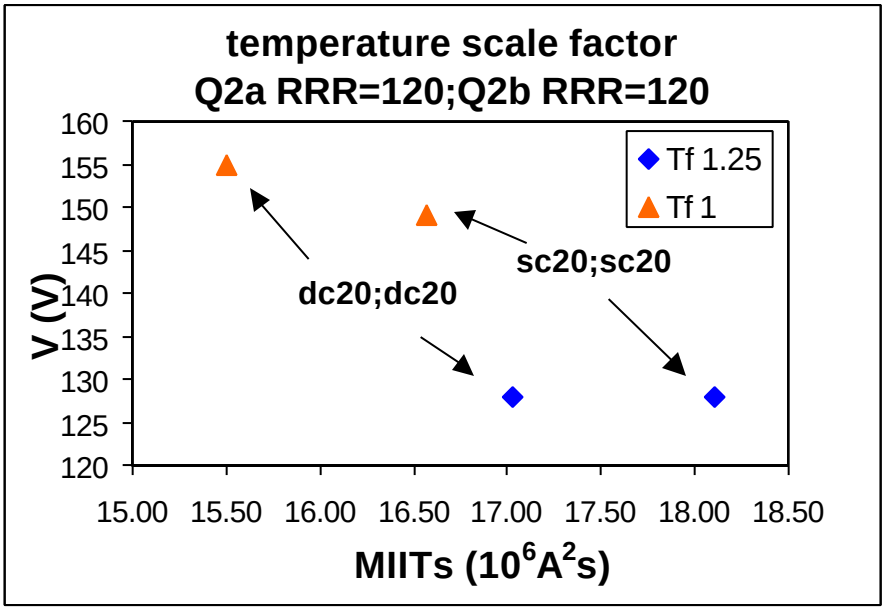

Fig. 6.14b Peak voltage as a function of different scale temperature factor. We can see that in condition of symmetry (both magnets half covered or both double covered) this quantity does not depend on coverage.

Before proceeding with our simulation we want to show the resistance and voltage trace in a standard case. In particular we considered a spot heater event with RRR=120 for both magnets fully covered by strip heaters. The peak temperature is calculated from MIITs value for the segment where the quench occurs while the peak voltage is the maximum excursion recorded between the two magnets (hooked in series from Q2a inner and Q1b inner). In figures 6.15a-c we showed these quantities.

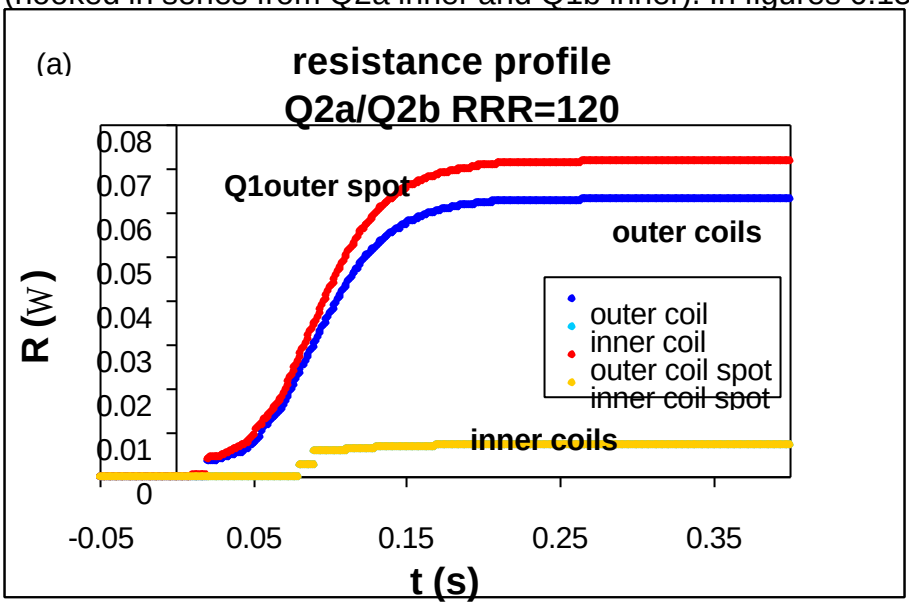

Fig. 6.15a Resistance profile for different coils Q1 outer develops more resistance since the spot is seated in that coil with the spot). Inner coils are not of interest in our simulation because they develop a resistance 80% lower than outer coils. For this reason the simulation in these coils is not very accurate.

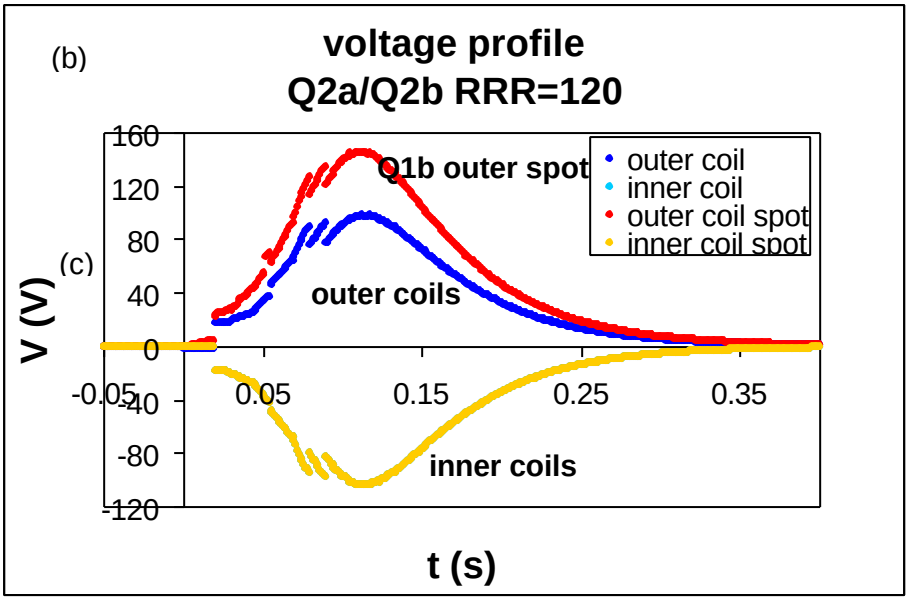

Fig. 6.15b Voltages profile for different coils.
The outer coil Q1 of magnet Q2b develops more voltage since is where the spot heater is situated. The visible interruption of the curves around 80ms is the effect of quench back (strong imbalance inductive/resistive voltage, inductive voltage is more uniform while resistive one changes rapidly). Also for model magnets we could observe a similar trend.

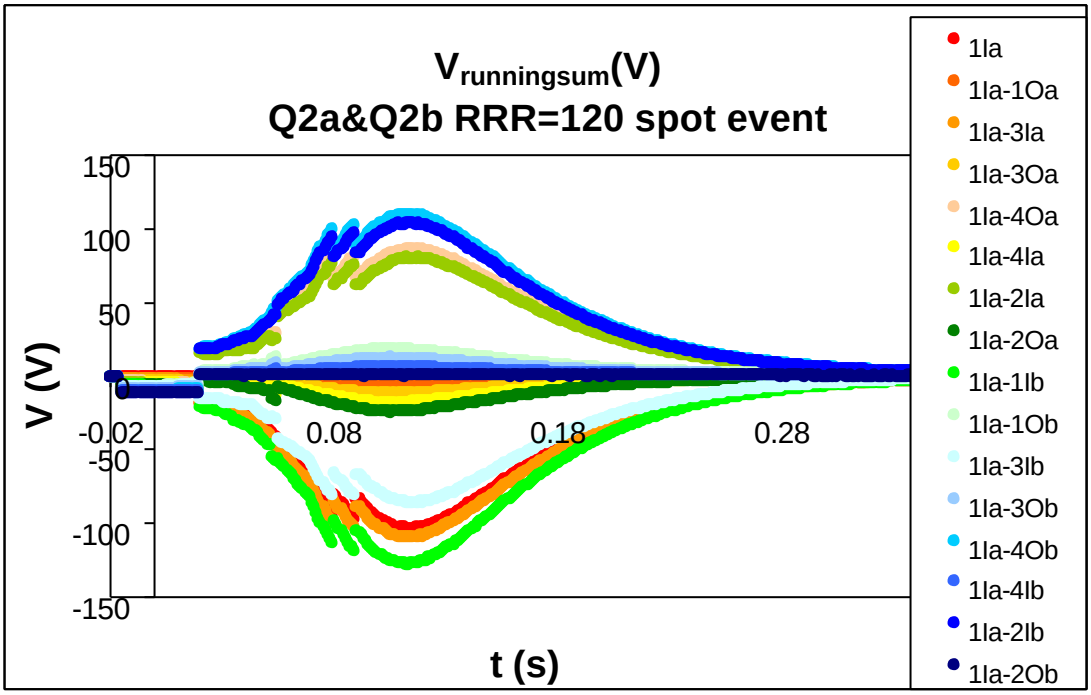

Fig. 6.15c Running sum of the voltages across every single eight coil of the two magnets. The peak voltage is taken as the maximum excursion in voltage in this plot.

- **effect of difference in RRR between the magnets**

In table 6.12 we reported the results of simulations for spot heater events with different RRR in different events and different RRR between the magnets. We considered also different configurations for the heater and we supposed they are fired at 20ms.
We can notice from figure 6.16a that from a peak temperature point of view the worse case is when both the magnets are half covered because the heat given by heaters is less so that the heat is not spread so quick as when both are fully covered.

For peak voltage instead (fig. 6.16b), the most dangerous case is in presence of any asymmetry between the two magnets.
As we can see even with a change in RRR between magnets of 25% the difference in peak temperature and peak voltage is not significant and for lower RRR we get lower values because the MIITs collected are less (higher resistance so that we have faster current decay see fig. 6.13).

Table 6.12 Effect of different RRR (quench induced in Q2b coil 1 outer).

Q2a RRR	Q2b RRR	coverage Q2a	coverage Q2b	$MIIts_{spot}$ (10^6 A^2s)	T_{peak} (K)	V_{peak} (V)
120	120	double	double	17.03	236	128
		single	single	18.10	271	128
		single	double	17.54	252	313
150	150	double	double	17.25	239	129
		single	single	18.33	274	129
		single	double	17.75	255	314
150	120	double	double	17.14	240	170
		single	single	18.21	275	164
		single	double	17.64	255	352
200	150	double	double	17.34	242	165
		single	single	18.42	277	162
		single	double	17.84	258	352

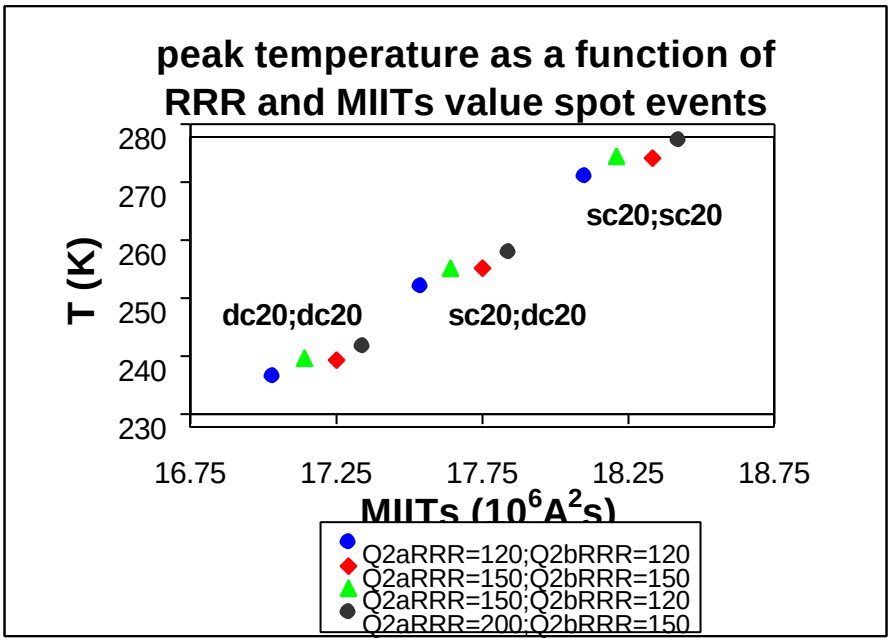

Fig. 6.16a Peak temperature as a function of different RRR.
The most dangerous condition is when both the magnets are half covered while the difference in RRR values does not introduce a big change.

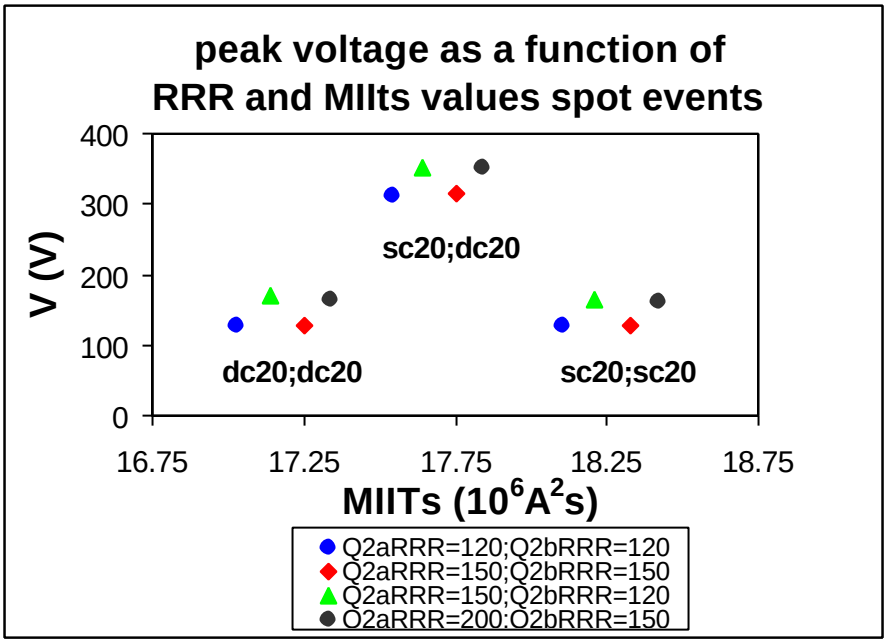

Fig. 6.16b Peak voltage as a function of different RRR.
The highest peak voltage to ground is recorded in condition of asymmetry of the coverage between the two magnets.

- **effect of delay of the heaters**

In table 6.13 we reported the effect of a systematic delay of heater circuit of one magnet or both of them in different configuration of coverage. We simulated again a spot event (spot in **Q2b** coil **1 outer**) with both the magnets with RRR=120.

Table 6.13 Effect of different effective time for heater. In the columns "heaters Q2a or Q2b" is reported the time when the heaters become effective. Since the quench is originated in Q2b the two magnets are not completely symmetric so that we studied cases with Q2a 20ms; Q2b 25ms and Q2a 25ms; Q2b 20ms.

coverage Q2a	coverage Q2b	heaters Q2a (ms)	heaters Q2b (ms)	$MIIts_{spot}(10^6\ A^2s)$	T_{peak} (K)	V_{peak} (V)
double	double	20	20	17.03	236	128
double	double	25	20	17.31	245	226
double	double	30	20	17.56	253	320
double	double	30	30	18.14	272	131
double	double	20	25	17.31	245	174
double	double	20	30	17.55	253	262
single	single	20	20	18.1	271	128
single	single	25	20	18.35	280	210
single	single	30	20	18.59	288	290
single	single	30	30	19.09	307	138
single	single	20	25	18.34	279	143
single	single	20	30	18.56	287	209
single	double	20	20	17.54	252	313
single	double	25	20	17.77	259	**395**
single	double	30	20	17.97	266	**474**
single	double	30	30	18.60	289	304
single	double	20	25	17.84	262	229
single	double	20	30	18.12	271	142

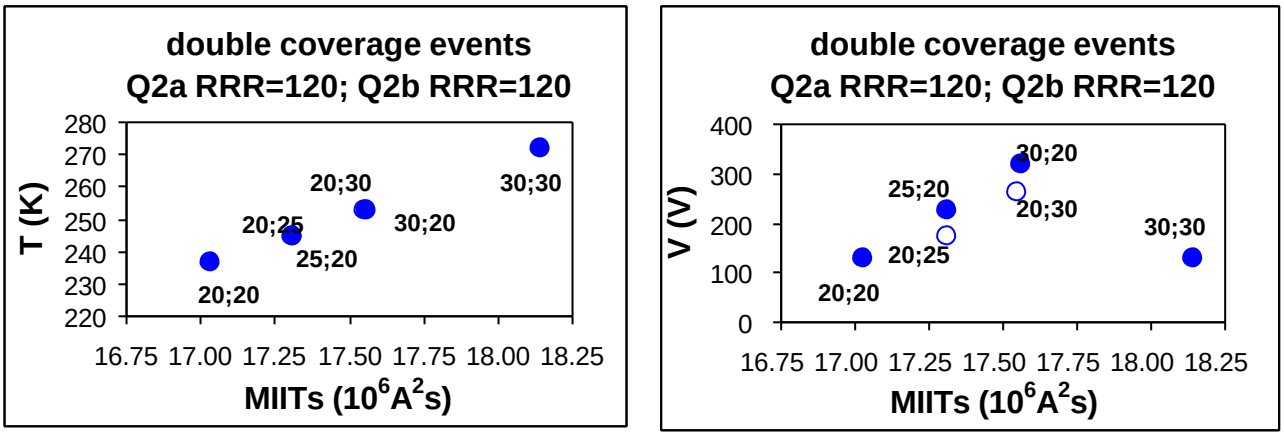

Fig. 6.17 Peak temperature and peak voltage as a function of delay time of heater Q2a and Q2b double covered. Open symbol are used to indicate that heaters circuit of Q2a started earlier then Q2b circuit. As shown this difference does not change peak temperature but changes the peak voltage value.

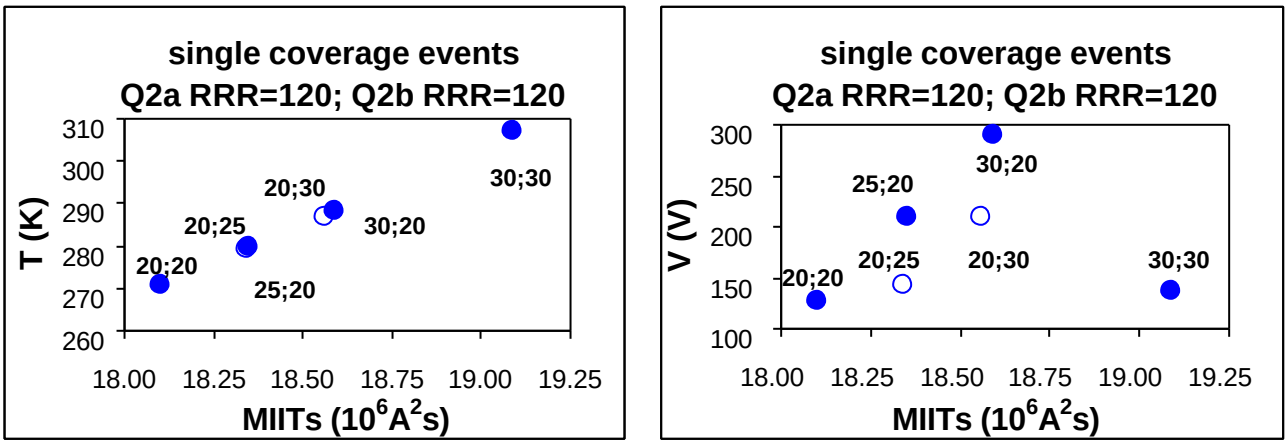

Fig. 6.18 Peak temperature and voltage as a function of delay time of heaters Q2a and Q2b single covered. Peak temperatures are higher than the case of double coverage while peak voltages are very similar.

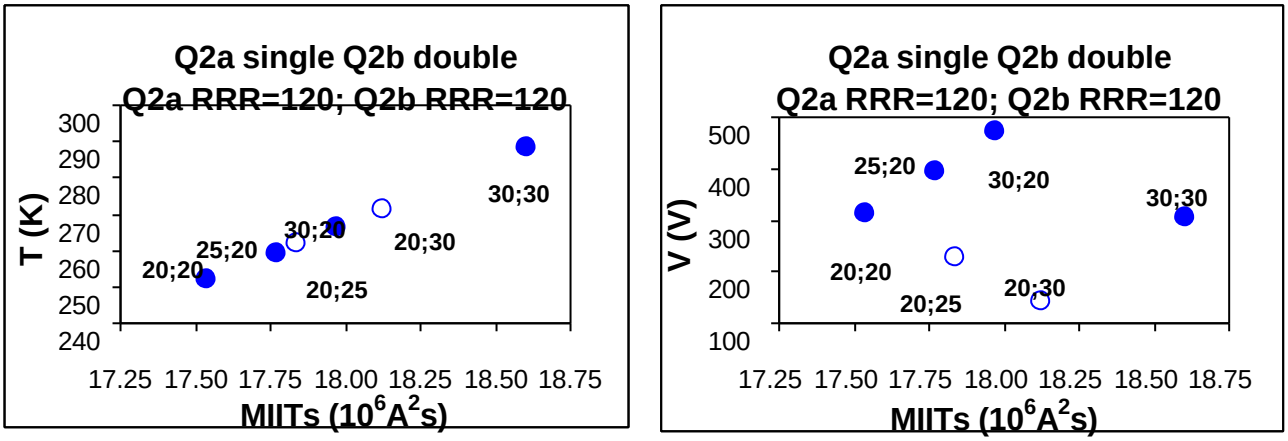

Fig. 6.19 Peak temperature and voltage as a function of delay time of heaters Q2a single covered and Q2b double covered. As one can see in some cases we reach values close to the upper limit but it has to be noticed that they are reached under **double failure conditions** (systematic **delay** of a circuit of heater and **failure of one heater circuit** in one magnet).

As one can observe from the plots reported in figures 6.17-6.19 we can conclude that from a peak temperature point of view the later the heater become effective the higher is the temperature reached.

This was expected since if the heater becomes effective later the initial quenched zone, originated by the spot heater has more time to develop resistance by itself before the heat is spread everywhere else.
From a point of view of peak voltage the dangerous case are again when there is asymmetry between the two magnets so that one develops resistance before the other and creates an imbalance in voltage. In particular we can observe that since the spot heater is located in if Q2b, Q2a develops less resistance and the inductive contribute predominates in this magnet. So if Q2b is delayed the two magnets are more similar and the voltage to ground is lower.
We verified also that if the two magnets have difference in RRR values of 15-20% we have a similar behavior on peak voltages and peak temperatures as in this case (in which Q2a and Q2b have the same RRR value).

- **complete failure of two circuit of heater in the same magnet**

In our simulation we consider finally the case when one magnet is completely uncovered because the two heater circuits both fail. In this case the concern is more for peak voltage to ground (the two magnets are completely asymmetric) than for peak temperature. In fact we can see from table 6.14 that the peak temperature is still below the upper limit allowed while the voltage to ground developed between the coils is very large and it could create problems to the system even if in this case we have a double failure in the system and it should be a very rare condition (**both heater circuits of the same magnets do not work**). The quench is induced again in magnet Q2b coil Q1 outer.

Table 6.14 Effect of complete failure of two heaters circuits in the same magnet.

coverage Q2a	coverage Q2b	$MIIts_{heaters}$ (10^6 A^2s)	T_{peak} (K)	V_{peak} (V)
no coverage	single	20.73	**373**	**1060**
no coverage	double	19.76	**330**	**1130**
single	no coverage	20.73	**374**	**974**
double	no coverage	19.75	**329**	**1046**

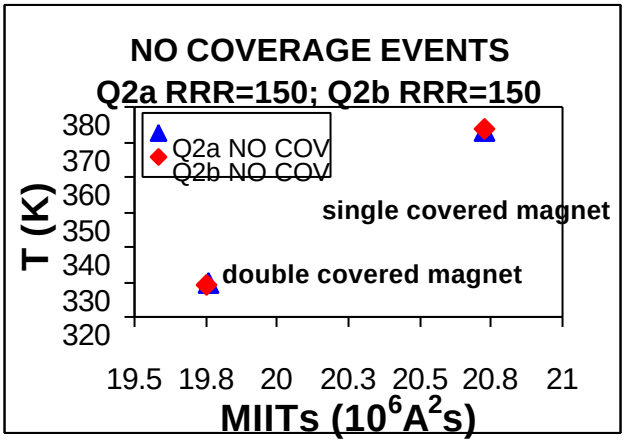

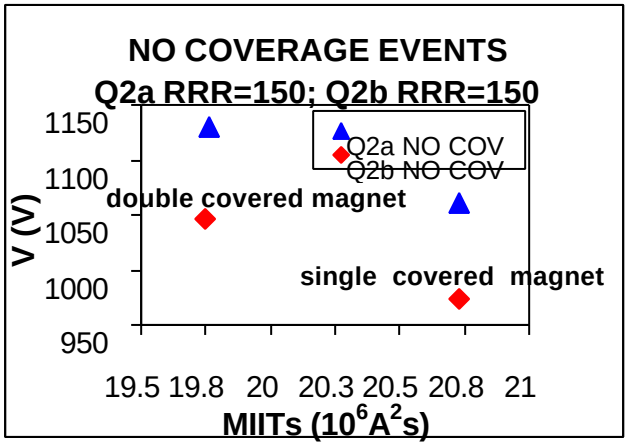

Fig. 6.20 Peak temperature and peak voltage in failure condition. As we can see what creates more concern is peak voltage to ground since we have a situation of complete asymmetry.

Comparing the results between standard condition (Q2a/Q2b double covered) and non standard condition we can see that the change in temperature is on the order of 30% while the change in peak voltage to ground is almost of 90%. In fact the peak temperature depends on the segment which quenches first and it does not see where the heat comes so that the amount of heat received from a double covered magnet or two single covered magnets is more or less the same for it. While the peak

voltage to ground depends directly from asymmetry of the two magnets and this condition is the worst for them (see fig. 6.21).

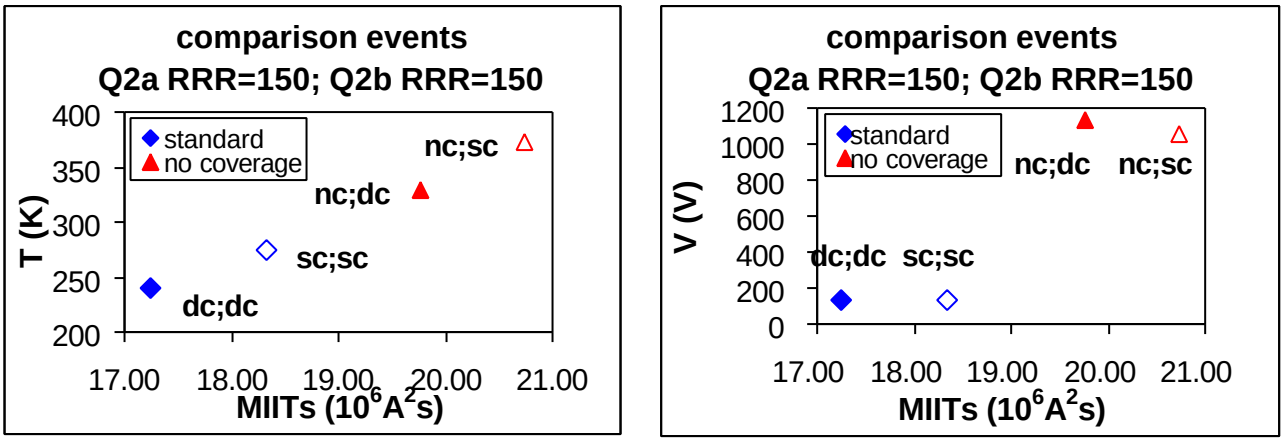

Fig. 6.21 Comparison of peak temperatures and peak voltage for standard (Q2a&Q2b double covered) and non standard condition.

If we plot the running sum across the two magnets for this case we can see that the imbalance between the two magnets in much bigger than the standard case (fig. 6.15c)

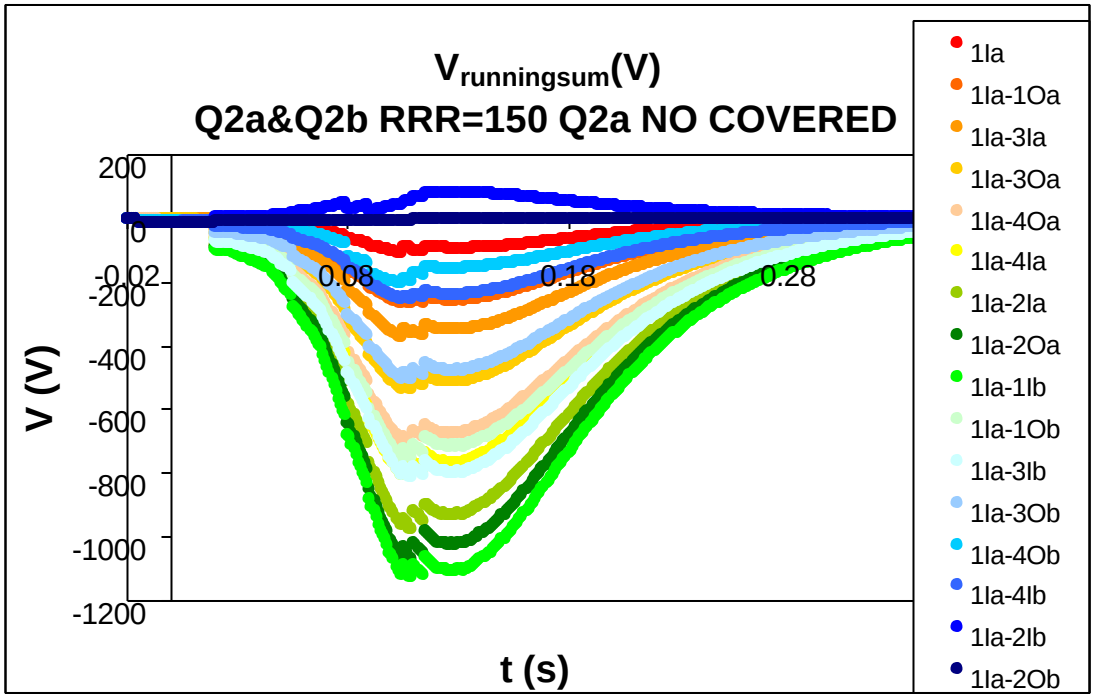

Fig. 6.22 Running sum of voltage across every single eight coil of the two magnets. The peak voltage is very large since magnet Q2a develops a small amount or resistance and this creates a large imbalance between the two magnets.

- **different starting time of quench back**

In our simulation we supposed that after a certain amount of time the magnet is all quenched due to the so-called quench back effect. This effect was seen in all the model magnets, so is reasonable to think that this will happen also in the final system. But we wanted to see what happen for peak voltage and peak temperature if this effect starts before o starts later.

As expected and reported in table 6.15 if this effect starts earlier the peak temperature and peak voltage are reduced while if this effect starts later the peak temperature and voltage are higher. This change is reduced in the second case because later we start to collect MIIts lower is the current and the temperature reached (the heaters are fired independently from quench back and the current decays) .

Table 6.15 Effect of different starting time for quench back effect (spot heater in Q2b coil Q1outer).

coverage Q2a	coverage Q2b	$MIIts_{heaters}$ (10^6A^2s)	T_{peak} (K)	V_{peak} (V)	t quench back (ms)
double	double	17.03	236	128	80
double	double	17.12	239	137	90
double	double	16.59	223	100	50

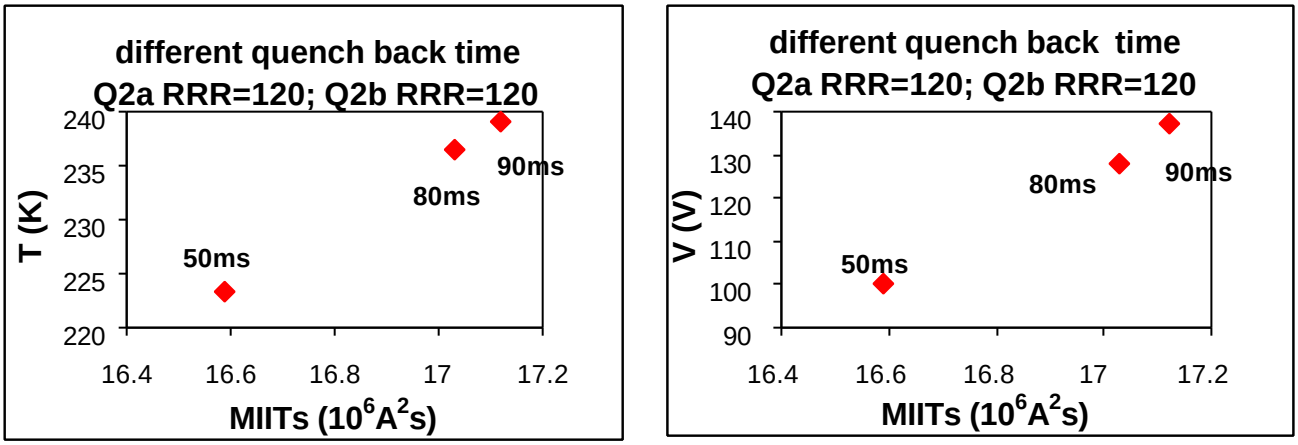

Fig. 6.23 Effect of different starting time of quench back effect.

6.4 Conclusions

After all these different cases simulated we can conclude that the system Q2a/Q2b is well protected under **standard condition** and the peak temperature are below 400K as requested while peak voltage to ground are lower than 400V.
In **standard conditions** the highest peak temperature is reached when both the magnets are half covered and is even higher if one of them has heater circuit systematically delayed. The highest peak voltage to ground is reached when the two magnets have asymmetry in coverage or in starting time of heater circuit.
In **non standard conditions** for example complete failure of two heater circuits of the same magnet the peak temperatures reached are again in the safe range below 400K, but the voltage across the two magnets is above 1000V and it can creates a dangerous condition in the system and Hi-pot test. It has to be underline again that this is a very rare condition and it supposes a **double failure** in the system.

Chapter 7

CONCLUSIONS

In this chapter we would like to summarize all the steps made to arrive to our final goal in estimating quantities directly related to quench protection issue. We will recall quantities and results already mentioned in the chapters of this thesis.
Fermilab, as already said, is commissioned for the production of the superconducting quadrupoles Q2a/Q2b (5.5meter long) of inner triplets of the LHC.
In this thesis we tried to estimate critical factors such as peak temperature and peak voltage to ground for the final system Q2a/Q2b using the data from the models tested in the vertical dewar during the last two years.
As already mentioned the quench protection system is needed in LHC in order to:

- avoid failure of the magnet
- avoid loss of time and money, in case of failure, when the system is running

In particular we had to verify that, under standard conditions, the quench protection system (heaters) is able to:

- reduce peak temperature in the point where the quench starts or in every other segment to values **< 400K**
- reduce peak voltage to ground (running sum) to values **< 400V** (more for practical reasons than dangers for the magnets themselves in fact for Hi-pot test it is required to test the magnets at room temperature with $V=500+2*V_{peak}$).

The analysis made in this thesis started considering actual measurements from model magnets. It was verified that in these magnets the peak temperatures and peak voltages were well below the critical values.
From these data we estimated all the quantities necessary to develop an adiabatic model to predict these critical quantities in the final system Q2a/Q2b.
The model used is based on adiabatic assumptions and developed on the so-called "MIITs method" introduced in chapter 4. As shown this quantity can be easily related to temperature, which is then related to resistance (via resistivity) and finally to voltage. As already explained, the model supposes a starting current and divides the magnets in different quadrants and each quadrant is divided in more parts in order to consider different magnetic field. Each part has a different starting time, chosen appropriately in relation with the model magnets, to collect MIITs as a function of time.
From the relation between MIITs, temperature and field, we can calculate the temperature profile as a function of time and consequently the resistivity and resistance profile. From resistance then it is

possible to find the resistive voltage profile and estimates the total voltage considering a constant inductance of the magnet and the current change in time. This model was used to predict peak temperature and peak voltage to ground for the system Q2a/Q2b (two 5.5m long magnets). These quantities are predicted both for standard conditions and for particular events in which some failures in protection system is simulated (the protection system is composed of two circuits of heaters in series for each magnet and located near the outer coils). In fact in ideal conditions the two magnets in series should be exactly the same. The quench protection system should work in symmetric way and the peak voltage should be zero. But in a real magnet, there are several factors, which can increase this voltage, to take in consideration.
For examples:

- **Spontaneous quench origin**. The quench occurs in a particular place in the magnet so one coil starts to develop resistance voltage first.
- **Variations in strip heater efficiency**. If resistance is not started at the same time on each quadrant, the resistance will not be the same quadrant to quadrant even if measurements seem to show that the difference in starting time is less than 5/10ms at operating current of 12 kA. It is important to consider the possibility that the heater firing units could introduce similar delay.
- **Variation in RRR**. There can be variation in RRR both between inner and outer coils, between quadrant to quadrant and also magnet to magnet. The inner to outer coil RRR variation is usually large but it is not a problem because the outer coil develops most of the resistance due to the heater position. The other two kinds of variation can be more critical.
- **Failure modes**. In the normal LHC operation, Q2a Q2b will both have two circuits of heaters hooked up in series. We considered a possible case where one magnet has only one operational circuit, which should be safe from the point of peak temperature but it creates a resistance imbalance. Unluckily we did not take any data with two complete circuits fired, but we did take data with different combinations of heaters so we were able to extrapolate the parameters necessary to set up our model.

The main assumptions made in this model are:

- for MIITs calculations it was **neglected the contribution of helium** (adiabatic assumption)
- once a quench occurred the **only contribution to resistance is from the copper** part of the cable so that resistivity calculation as a function of temperature, RRR and field were made supposing to have only copper
- **the contribution from insulation (Kapton and Epoxy) was disregarded** in calculation because is several order of magnitude smaller compared to the one from composite NbTi/Cu of the cable (see chapter 4)
- in these calculations we considered **the field constant** but in a real test once a quench occurs the current decays exponentially and the field reduces with the current
- **the field is an averaged** value calculated from field map of model magnets
- we simulated **induced quenches** in a **high field position** (coil Q1 outer of magnet Q2b)
- **the current used in simulations is always 12kA** because is the operational current and the highest used in these quadrupoles
- we supposed that **after a certain amount of time the magnet quenches completely** (probably due to quench back phenomenon seen in all model magnets)
- we introduced **a scale factor of 1.25 for temperature values based on EMPIRICAL STEP** after data analysis on model magnets

Several conditions were tested in order to verify that the parameters concerning the protection were respected. We simulated two different kinds of events: “manual trip” events and “spot heater induced quenches” events both at 12kA.

Particular attention was posed on:

- **different RRR values** for the two magnets in the string
- **different effective time of the heaters** between the two magnets
- **different configurations of heaters in case of failure** of the system

3. **manual trip events**, where the heaters are fire at t=0ms but become effective after a certain amount of time. In these simulations we are interested in peak voltage to ground developed in the string. We set different conditions in order to see how they effect the final results and in particular we studied:

- effect of difference in RRR between the magnets

4. **spot heater events**, where a quench was induced in a high field position and the heaters were fired after an interval of time chosen in relation to data taken with model magnets and considering that they should become effective after the voltage is above a set threshold of 500mV. In these simulations we were interested to peak temperature reached by the segment where the quench occurs and the peak voltage developed across the string. Also in this case we set different conditions to see their effect on results:

- effect of difference in RRR between the magnets
- effect of delay of the heaters
- complete failure of two circuit of heater in the same magnet
- earlier effect of quench back

After all these different cases simulated we can conclude that the system Q2a/Q2b is **well protected** under **standard conditions** (each kind of coverage and heaters effective at the same time in both magnets) and the peak temperatures are below **400K** as requested while peak voltages to ground are lower than **400V.**

In particular we can conclude that:

- the highest peak temperature is reached when both the magnets are half covered
- the highest peak voltage to ground is reached when the two magnets have asymmetry in coverage (one magnet double covered and the other half covered)
- the difference in RRR between the magnets does not affect dramatically the results and the highest temperature is for the highest RRR while the highest voltage is for the highest difference in RRR value between the two magnets

If we have systematic delay of protection system for the same magnet:

- the highest the delay the highest the peak temperature reached
- the highest peak voltage is reached when the two magnets have the highest difference in starting time for the protection circuit and have non symmetric coverage

In these case the peak temperatures are lower than **400K** and peak voltages to ground are lower than **500V** (value reached with the double failure of delay+different coverage)

If the effect of total transition to normal state is:

- **later**, then the peak temperature and peak voltage are higher
- **earlier**, then the peak temperature and peak voltage are lower

In these case the peak temperatures are lower than **400K** and peak voltages to ground are lower than **400V** in standard conditions.

If we have the complete failure of two heater circuits of the same magnet:

- the **peak temperature** reached is again in the safe range below **400K**
- the **peak voltage** across the two magnets is above **1000V** and it can create a dangerous condition for the electrical system (this value is reached with the double failure of quench protection system of the same magnet)

The system Q2a/Q2b is well protected with the protection system designed and only in particular cases in which more than one failure happens we could have dangerous conditions.

APPENDIX A

CAPACITANCE PROBE FOR SUPERFLUID HELIUM LEVEL

A.1 Introduction

Next step to be done at Fermilab for the inner triplet of LHC is to test a prototype of a full-scale magnet and test together the system Q2a/Q2b (for which Fermilab is responsible).
The geometry of the system where the test will take place, is not longer vertical and the dewar will lie horizontally.
One of the parameter necessary to know during a test full of cryogens is the liquid level. Devices used to read this level can be of different types. In particular we will speak about two of them [29; 30]:

1. superconducting liquid level probe
2. capacitance liquid level probe

A.2 Superconducting level probe: characteristics and limitations

This kind of probe works in a very simple way. It measures the resistance of a superconductive filament contained within a protective tube. The current through the sensor maintains the filament through the normal (resistive) state in the helium gas and through the superconductive state in the

liquid. The resulting voltage is proportional to the length of filament above the liquid helium and provides a continuous measure of helium depth. This design however has problem with temperatures around λ-point of helium (transition from liquid to superfluid helium ~2.17K) so a new design independent on temperature is required. In fact this device fails around the λ-point and it is not able to read the level. In particular this kind of probe seated in a dewar is exposed not only to liquid helium but also to helium gas, which turn segments of the probe superconducting even if they are not wetted by helium (the probe becomes completely superconductive and the dewar is apparently full of liquid). Another problem is the time of recovery for this probe, which is too long compared to the time it has to be used.
All these observations were confirmed not only during the tests of short models, where the dewar was furnished with superconducting liquid level probe which could not help in knowing the liquid level for this particular range of temperature around λ-point (which was the range of temperatures used mostly during the tests), but also during our test.

A.3 Capacitance liquid level probe: characteristics and limitations

A possible solution is to use a capacitance liquid level probe, which reads capacitance that changes with temperature because its dielectric strength changes. Unluckily the dielectric strength of helium is very closed to the vacuum one so that the readings of capacitances have to be very precise.
The usual geometry for these devices is a two coaxial sensing electrodes and an intermediate-shielding electrode. In operation, the outer electrode is grounded, while the inner one is driven by a capacitance-measurement voltage at a suitable measuring frequency. Exploiting the driven-shield principle, the shielding electrode is excited at the same voltage as that applied to the central electrode so that the effects of the mounting-part and cables are eliminated.
So the only factors that affect the measured capacitance are the geometry of the electrodes, the level of the liquid, and permittivities of the liquid and vapour.
Neglecting the fringing effect of the ends, the basic theory of electrostatics yields the following equation for the capacitance C between the coaxial sensing electrodes [29]:

$$C = \frac{2p e_0 (x e_{liquid} + (h - x) e_{vapor})}{\ln\left(D_2 / D_1 \right)} \qquad \text{(A.1)}$$

where h is the total length of the probe and x is the liquid level, D_1 and D_2 the outer and inner diameters of electrodes, ε_{liquid} the relative permittivity of the liquid,
ε_{vapour} the relative permittivity of the vapour, and $\varepsilon_?$ the permittivity of the vacuum.
So if we invert the equation and we express x as a function of everything else we can read x as a function of capacitance which is the only thing changing with x.

In our case we chose to change the geometry of the probe and utilize the same principle. The choice to consider a different geometry was not only to build easily a prototype of this device and test it, but also for geometry constrain of the pipe where this probe will seat. This probe will be in a horizontal pipe so we decided to try with the easiest geometry we could: parallel plates which are easy to manage and build and one can also increase the value of capacitance reading putting several parallel plates connected in parallel.
In particular we chose three parallel plates of copper: the inner one is thicker, shorter and the outer ones are thinner and are grounded.
Outside these plates there are other two plates of copper of the same thickness of the outer ones and they work as shielding and constrain for the probe. The inner plate is thicker because thickness does not affect the capacitance values and it is shorter in order to reduce outside effects of everything else

besides the shielding itself. This difference in length between plates should not effect the final reading because it is very small compared to the entire length of the probe itself.
In this case the capacitance is:

$$C = 3 \cdot \left(\frac{e_0 e_{liquid}(T) x \cdot w}{d} + \frac{e_0 e_{vapor}(h - x) \cdot w}{d} \right) \qquad \text{(A.2)}$$

where *d* is the distance between plates, *h* and *w* the height and width of the plates and the factor 3 is due to the fact that we have three plates in parallel. We need to observe that ε_{liquid} and ε_{vapour} (liquid is nitrogen or helium) change with temperature so it was necessary to use different values for different temperatures to simulate results (see Fig. A.1, [31]).
We tested the probe before in Nitrogen and then in Helium and both measurements were taken with the probe in vertical position. In fact with these tests we wanted only to see if it was possible to read out the liquid level with this method and over all to see the reliability of this system before actually put it in the final system. Besides, capacitance depends directly from the area, which is the same in vertical or horizontal position.
Here there is a table with all the characteristics of the probe for our test (in the final design width and length will be exchanged):

Length inner plate	[m]	0.472
Length outer plate	h [m]	0.483
Length shield plates	[m]	0.533
d	[μm]	400
ε_0	C^2/Nm^2	$8.85 \cdot 10^{-12}$
ε_{air}		1.0006
Width inner plates	w [m]	0.067
Width outer plates	[m]	0.067
Width shield plates	[m]	0.081

Table A.1 Specifics of the capacitance probe and some constant parameter.

In figures A.1 we report permettivity of helium (ε_{He}) as a function of temperature for liquid and vapour state ([31]).

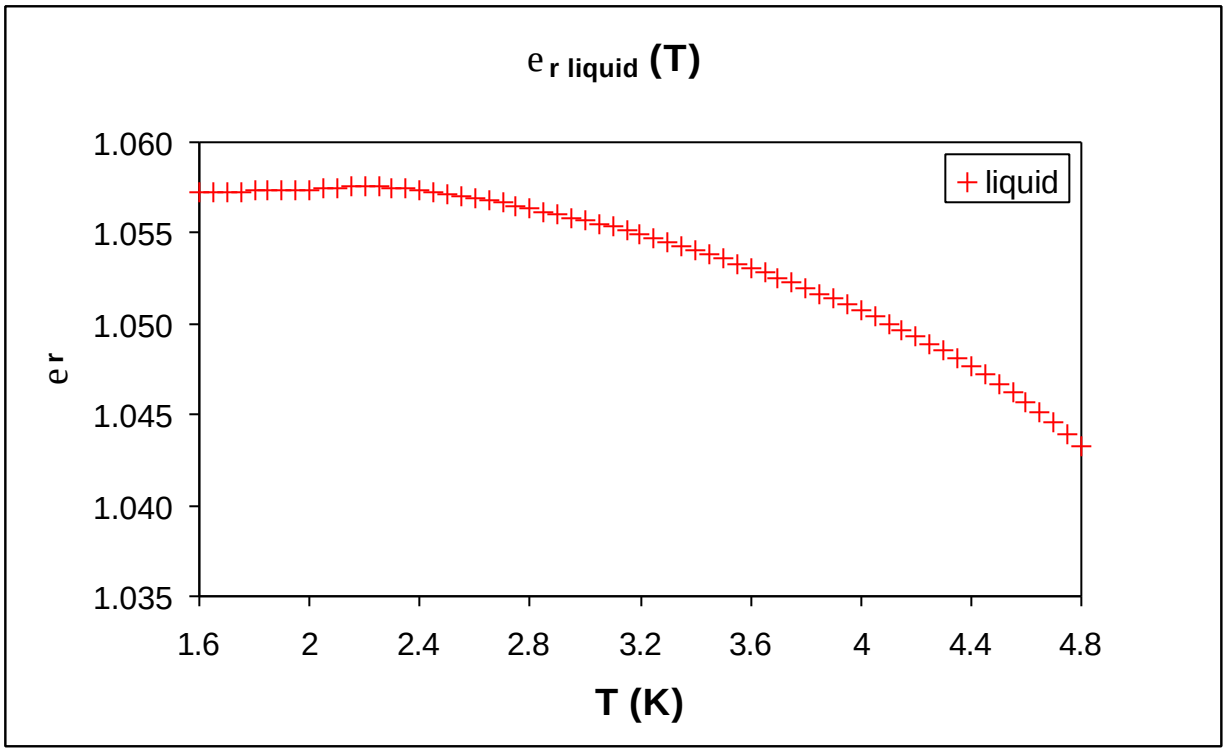

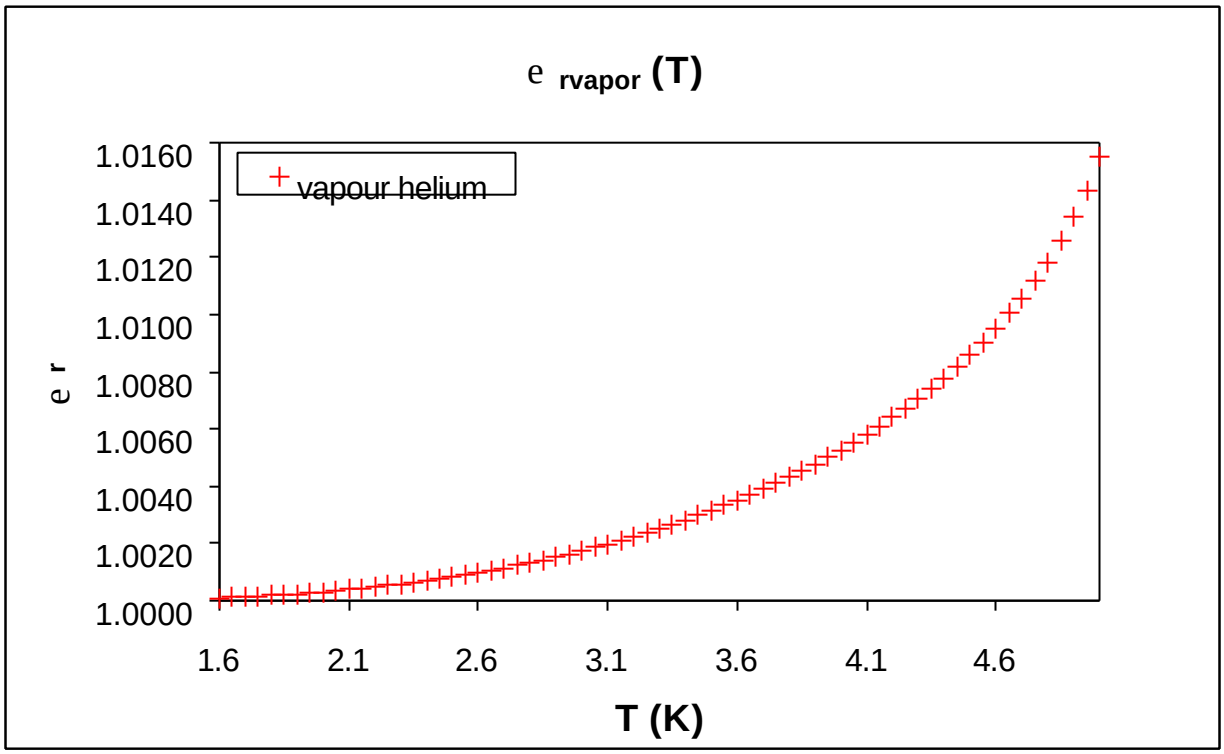

Fig. A.1 Dielectric strength of liquid and vapour helium as a function of temperature. As one can notice, the function which describe liquid dielectric strength has a sudden change when the temperature goes through the λ point (2.17K).

We calculated capacitance as a function of length for different temperatures and different distance between the plates in the final status where the probe will be seated **horizontally** (Fig. A.2) and for the actual test a **vertical** dewar (Fig. A.3).

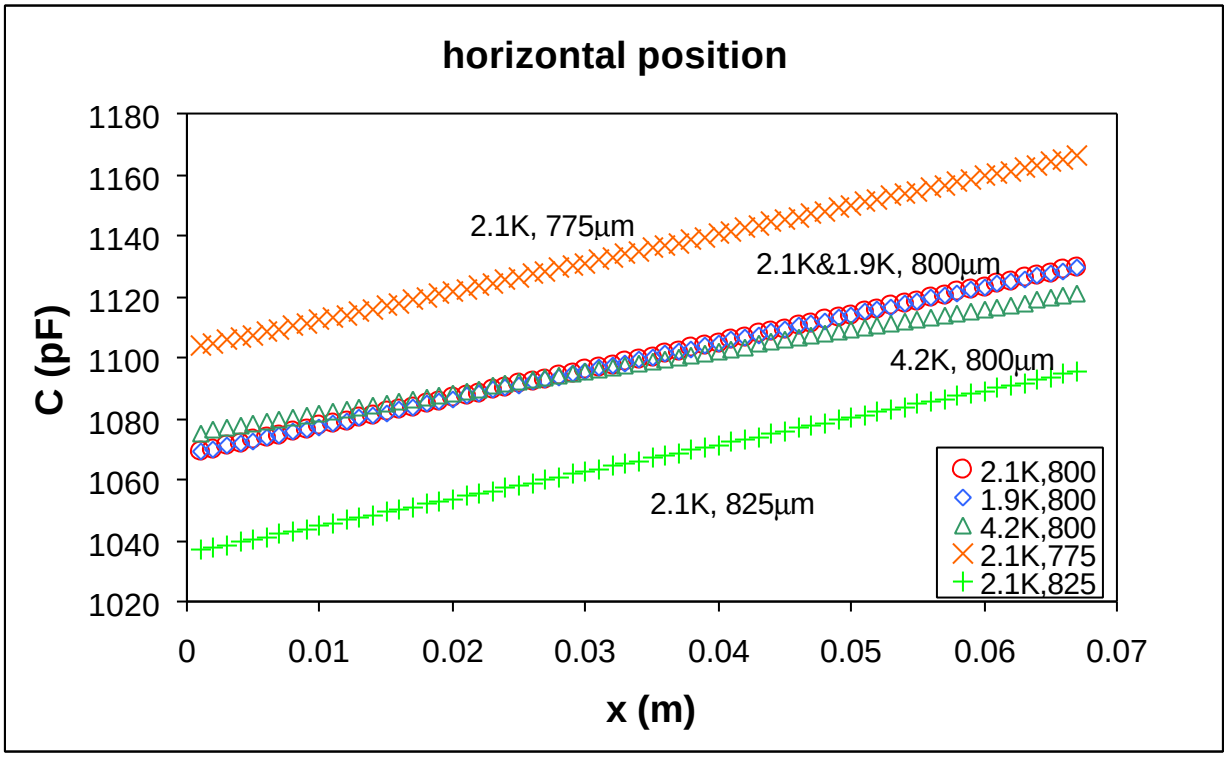

Fig. A.2 Calculation of capacitance for horizontal position. The change is of the order of 50pF over a total height of 7cm. The values are higher for lower distance between the plates.

Several observations can be made for figure A.2. In particular one can see that the distance between plates is a crucial parameter for the values of the capacitance, which as expected decrease for increasing distance.
The major limitation is to make this distance as uniform as possible and as small as possible because unluckily the specific of 400µm, given in base of the material used to separate the plates, is not reachable in reality.
For changes in temperature the difference is not so dramatic and a change in slope can be seen for temperature of 1.9K and 4.2K because, as seen in figure A.1, the dielectric strength of vapour (x=0m) is higher for 4.2K while the dielectric strength of liquid (x is the full length of the probe) is higher for 1.9K. Instead the difference for a temperature of 1.9K and 2.1K does not introduce considerable error (less than 1%).

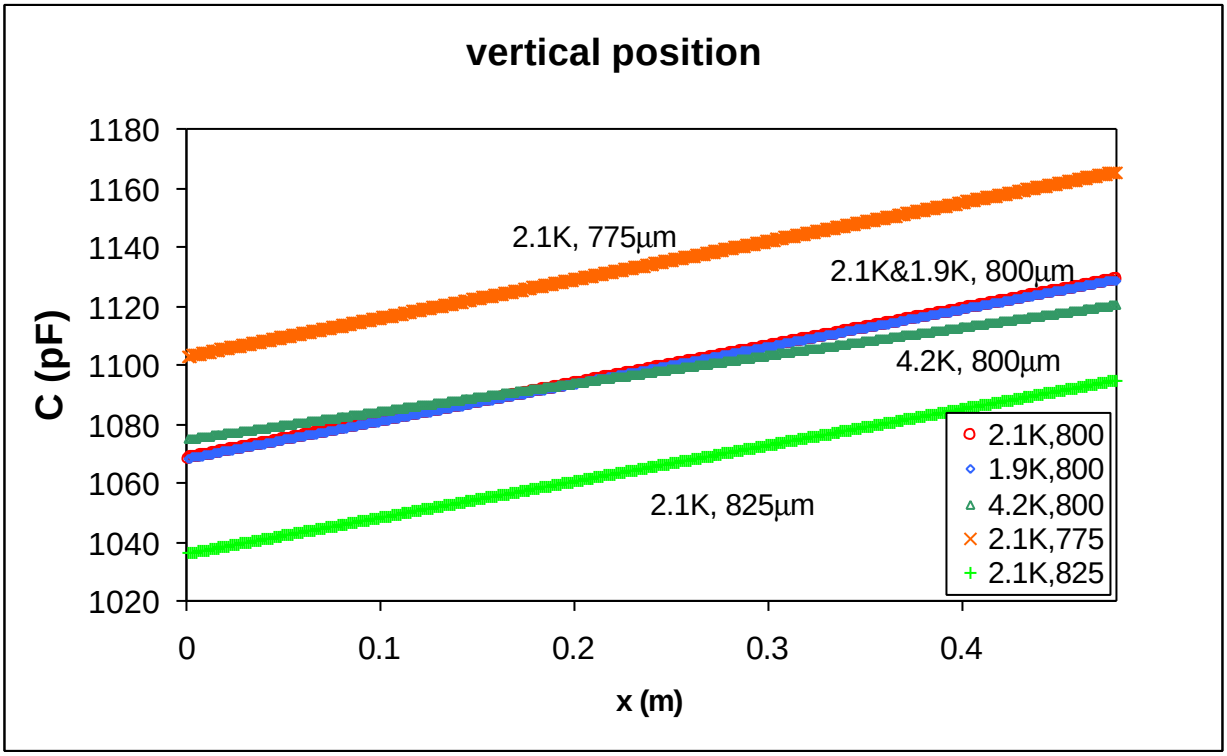

Fig. A.3 Calculation of capacitance for vertical position. The change is of the order of 50pF over a total height of 46cm. The values are higher for lower distance between the plates.

The same observations made for figure A.2 can be made for figure A.3.

Also comparing the two we can make some observations:

- the initial and final values are the same because the capacitance in these two extremes depend only on the total area of the plate, which is the same in both cases
- the rate of change is faster for the horizontal case because in this case the width of the probe is much larger while the height is much shorter in particular considering three different cases (*d* = 400, 600, 800µm) for the two positions we have:

Table A.2 Comparison for different distances for the two different positions.

d (mm)	**DC/cm vertical (pF/cm)**	**DC/cm horizontal (pF/cm)**
400	2.5	18
600	1.7	12
800	1.25	9

The last observation is very important because the aim of this device is to estimate the level within 1cm in the final design. So, while for the vertical case the change can be of the same order of the error in the reading, in the horizontal case the change is higher so that even if there is an error one can evaluate the level.
Now we would like to discuss in detail all the steps made to take measurements beginning with the construction of the probe and all the wiring necessary to the actual measurements made in liquid nitrogen and liquid helium.

A.4 Construction of liquid level probe and preliminary test

After receiving all the parts the first thing to do was to assemble the probe itself and decide all the details such as reading system, wiring system and materials to put between plates to avoid shorts. In order to have readings as clean as possible it was necessary to level the plates reducing all the imperfections on the them, in particular for both the sides of the inner plate and the internal side of the outer plates (fundamental parts for the reading of signals).
Between the inner plate and the outer ones we put a string of kevlar, which wraps the inner plate passing through equally spaced slots (5cm). This string ideally could make *d=400mm* but in reality this was not possible because we tried to tight the plates and obtain the smallest gap but beyond a certain point the plates were not longer parallel and they could also touch each other and short. Between outer plates and shielding plates we decide to put two sheets of kapton because during cool down the probe shrinks and the plates can slip on one another so we have to prevent eventual shorts.
The external plates used as shielding are wider than the other plates because we had to use them also to clamp the plates together. Along the entire length of these external plates, there are several holes (7.6cm between each other) where to put screws and nods of stainless steel tighten later.
On each screw, we put a shrink tube because copper shrinks less than stainless steel at cryogenic temperature so that again it has been necessary to avoid possible shorts between plates and screws.
After inserting all the screws we tight them as much as we could maintaining uniformity all along the probe because as seen a difference in distance between the plates can create a big difference in capacitance reading.
In the final set up we have limited space not only for the probe itself but also for the wiring system which is needed to read the signal. So we had to choose particular small cables with constant capacitance value as a function of temperature in order to read only the variation in capacitance of the probe and not of the wires. The choice was for a twinax cable, composed of two wires plus the shielding. Before using this cable we verified that its capacitance value is not sensitive to temperature changes (the value of capacitance at room temperature and Nitrogen was the same).

After the assembling of the probe we tested it in Nitrogen (ε_N=1.45) in order to see if at least the capacitance probe could read the liquid level and have the linear path we expected with liquid level.
Before attaching the wires we measured the capacitance of the probe itself and we found a value of 1050.2pF, which corresponds a value of d =814μm (much higher than expected). We attached twinax cables (3.3m long in order to simulate the final condition) to the probe and we took again a room temperature measurement and we measured a value of 1231.0pF. This difference was mainly due to the constant capacitance of the wires and probably we changed also the capacitance value of the probe itself by soldering and managing it. Our first set of values were taken by putting the probe in an open dewar with the probe not even completely deep in Nitrogen. The dewar was 50cm tall even the real height from the bottom was 41cm. We filled up the dewar to the top and we let the nitrogen dry out until the dewar was empty while we took measurement of height of liquid with a ruler and capacitance with the LCR meter (with a 4-wire measurement technique).

The electrical set up was:

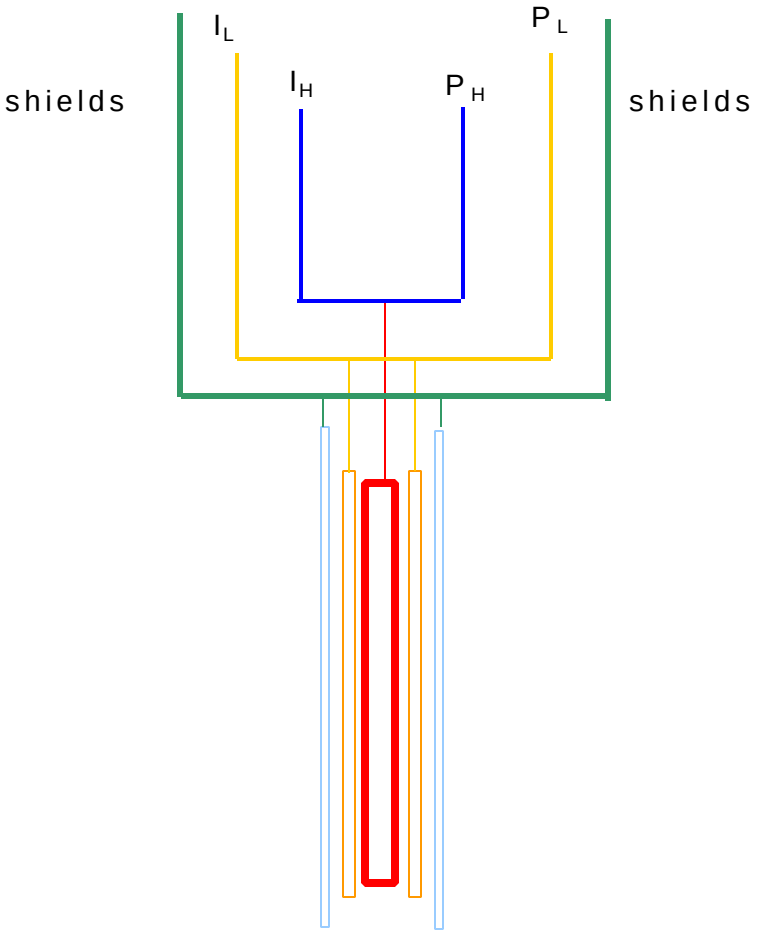

Fig. A.4 Set up of electrical system for measurements taken at Nitrogen temperature.

The set of measurements taken in liquid Nitrogen is:

Table A.3 Measurements taken in liquid Nitrogen.

x (m)	C (pF)	x (m)	C (pF)
0	1231.0	0.267	1442.2
0.337	1510.0	0.260	1436.8
0.324	1497.0	0.254	1430.3
0.311	1490.8	0.248	1422.6
0.308	1481.0	0.241	1417.0
0.305	1478.0	0.229	1406.5
0.302	1476.0	0.216	1395.0
0.295	1470.0	0.203	1384.7
0.292	1467.0	0.191	1372.0
0.286	1460.4	0.175	1359.0
0.279	1454.5	0.165	1349.5
0.273	1447.2	0.159	1343.1

The expected value for the room temperature measurement with *d=400mm* was around 2200pF so we tried to scale the calculation in order to find 1231pF at *x=0m* and we found *d=700mm*. But with this distance we could match only the room temperature value. So we took directly the measurements and we calculated the distance from these values and we estimated *d=920mm*. In fact we can express

$$C = kx + C_0 \qquad \text{(A.3)}$$

where C_0 is the value when the dewar is empty ($C_0 = e_0 e_{vapour} wL/d$ is 1231pF for 78K) and k is a function of d and dielectric strength i.e. the linear coefficient k is:

$$k = \frac{3e_0(e_{liquid} - e_{vapor})w}{d} \qquad \text{(A.4)}$$

Using our data for our measurements and considering ε_{liquid}=1.45 and ε_{vapour}=1.00039 we obtained:

k= (8.61x10^{-10} ± 1.63x10^{-11}) F/m

With these values d can be expressed as:

$$d = \frac{3e_0(e_{liquid} - e_{vapor})w}{k} \qquad \text{(A.5)}$$

and estimating the error for this quantity with the standard method of propagation of errors we obtain (eq.A.6):

$$s_d = \sqrt{\left(d^2 \left(\frac{s_w}{w} \right)^2 + d^2 \left(\frac{s_k}{k} \right)^2 \right)} \qquad \text{(A.6)}$$

so we have:

d = (920.8 ± 22.2) mm

With this new value we calculated again the capacitance and as expected we found a line parallel to the one of the measurements and shifted by ~250pF.

We realized that this difference is due to the constant contribution of the cables that is around 200pF by specifics given from the factory and it is independent from temperature. But probably the fact that the dewar was open is the main reason on the uncertainty of this set of measurement, which has the aim to see if this probe could work and read the liquid level linearly as expected. Then we verified that the signal, read with the LCR meter, is stable within ± 2pF.

We can conclude that the device in liquid Nitrogen works as expected even if we realized that the distance between the plates can not be reduced as much as wanted and this can dramatically effect

the sensitivity during the test in helium, where the change over the entire length is much smaller than in Nitrogen.
In figure A.5 we reported the results of the test and the calculation made for different distances. In particular one can see the prediction for *d=400mm* (as reached from specifics given for kevlar string) and for *700mm* (first estimated distance from room temperature measurement without considering the cables). Then we reported the set of measurements and the linear fit, which enables us to estimate the real distance between the plates. Once again we can notice the offset between the set of measurement and the calculation made for a distance of *921mm* due to the capacitance of the cables and the environment of the test.

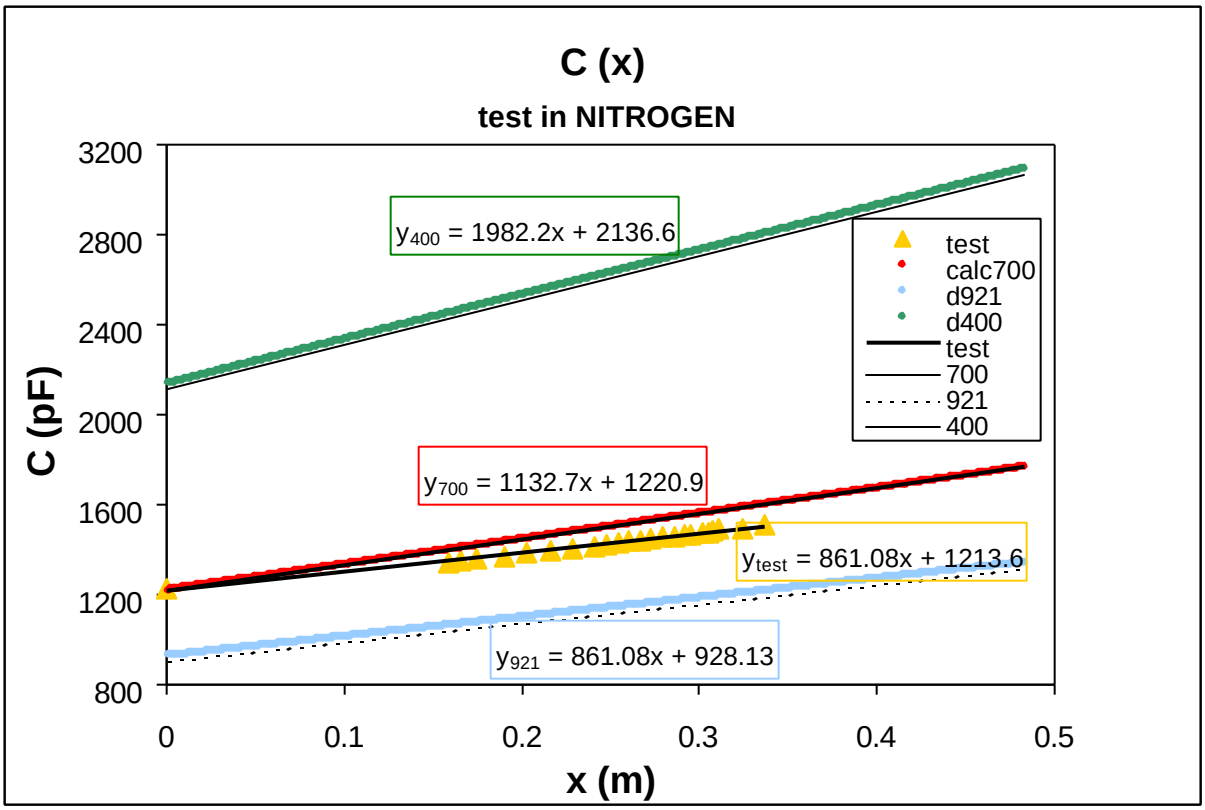

Fig. A.5 Measurements and simulation for test in Nitrogen. We reported the real measurements taken during the tests and the calculation made for different distances between plates.

Before testing the probe in helium, it was necessary to create all the parts in order to take measurements in a vertical dewar. In particular the top plate has to be built together with all the electrical parts necessary to read out the signals properly. In the previous test in Nitrogen we did not need all this because we used an open dewar to have simply a rough idea of the measuring system.

A.4a Test in liquid helium

The test in helium was performed in the Engineering Lab at Fermilab where we could use a vertical dewar 1.20m tall. The internal chamber is 1.10m tall with a neck of 0.58m and 0.16m outer diameter and the main part with an inner diameter of 0.51m and 0.51m tall. The dimensions for the top plate and the structure to attach the probe were chose to fit these dimensions while the dimensions of the probe itself were chosen to fit the final design of the horizontal pipe where it will be seated.
The top plate has three holes: one for the transfer line (for liquid helium), one for a 19pin connector and one for a coaxial BNC connector.
Besides the capacitance probe inside the dewar we have two thermometer sensors (CERNOX sensors) at the top and bottom of the probe and a usual strain gauge probe (AMI) in order to compare the readings with both devices.
Below the top plate (inside the dewar) we have three rods that go all the way until the end of the dewar. Attached to these rods we have four baffles of stainless steel in order to reduce heat dispersion and reflect part of the heat on the top part of the dewar. Then we have three more plates, one after the baffles where the probe is hanging with two clamping parts, one at the bottom of the probe to sustain better the probe and the last one where the usual AMI probe ends.
Figure A.6 shows the probe and its part in the final scheme ready to be inserted in the dewar for the test. In particular starting from the left we showed a top view of the probe, a particular zoom between the plates, the total view of the device and the top plate (transfer line, BNC connector and 19 pin connector).

Fig. A.6 Assembling for the test in helium (top plate and particular of the probe).




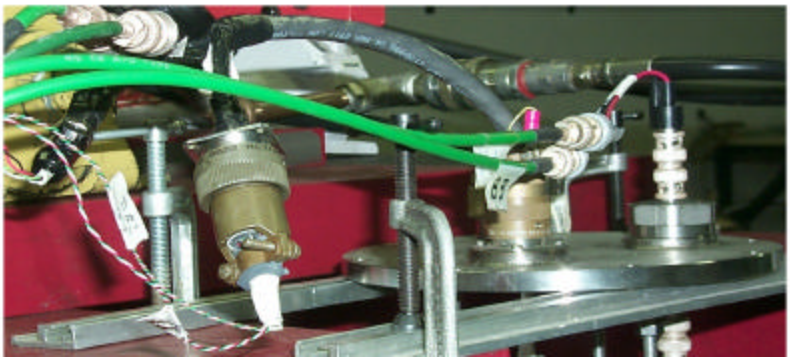

The wiring system is rather simple because we have four channels to read. Figure of the wiring system is shown in figures A.7.

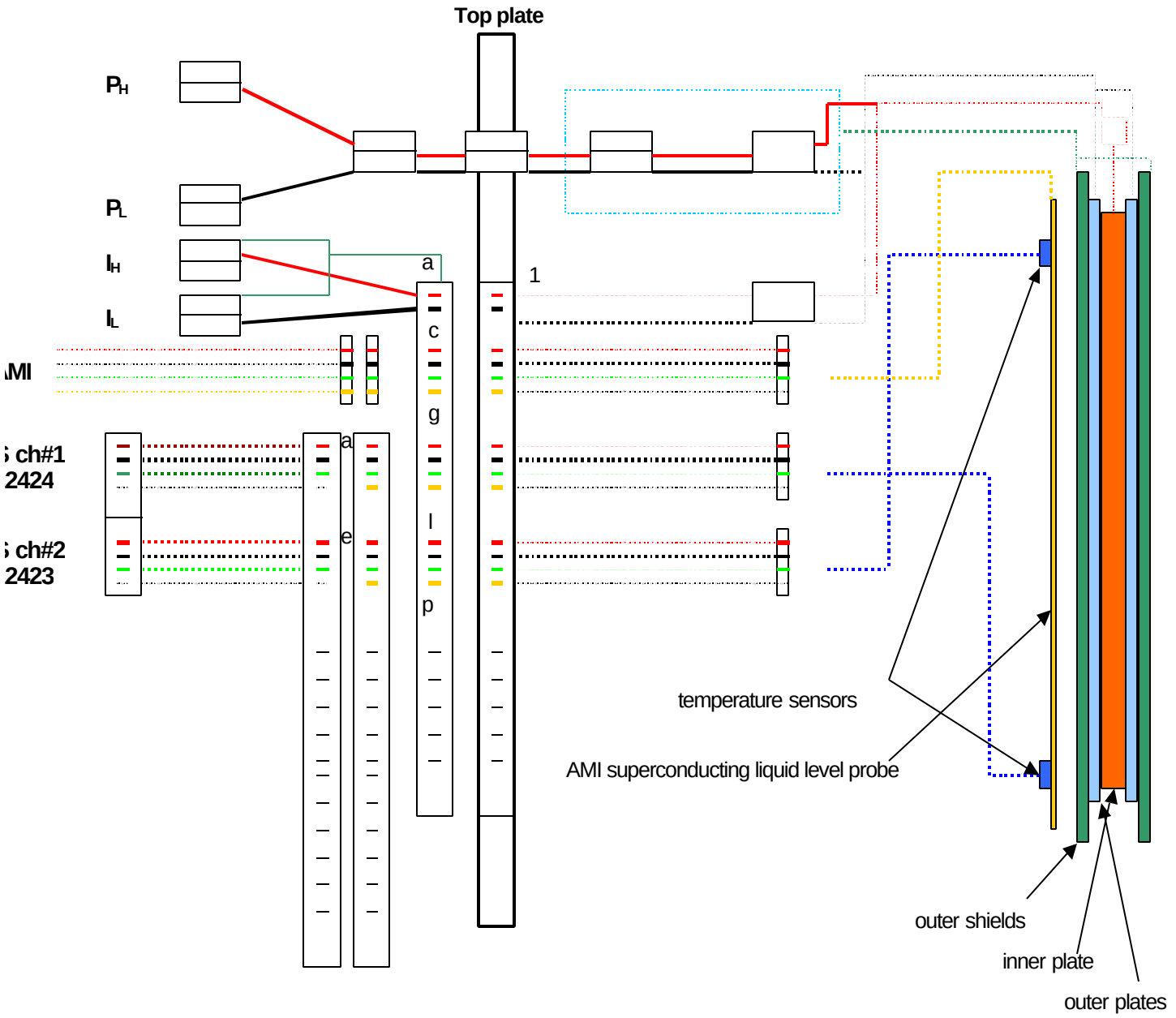

Fig. A.7 Wiring system for the test in helium.

Following the figure we have:

- four wires for each thermometer sensors (two of them bring current, two voltage) which go from the two sensors to the 19 pin connector on the top plate (channels g-p) and then are attached to another 19 pin connector (channels a-h) and final they reach the reading system calibrated for the two by inserting measured values for temperature and resistance on logarithmic scale (these kind of sensors are tested by the factory, which produce them and read the temperature as a function of their resistance)
- four wires for the standard AMI superconducting probe which go from the probe to the 19 pin connector on the top plate (channels c-f) and then are attached to a standard MS 4 pin and finally

to the instrument calibrated for this probe (61cm high) where we can read the level in percentage respect to the full scale (100% is 61cm)

- the signal of the probe is read with a LCR meter using a four wires measurement. The signal of the probe is read with a LCR meter using a four wires measurement. We have two twinax cables, one twinax cable supplies the current (labeled I_H and I_L), the other is used to read out the voltage (labeled P_H and P_L) across the capacitive probe. The I_H and P_H cables are attached to the inner plates (blue wires) while the I_L and P_L cables are attached to the outer plates. Before the top plate the current signals go to the 19 pin connectors with the ground attached to the connector itself, the voltage signals go to the BNC connector. After the top plates the four signals are split in four BNC connector which are attached to the LCR meter where we read the value of capacitance with a sensitivity of 0.1pF.

From calculation made for different condition, such as temperature and distance between plates, we verified that the total excursion from *x=0m* (no liquid) to the condition of *x=0.48m* (full of liquid) is only around *60pF* if the distance can not be lower than *600mm* (as seen in the test in Nitrogen).

In order to consider this method of reading liquid level reliable we needed to repeat the test in helium at least twice in order to see that the sensitivity and stability of signals were reproducible. So we made two different set of measurements in two different cool down.

A.4b First cool down

When the assembling of the probe and all the connections were made we checked the entire channels (temperature sensors, AMI probe and capacitance probe). Then we hooked up the capacitance probe to the LCR meter and we took several measurements at room temperature outside the dewar. First we verified that the values were not sensitive to movements of the wires. Later we inserted the probe inside the dewar that was at room temperature and we verified that the room temperature values were the same and the dewar did not effect the reading with some unexpected coupling of capacitance even after purging the system (we create vacuum inside the dewar).
The average of the measured capacitance of the probe plus wires at room temperatures is:

$$\mathbf{C_{probe+wires} = (1257.5 \pm 1)pF}$$

Considering that the wires add a capacitance of 229pF (12 feet, 19pF/foot) the measured value of the only probe is:

$$\mathbf{C_{probe} = (1028.5 \pm 1)pF}$$

With this value we can calculate the distance *d* between the plates in fact:

$$d = 3 \cdot \left(\frac{e_0 e_{air}(T) h \cdot w}{C} \right) \qquad \text{where } \varepsilon_{air} \text{ is 1.0006} \qquad (A.7)$$

Considering a possible error on *C* of 1pF and 1mm on length *h* and width *w* we can express the standard deviation of the distance *d* as:

$$s_d = \sqrt{\left(\frac{d}{h}\right)^2 s_h^2 + \left(\frac{d}{w}\right)^2 s_h^2 + \left(\frac{d}{C}\right)^2 s_C^2} \qquad (A.8)$$

so we have

$$\boxed{\mathbf{d = (831 \pm 13)\,mm}}$$

with an error of 2%.

After this preliminary test to estimate the distance between the plates we started to cool down the probe with liquid helium at 4.2K monitoring the AMI liquid level probe, the thermometers and the values of the capacitance. Initially we saw big temperature gradient between top and bottom of the probe because the helium inserted was cooling the dewar gradually and of course, at the beginning it was turned completely in helium gas because inside we had room temperature gas.
Once the dewar was stable at 4.2K we started to fill up the dewar with liquid helium and we took measurements of capacitance as a function of liquid level monitored with the standard AMI probe. The temperatures were read with both the sensor:

- in the first set the bottom temperatures were between 4.290K and 4.301K, the top temperatures were between 4.298K and 4.320K
- in the second set the bottom and top temperatures were between 4.298K and 4.302K
- in the third set the bottom and top temperatures were between 4.295K and 4.300K

Tables A.4a, A.4b, A.4c show the results:

Table A.4a First set of measurements at 4.3K, Table A.4b Second set of measurements at 4.3K, Table A.4c Third set of measurements at 4.3K **(x(m)Û %liquid level refers to the first column but we have the same relation for the other columns 100%=61cm).**

x (cm)	% AMI probe	C (pF)±1pF	% AMI probe	C (pF)±1pF	% AMI probe	C (pF)±1pF
1.22	2	1256.0	30	1275.2	28	1277.3
2.44	4	1260.8	32	1276.4	29	1278.3
3.05	5	1261.7	34	1277.7	30	1278.9
3.66	6	1262.3	36	1278.9	31	1279.9
4.27	7	1263.0	38	1280.0	32	1280.1
4.88	8	1263.5	39	1280.6	33	1280.7
5.49	9	1264.0	40	1281.3	34	1281.3
6.10	10	1264.5	41	1282.1	35	1282.7
6.71	11	1265.2	42	1282.6	37	1282.8
7.32	12	1265.8	43	1283.1	38	1283.4
7.92	13	1266.4	44	1283.7	39	1283.9
8.53	14	1267.1	45	1284.2	40	1284.5
9.14	15	1267.8	46	1284.8	41	1285.2
9.75	16	1268.3	47	1285.3	42	1285.7
10.36	17	1268.8	48	1285.8	43	1286.4
10.97	18	1269.5	49	1286.4	44	1286.9
11.58	19	1269.9	50	1286.9	45	1287.7
12.19	20	1270.5	51	1287.4	46	1288.2
13.41	22	1271.5	52	1288.1	47	1288.9
14.02	23	1272.1	53	1288.6	48	1289.5
14.63	24	1272.7	54	1289.1	49	1290.1
15.24	25	1273.3	56	1290.3	50	1290.5
15.85	26	1273.8	58	1291.2	51	1291.2

17.07	28	1275.0	60	1292.3	52	1291.8
17.68	29	1275.4	70	1297.3	53	1292.2
18.29	30	1276.2	75	1300.1	54	1292.9
18.90	31	1276.6	80	1301.6	55	1293.6
19.51	32	1277.1	90	1301.6	56	1294.0
20.12	33	1277.4	100	1301.7	57	1294.5
20.73	34	1278.0	100	1302.0	58	1295.0
21.34	35	1278.5			60	1296.0
21.95	36	1278.9			70	1301.0
22.56	37	1279.4			75	1303.9
23.16	38	1280.0			80	1305.5
23.77	39	1280.6			90	1305.6
24.38	40	1281.3			100	1305.7
24.99	41	1281.8				
25.60	42	1282.4				
26.21	43	1282.9				
26.82	44	1283.3				
27.43	45	1283.7				
28.04	46	1284.4				
28.65	47	1285.0				
29.26	48	1285.7				
29.87	49	1286.2				
30.48	50	1286.8				
31.09	51	1287.3				
31.70	52	1287.7				
32.31	53	1288.3				
32.92	54	1288.8				
33.53	55	1289.8				
34.14	56	1290.3				
34.75	57	1291.0				
35.97	59	1291.5				
42.06	69	1297.0				
42.67	70	1297.7				
47.55	78	1301.5				
49.99	82	1301.6				
53.64	88	1301.6				
58.52	96	1301.7				
60.96	100	1301.7				
60.96	100	1301.8				
60.96	100	1302.1				
60.96	100	1302.9				
60.96	100	1302.5				

(A.4a) (A.4b) (A.4c)

From these results we can see that the temperature sensors read the same temperature in within few *mK* (difference which does not effect the capacitance readings). We have to observe that the standard AMI probe is 61cm tall while the capacitance probe is 48cm tall so that at the reading of 80% for the standard liquid level probe the other one is covered on the entire length. So the value of capacitance is not changing after 80% or the change is within tenths of *pF*.

The major uncertainty on these readings is of course the percentage of liquid level read with the standard liquid level probe because we had an analog read out system with step percentage of 2%. The uncertainty on this reading is estimated to be of 1% (0.6cm). Instead the readings of capacitance were very stable in within *0.1pF* and as expected the entire change in capacitance is on the order of *50pF*.
This change is very low and if the signal had not been so stable it would have been a problem for the real utility of this device.
With this set of measurements taken, we calculated again the distance between the plates in fact, as already done for the test in Nitrogen, we could interpolate the data with a liner fit that relates capacitance as a function of distance.
In particular using equations A.3 and A.4, where again C_0 is the value when the dewar is empty ($C_0 = e_0 e_{vapour} wL/d$ is 1259.5pF for 4.3K), and taking our data for the three cases considered we obtained:

$$\mathbf{k_1 = (9.01 \times 10^{-11} \pm 7.94 \times 10^{-13})\ F/m}$$
$$\mathbf{k_2 = (8.82 \times 10^{-11} \pm 1.01 \times 10^{-12})\ F/m}$$
$$\mathbf{k_3 = (9.08 \times 10^{-11} \pm 9.30 \times 10^{-13})\ F/m}$$

With these values *d* and its error can be expressed with equation A.5 and A.6 we have:

$$\mathbf{d_1 = (814.8 \pm 14.2)\ mm}$$
$$\mathbf{d_2 = (832.1 \pm 15.7)\ mm}$$
$$\mathbf{d_3 = (808.1 \pm 14.7)\ mm}$$

In figure A.8 we report a plot of data taken at 4.3K for the three set of measurements and the curve calculated with a distance of *834mm*. As already pointed out after x=0.5m we do not see changes in capacitance values because the probe is completely wetted. The scattering of data around the calculated curve is probably due to the uncertainty of x value from the standard AMI probe and also because the values were read while we were filling the dewar and this process was quite fast once reached the temperature.

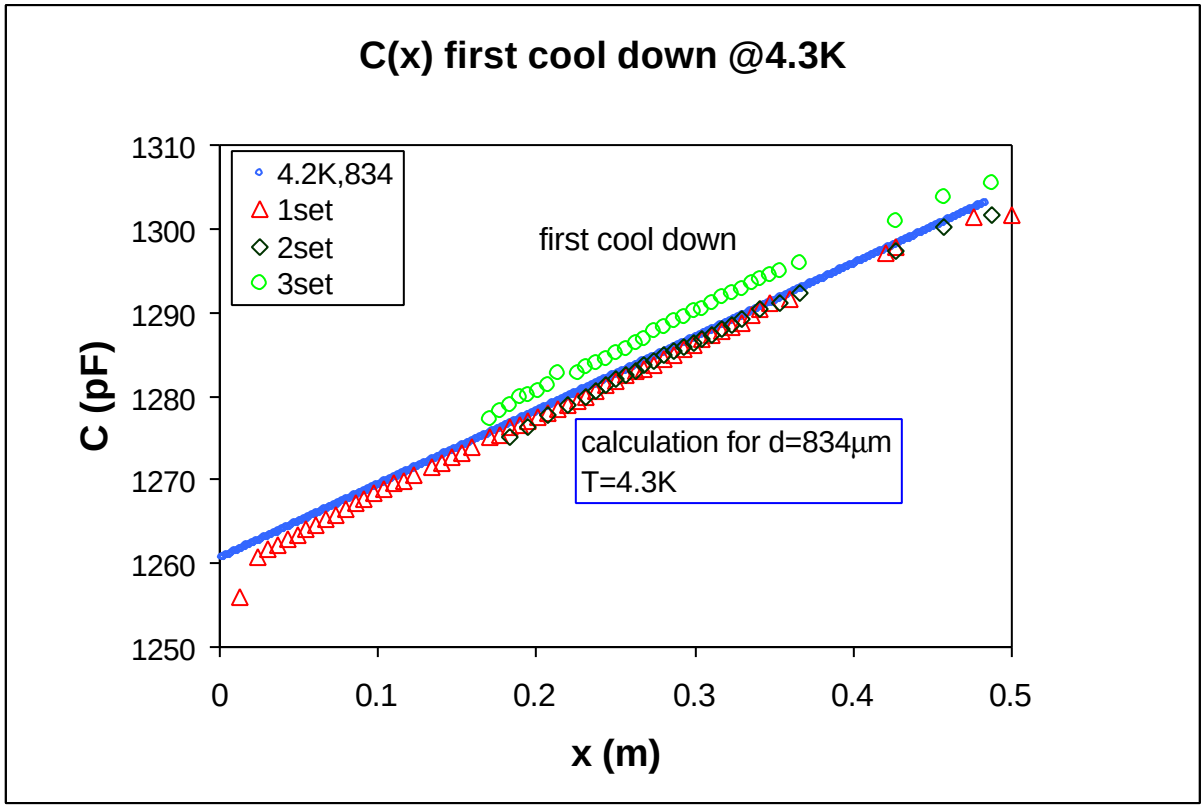

Fig. A.8 Measurements at 4.3K. We reported measurements taken and our calculation with the estimated distance between plates and temperature of 4.3K.

After taking these data at 4.3K we activated the pump in order to reduce the temperature down to 1.9K (~18torr). This operation was more difficult than expected first of all because pumping inside the dewar we reduced not only the temperature but also the liquid level so that we could not reach 1.9K with more than 54% of liquid inside. In fact the device occupied the entire height of the dewar so that the space available to add some liquid was only the top part of the dewar, which is not big enough in order to achieve 1.9K only by pumping on helium. During this cool down both the temperature sensors failed first the one in the top and then the one in the bottom so that we had to use the pressure gauge in order to monitoring the temperature. With calculation we verified that between 1.9K and 2.1K the change in capacitance is irrelevant so we decided to stop around 2K and we took it within 100mK monitoring the pressure. Another problem we had during the second set of measurement was that the main pressure valve of the dewar broke. So while in the first case we controlled the pressure by opening and closing this valve in the second case we had to add helium gas at 4.2K to take the pressure stable. The consequence of this was that the standard liquid level probe went blind several times probably because the gas added was converting part of the probe superconducting even if not deep in liquid. The capacitance probe instead seemed pretty stable and had a linear change in capacitance with the time (before having problems the rate of change for the liquid was 1% every 45 minutes).

Following in tables A.5a, A.5b the value read in these two sets of measurements:

Pressure = 25.5torr 2.02K			Pressure = 21torr 1.96K		
% AMI probe	x (cm)	C (pF)±1pF	% AMI probe	x (cm)	C (pF)±1pF
50.0	30.48	1292.0	54.0	32.92	1294.3
50.0	30.48	1291.3	52.0	31.70	1292.3
49.0	29.87	1290.4	51.0	31.09	1291.4
48.0	29.26	1288.6	50.0	30.48	1290.8
46.0	28.04	1288.1	49.0	29.87	1290.3
45.0	27.43	1287.8	48.0	29.26	1289.5
44.0	26.82	1287.3	46.0	28.04	1287.5
43.0	26.21	1286.4	**40.0**	24.38	1284.0
42.5	25.91	1286.0	**39.5**	24.08	1283.3
42.0	25.60	1285.1	**39.0**	23.77	1282.9
41.0	24.99	1284.5	**38.0**	23.16	1282.2
40.0	24.38	1284.0	**37.0**	22.56	1280.9
39.0	23.77	1283.4	**36.0**	21.95	1280.2
38.0	23.16	1282.7	35.0	21.34	1279.6
37.0	22.56	1282.0	34.5	21.03	1279.3
36.0	21.95	1281.5	34.0	20.73	1278.7
34.0	20.73	1279.2	31.5	19.20	1278.2
33.0	20.12	1278.7	31.0	18.90	1277.7
32.0	19.51	1278.3	30.0	18.29	1275.6
31.0	18.90	1276.8	**26.0**	15.85	1273.7
30.0	18.29	1276.3	24.0	14.63	1273.2
29.0	17.68	1275.7	**Table A.5a** First set of measurement in superfluid, **Table A.5b** Second set of measurement taken in superfluid. **Bold** values for the liquid level were extrapolated from previous set and considering a constant rate of change with time for liquid level.		
28.0	17.07	1275.4			
27.0	16.46	1274.5			
26.0	15.85	1273.7			
25.0	15.24	1273.2			
0.5	0.30	1254.7			

(A.7a) (A.7b)

For the second set of measurements we had to guess the liquid level in several points because the liquid level probe was blind. Considering a rate change of 1% in 45 minutes for the liquid level and comparing the values of capacitance read when the AMI probe was blind we could estimate the liquid level. When the probe started to work again the liquid level agreed well with our prevision.
Using our data we fitted them with two lines where again the linear coefficient is related to the distance between plates as already shown in equations A.4 and these coefficients are:

$$\mathbf{k_1 = (1.21 \times 10^{-10} \pm 1.18 \times 10^{-12})\ F/m}$$
$$\mathbf{k_2 = (1.18 \times 10^{-10} \pm 2.08 \times 10^{-12})\ F/m}$$

and so from equations A.5 and A.6 we obtain:

$$\mathbf{d_1 = (836.9 \pm 14.9)\ mm}$$
$$\mathbf{d_2 = (858.8 \pm 19.9)\ mm}$$

As we can see the second set of measurements present a larger margin of error as expected because the data were not so easy to take. We can also observe that the distance between plates

seem to increase as the temperature goes down and probably this is due to the fact that the screws are made of stainless steel so that they shrink more than copper and they can loose the plates.
In figure A.9 we report a plot of data taken in superfluid condition for the two sets of measurements.

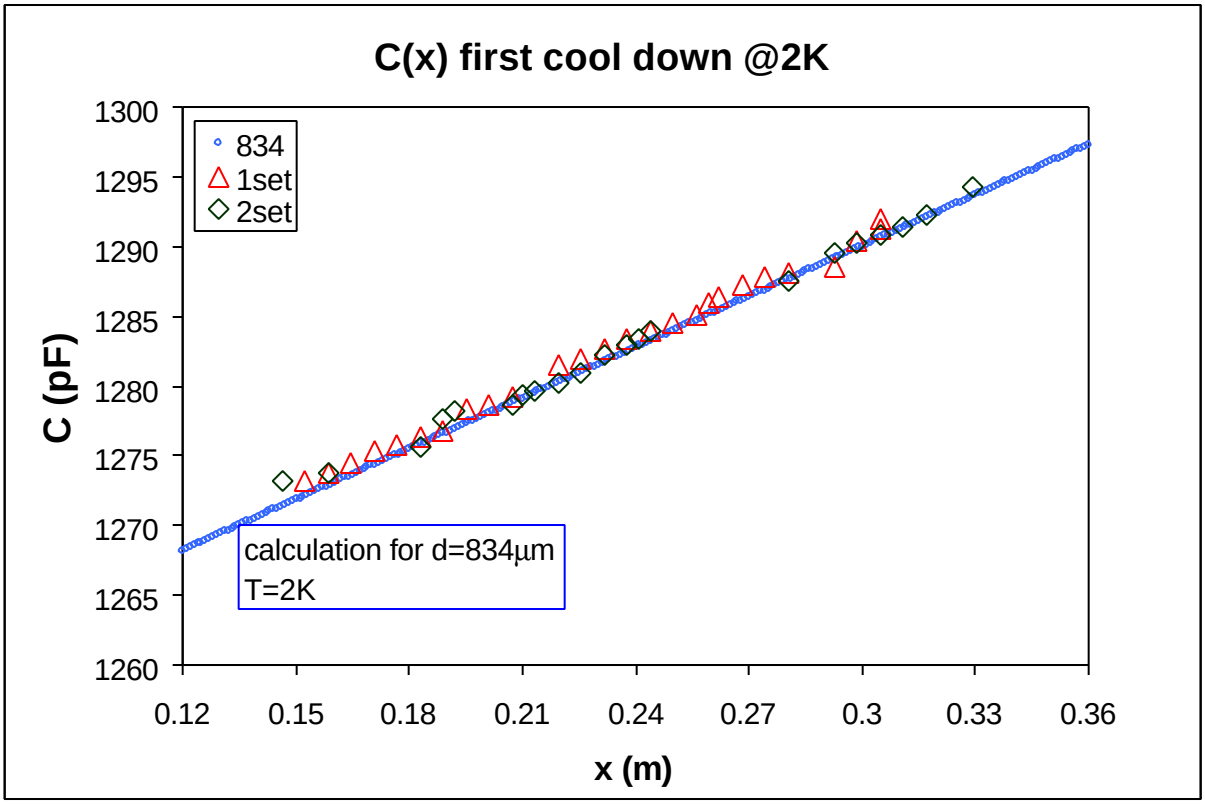

Fig. A.9 Measurements in superfluid helium. In the plot we reported also the calculation made for estimated distance and temperature of 2K.

Comparing figures A.8 and A.9 we can observe the difference in slope for the two different ranges of temperature as it was expected. In figure A.9 we reduced the x-axes to the points taken and one can observe the data taken in are more scattered than in the previous measurement at 4.3K. Probably this is due to the fact that the standard AMI probe went blind in several points and sometimes we realized that it was missing after a certain time, which could effect the reading for the capacitance probe.
After these sets of measurement in superfluid, the probe was reported at room temperature and we took another set of measurement outside the dewar to see if the value read before the cool down was still the same or if something changed.
The average of the measured capacitance of the probe plus wires at room temperatures is:

$$\mathbf{C_{probe+wires} = (1260.5 \pm 1)pF}$$

Subtracting the capacitance value of the wires the only probe has a capacitance of:

$$\mathbf{C_{probe} = (1031.5 \pm 1)pF}$$

For this set of measurements *d* and its standard deviation are estimated with equations A.7 and A.8 and we obtain

$$\mathbf{d = (829 \pm 13)\ mm}$$

with an error of 1.5%.

The difference in capacitance before cool down and after warm up is of the order of 4pF. This error can be very crucial during test because as we already observed for the vertical test with d=800mm we have a change of 1.25pF/cm in a vertical dewar and for the horizontal case is 9pF/cm so that an error of 3pF can effect deeply the measurement.

From this first cool down we can conclude that the probe can help in the measurement in the horizontal pipe even if probably it has to be used together with a standard AMI probe in order to re-calibrate it every time and use it when the standard one goes blind. For the second cool down it was decided to substitute the screws and we tried to reduce the distance between the plates. We decided to take measurements only at 4.3K because it is a easier condition to obtain and we verified in the first cool down that the probe works correctly in superfluid region.

A.4c Second cool down

As already said, in this second cool down we tried to improve the measurements reducing the distance between the plates. One of the main concern about the measurements taken in the first cool down was the fact that probably during cool down the screws were loosing and increasing the distance between the plates because stainless steel shrinks more than copper.

To prevent or at least reduce this phenomenon before the second cool down we substituted all the screws in stainless steel with screws made of brass (league of copper and zinc) because this kind of material shrinks in a similar way as copper does. If both shrink in the same way we should prevent or reduce the loose of the plates. Then we tried to tight the plates in the same way applying the same pressure (2lbs/inch) to the screws using a torque in order to make the distance as uniform as possible. But at the ends we could not apply this kind of pressure to avoid shorts and in the central part of the probe we had to loose a pair of screws to avoid deformation of the plates.

Using feeler gages of different thickness we verified that the distance between the plate was uniform and less than 520μm. The problem in estimating this quantity was that we could not reach the center of the plates (not to ruin them) so that we could not estimate an eventual deformation of the plates in the central part.
This deformation can occur due to the fact that the screws are located externally and they impose higher pressure in the external part. We used a micrometer to see if this difference was real and we could estimate a difference in thickness of the order of 100μm. We could not estimate whether this difference is mainly on the outer shields or if it is reflected also on the plates of the probe. For sure this is one of the main problem to solve before using this probe in the horizontal pipe.

Later we inserted the probe in the dewar and before purging and filling with helium we took a set of measurements at room temperature and we estimated the distance between the plates.

The average of the measured capacitance of the probe plus wires at room temperatures inside the dewar is:

$$\mathbf{C_{probe+wires} = (1325.9 \pm 1)pF}$$

Subtracting the capacitance value of the wires the only probe has a capacitance of:

$$\mathbf{C_{probe} = (1096.9 \pm 1)pF}$$

Using this averaged value of capacitance we can estimate *d* and its deviation with equation A.7 and A.8:

$$\mathbf{d = (779 \pm 11.8)\ mm}$$

and as already told probably the distance is not so uniform over the entire plates and in the center the distance can be higher than expected.

In this set of measurements we cooled down the probe at 4.2K so that we avoided problems in maintaining stable pressure and we could take a measurement starting when the probe is deep completely in helium. In fact to reduce temperature we had to pump on liquid so that we lost a lot of helium and we could not take measurements in the upper part of the probe.

The first set of measurement at this temperature was taken when we filled the dewar the second one was taken while the helium was evaporating naturally from the dewar.

In table A.6a and A.6b we reported the data of the first set and using equations A.4, A.5 and A.6 we estimated the angular coefficient *k*, the distance *d* and its error **(x(m) Û %liquid level refers to the first column but we have the same relation for the other columns 100%=61cm)**.

Table A.6a First set of measurements for the second cool down. Top temperatures between 4.290K and 4.297K, bottom temperatures between 4.396K and 4.295K.
Table A.6b Second set of measurements at 4.25K. Top temperatures between 4.249K and 4.256K, bottom temperatures between 4.245K and 5.500K.

(A.6a) (A.6b)

x (cm)	% AMI probe	C (pF)±1pF	% AMI probe	C (pF)±1pF
0.61	1	1333.1	78	1378.2
1.22	2	1333.5	77	1377.6
1.83	3	1334.1	76	1377.0
2.44	4	1334.6	75	1376.4

3.05	5	1335.2	74	1375.8
3.66	6	1335.8	73	1375.2
4.27	7	1336.4	72	1374.6
4.88	8	1336.8	71	1374.0
5.49	9	1337.5	70	1373.3
6.10	10	1338.1	69	1372.7
6.71	11	1338.6	68	1372.1
7.32	12	1339.3	67	1371.5
7.92	13	1340.1	66	1370.9
8.53	14	1340.9	65	1370.2
9.14	15	1341.6	64	1369.4
9.75	16	1342.1	63	1368.7
10.36	17	1342.7	62	1368.0
10.97	18	1343.3	61	1367.3
11.58	19	1343.8	60	1366.6
12.19	20	1344.3	59	1366.0
12.80	21	1344.8	58	1365.5
13.41	22	1345.4	57	1364.9
14.02	23	1346.0	56	1364.3
14.63	24	1346.7	54	1363.0
15.24	25	1347.2	53	1362.6
15.85	26	1347.9	52	1362.0
16.46	27	1348.5	51	1361.4
17.07	28	1349.1	50	1360.8
17.68	29	1349.7	49	1360.2
18.29	30	1350.2	48	1359.5
18.90	31	1350.8	47	1358.8
19.51	32	1351.3	46	1358.3
20.12	33	1351.8	45	1357.7
20.73	34	1352.3	44	1357.2
21.34	35	1352.9	43	1356.6
21.95	36	1353.4	42	1356.0
22.56	37	1354.0	41	1355.4
23.16	38	1354.6	40	1354.8
23.77	39	1355.3	39	1354.1
24.38	40	1356.0	38	1353.5
24.99	41	1356.5	37	1352.8
25.60	42	1357.1	36	1352.3
26.21	43	1357.6	35	1351.7
26.82	44	1358.2	34	1351.1
27.43	45	1358.7	33	1350.5
28.04	46	1359.3	32	1350.1
28.65	47	1359.8	31	1349.6
29.26	48	1360.4	30	1349.0
29.87	49	1361.0	29	1348.4
30.48	50	1361.6	28	1347.8
31.09	51	1362.1	27	1347.3
31.70	52	1362.7	26	1346.6
32.31	53	1363.3	25	1346.0

32.92	54	1363.8	24	1345.3
33.53	55	1364.3	23	1344.6
34.14	56	1365.1	22	1344.0
34.75	57	1365.6	21	1343.4
35.36	58	1366.1	20	1342.9
36.58	60	1367.1	19	1342.3
39.01	64	1369.0	8	1335.0
42.67	70	1373.2	7	1334.4
43.89	72	1374.5	6	1333.8
45.11	74	1375.5	5	1333.2
47.55	78	1376.6	4	1332.6
48.77	80	1378.0	3	1332.0
51.21	84	1378.0	2	1331.5
53.64	88	1378.0	1	1330.7
54.86	90	1377.9	0	1330.1
60.96	100	1378.1		
60.96	100	1377.9		
60.96	100	1378.1		
60.96	100	1377.9		
60.96	100	1378.2		
60.96	100	1377.9		
60.96	100	1378.3		
60.96	100	1378.2		
60.96	100	1378.1		
60.96	100	1378.4		
60.96	100	1378.5		

Estimating the linear coefficient and the distance for the first set of measuremets we obtain:

$$\mathbf{k_1 = (9.47 \times 10^{-11} \pm 2.72 \times 10^{-13})\ F/m}$$

$$\mathbf{d_1 = (775.3 \pm 11.8)\ mm}$$

The second set of measurements is reported in table A.6b and again we calculated *k* and *d*:

$$\mathbf{k_2 = (1.004 \times 10^{-10} \pm 2.07 \times 10^{-13})\ F/m}$$

$$\mathbf{d_2 = (730.9 \pm 11.1)\ mm}$$

In this second set of measurement the distance between plates seem to be lower than before even if this is probably due to an imbalance in temperature between top and bottom, which creates a bigger uncertainty on measurements. For the first set of measurements this was not a problem because we were filling up the dewar and the temperatures in the top and the bottom part were the same.

In figure A.10 we report the results for these two sets of measurements:

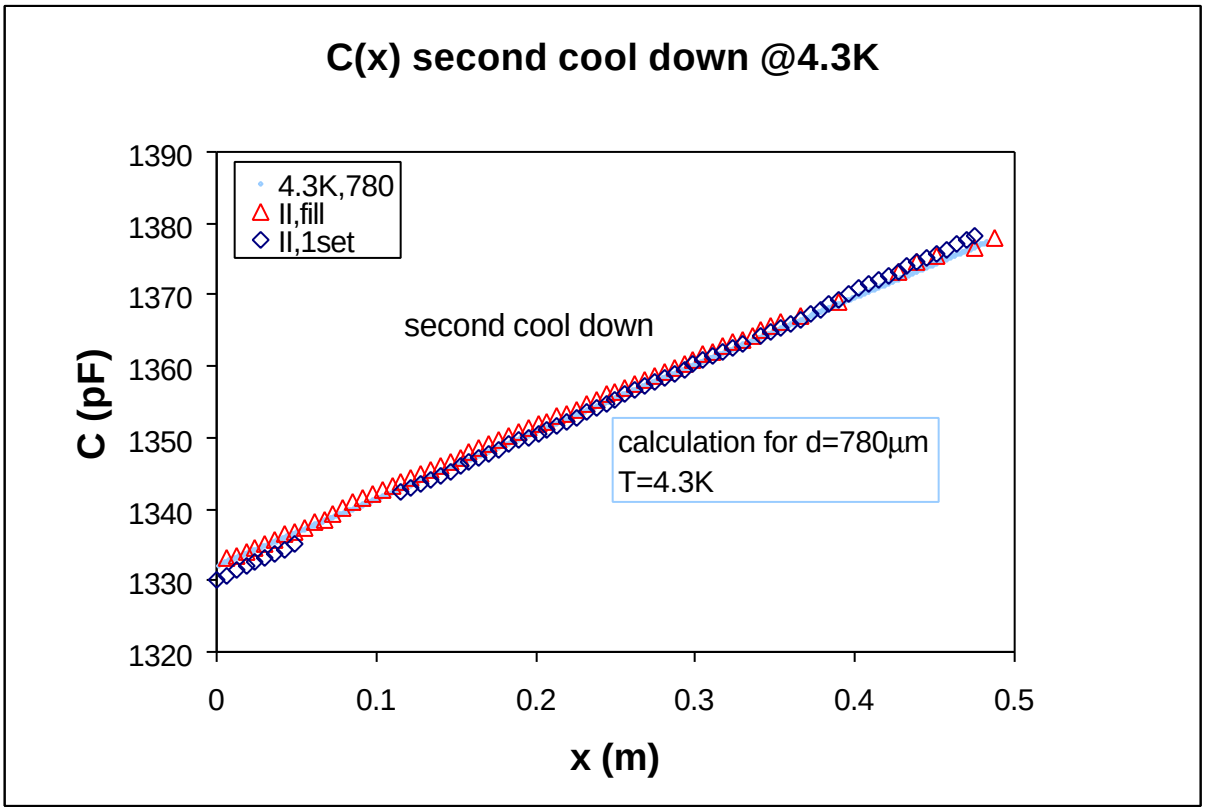

Fig. A.10 Measurements in second cool down at 4.3K. In the plot there is also the trend of calculation made for estimated distance and temperature of 4.3K.

As all the sets of measurements taken the capacitance probe follow a linear path with decreasing and increasing of liquid level but even if we gain in the distance between the plates the change over the entire length is still on the order of 50pF.

After this second cool down we decided to leave the probe inside the dewar in order to take a room temperature measurement inside the dewar after the cool down to see if the value of capacitance is the same. In the first cool down in fact the probe was pulled out when the temperature inside the dewar was not at room temperature and so we want to see if this effected the measurement taken for problems of contamination or sudden change of conditions for the probe.
The averaged values read after the second cool down **inside** the dewar are:

$$\mathbf{C_{probe+wires} = (1332.7 \pm 1)pF}$$

Subtracting the capacitance value of the wires the only probe has a capacitance of:

$$\mathbf{C_{probe} = (1103.7 \pm 1)pF}$$

With this value we can estimate *d* and its the error:

$$\boxed{d = (774.5 \pm 11.7)\ \mu m}$$

We can see that, as in the first cool down in helium, the value of capacitance after warm up is higher than before cooling down but the difference now is of the order of 7pF. This difference is probably higher than before because the readings were done inside the dewar where there is still vacuum. In order to see if this can effect capacitance reading we pulled out the probe from the dewar and we took other readings at room temperature in air.
The averaged values read after the second cool down **outside** the dewar are:

$$C_{probe+wires} = (1333.9 \pm 1)pF$$

Subtracting the capacitance value of the wires the only probe has a capacitance of:

$$C_{probe} = (1104.9 \pm 1)pF$$

With this value we can estimate *d* and its the error:

$$\boxed{d = (773.6 \pm 11.7)\ \mu m}$$

As we can see even if the values are slightly different the average and the estimated distance are practically the same.

A.5 Conclusions and improvements

The test made on this capacitance probe with three parallel plates was very useful to understand the limit and the problems with this kind of device which will be improved in order to be used correctly in the final settlement (horizontal pipe).
In this paragraph we want to summarize the results and underline what is good of this probe and its limitations.

First of all we would like to summarize the data taken with a plot of all measurements showed in figure A.11:

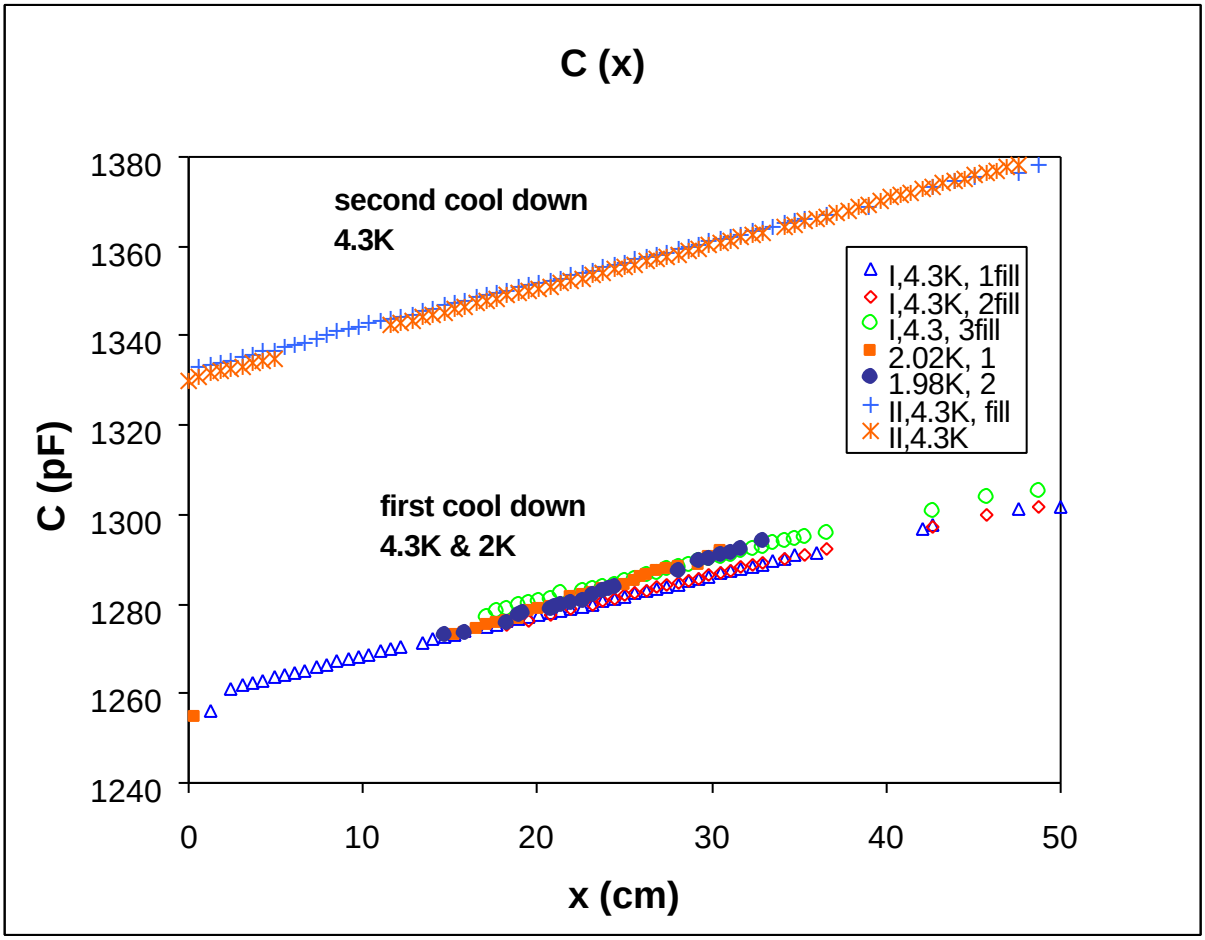

Fig. A.11 Summary of measurements at different temperatures and for different conditions (between first and second cool down we tried to reduce the distance between plates).

From figure A.11 we can see the linear trend of the measurements taken independently from temperature, distance between plates and different cool down. The difference in temperature can be seen in the difference of slope (sharper for lower temperature), while the difference in distance can be seen from the value of capacitance (bigger values smaller gap). As shown in the second cool down we tried to reduce the gap between the plates but we did not obtain the improvement expected and the overall change in capacitance was still around 50pF.

In table A.7 we summarize results with calculations for the gap between plates for different sets of measurements supposing the linear trend (the distance was calculated both from the linear coefficient and from the intercept $C=mx+b$). Once again we see the difference in distance between the cool downs but we verified the same order of magnitude for this quantity (using independently "m" or "b").

Table A.7 Summary of calculated distance for different sets of measurement.

T (K)	m (F/m)	d(μm)	s_d(μm)	err%
4.3	9.00669E-11	814.80	14.18	1.74
4.3	8.81932E-11	832.11	15.73	1.89
4.3	9.08111E-11	808.12	14.68	1.82
2.02	1.20782E-10	836.91	14.97	1.79
2.02	1.17700E-10	858.82	19.89	2.32
4.3 (second cool down)	9.46594E-11	775.27	11.84	1.53
4.25(second cool down)	1.00406E-10	730.89	11.06	1.51
78K	8.61085E-10	920.81	22.24	2.41
T (K)	**b (F)**	**d(μm)**	**s_d(μm)**	**err%**
4.3	1.25917E-09	835.14	12.65	1.51
4.3	1.25982E-09	834.61	12.64	1.51
4.3	1.26261E-09	832.36	12.60	1.51
2.02	1.25450E-09	833.32	12.62	1.51
2.02	1.25492E-09	832.98	12.62	1.51
4.3 (second cool down)	1.33265E-09	779.54	11.80	1.51
4.25(second cool down)	1.33032E-09	781.19	11.83	1.51
78K	1.21356E-09	868.04	13.48	1.55

Several aspects of this device are very useful and appropriate to read the liquid level. In fact this probe is able to read the liquid level in the region where the standard liquid level probe is blind. The standard liquid level probe seems to be blind around the λ-point but also in other region around that range of temperature. We were able to see this effect also during our test, where in several points it was not possible to estimate the liquid level with this standard device, while the capacitance probe seemed to fall linearly without problems.
In fact capacitance readings are not affected by the peculiar behavior of helium in this region. The readings were stable along the entire probe and they were very linear as expected.

The limitation of this probe is the sensitivity, which was about 50pF change in capacitance over the length of the probe. This leads to severe restriction in possible reading error and one could be off by 1-3pF and have a big error in the estimation of the liquid level. This problem can be due to the fact that the plates shrink during cool down loosing the pre-stress and the small distance achieved with a torque. Also the probe has external screws that create smaller gap externally but probably leave a bigger gap in the middle o that the distance between plates is not so uniform as wanted. This kind of problem is not so crucial in the vertical set up because this problem effect the width and not the height of the probe. In the horizontal case instead the problem effects the height of the probe (width and height are inverted) so that also the reading of the liquid level can be wrong. In fact in such a case the readings could change slope and values depending on the level (in the center the distance would be higher and capacitance lower so that one could think not to have enough liquid as in reality) leading to uncertainty not controllable.

Several improvements are necessary to reach the final design of this device.

Due to space restrictions this device can not be changed in length or width so that in order to obtain higher sensitivity one could work on the distance between the plates or reduce their thickness, which do not effect capacitance readings, and add other plates.

As the data show neither stainless steel nor brass screws can hold the probe so that if one starts with a known distance between the plates for sure during the cool down the distance will grow due to the different shrink of copper and the other materials. It is necessary then to reduce as much as possible this distance in order to gain as much as possible in helium.
Another problem is to maintain this distance as uniform as possible in the horizontal pipe to avoid changes in slope due to changes in distance over the height of the probe which read the liquid level. A possible solution for this could be to clamp the plates in different points for example externally as in the test but also in the center. This pressure would be applied on the external plates, which work as shields so that measurements should not be affected. In order to reduce the gap as much as possible before cool down one could compress the probe with a torque and put the screws when the torque is still applied on the probe and then release everything.

As already mentioned another possibility to improve the readings should be to reduce as much as possible the thickness of the plates and put more than three plates in parallel (capacitance is proportional to the number of plates). The problem in this case is the precision one can reach with thickness avoiding possible problems of deformation of the plates, which are more delicate when thickness is reduced. Another problem with this kind of configuration would be the electrical schemes and how to divide so many plates. In fact due to space restrictions only two coaxial wires can fit in the pipe which reaches the instrumental tree. So the external plates should be electrically attached together (as we did for the two external plates in our test) and they could bring two signals (I_L, V_L) while the inner one could bring the other two (I_H, V_H). To divide the plates we could use kevlar strings as done for our test even if a big quantity of this material could effect unexpectedly the measurements or introduce a temperature dependence on the measurements not visible in our case because we had a little amount of this material.

We can conclude that this capacitance probe could help during the measurements because is very stable and can read where the standard one is blind and one could improve the readings as described before. But due to its low sensitivity and low overall change in capacitance value it should be worthy to use it together with the standard liquid level probe in order to compare the two and use the capacitance probe when the other one is blind.

APPENDIX B

PARTICLES BEAM FOCUSING WITH QUADRUPOLES [1)]

B.1 Introduction

A group of particles creates a beam when all the particles move in the same direction with a little spread in the plane perpendicular to the direction of movement and with more or less the same momentum.
The dynamic of the beam is driven by the magnetic structure of the machine. The LHC will be a machine with separate functions, i.e. where bending magnets (made to maintain the beam on radius of reference) are separated from focusing magnets (the ones which prevent the spread of the particles in the beam).
To study the dynamic of the beam is useful to represent every particle as a point in a six-dimension space, called phase-space, in which the first three coordinates specify the position and the other three the momentum of a particle. The beam occupies a position in the phase-space, in which one takes a particle as reference, more or less in the center of the distribution of the particles, which is transported in the accelerator. We take the path of this particle as trajectory of reference (orbit) in the magnetic system and its momentum as momentum of reference. If the beam has to remain the same the accelerator has to guarantee that every particle initially "near" in the phase space to the particle of reference remains "near" to it all the time oscillating around it. The oscillations for longitudinal position and momentum are coupled and are called "synchrotron oscillations" while the ones for transversal position to the direction of movement are called "bethatron oscillations" and they can be limited by quadrupoles.
In a uniform magnetic field, a charged particle, with velocity vector perpendicular to the magnetic field, moves on a circular path, in which the radius r is linked to the momentum p of the particle, to the charge q and to the density of flux B_0 from:

$$p = qB_0 r \qquad \text{(B.1)}$$

The momentum of reference is used to determine the field which bending magnets have to produce to maintain the particle of reference on the radius of the machine. In the machine with separate functions this field is produced from dipoles. The product ρB is called "rigidity of the beam".

B.2 Motion of a charged particle in a quadrupole

A charged particle in a magnetic-static field **B** experiences a force **F** given by:

[1)] Reference in [4]

$$\mathbf{F} = q\mathbf{v}\times\mathbf{B} \qquad \text{(B.2)}$$

where q is the particle charge and **v** its velocity. But a force is the time derivative of the momentum and the velocity is the time derivative of the position so we can use the equation to obtain a differential equation of the motion with time as independent variable. But we are interested in motion of particles closed to the one of reference. The magnetic system of the machine has guarantee that motion of these particles is stable, i.e. every particle, initially given a little movement and a little angle respect to the orbit of reference, has to stay near to this orbit for all successive times. Let us call **P** the position of this particle with these coordinates:

- s: distance on the equilibrium orbit measured from a casual point chosen to the point on the orbit closest to **P**
- x: the horizontal component of the motion of **P** from the equilibrium orbit
- z: the vertical component of motion

So we have:

$$m\frac{d^2x}{dt^2} = q(v_sB_z - v_zB_s)$$
$$m\frac{d^2z}{dt^2} = q(v_xB_s - v_sB_x) \qquad \text{(B.3)}$$

Now we have to ask that:

- a particle is not deflected on a reference trajectory
- the equations B.3 are decoupled and linear

So we get:

- $B_x(s,0,0)$ and $B_z(s,0,0)$ are equal to zero
- $B_s(s,0,0)$ is zero
- $B_x(s,x,z)=cz$ and $B_z(s,x,z)=cx$ with c arbitrary constant

From Maxwell's equations for magneto-static in vacuum we have:

$$div\mathbf{B} = 0$$
$$\mathbf{curlB} = 0 \qquad \text{(B.4)}$$

It follows that a scalar potential function f exists and:

$$\mathbf{B} = \mathbf{grad}\, f$$
$$\nabla^2 f = 0 \qquad \text{(B.5)}$$

The simplest potential is in the form:

$$f(s,x,z) = G(s)xz \qquad \text{(B.6)}$$

So that

$$\begin{cases} B_s = \dfrac{\partial f}{\partial s} = G'(s)xz \\ B_x = \dfrac{\partial f}{\partial x} = G(s)z \\ B_z = \dfrac{\partial f}{\partial z} = G(s) \end{cases} \qquad \text{(B.7)}$$

An ideal quadrupole is an object which has a potential like B.6 with *G(s)* constant for all the length of the quadrupole itself (obviously this is an approximation).
In such a case the equations B.3 become:

$$\begin{aligned} m\frac{d^2x}{dt^2} &= qv_sGx, \\ m\frac{d^2z}{dt^2} &= qv_sGz, \end{aligned} \qquad \text{(B.8)}$$

But using B.1, $v_s \approx v$ and s as independent coordinate we have:

$$\begin{aligned} \frac{d^2x}{ds^2} - \frac{qG}{p}x &= 0 \\ \frac{d^2z}{ds^2} + \frac{qG}{p}z &= 0 \end{aligned} \qquad \text{(B.9)}$$

This is a system of decoupled equations and each of them is of the form:

$$\frac{d^2y}{ds^2} = -K(s)y \qquad \text{(B.10)}$$

where *y* represents both, vertical and horizontal motion.

The solution of a linear equation of the second order as B.10 (with K(s) variable) is determined uniquely from the initial values of *y* and its derivative *y'*:

$$y(s) = ay(s_0) + by'(s_0)$$
$$y'(s) = cy(s_0) + dy'(s_0) \qquad \text{(B.11)}$$

or in matrix form:

$$Y(s) = \begin{bmatrix} Y(s) \\ Y'(s) \end{bmatrix} = M(s \mid s_0)Y(s_0) = \begin{bmatrix} a & b \\ c & d \end{bmatrix} \cdot \begin{bmatrix} y(s_0) \\ y'(s_0) \end{bmatrix} \qquad \text{(B.12)}$$

The utility of the matrix form is to divide the properties of the general solution of the problem from the specific properties of the particular solution: the matrix M depends exclusively from the function *K(s)* between s_0 and s.
Then the matrix of every interval composed from sub-intervals is the product between the sub-intervals themselves i.e.:

$$M(s_2 \mid s_0) = M(s_2 \mid s_1)M(s_1 \mid s_0) \qquad \text{(B.13)}$$

But the equation B.10 is linear and does not contain derivative at the first order so that det(M)=1.
In our case if we indicate L as the length of the quadrupole and with $K=qG/p$, $G>0$, the transfer matrixes are:

$$M_x = \begin{bmatrix} \cosh(K^{1/2}L) & K^{-1/2}\sinh(K^{1/2}L) \\ K^{1/2}\sinh(K^{1/2}L) & \cosh(K^{1/2}L) \end{bmatrix} \qquad \text{(B.14)}$$

$$M_x = \begin{bmatrix} \cos(K^{1/2}L) & K^{-1/2}\sin(K^{1/2}L) \\ -K^{1/2}\sin(K^{1/2}L) & \cos(K^{1/2}L) \end{bmatrix} \qquad \text{(B.15)}$$

So we have a **focusing** effect in axial direction ("*c*" factor of the matrix is >0) and **defocusing** effect in radial direction ("*c*" factor of the matrix is <0). If we rotate the quadrupole of 90° the directions are inverted.
In a quadrupolar field where $f(s,x,z)=Gxz$ we have:

$$|\mathbf{B}| = (B_x^2 + B_z^2)^{1/2} = G(x^2 + z^2)^{1/2} = Gr$$
$$\frac{\partial B}{\partial r} = G \qquad \text{(B.16)}$$

The peak field B_{max} on the poles of the ideal quadrupole is then Ga, where "*a*" is the aperture of the quadrupole. Using B.10 K can be expressed as:

$$K = \frac{qB_{\max}}{ap} \qquad \text{(B.17)}$$

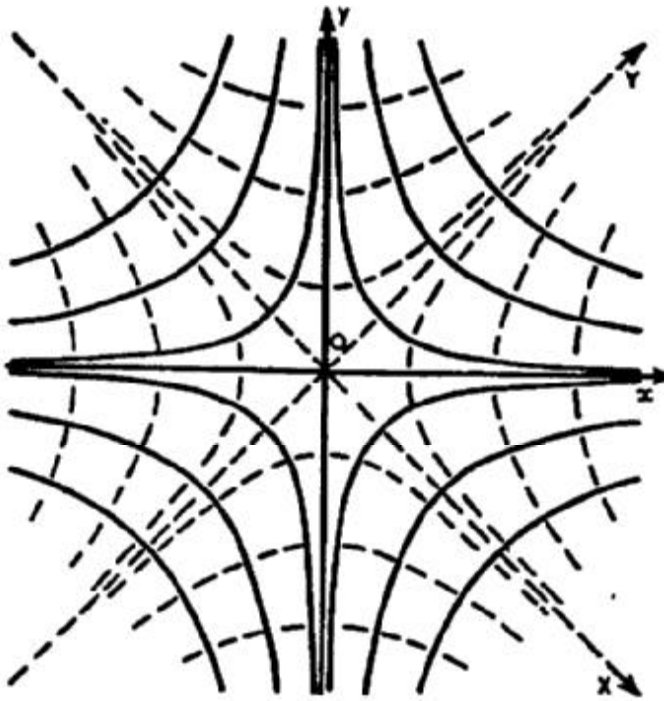

Fig. B.1 Ideal magnetic field in a quadrupole.

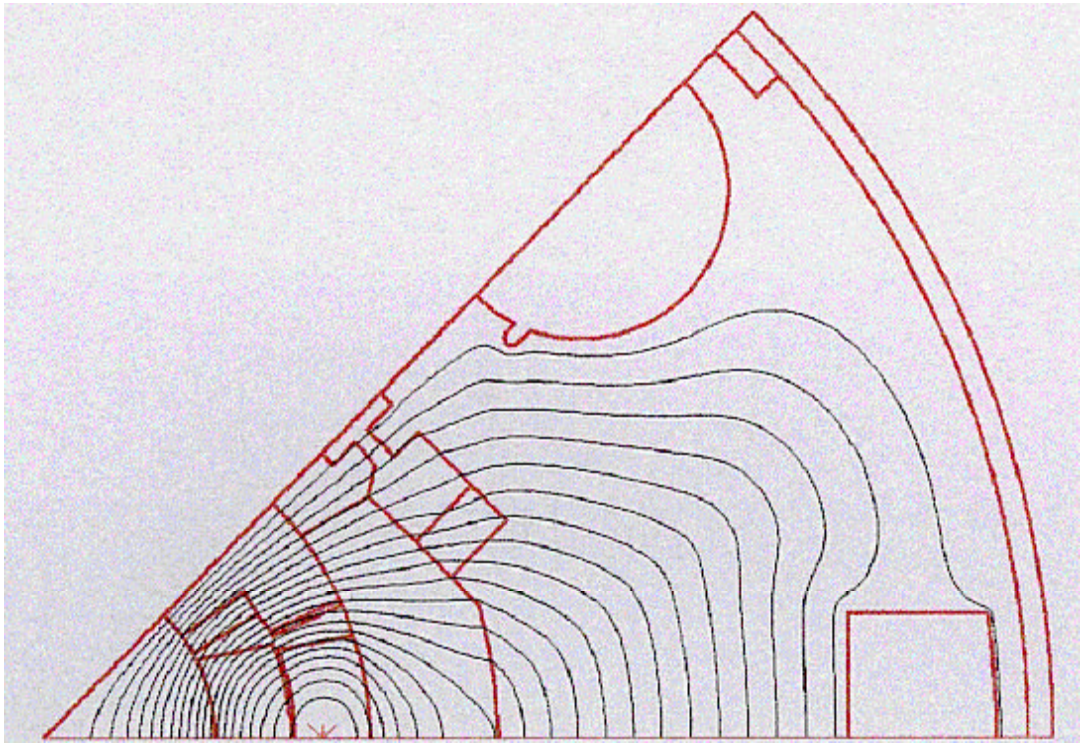

Fig. B.2 Field lines distribution in HGQ cross section.

B.3 Equivalence between a quadrupole and a thin lens

A big simplification in studies of focusing systems can be obtained by introducing the concept of thin lens. A thin magnetic lens is defined in analogy with thin lenses in optics. Its function is to focus the trajectory of a particle without adding transversal motion: moving through a plane perpendicular to the reference orbit in a given point, the direction of movement of the particle is changed by an angle proportional to the distance from the reference orbit (see Fig. B.3).

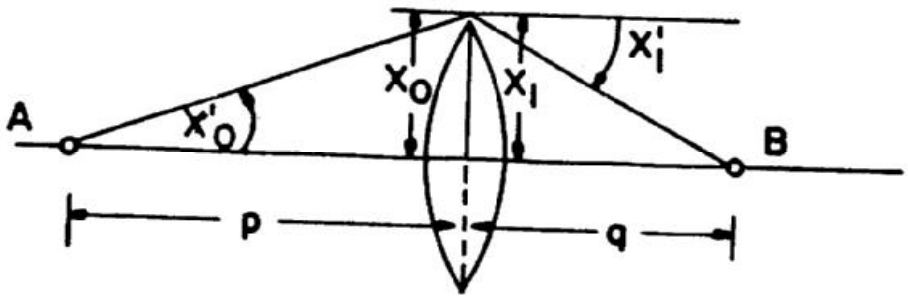

Fig. B.3 Trajectory of a particle in a thin lens.

If we consider one of the transverse directions the transfer matrix is (**focusing** lens):

$$\begin{bmatrix} x_1 \\ x'_1 \end{bmatrix} = \begin{bmatrix} 1 & 0 \\ -\frac{1}{f} & 1 \end{bmatrix} \cdot \begin{bmatrix} x_0 \\ x'_0 \end{bmatrix} \qquad \text{(B.18)}$$

where *f* is the focus length of the lens.
The following transfer matrix represents the effect of a **defocusing** lens:

$$\begin{bmatrix} x_1 \\ x'_1 \end{bmatrix} = \begin{bmatrix} 1 & 0 \\ \frac{1}{f} & 1 \end{bmatrix} \cdot \begin{bmatrix} x_0 \\ x'_0 \end{bmatrix} \qquad \text{(B.19)}$$

The transfer matrix of a **free space** of length *d* is:

$$\begin{bmatrix} x_1 \\ x'_1 \end{bmatrix} = \begin{bmatrix} 1 & d \\ 0 & 1 \end{bmatrix} \cdot \begin{bmatrix} x_0 \\ x'_0 \end{bmatrix} \qquad \text{(B.20)}$$

If we make a system where the free space of a length d precedes and follows a **convergent** thin lens, the total transfer matrix is:

$$\begin{bmatrix} 1 & d \\ 0 & 1 \end{bmatrix} \cdot \begin{bmatrix} 1 & 0 \\ -\frac{1}{f} & 1 \end{bmatrix} \cdot \begin{bmatrix} 1 & d \\ 0 & 1 \end{bmatrix} = \begin{bmatrix} 1-\frac{d}{f} & 2d-\frac{d^2}{f} \\ -\frac{1}{f} & 1-\frac{d}{f} \end{bmatrix} \qquad \text{(B.21)}$$

If we equalize the transfer matrix of the **focusing** plane of a quadrupole (B.15) with B.21 we obtain:

$$\frac{1}{f} = K^{1/2}\sin(K^{1/2}L)$$
$$d = \frac{1}{K^{1/2}}\tan\left(\frac{K^{1/2}L}{2}\right) \qquad \text{(B.22)}$$

An analogous procedure done for a **defocusing** lens and the transfer matrix of the defocusing plane of a quadrupole (B.14) gives:

$$\frac{1}{f} = K^{1/2}\sinh(K^{1/2}L)$$
$$d = \frac{1}{K^{1/2}}\tanh\left(\frac{K^{1/2}L}{2}\right) \qquad \text{(B.23)}$$

Usually the focusing length is much bigger than the geometric length of a quadrupole so:

$$f >> L \qquad \text{(B.24)}$$

i.e.

$$K^{1/2}L\sin(K^{1/2}L) << 1 \qquad \text{(B.25)}$$

Indicating with *F* the quantity related to focusing plane and *D* the quantities related to defocusing plane we could develop the equations and get:

$$f_F = \frac{1}{K^{1/2}\sin(K^{1/2}L)} = \frac{1}{KL}\left(1+\frac{KL^2}{6}+\ldots\right)$$
$$f_D = \frac{1}{K^{1/2}\sinh(K^{1/2}L)} = \frac{1}{KL}\left(1-\frac{KL^2}{6}+\ldots\right)$$
$$L_F = \frac{1}{K^{1/2}}\tan\left(\frac{K^{1/2}L}{2}\right) = \frac{L}{2}\left(1+\frac{KL^2}{12}+\ldots\right) \qquad \text{(B.26)}$$
$$L_D = \frac{1}{K^{1/2}}\tanh\left(\frac{K^{1/2}L}{2}\right) = \frac{L}{2}\left(1-\frac{KL^2}{12}+\ldots\right)$$

So at the first order we get:

$$f_F = f_D = \frac{1}{KL} = \frac{ap}{qB_{\max} L} = \frac{B_0 r}{GL} \qquad \text{(B.27)}$$

$$L_F = L_D = \frac{L}{2} \qquad \text{(B.28)}$$

Relations B.27 and B.28 give the equivalence between the action of a quadrupole in a chosen plane and the action of an optic system made of a thin lens (focusing or defocusing depending on the considered plane). This lens would be positioned at the center of the length (considered free space) of a quadrupole.
Magnetic quadrupoles are commonly described in terms of their polarity. The polarity gives which magnetic pole is north and which south. Inverting polarity we invert the magnetic field and exchange focusing planes in defocusing ones. In magnetic optic, the polarity of a quadrupole specifics if the horizontal plane is focusing or defocusing using the letters *F* and *D*. So a couple of magnetic quadrupoles can be labeled as *DF*, when the first is horizontally defocusing and the second horizontally focusing. In a draw in which the polarity is shown, a horizontally focusing quadrupole is represented with a convex lens while the defocusing one is represented with a concave lens as shown in figure B.4.

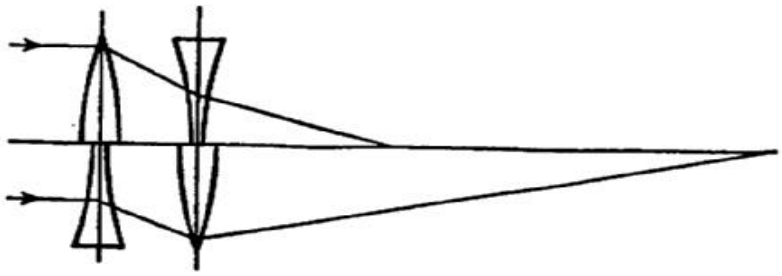

Fig. B.4 Couple of quadrupoles DF.

The low-beta insertions for the LHC are constituted of two triplets of quadrupoles. The transfer matrix of a triplet *DFD* in the horizontal plane is:

$$\begin{bmatrix} 1-2\frac{L^2}{f^2} & 2L\left(1-\frac{L}{f}\right) \\ -2\frac{L}{f^2}\left(1+\frac{L}{f}\right) & 1-2\frac{L^2}{f^2} \end{bmatrix} \qquad \text{(B.29)}$$

Where $f_F/2 = f_D/2 = f/2$ and L is the space between quadrupoles. To have the action of the triplet in the vertical plane we can just invert f with $-f$.
The triplet is useful because brings the symmetric beam of the two planes in a beam still symmetric.

In the LHC they are used to shrink to a minimum value the geometric dimensions of the beam in the two planes for the intersection point. Seen the symmetric geometry of the system, the triplets can also bring the beam from the point of intersection where the dimension is minimum but the divergence maximum to a situation with bigger dimensions but acceptable divergence for the structure of the whole machine. Figure B.5 shows these characteristics.

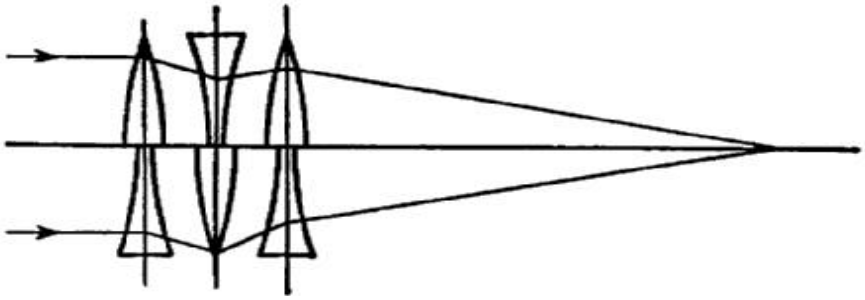

Fig. B.5 Triplet *DFD*.

BIBLIOGRAPHY

[1] **M.N. Wilson**, *Superconducing Magnets*, Oxford University Press (N.Y. 1983)

[2] **S. Fehers**, *Superconducting Accelerator Magnets*, Fermilab Seminar, Summer 1999

[3] **L. Rossi**, *Superconducting Magnets Academic Training CERN*, June 2000

[4] **F.M. Ametrano**, *Studio di un Quadrupolo Superconduttivo in Nb_3Sn per le Inserzioni low-b di LHC, Tesi di Laurea*, Università degli studi di Milano

[5] **V. Maroussov**, **A. Siemko**, *A Method to Evaluate the Temperature Profile in a Superconducting Magnet During a Quench*, Proc of Conf. ASC'98, September 1998

[6] **V. Maroussov**, **S. Sanfilippo**, **A. Siemko**, *Temperature Profiles During Quenches in LHC Superconducting Dipole Magnets Protected by Quench Heaters*, Proc. of Conf. MT-16, March 1999

[7] **L.R. Evans**, *The Large Hadron Collider*, Proc. of Conf. PAC'95, 1995

[8] **A.V. Zlobin et al.**, *Quench Performance of Fermilab High Gradient Quadrupole Short Models for the LHC Interaction Regions*, Proc. of Conf. PAC'99, 1999

[9] **M.J. Lamm et al.**, *Quench Protection Studies of LHC Interaction Region Quadrupoles at Fermilab*, Proc. of Conf. PAC'99, 1999

[10] **J. Kerby et al.**, *Status of the LHC Inner Triplet Quadrupole Program at Fermilab*, Proc. of Conf. ASC'00, September 2000

[11] **P. Schlabach et al.**, *Field Quality in Fermilab-built Models of Quadrupole Magnets for the LHC Interaction Region*, Proc. of Conf. ASC'00, September 2000

[12] **S. Fehers et al.**, *Quench and Mechanical Performance for Fermilab Model Magnets for the LHC Inner Triplet Quadrupoles*, Proc. of Conf. ASC'00, September 2000

[13] **T. Peterson et al.**, *Thermal Studies of a High Gradient Quadrupole Magnet Cooled with Pressurized, Stagnant Superfluid*, Proc. of Conf. ASC'00, September 2000

[14] **P. Bauer et al.**, *Busbar Studies for the LHC Interaction Region Quadrupoles*, Proc. of Conf. ASC'00, September 2000

[15] **M.J. Lamm et al.**, *Quench Protection of the LHC Inner Triplet Quadrupoles Built at Fermilab*, Proc. of Conf. ASC'00, September 2000

[16] **G. Sabbi**, *Load Lines and short sample limits for HGQ S01*, Fermilab TD-97-034, April 1997

[17] **G. Sabbi**, *Magnetic Field Parameters of HGQ06 Coils Ends*, Fermilab TD-99-003, January 1999

[18] **G. Sabbi**, **P. Bauer**, *Critical Current Parametrization and Short Sample Limit Calculation for the LHC IR Quadrupole Magnets*, Fermilab TD-99-007, March 1999

[19] **S.W. Kim**, **G. Sabbi**, **P. Bauer**, **J. Ozelis**, **R. Bossert et al.**, *Superconducting Strand and Cable*, HGQ Short Model R&D, 2000

[20] **A. Zlobin**, *Interaction Region Quad (IRQ) Quench Protection Analysis*, Fermilab TD-95-008, November 1995

[21] **M.J. Lamm**, **R. Ostojic**, *Test Results of the 1-m 70mm Aperture CERN-Oxford Quadrupole Q3*, LHC Project Note 157, July 1998

[22] **R. Bossert et al.**, *Study of Kapton Insulated Superconducting Coils Manufactured for the LHC Inner Triplet Model Magnets at Fermilab*, Proc. of Conf. PAC'99, 1999

[23] **J.P. Ozelis et al.**, *Mechanical Design and Analysis of LHC Inner Triplet Quadrupole Magnets at Fermilab*, Proc. of Conf. PAC'99, 1999

[24] **J. Kerby et al.**, *Design, Development and Test of 2m Quadrupole Magnets for the LHC Inner Triplet*, Proc. of Conf. ASC'98, September 1998

[25] **M.J. Lamm et al.**, *Quench Protection Studies of Short Model High Gradient Quadrupole*, Proc. of Conf. ASC'98, September 1998

[26] **K.H. Mess**, **P. Schmuser**, **S. Wolff**, *Superconducting Accelerator Magnets*, World Scientific 1996

[27] **A. P. Verweij**, *Electrodynamics Of Superconducting Cables in Accelerator Magnets*, PhD Thesis, Twente University

[28] **CERN Accelerator School**, *Superconductivity in Particle Accelerators*, Yellow Book CERN 96-03, May 1996

[29] **NASA Tech Briefs.**, *Improved Capacitance Liquid-Level Probe*, Cleveland, 1995

[30] **Ryan D. Swain**, *The Designing and Application of the Helium Liquid-Level Capacitance Probe*, Fermilab, Summer 1996

[31] **Vincent D. Arp**, **Robert D. McCarty**, *Thermophysical Properties of Helium-4 from 0.8 to 1500 K with Pressures to 2000 MPa*, NIST Technical Note 1334, National Institute of Standards and Technology (NIST), 1989

THANKS

It should be the easiest part of this thesis but I do not know where to start…
First of all I would like to thank all the people who helped me to live a great experience which taught me many things about physics and not only…Thanks to **Lucio Rossi** who believed in me found the possibility to send me at Fermilab (probably I stressed him too much!!!), where **Peter Limon** and **John Tompkins** accepted to have me for more than one year…
A special thank to **Mike** who taught me everything he can about his experience in superconducting magnet. Not only I learned many things about magnets but also how to enjoy research in physics and learn always new things…unluckily I'll never be a good "salesman"…thanks Mike for all your patience…
Thanks to **Sandor** who taught me how to be helpful during the tests a lot better than I taught him few words in Italian…thanks to everyone in IB1 especially **Tom P.**, **Roger R.**, **Roger N.**, **Joe**, **Darryl**, **Ruben**, **Irene**, **Dean**, **Danny**, **Penny**, **Katie** who probably were afraid of my problems all the times I went to their offices…thanks to **Tom W.** and his great help for the tests of the capacitance probe…thanks to **Sharon** and her great disposability…

Thanks to **Stephan** for coffee, cookies, Santa Klaus, lobsters and his experience always shared in discussions…Thanks to **Janaya** and **Dawn** who helped me when I arrived in the "boring" Illinois (it's not even so boring!!!) without knowing anyone and anything…siete fantastiche…
And now please let me stop writing in English…I seem so intellectual but it is only because if I write in English I have an excuse…if I write something wrong I can say it's not my mother tongue and I can hide my terrible Italian…spero mi perdoniate gli errori…
Continuo coi ringraziamenti a persone incontrate lungo la strada in questo ultimo anno…grazie a **Cristian** che mi ha introdotto nell'ambiente e mi ha spiegato ogni cosa da fare all'arrivo e come sopravvivere prendendo in cambio un cattivo rimedio contro la tosse…grazie a **Fabietto** e le sue cenette, **Andrea** e ai suoi cd…**Giovanni** e **Gianpaola** per l'aiuto che mi hanno dato in ogni difficoltà…
Un grazie particolare agli amici di viaggio degli ultimi mesi…**Lucio** e la sua capacità di dare consigli e infondere certezze con l'aiuto degli amichetti "boh" e "mah"…**Michela** e la sua simpatia, comprensione, aiuto, sostegno, affetto, per gli innumerevoli passaggi ovunque, le belle chiacchierate, il fantastico panello…GRAZIE di cuore…

Ora posso riprendere da oltre oceano dove tante altre persone anche se lontane mi sono state vicinissime…e non solo in questo ultimo anno ma da molto più tempo…
Innanzi tutto grazie a **mamma** e **papà** che mi hanno sempre spronato ad esperienze nuove e mi hanno sempre appoggiato e sostenuto in ogni passo…e sono tanti in 24 anni…grazie al mio fratellino **Matteo**…la sua energia e le sue chiacchiere…ai miei **nonni** e le meravigliose estati con loro…**Fabio** e **Laura**… a zio **Gianni** che mi ha insegnato molto…prima o poi anche la trasgressione…a zia **Elena** per l'aiuto e le poche correzioni (ti ho lasciato poco tempo di proposito!!!)…zia **Emilia** e zio **Paolo**…

Un grazie speciale a **Michele** e a tutta la pazienza che ha mostrato nel sopportare una pazza lunatica come me…all'appoggio che mi ha dato nei momenti difficili durante tutto il periodo universitario…grazie per l'attesa e la fiducia…

Grazie alle amichette del cuore che hanno reso più piacevole la vita universitaria…**Alessandra**, **Silvia** e **Francesca**…grazie per le chiacchierate più o meno colte di tutti questi anni e perché è bello non essere soli nella confusa strada da percorrere nella vita…forse ancora meglio un bar che serve tè con biscotti al cioccolato…

Grazie ad **Anna** e **Pata&Mauro**…e poi…e poi **Roberto** e i suoi racconti incompiuti, **Gigi** e i suoi consigli, **Maurizio** e la compagnia nelle innumerevoli corse al Giuriati, **Marco** e **Daniela**, **Gala** e **Marta**, **Cicu** per la simpatia e le belle serate in compagnia…**Silvia** e **Danilo, Massi** e **Claudia**, **Luca** amici musicisti da tanto tempo…a **Mello**, **Paco**, i **bufali**, le **oche**, gli **scoiattoli** e la **neve**, e a tutto ciò e tutti quelli che ho dimenticato…

ps…perché non si è mai detto tutto vero?!?

Grazie a tutti!!!